Nano-precipitation and Transformations in Borosilicate Glasses by Electron Irradiation

Mohammed Faeq Mohammed Sabri

Department of Materials Science and Engineering

The University of Sheffield

This thesis is submitted in partial fulfilment of the requirements for
the degree of Doctor of Philosophy in
Materials Science and Engineering

June 2016

Abstract

Nanoprecipitation has been achieved in different types of oxide glass using an electron irradiation technique in transmission electron microscope (TEM). The widely used methods to precipitate nanoparticles in glass include conventional annealing methods, ion implantation and laser irradiation. Furthermore, all the previous studies that utilised electron irradiation for precipitation were performed using conventional irradiation via a wide un-converged electron beam without any patterning attempts. In this project, different varieties of borosilicate (BS) glass were loaded and doped with different cations and were irradiated using both a conventional stationary converged electron beam of different diameters, and a newly introduced irradiation method for patterning. For this purpose, a transmission electron microscope operating at 200 and 300 keV was used. The main aim was to induce local precipitation of nanoparticles in these glasses as well as nano-patterning using the two aforementioned irradiation methods, while the region outside the electron beam (e-beam) remains un-affected.

Several borosilicate glasses, loaded and doped with three different cations of Zn, Cu and Ag, were investigated by means of electron beam irradiation in TEM. While the former cations (Zn and Cu) were the only loaded cations in their respective glasses, Ag was doped with extra dopants. Upon electron beam irradiation, a variety of patterns and nanoparticles (NPs) of different shapes and sizes were achieved in the Zn and Cu glasses. The Ag-doped glass, however, showed a different behaviour under electron beam irradiation, with the main electron irradiation contributing to phase separation in addition to the occurrence of precipitation and phase separation at the same irradiated region.

While the main effect of the electron beam irradiation was nanoprecipitation, a few other secondary effects of irradiation were observed, including: the occurrence of self-ordered

nanoparticles in Zn glasses, copper sodium borosilicate glass of high Cu content (CuNBS-A) and sodium borosilicate glass doped with silver and cerium (NBS-AC); the formation of nanoparticle chains in Zn and CuNBS-A glasses; the sudden transformation of a glass fragment into a ball shape in the CuNBS-A glass; and the rounding and smoothing of the glass fragment in all these glasses.

An *in-situ* heating experiment in the zinc borosilicate glass of high Zn content (ZBS-A), on the other hand, did not trigger any particle formation at temperatures between 100-300 ^{o}C and also did not change the overall glass fragment.

Exploring morphological transformation in some other types of oxide glass under electron beam irradiation at energies of 120, 200 and 300 keV revealed that this phenomenon occurs due to materials flow via radiation-induced fluidity (RIF), as evidenced by the rounding of the glass fragments.

Acknowledgements

First of all, I would like to express my deep thanks to my respected supervisor Dr Günter Möbus for his valuable help, advice and guidance throughout this research. I really appreciate his continuing kindness, support and encouragement. My thanks and acknowledgements also go to Prof. Russell Hand for his valuable help in a variety of ways.

I would like to thank Mrs Jean Simpson and all my current and past colleagues in the NanoLab for their help and assistance during this research.

I would also like to thank Dr Lisa Hollands and Mr Ian Watt for their help and guidance during glass melting. My thanks also go to Mr Michael Bell, who trained me in the cutting and polishing of glass samples. Thanks also go to Dr Nik Reeves for his training on the X-ray diffraction (XRD) instrument. I would like to thank and acknowledge Dr Peng Zeng, Dr Le Ma and Dr Peter Korgul for their valuable advice and training in transmission electron microscopy (TEM) and scanning electron microscopy (SEM) at the Sorby Centre. I also thank Dr Ian Mark Ross for his high resolution transmission electron microscopy (HRTEM) training. Thanks also go to all the staff in Department of Materials Science and Engineering who have helped and assisted me during my study.

I would like to thank my lovely wife Mrs Neveen Botani for her valuable help, support, tolerance and encouragement during daily life and also when I was facing difficulties throughout my study. My thanks also to my dear son Miran and my lovely daughter Nazli. Thanks also go to my dear mother for her support, my late father, who was wishing to see this day, my lovely aunts, my mother-in-law for her enormous help and encouragement, my brother and sisters, relatives and all my friends for their help and encouragement.

Finally, I would like to thank the Iraqi Kurdistan Regional Government (KRG)/Ministry of Higher Education and Scientific Research-Human Capacity Development Program (HCDP) for their funding, without which this research would not have been possible.

List of contents

Abbreviations used in this thesis

TEM: transmission electron microscopy.

BS: borosilicate glass.

e-beam: electron beam.

NPs: nanoparticles.

CuNBS: copper sodium borosilicate glass.

NBS-AC: sodium borosilicate glass doped with silver and cerium.

ZBS: zinc borosilicate glass.

RIF: radiation-induced-fluidity.

ABS: alkali borosilicate glass.

NBOs: non-bridging oxygens.

PS: phase separation.

GC: glass-ceramic.

T_g: glass transition temperature.

T_m: melting temperature.

BF: bright field image.

EFED: energy filtered electron diffraction.

NED: nano electron diffraction.

STEM: scanning transmission electron microscopy.

EELS: electron energy loss spectroscopy.

EDS: energy dispersive X-ray spectroscopy.

FIB: focused ion beam.

ADF: annular dark field image.

HRTEM: high resolution transmission electron microscopy.

FFT: fast Fourier transformation.

SAED: selected area electron diffraction.

RED: radiation enhanced diffusion.

BO: bridging oxygen.

XRD: x-ray diffraction.

NP: nanoparticle.

SEM: scanning electron microscopy.

EDX: energy dispersive x-ray.

JEOL: Japanese electron optics laboratory.

CCD: charged coupled device.

SE: secondary electron.

BSE: backscattered electron.

FE: field emission.

LaB_6: lanthanum hexaboride.

FEG: field emission gun.

CA: condenser aperture.

SIM: stationary irradiation mode.

LSIM: line scan irradiation mode.

CCU1: carbon coater unit one.

KBS-AFCN: potassium borosilicate glass doped with silver, iron, cerium and neodymium.

NLBS-CCZ: sodium lithium borosilicate glass doped with cerium, chromium and zirconium.

NBS: sodium borosilicate glass.

AR: aspect ratio.

AlCBS: aluminium calcium borosilicate glass.

List of tables

List of appendix tables

List of figures

List of appendix figures

List of publications and conferences

Reviewed journal publications

[1] **M.M. Sabri**, R.J. Hand and G. Möbus. Zn nanodot patterning in borosilicate glasses by electron irradiation. Journal of Material Research, 2015, **30**, 1914-1924.

[2] **M.M. Sabri** and G. Möbus. Electron irradiation induced nanocrystal formation in Cu-borosilicate glass. Journal of Nanoparticle Research, 2016, **18**, 1-9.

[3] **M.M. Sabri** and G. Möbus. Particle precipitation by electron beams in multiple borosilicate glasses (In preparation).

Refereed conference proceeding

[1] **M.M. Sabri**, R.J. Hand and G. Möbus. Nanoparticle Formation in Borosilicate Glasses under Electron Irradiation. Published in The University of Sheffield Engineering Symposium (USES) Conference Proceeding. USES Conf. Proc. **02** (2015); doi: 10.15445/02012015.25.

[2] **M.M Sabri** and G. Möbus. Electron Beam Writing in Oxide Glasses via Irradiation Induced Metal Nanodots. Institute of Physics EMAG 2016 Conference. Durham-UK, 6-8 April 2016. Published in the abstract book of EMAG 2016, Electron Microscopy and Analysis Group Conference 2016, pp 39-40.

[3] **M.M. Sabri**, R.J. Hand and G. Möbus. Electron Beam Patterning of Glasses via Metal Nanoparticle Precipitation. European Society of Glass 2016 Congress. Sheffield-UK, September 2016.

Oral presentation at conferences

[1] **M.M. Sabri**, R.J. Hand and G. Möbus. Nanoparticle Formation in Borosilicate Glasses under Electron Irradiation, 24 June 2015, University of Sheffield Engineering Symposium (USES), the Octagon Centre.

Poster presentation at conferences

[1] **M.M. Sabri**, U.M. Bhatta, G. Möbus and R.J. Hand. Electron irradiation-induced nanoscale shape transformations. The 7th International nanoscience Student Conference, 19-22 August 2013, the London Centre for nanotechnology, London.

[2] **M.M. Sabri**, R.J. Hand and G. Möbus. Irradiation Engineering of Materials for Tuning Optical and Mechanical Surface Properties of Glasses. University of Sheffield Engineering Symposium (USES), 24 June 2014, the Octagon Centre.

[3] **M.M. Sabri**, R.J. Hand and G. Möbus. Irradiation Induced Zinc Nanodot Pattern Formation in Borosilicate Glasses. Microscience Microscopy Congress, 30 June – 03 July 2014, Manchester Central.

[4] **M.M. Sabri** and G. Möbus. Nanoparticle Formation in Borosilicate Glasses Under Electron Irradiation. Institute of Physics EMAG 2016 Conference. Durham-UK, 6-8 April 2016.

Attended conferences

[1] The 5th Annual Postgraduate Symposium on Nanotechnology, 14 December 2015, University of Birmingham-School of Chemistry.

Thesis outline

This thesis is organized as follows. Chapter one provides an introduction to the study and sets out its aims. Chapter two is a literature review, covering work on glass in general and, in particular, the irradiation of the glass in TEM. In the second part of this chapter, some important studies on electron beam-induced precipitation and nanoparticle formation in glass and electron beam-induced shape transformations are explored. The materials and also the techniques used throughout this research work will be articulated in chapter three. Chapter four presents the important findings of the study in respect to electron irradiation in Zn glasses followed by the electron irradiation studies in Cu glasses in chapter five. In chapter six, the results obtained from the irradiation of Ag borosilicate glasses will be presented. Electron irradiation-induced morphological transformations in various glasses will be presented in chapter seven. Chapter eight discusses these findings and chapter nine summarises the main conclusions of the research.

Chapter One

Introduction

1.1 Electron beam irradiation-induced transformations in oxide glasses

The interaction of radiation with matter has become an important branch of modern science due to the motivation of studying the phenomena caused by this interaction. In particular, ionizing radiation has the ability both to provide local irradiation and to irradiate the entire volume of the material. Investigating oxide glass under electron irradiation is of particularly great interest [Jiang and Silcox, 2002, Sun *et al.*, 2004, Sun *et al.*, 2005, Ollier *et al.*, 2006, Möbus *et al.*, 2008 and Möbus *et al.*, 2010] due to its importance not only for nuclear applications but also for applications in nanotechnology. As reported in [Egerton and Malac, 2004], electron irradiation effects can be classified as shown in Fig. 1-1.

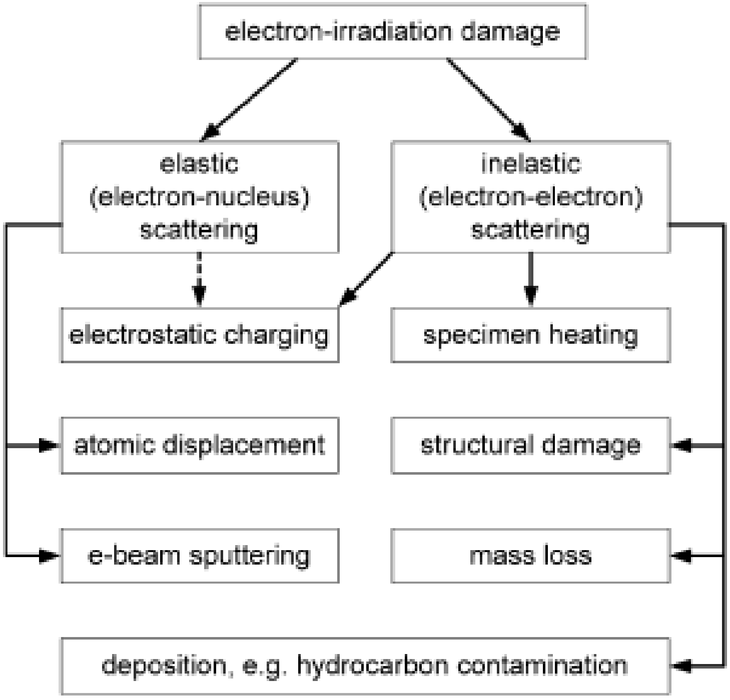

Figure 1-1: Categorization of electron irradiation effects in the specimen depending on the types of electron scattering [Egerton and Malac, 2004].

The electron beam generated by a transmission electron microscope (TEM) can be used for direct-write inorganic lithography, while the sub-nm electron beam can be used to produce nano-rings and nanopores in glass and other amorphous materials. Electron beam irradiation is a powerful technique for the fabrication and manipulation of nanostructures. In addition, it is used to modify the local properties, structure and composition of glass *in-situ* [Jiang, 2013]. The modifications obtained by high-energy electron irradiation include phase separation [Sun *et al.*, 2004], precipitation [Jiang *et al.*, 2000], gas bubble formation [Ollier *et al.*, 2006], alkali migration [Jiang and Silcox, 2002 and Sun *et al.*, 2004], crystallization, fluidity enhancement and shape transformation [Möbus *et al.*, 2008 and Möbus *et al.*, 2010]. Of particular interest is the irradiation-induced precipitation of nanoparticles in glass. It has been known that precipitation of nanoparticles in glass can be obtained via thermal treatment above the glass annealing temperature, but it is difficult to control the spatial distribution of nanoparticles by thermal treatment alone. Electron irradiation can be an alternative, and very effective, approach to precipitate nanoparticles in glass without any thermal treatment [Jiang *et al.*, 2007]. The electron beam irradiation effect can result in extraordinary microstructures or great size distributions of embedded nanoparticles in the host glass matrix. These extraordinary nanostructures can be exploited for use in optical devices [Singh and Karmakar, 2011].

Oxide glass, especially alkali borosilicate (ABS), is chosen as a host matrix for nanoparticle formation/precipitation because of its relative flexibility and homogeneity, which allows a large range of extra metal cations to be added. In comparison with crystalline materials, there are more unfilled sites in glass that can accommodate the atoms being displaced [Jiang *et al.*, 2004]. In addition, glass can serve as a matrix for nanostructures as it can be designed and tuned according to requirements, and also its fabrication is usually feasible and inexpensive [Bach, 1998 and Jiang, 2010] and can be used in the immobilization of radionuclides [Weber *et al.*, 1997]. In the latter application, elements can be immobilized by chemical bonding into the glass structure. If the chemical solubility is exceeded, however, a wide range of nanocrystal precipitation will occur in the volume of the glass, as well as in the glass surface.

Metal nanoparticles in glass reveal a wide range of useful physical features and provide excellent prospects for significant technological applications in comparison with bulk metal [Wang *et al.*, 2005] and may improve the nonlinear optical properties of the glass [Beecroft and Ober, 1997 and Ren *et al.*, 2009]. Electron irradiation can be used to generate metal nanoparticles in oxide glasses and therefore micro/nano-structures with a large size distribution of nanoparticles embedded in the glass can be obtained via this technique. While these are commonly achieved by laser irradiation and sometimes by ions, little attention has been paid to electron beam irradiation-induced metal nanoparticles in oxide glasses. It is therefore important to explore this effect in different oxide glasses containing several glass-formers and modifiers.

Another particular interest in respect to electron irradiation is its potential to change the local or overall shape of glass and amorphous materials. It has been reported that irradiation of amorphous materials with high-energy radiation results in changes in the surface of those materials, such as roughening and smoothing, and this in turn leads to nanopatterning [Mayr and Averback, 2001]. Electron irradiation-induced modifications in the glass surface, such as shape changes and smoothing of the surface, has been occasionally reported such as in [Jiang *et al.*, 2005 and Singh and Karmakar, 2011]. During the experimental research for these studies, the aforementioned modifications have been observed alongside the main objective of these studies, which were focused on *e*-beam-induced precipitation. Möbus *et al.*, however, has explored this phenomenon in more detail in a few types of borosilicate glass during an electron irradiation study [Möbus *et al.*, 2010]. These glasses were exploited for nano-transformation purposes via radiation-induced fluidity (RIF) under e-beam irradiation, which can be obtained by locally changing the shape of the glass. Usually, the energy delivered by the electron beam is high enough to change the shape of the glass being irradiated by electron irradiation. The phenomenon of morphological transformation under electron beam irradiation has not only been observed in glass and amorphous materials, but also in metals embedded in an amorphous matrix (this will be discussed in more detail in chapter-2).

1.2 The research aims

All previous studies in electron irradiation-induced nanoparticle formation/precipitation in glass have only used uniform irradiation delivered by means of unconverged, and extremely wide, electron beams without attempting to achieve patterning. It is the aim of this research to use the electron beam irradiation technique for the purpose of inducing metal precipitation, and formation of metallic nanoparticles, in a range of oxide glasses loaded and doped with various cations via a stationary converged electron beam, as well as via a newly introduced method of irradiation involving line-scan patterning. The study aims to generate spatially localised regions of metal nanoparticle precipitation via both stationary and line-scan irradiation modes while leaving the glass outside the electron beam unchanged.

Using TEM means that modifications induced by the electron beam irradiation can be observed live and this opens the possibility of discovering novel phenomena, such as morphological transformation of glass under the impact of electron irradiation, which is the next aim of this research. The importance of morphological transformation via radiation-induced fluidity (RIF) is in its capability for surface modification of oxide glass, towards both smoothing and roughing, as well as homogenisation and local fluidising of the materials without affecting the entire sample, leading to nano-transformation.

1.3 References

Bach N N H 1998 The Properties of Optical Glass *Springer-Verlag*, Barlin.

Beecroft L L and Ober C K 1997 Nanocomposite Materials for Optical Applications *Chem. Mater*. **9**, 1302-1317.

Egerton R F, Li P and Malac M 2004 Radiation damage in the TEM and SEM *Micron.* **35** 399-409.

Jiang N 2010 Electron-beam fabrication of nanostructures in glasses *Microsc. Microsnal.* **16**, 1660-1661.

Jiang N 2013 Damage mechanism in electron microscopy of insulating materials *J. Phys. D: Appl. Phys*. **46**, 305502-11.

Jiang N and Silcox J 2002 Electron irradiation induced phase decomposition in alkaline earth multi-component oxide glass *J. Appl. Phys*. **92**, 2310-2316.

Jiang N, Qiu J and Silcox J 2004 Effects of high-energy electron irradiation on heavy-metal fluoride glass *J. Appl. Phys*. **96**, 6230-6233.

Jiang N, Qiu J and Spence J C H 2005 Precipitation of Ge nanoparticles from GeO_2 glasses in transmission electron microscope *Appl. Phys. Lett.* **86** 143112-3.

Jiang N, Wu B, Qiu J and Spence J C H 2007 Precipitation of nanocrystals in glasses by electron irradiation: An alternative path to form glass ceramic *Appl. Phys. Lett.* **90**, 161909-3.

Mayr S G and Averback R S 2001 Surface Smoothing of Rough Amorphous Films by Irradiation-Induced Viscous Flow *Phys. Rev. Lett.* **87**, 196106-4.

Möbus G, Ojovan M, Cook S, Tsai J and Yang G 2010 Nano-scale quasi-melting of alkali-borosilicate glasses under electron irradiation *J. Nucl. Mater.* **396**, 264-271.

Möbus G, Tsai J, Xu X J, Bingham P and Yang G 2008 Nanobead formation and nanopatterning in glasses *Microsc. Microanal.* **14**, 434-435.

Ollier N, Rizza G, Boizot B and Petite G 2006 Effects of temperature and flux on oxygen bubble formation in Li borosilicate glass under electron beam irradiation *J. Appl. Phys.* **99**, 073511-6.

Ren F, Xiao X H, Cai G X, Wang J B and Jiang C Z 2009 Engineering embedded metal nanoparticles with ion beam technology *Appl. Phys. A* **96**, 317-325.

Singh S P and Karmakar B 2011 In situ electron beam irradiated rapid growth of bismuth nanoparticles in bismuth-based glass dielectrics at room temperature *J. Nanopart. Res.* **13** 3599–3606.

Sun K, Wang L M, Ewing R C and Weber W J 2004 Electron irradiation induced phase separation in a sodium borosilicate glass *Nucl. Instrum. Methods Phys. Res. Sect. B.* **218**, 368-374.

Sun K, Wang L M, Ewing R C and Weber W J 2005 Effects of electron irradiation in nuclear waste glasses *Philos. Mag.* **85**, 597-608.

Wang X, Zhuang J, Peng Q and Li Y 2005 A general strategy for nanocrystal synthesis *Nature* **431**, 121-124.

Weber W J, Ewing R C, Angell C A, Arnold G W, Cormack A N, Delaye J M, Griscom D L, Hobbs L W, Navrotsky A, Price D L, Stoneham A M and Weinberg M C 1997 Radiation effects in glasses used for immobilization of high-level waste and plutonium disposition *J. Mater. Res.* **12** 1946-1978.

Chapter Two

Literature review

2.1 Introduction

This chapter reviews significant studies and research about the irradiation of glass and amorphous materials by a high-energy electron beam. It starts with section 2.2, which gives some definitions of glass, types of oxides, alkali-borosilicate glass and phase separation, in addition to the crystallisation in glass. Some information about transmission electron microscopy (TEM) and its use in the field of glass research will be given in section 2.3. Section 2.4 presents the effects of electron beam (e-beam) irradiation in glass, including radiolysis, knock-on and heating. The next section, 2.5, presents some important studies into electron irradiation-induced precipitation and nanoparticle (NP) formation in glass, in addition to summarizing some other techniques frequently used in precipitation and NP formation in glass. This section also includes some useful studies and findings on the phenomenon of radiation-induced-fluidity (RIF) and "quasi-melting". These are discussed in terms of the shape transformation of metal nanoparticles, glass particles and amorphous materials under e-beam irradiation. In the last section, 2.6, a brief account of the important applications of electron irradiation in glass will be given.

2.2 Glass: history and definition

Glass production has a long history. It was first produced in ancient Egypt by ancient Egyptians about 4000 years ago [Vogel, 1985]. Although these early forms of glass were based on silica, many types of glass can be formed without silica [Shelby, 2005]. At that time, the first application for glass was jewellery, but soon it began to be used in containers, windows and lenses. A variety of definitions have been used to describe glass, and although it has been defined as an amorphous solid prepared by cooling from the melt [Zallen, 1998], in fact, glass can also be prepared by vapour deposition, *sol-gel* processing of solutions and irradiation of crystalline materials [Shelby, 2005]. Another definition of glass given by Cohen *et al*. stated that glass is amorphous, disordered and metastable and can be formed by cooling the melt very fast to prevent crystallization [Cohen *et al.*, 1979]. All types of glass have two similar aspects: first, the lack of long range and periodic arrangement of atoms; second, the exhibition of time-dependent glass transformation behaviour, which occurs over a temperature range known as the glass transformation region.

2.2.1 Oxide glass

In oxide glass, oxides can be classified into two essential types: (i) glass forming oxides and (ii) glass modifying oxides [Stanworth, 1950]. Glass forming oxides are the most fundamental component of any glass batch and are also called network formers. The glass formers easily form glass and include, for example, silica (SiO_2), boric oxide (B_2O_3), zinc oxide (ZnO) and phosphoric oxide (P_2O_5) [Paul, 1982]. Glass modifying oxides, on the other hand, include soda (Na_2O), aluminium oxide (alumina-Al_2O_3) and alkaline earth and transition metal oxides. The addition of these oxides to the glass batch serves to reduce the required temperature for melting the glass. Adding modifiers to the glass has a significant effect on the network structure, such as loosening the bonds in the glass network [Greaves, 1985]. As a result, gaps can be created in the continuous network structure, hence changing the characteristics of the glass, such as reducing its viscosity and increasing its thermal expansion coefficient [McMillan, 1964]. Figure 2-1 shows the structure of pure silica (SiO_2) and the same structure after adding a modifier such as soda (Na_2O), which results in the formation of non-bridging oxygens (NBOs).

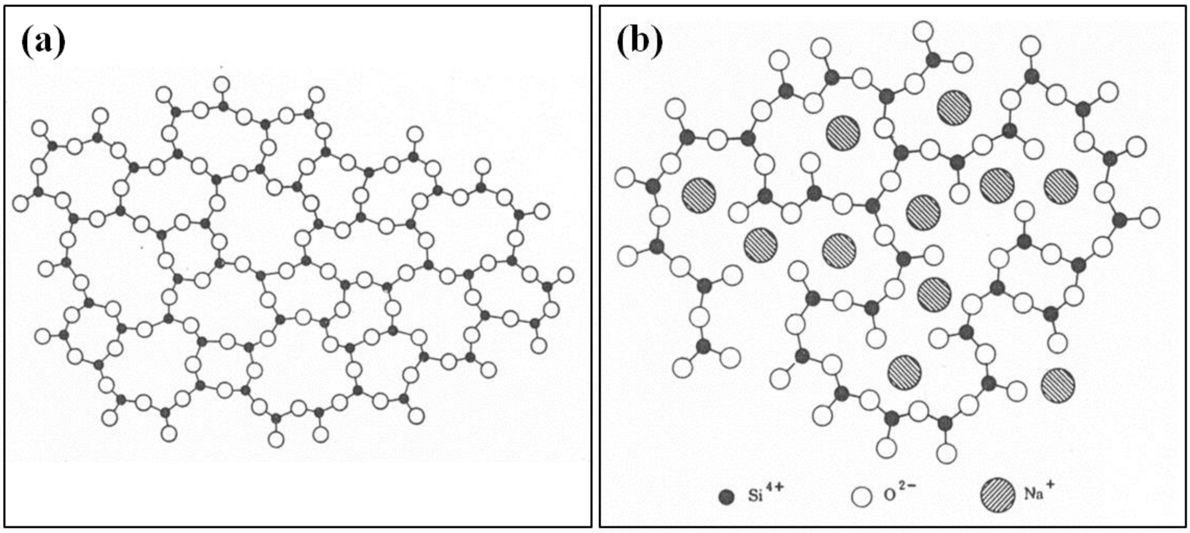

Figure 2-1: The structure of pure silica in (a) and the structure of pure silica after the addition of Na_2O in (b). The large Na^+ in (b) is formed after the breaking of oxygen bridges located in the new large cavities [Modified from Pye *et al.*, 1972].

2.2.2 Alkali borosilicate (ABS) glasses and phase separation (PS)

Borosilicate glasses are important due to their unique properties and industrial applications. In particular, they have low thermal expansion coefficients, relatively low melting points and good chemical resistance. Alkali borosilicate glasses are used in a variety of technological applications, such as in nuclear industries due to their good chemical stability and mechanical strength [Pfaender, 1966]. The structure of alkali borosilicate glass is sophisticated due to the existence of two glass network forming oxides. In the first place, boron oxide (B_2O_3) can adopt two competing types of network forming units, BO_4 tetrahedra and BO_3 planar ring structures. Silicon oxide (SiO_2), on the other hand, is purely based on SiO_4 tetrahedra. It has been reported, therefore, that the structure of alkali borosilicate glass is dependent upon the quantity of alkali ions associated with both the silicate and borate networks [Vedishcheva *et al.*, 2003].

The majority of these types of glass are transparent and phase separated at a very fine-scale morphology. Phase separation or liquid-liquid immiscibility is a common phenomenon in melt systems [Zhonghong, 1989, Shelby 2005] and has become a fundamental subject in glass since 1950 [Vogel, 1985]. In 1982, Paul defined liquid-liquid phase separation as "the growth of two or more non-crystalline glassy phases each of which will have a different composition from the over melt" [Paul, 1982]. Two essential types of glass in glass phase separation have been pointed out. These are spinodal decomposition and homogeneous nucleation. In spinodal decomposition, spontaneous separation of the melt into two phases occurs due to small fluctuations in the composition. The phase boundaries are diffuse and no crystallization takes place. Homogeneous nucleation, on the other hand, occurs due to formation of a nucleus of a critical size in the melt. It is not spontaneous, and the free energy barrier for the formation of the nucleus has to be overcome.

It has been reported that glass containing less than 20% Na_2O consists of two homogeneous phases: a silica-rich phase and an alkali borate-rich phase [Shelby, 2005]. The alkali borate-rich phase can be leached from the glass by acid such as H_2SO_4, and hence porous silica can be obtained [Elmer, 1991]. This process is usually used to produce "Vycor" glasses. Figure 2-2 shows ternary sodium borosilicate glass with an immiscibility dome and the position of "Vycor" and "Pyrex" glasses [Molchanova, 1957]. "Pyrex" is a borosilicate type of glass located outside the region of phase separation at high SiO_2 contents (~ 80%) [Cited in Vogel, 1985].

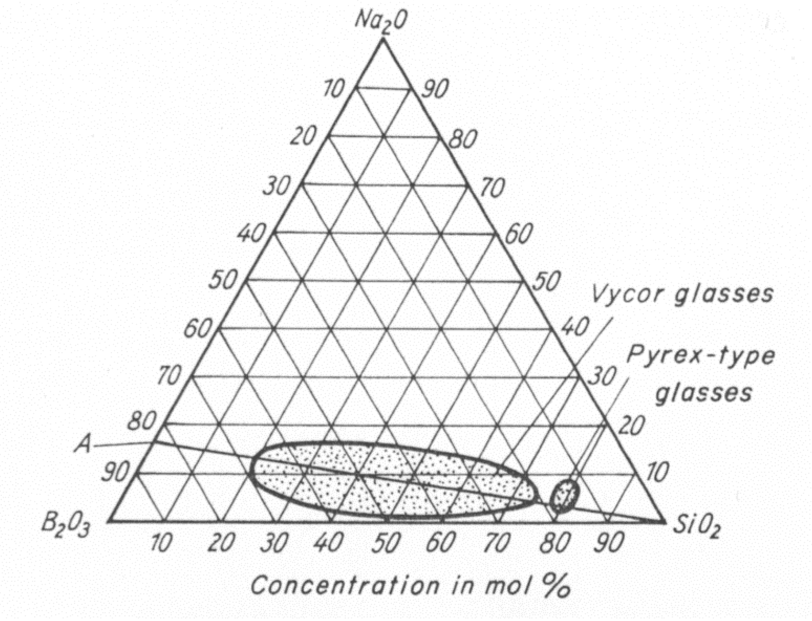

Figure 2-2: A ternary Na_2O-B_2O_3-SiO_2 glass system with an immiscibility region and the position of "Vycor" and "Pyrex" glasses [Molchanova, 1957]. The straight line indicated by the letter "A" represents the increase in the SiO_2 content at a constant Na_2O:B_2O_3 ratio [Cited in Vogel, 1985].

2.2.3 Crystallisation in oxide glass

2.2.3.1 Glass-Ceramic (GC) materials

Karpukhina *et al.* have provided a comprehensive review of the crystallisation process in oxide glasses [Karpukhina *et al.*, 2014]. As an amorphous solid, glass exhibits a characteristic glass transition temperature (T_g) and can be obtained via rapid cooling, quenching the melt to a temperature beneath the glass transition so as to avoid crystallisation. Oxide glasses can crystallise from the amorphous state via a crystallisation process due to heat treatment, and this results in a partial conversion from an amorphous component to a crystalline material. After the completion of the heat treatment process, the final solid consists of crystalline as well as residual amorphous phases, and the final product is usually called glass-ceramic, and has totally different physical and chemical properties to that of the glass prior to the crystallisation. The existence of more than one phase changes a wide range of properties, with strengthening of the glass being just one of these. Figure 2-3 shows a schematic diagram of a melt under rapid cooling to form a glass via a glass transition temperature (T_g) and under slow cooling to form a crystal at the melting temperature (T_m).

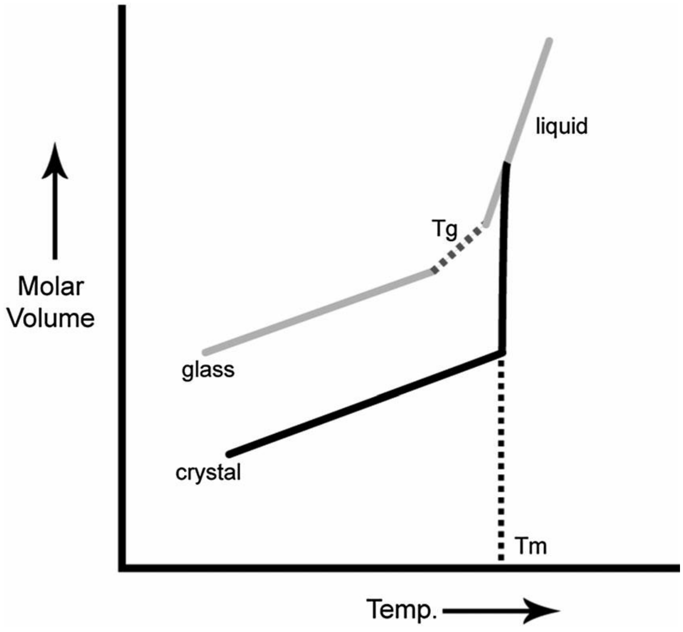

Figure 2-3: A schematic for glass formation upon rapid cooling of a melt (upper pathway) and crystal formation upon slow cooling of the melt (lower pathway) [Karpukhina *et al.*, 2014].

2.2.3.2 Nucleation and crystal growth in oxide glass

There are two basic stages of crystallisation in oxide glasses: nucleation and crystal growth. For the crystallisation stage to be initiated a nucleus is required, this is initially formed in the nucleation stage at the nano-scale size. The subsequent growth of this nucleus into a detectable size will be via the crystal growth stage. Figure 2-4 is a schematic diagram showing the rate of nucleation and crystal growth as a function of temperature.

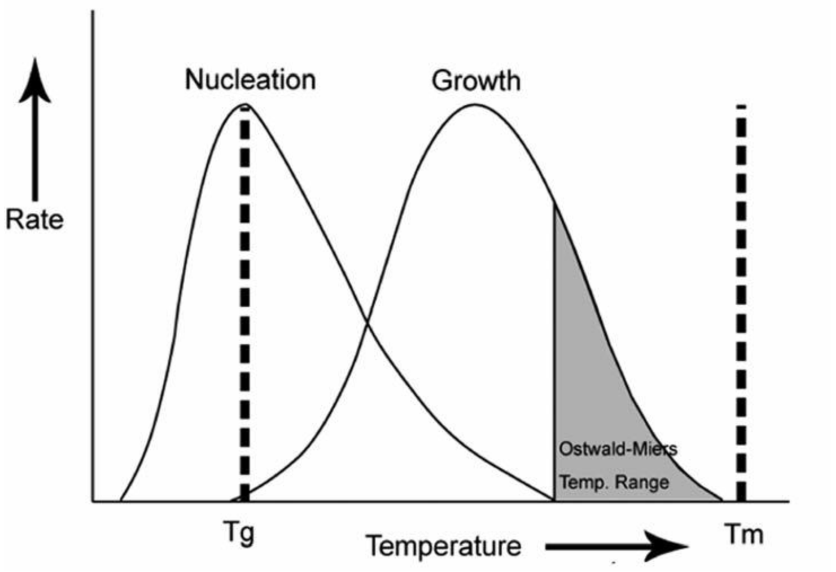

Figure 2-4: A schematic of the rate of both nucleation and crystal growth as a function of temperature [Karpukhina *et al.*, 2014].

It is obvious that the nucleation stage usually happens at temperatures at or just above T_g, while the crystal growth stage usually happens at higher temperatures up to the melting temperature (T_m). At this point, no formation of new nuclei occurs, meaning that only those formed initially at lower temperatures would grow. In contrast, the glass directly quenched from the melt down to this temperature range and heat treated there would not crystallise due to a lack of nucleation. In the case of a lack of nuclei, no crystal growth will occur and the glass will form. If nuclei exist, but no growth has occurred, the detection of the nuclei will be difficult due to their small size and the low volume fraction of the nuclei and hence the solid is still a glass.

The nucleation stage in the glass normally consists of two mechanisms; homogeneous nucleation and non-homogeneous (heterogeneous) nucleation. In the former mechanism, the nucleus will form spontaneously within the melt, while in the latter, the nucleation initiates at the interface boundaries and surfaces and is catalysed by the existence of foreign (unknown) impurities and nucleating agents [Karpukhina *et al.*, 2014].

2.3 Transmission electron microscopy (TEM)

Generally, TEM has been used as a powerful tool in materials characterisation and an enormous number of studies have been conducted using this instrument [Goodhew and Chescoe, 1980, Bando *et al.*, 1996, Kleebe *et al.*, 1996, Newbury and Williams, 2000, Wang, 2003 and Müller *et al.*, 2008,]. In the field of glass research, TEM has been used both for imaging and to induce modifications in the properties and structures of glass by exploiting the high-energy electron beam. Our project lies in this category, with an electron beam being used to irradiate a variety of oxide glasses and to then photograph the outcomes.

2.3.1 The history of using TEM in glass

In 1952, Slayter managed to give evidence of the presence of micro heterogeneity in glass using TEM bright field (BF) imaging [Slayter, 1952]. This was the first time that a TEM was used in glass research, and was also the first occasion on which the occurrence of modifications in glasses under fast electrons was demonstrated. The advantages of using a TEM in the characterization of glass and the changes in its structure and microstructure over other techniques are, first, the high energy e-beam, which can be used to damage the glass in such a way as to simulate the effects of ionization and electron excitations from β-particles and γ-rays (Weber *et al.*, provides a very useful review of this topic [Weber *et al.*, 1997]). The second advantage is, the availability of several useful characterization techniques in a modern TEM that, can be used for *in-situ* studies of the effects of irradiation damage in glass and to obtain useful data at the nanoscale on its structure, microstructure, chemical and electronic structure [Sun *et al.*, 2005]. These techniques include energy filtered electron diffraction (EFED), which was pioneered by Graczyk and Moss in 1969 [Graczyk and Moss, 1969] and has been used on different types of glass [Qin and Hobbs, 1995] to study the short range order. The medium range microstructure and medium range order of the glass have also been detected by nano electron diffraction (NED) [Cowley, 2002]. In addition, scanning transmission electron microscopy (STEM) combined with electron energy loss spectroscopy (EELS) and energy dispersive X-ray spectroscopy (EDS), which can give resolutions of 1-20 nm, have also been used in glass characterisation research [Risbud, 1982, Egerton, 1996, Kleebe *et al.*, 2001 and Jiang *et al.*, 2008]. Furthermore, bright field images together with energy dispersive X-ray spectroscopy have also been exploited comprehensively in glass characterisation. Nowadays, the existence of all the above mentioned techniques in a single modern TEM means that they can each be used much more efficiently and successfully in glass research.

2.4 Effects of electron irradiation in glass

The effect of electron beam irradiation in glass is an important topic and has hence attracted much scholarly attention [Weber, 1991, Ehrt and Vogel, 1992, DeNovion and Barbu, 1992, Ewing *et al.*, 1995, Jiang *et al.*, 2004 and Jiang *et al.*, 2005]. Despite giving useful information, however, all materials, often suffer damage [Egerton *et al.*, 2004] when subjected to the electron beam in TEM [Hobbs, 1987]. The effects of radiation damage in glass have therefore been reviewed extensively [DeNatale and Howitt, 1982, DeNatale and Howitt, 1984, Manara *et al.*, 1984, Antonini *et al.*, 1985, Weber, 1988, Sun *et al.*, 2003, Jiang, 2013 and Yang *et al.*, 2013]. In his review, Jiang reported that electron beam damage can cause irreversible displacement of atoms and that the damage mechanism is material dependent and differs widely between conducting and insulating materials [Jiang, 2013]. Surprisingly, a complete recovery of electron damage in oxide glass at ambient temperature has been reported by Mkhoyan and his co-workers in which nanoscale calculations showed that the Ca ions migrate away by about 10 nm during electron irradiation and then return during recovery [Mkhoyan *et al.*, 2006]. Under the effects of electron irradiation, modifications in composition, structure and properties of the glass and amorphous materials can occur, such as phase separation [Jiang and Silcox, 2002, Sun *et al.*, 2003, Sun *et al.*, 2004 and Ojovan *et al.*, 2010], gas bubble formation [Lineweaver, 1963, Sacchi *et al.*, 1985 and Ollier *et al.*, 2006], alkali migration [Usher, 1981 and Gedeon *et al.*, 1999], phase transformation [Rauf, 2008], precipitation [Jiang *et al.*, 2000, Jiang *et al.*, 2005 and Jiang *et al.*, 2007], crystallization [Jencic *et al.*, 1995, Klimenkov *et al.*, 2001 and Carrez *et al.*, 2002], fluidity enhancement and shape transformation [Möbus *et al.*, 2008 Möbus *et al.*, 2010]. Radiation effects in glass materials have been found to be significant under electron beam irradiation. This is due to the high homogeneity of glass among other materials. The effect of electron beam irradiation can result in an extraordinary microstructure, which can be exploited in future generations of optical devices. In the following, the significant damage effects which occur in glass under electron irradiation will be explored further.

2.4.1 Radiolysis and knock-on damage

Two types of electron irradiation damage are involved in electron-solid interactions. These are radiolysis (ionization and electronic excitation processes) [Howitt *et al.*, 1991] and knock-on (elastic collisions) [Hobbs, 1987]. Radiolysis damage includes bonds breaking in compounds with an electric field [Cazaux, 1986, Cazaux, 1995 and Cazaux, 1999] being created in the region of the specimen under the centre of the electron beam that will be positively charge due to ionization [Humphreys, 1989]. Radiolysis has been proposed as a major mechanism for describing the microstructural changes of glass under electron irradiation [De Natale and Howitt, 1982]. Knock-on damage, on the other hand [Humphreys, 1989], is the direct displacement of the atoms by fast electrons with energy larger than the threshold energy for displacement of atoms from their original sites inside the solid.

As has also recently been reviewed by Jiang, knock-on usually results from large-angle scattering and therefore it is a slow and localized mechanism [Jiang, 2013].

2.4.2 Electron irradiation-induced heating

During electron-specimen interaction, appreciable amounts of incident electron energy will transfer to the specimen via inelastic scattering, causing the specimen to heat up [Williams and Carter, 1996]. This results in an increase in the local temperature (T) of the specimen under irradiation in comparison with the surrounding temperature (T_o). Generally, at high electron doses more energy will be transferred to the specimen and a larger temperature increase will occur. It has been reported by Stenn and Bahr that the amount of energy transferred from the electron beam to the specimen is voltage dependent [Stenn and Bahr, 1970]. While the heating is negligible in TEM for conducting materials, such as metals [Hobbs, 1979], it is considerable in insulating materials such as glass, and sometimes exceeds 100 ^{o}C [Hobbs, 1987].

There are many parameters which may influence the temperature increase in the specimen being irradiated by the electron beam, and hence it is extremely difficult to calculate the temperature increase of oxide glasses in TEM precisely. Various calculations have given contradictory results ranging from a few degrees to a few hundreds of degrees. For example, the maximum temperature rise in silicate glasses [Möbus *et al.*, 2010] is estimated to be ≤ 2.4 K, while theoretical measurements done by Klimenkov and his co-workers showed a maximum temperature increase of about 20-30 K in silica during e-beam irradiation [Klimenkov *et al.*, 2000]. Also, different values for the temperature increase in silica during electron beam irradiation of different current intensities are reported by Du *et al*. [Du *et al.*, 2003 and Du *et al.*, 2005]. They found an increase in temperature to about 21 K when the beam current intensity is 15 A/cm^2 [Du *et al.*, 2005], while it is about 168.27 K when the beam current intensity is 100 A/cm^2 [Du *et al.*, 2003]. Based on the method of Blandford and Crater [Blandford and Crater, 2003], Sun *et al.* found that the temperature rise in glass using an electron beam of diameter of ~ 600 nm and e-beam current of ~ 5.65 nA is less than 20 ^{o}C [Sun *et al.*, 2004] assuming a good connection between the specimen and the TEM holder. It has also been reported that the temperature rise due to electron beam-induced heating may not be larger than several degrees if the specimen is in a good contact with the substrate. Whereas, it could approach several hundred degrees in a nanoparticle when the specimen is in an extremely poor contact with the substrate, depending on e-beam intensity and the nanoparticle size [Gryaznov *et al.*, 1991].

Precautions have to be made in order to reduce the influence of heating in the specimen under electron irradiation in TEM. For instance, use of a thin specimen is recommended in order to minimise the probability of the electrons colliding with the atoms in the specimen, as well as coating the specimen with conducting materials such as Au or C in addition to promote cooling.

2.5 Irradiation of the glass

2.5.1 Precipitation and formation of nanoparticles in glass

Glass can be designed and engineered with a broad range of properties and in different forms that make it a valuable material for a variety of technological applications [Brow and Schmitt, 2009]. Since glass, as a metastable phase has a lower density than the corresponding crystals (e.g. the density of quartz is about 2.62 g/cm^3 while it is about 2.20 g/cm^3 in fused silica [Jiang, 2010]), the atoms in glass are packed less densely than in the corresponding crystalline forms. This makes the displacement energies of atoms in glass relatively low. The rapid development in optical communications and the requirements of solar energy, and the consequent increased use of glass in electronic applications and nanostructures, have made the technique of micro/nano-patterning and lithography in oxide glass types one of the most interesting current research topics [Jiang, 2010]. Glass is, therefore, considered to be a promising candidate for the fabrication of nanostructures by adding different species into a glass matrix to obtain the desired composition. Different irradiation techniques have been used for the purpose of precipitating and forming nanoparticles in glass, such as electron beam irradiation [Jiang *et al.*, 2000, Jiang *et al.*, 2002, Du *et al.*, 2003, Jiang *et al.*, 2003, Choi *et al.*, 2005, Du *et al.*, 2005, Jiang *et al.*, 2005, Jiang *et al.*, 2007 and Singh and Karmakar, 2011], the laser irradiation technique [Qiu *et al.*, 2002, Zeng *et al.*, 2005 and Jiang *et al.*, 2010], the ion implantation technique [Battaglin *et al.*, 1996, Battaglin *et al.*, 1999, Wang *et al.*, 2009 and Guan *et al.*, 2013], the UV-light irradiation technique [Sheng *et al.*, 2009] and the focused ion beam (FIB) technique [Sun *et al.*, 2008].

Out of all these techniques, electron beam irradiation has the following advantages: (i) avoiding oxidation issues due to the high vacuum environment and (ii) being simple, fast and flexible since the nanoparticles can be easily controlled [Gnanavel and Möbus, 2012]. In the following sections, electron irradiation-induced precipitation and nanoparticle formation in a variety of oxide glasses will be presented, followed by a brief discussion of some other irradiation techniques, such as laser irradiation and ion implantation, which have also been widely used to precipitate nanoparticles in glass.

2.5.1.1 Electron irradiation-induced precipitation and formation of nanoparticles in glass

Irradiating the glass by high-energy electron beam is of great interest since the beam has the ability to modify the structure, properties and the composition of the glass and hence obtaining fascinating phenomena as a result of electron-glass interactions. Among the widely-reported effects of electron beam irradiation of the glass are nanoprecipitation and nanoparticle formation.

A STEM/EELS study done by Jiang and his co-workers showed the formation of metallic Zn nanoparticles in high Zn borosilicate glass [Jiang *et al.*, 2000 and Jiang *et al.*, 2003]. The sensitivity of this glass under the electron irradiation made the Zn nanoparticles, with an average size of about 7 nm, precipitate rapidly under highly intense electron beam irradiation, with the size of the Zn nanoparticles increasing in line with the irradiation time, as shown in Fig. 2-5.

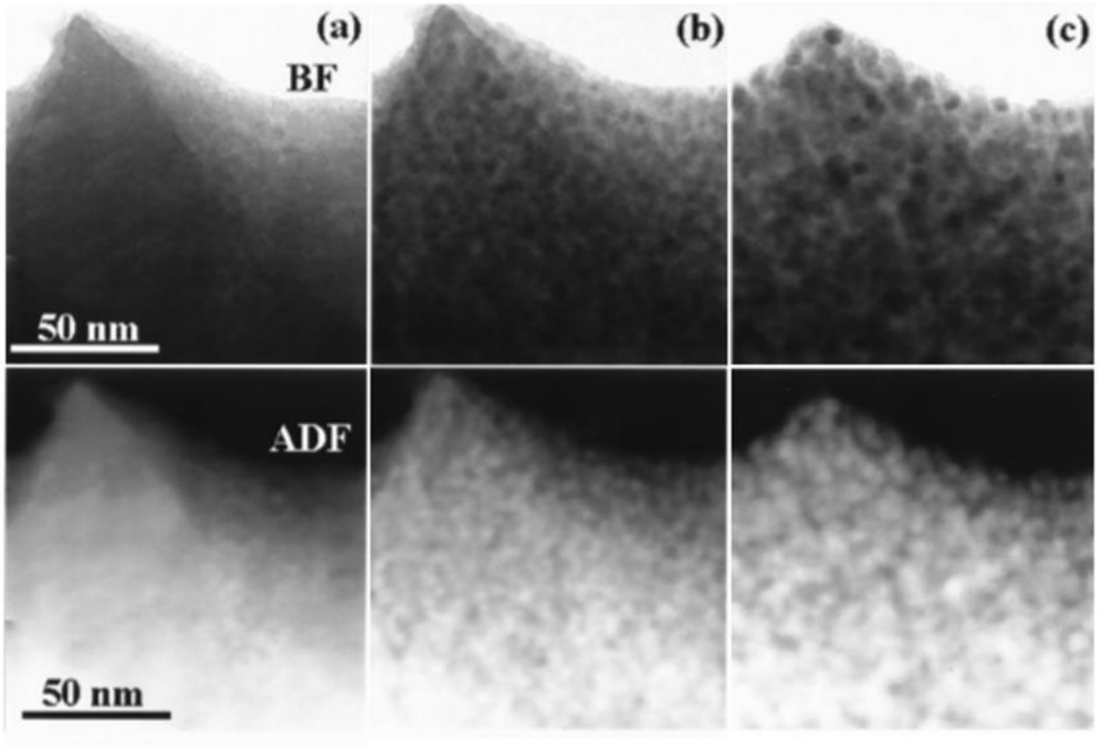

Figure 2-5: TEM micrographs illustrating bright field (BF) images in the upper row and annular dark field (ADF) images in the lower row for Zn borosilicate glass and showing nanoparticle formation and growth, with the nanoparticles size increasing in line with the irradiation time [Modified from Jiang *et al.*, 2000].

According to this study, the technique for the precipitation of Zn nanoparticles under electron beam irradiation involves ionization and field-induced migration processes. The identification of the chemistry of the Zn nanoparticles was performed using both electron energy loss spectroscopy (EELS) and diffraction patterns, and revealed that the precipitated crystalline particles are metallic Zn. Jiang *et al*. also showed that the formation of Zn nanoparticles in Zn borosilicate glass by electron irradiation is very active. This is due to the fact that, in a short irradiation time, almost all the amount of the ZnO in the glass was converted to metallic Zn, with no Zn being left bonded to the oxygen.

Zn nanoparticles of a similar size were also achieved by Kim *et al.*, but using TEM with a higher voltage rather than the STEM used by Jiang and his research group [Jiang *et al.*, 2000 and Jiang *et al.*, 2003]. An electron beam of about 200 nm in diameter resulted in the formation of metallic Zn nanocrystals of about 7-10 nm in size embedded in an amorphous silica layer by a 300 keV electron beam irradiation of a ZnO thin film on a silicon substrate [Kim *et al.*, 2007]. Amorphous Zn nanoparticles were initially formed under thermal annealing, followed by electron beam irradiation for about 30 minutes. At this stage, metallic Zn nanoparticles with an amorphous structure were formed as a result of thermal heating, and these remained embedded in the silica layer. Electron beam irradiation for a further 60 minutes resulted in phase transformation from amorphous into crystalline Zn nanoparticles. As a result of such prolonged irradiation, the thermal energy of the Zn nanoparticles can effectively minimize the nucleation barrier between Zn atoms and hence the crystallization will be much easier. The nature of the produced Zn nanoparticles has been analysed by HRTEM imaging and their corresponding fast Fourier transformation (FFT). The calculations of d-spacing between the lattice fringes for the Zn nanoparticles confirmed that these nanoparticles are single crystals and have hexagonal structures. Subsequent research done by the same group [Shin *et al.*, 2008] showed the formation of Zn nanocrystals arrays in a periodic state in amorphous material with less than a minute of electron beam irradiation. The time required for the formation of Zn nanoparticles in this study was much shorter than that in their previous study [Kim *et al.*, 2007] due to the use of an electron beam with a diameter as small as 7 nm in the irradiation.

Zn borosilicate glass is not the only glass to show sensitivity to electron beam irradiation. The same trend has also been observed in many other glasses such as Bi-doped oxide glass [Singh and Karmakar, 2011] and Ge-doped silica glass [Jiang *et al.*, 2002 and Jiang *et al.*, 2005]. Recently, Singh and Karmakar have reported the rapid formation of metallic Bi in bismuth-doped oxide glass by 300 keV electron beam irradiation [Singh and Karmakar, 2011]. They showed that under electron beam irradiation, nanocrystals precipitates with a higher local concentration than those formed using other methods can be achieved. The average size of Bi nanoparticles was found to increase with increasing irradiation time, along with morphological changes in the glass fragment as an another effect of electron beam irradiation, as shown in Fig. 2-6.

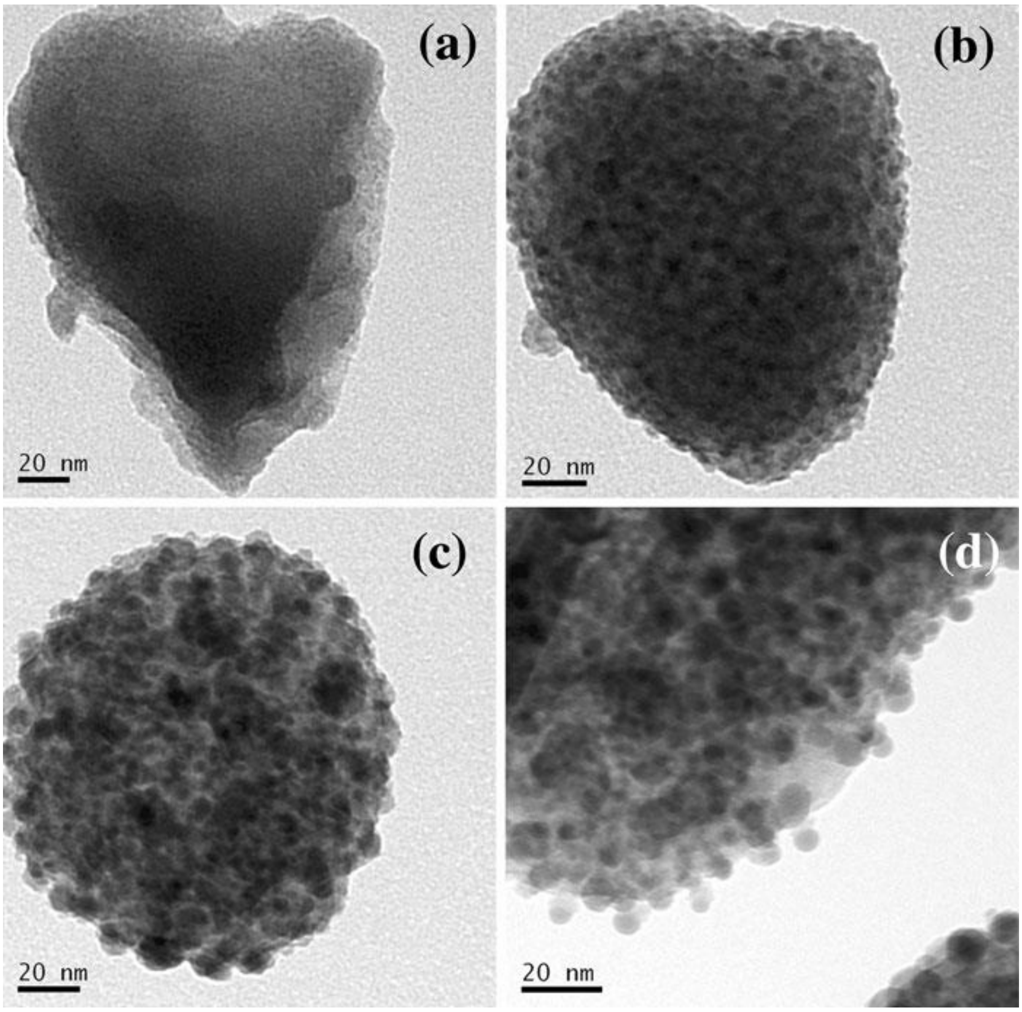

Figure 2-6: TEM micrographs of Bi-doped oxide glass under electron beam irradiation at (a) 0 min, (b) 2 min, (c) 4 min and (d) 8 min showing the formation of Bi nanoparticles and enhancing their size with the irradiation time [Singh and Karmakar, 2011].

According to this study, the size and the density of the Bi nanoparticles in the glass can possibly be controlled by changing the duration of the electron beam irradiation.

The HRTEM image after irradiation for 8 minutes confirms that the precipitated nanoparticles are metallic Bi with a rhombohedral structure. The stability of the nanoparticles at this stage facilitated the observation of such an image for the bigger Bi nanoparticles. In addition, the results of selected area electron diffraction (SAED) patterns showed that the diffraction spots correspond to the Bi nanocrystal randomly distributed in a plane with the increase in electron beam irradiation time, as shown in Fig. 2-7.

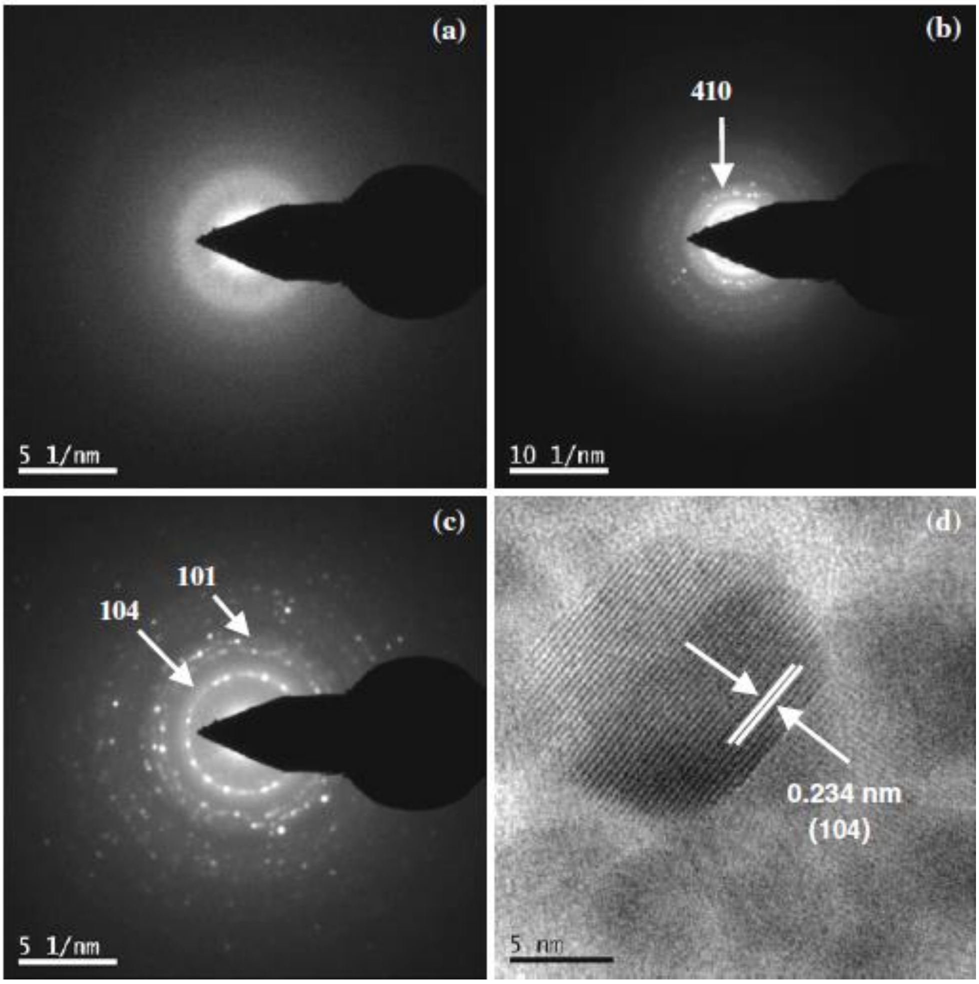

Figure 2-7: SAED micrographs of Bi nanoparticles in Bi-doped oxide glass under electron beam irradiation at (a) 0 min, (b) 4 min and (c) 8 min. (d) shows the HRTEM image of Bi nanoparticles at 8 min irradiation [Singh and Karmakar, 2011].

Fast decomposition of GeO_2-SiO_2 glass under electron beam irradiation is shown by Jiang *et al*. during a STEM/EELS study [Jiang *et al.*, 2002 and Jiang *et al.*, 2005]. Precipitation of Ge nanoparticles in GeO_2 glass under high energy electron beam irradiation has also been reported [Jiang *et al.*, 2005]. The initial 1 min irradiation resulted in the formation of amorphous nanoparticles with a diameter of less than 10 nm in the glass matrix, as shown in Fig. 2-8.

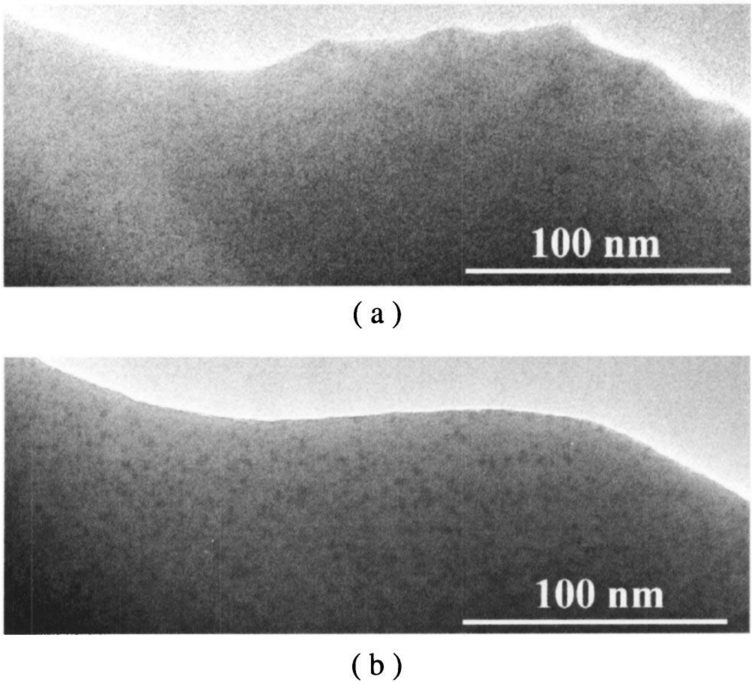

(a)

(b)

Figure 2-8: TEM images of GeO_2 glass (a) before electron irradiation and (b) after 1 min of electron irradiation showing the formation of amorphous Ge nanoparticles [Jiang *et al.*, 2005].

Increasing the irradiation time to around 3 min, however, resulted in a complete reduction of GeO_2 to Ge and the disappearance of oxygen from the irradiated region. Two mechanisms were involved in the formation of Ge nanoparticles in this experiment: firstly, the ability of electron irradiation to eliminate the Ge-O-Si configuration in silicate glass and therefore to decompose the glass phase into cation rich and poor phases and, secondly, the nucleation and growth on the glass surfaces. Another noticeable effect was smoothing of the rough edge of the glass fragment under electron beam irradiation due to significant surface diffusion (Fig. 2-8(b)). A mechanism for electron irradiation-induced diffusion of Ge in the silicon oxide matrix has also been suggested by Klimenkov *et al*. They reported the displacement of Si-O atoms in amorphous SiO_2 via collision with electrons, which then induce the diffusion of Ge atoms [Klimenkov *et al.*, 2000].

In addition to the formation of Ge nanoparticles in glass by electron beam irradiation, it is useful to mention the formation of Si nanoparticles in glass under the impact of e-beam irradiation. For example, e-beam irradiation-induced formation of crystalline Si nanoparticles in amorphous silica is reported by Du *et al*. Under 200 keV electron beam irradiation, amorphous SiO_2 is first transformed to amorphous Si and then the latter is transformed into crystalline Si. Electron beam heating and knock-on displacement were responsible for the transformation from amorphous Si to crystalline Si [Du *et al.*, 2003]. In the electron beam irradiation, both of these mechanisms can assist in crystallization, since e-beam heating has the ability to decrease the nucleation barrier and knock-on displacement is capable of increasing the potential energy above the ground state.

The precipitation of noble metals, such as silver and copper in Ag and Cu-doped glasses, electron beam irradiation, however, has only rarely been reported, in spite of being a powerful technique for *in-situ* formation of different nanocrystals. For example, in 1997, Hofmeister and co-workers reported the generation of high concentration metal Ag nanoparticles inside an ion-exchanged glass matrix [Hofmeister *et al.*, 1997]. Ag nanoparticles with a mean diameter of 4.2 nm were formed inside Ag-doped glass under electron beam irradiation. The produced Ag particles were homogeneously distributed in a narrow plane throughout the glass, as shown in Fig. 2-9. Hofmeister *et al*. claimed that the electron irradiation technique enhanced the diffusivity to some orders of magnitude larger than the corresponding thermal technique and that this favours the precipitation of Ag nanoparticles inside glass at lower temperatures and at significantly higher rates.

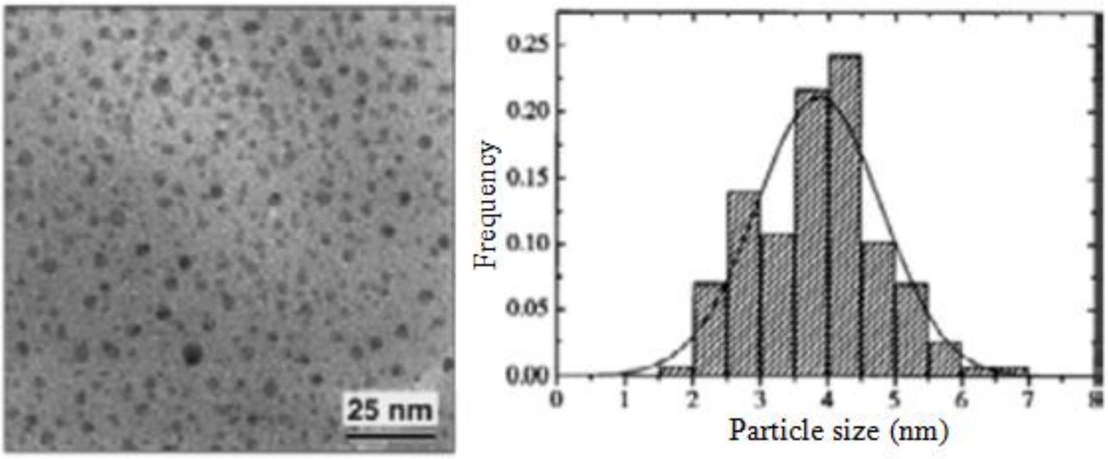

a) (b)

Figure 2-9: (a) TEM image showing the formation of Ag nanoparticles in Ag-doped glass under electron beam irradiation and (b) size distribution of Ag particles inside the glass [Hofmeister *et al.*, 1997].

Vostokov *et al.* reported the ability of electron beam irradiation to form 2D metallic nanostructures in Ag and Cu-doped glass [Vostokov *et al.*, 2009]. Studies on the formation of Ag nanoparticles of various diameters in glass under low energy electron beam irradiation have been reported by Nikonorov *et al.* [Nikonorov *et al.*, 2009, Vostokov *et al.*, 2009, Vostokov *et al.*, 2009 and Nikonorov *et al.*, 2010] and Brunov and co-workers [Brunov *et al.*, 2014]. These studies concentrate on general charge-induced surface aggregation observed ex-situ by light microscopy without nanoscale imaging of the actual particles' glass surfaces. Brunov *et al*. reported the formation of Ag nanoparticles of various diameters in glass under low energy electron beam irradiation [Brunov *et al.*, 2014]. They have shown that the Ag nanoparticles are not uniformly distributed across the volume, but are rather concentrated in thin layers in regions near the glass surface. This is because, under electron beam irradiation, an electric field will build up and this enhances the diffusion of Ag ions toward the glass surface. This means that the concentration of the formed Ag nanoparticles is rather high in the glass surface. The process of reduction also exists in the formation of Ag nanoparticles under electron beam irradiation. The electrons reduce the Ag ions to neutral atoms, which are then aggregate under the influence of electron irradiation to form Ag nanoparticles. This mechanism has also been reported in [Jiang *et al.*, 2002, Jiang *et al.* 2005 and Jiang *et al.*, 2007].

For the case of Cu, only the growth of pre-existing Cu nanoparticles in amorphous silica under electron beam irradiation has been reported. Ito and his research group described the growth of pre-existing metallic Cu nanoparticles of about 5 nm in diameter embedded in an amorphous SiO_2 film under a focused and intense electron beam with a diameter of about 1 nm in a scanning transmission electron microscope [Ito *et al.*, 1999]. According to this study, it was shown that once a small Cu particle was subjected to electron beam irradiation, it grew at the expense of the larger adjacent Cu particles by attracting atoms from those larger particles. It was shown that the reason behind this phenomenon is the electric field induced diffusion which is caused by the electron beam, and/or electron beam-induced charging of the Cu particle under electron beam irradiation. It was also observed that these large particles stretched at the same time as the smaller Cu particles were irradiated. This is due to the diffusion of Cu atoms towards the irradiated particle. Two significant effects were observed with further irradiation: first, a further increase in the size of the small Cu particle being irradiated and, second, the disappearance of some particles adjacent to the small Cu particle, while others changed their morphology and size and moved towards the small Cu particle. It is worth noting that outside the field of oxide glass; electron beam irradiation-induced formation of Cu nanoparticles of various diameters in different materials has also been reported such as in [Yen *et al.*, 2004, Zhou *et al.*, 2008 and Pham *et al.*, 2011].

2.5.1.2 Other irradiation techniques used in the precipitation and formation of nanoparticles in glass

In this section, a short review is presented of some other irradiation techniques used to precipitate nanoparticles in glass, with special emphasis on those based on the laser irradiation and ion implantation routes.

2.5.1.2.1 Laser irradiation-induced precipitation of nanoparticles in glass

Laser irradiation has been extensively used for the purpose of precipitating nanoparticles in glass and amorphous materials [Qu *et al.*, 2003 and Wackerow and Abdolyand, 2014]. A combination of laser irradiation and heat treatment will result in precipitation of nanoparticles in glass. The idea of nanoparticle precipitation in glass by laser irradiation and the following heat treatment is that, upon the irradiation, electrons and holes will be created in the glass via a multi-photon process [Hua *et al.*, 2007, Silva *et al.*, 2010 and Almeida *et al.*, 2012]. Two steps are involved in nanoparticle growth in this method: (i) the reduction of metal cations and (ii) the migration of metal atoms to form nanoparticles. The selection of the conditions of laser irradiation can then control the size and spatial distribution of the nanoparticles. Specifically, since metal cations act as centres to trap electrons, the free electrons reduce the metal cations into metal atoms. The following heat treatment then increases the mobility of the metal atoms to aggregate and form nanoparticles. Hua and co-workers reported the space-selective precipitation of metallic Cu and Ag in Cu and Ag-doped silicate glasses using femtosecond laser irradiation and subsequent heat treatment. Under the irradiation, Cu and Ag ions capture the free electrons being created by multi-photon processes and then reduced these to atoms. These atoms are then aggregated to form nanoparticles during an annealing process [Hua *et al.*, 2007]. A similar mechanism has also been reported by Qiu *et al.*, in which irradiation of silicate glass by laser and a subsequent annealing process at 550 ^{o}C resulted in the precipitation of metallic Ag [Qiu *et al.*, 2002].

2.5.1.2.2 Ion irradiation-induced precipitation of nanoparticles in glass

The mechanism of ion implantation has been widely used to generate metallic nanoparticles in glass and amorphous materials [Gonella, 2000, Johannessen *et al.*, 2005 and Tsang *et al.*, 2007]. This technique is usually conducting by adding a variety of metal ions into glass and amorphous materials such as noble metals ions (e.g. Ag, Au and Cu) [Battaglin *et al.*, 1996 and Wang *et al.*, 2009], Zn ions [Chen *et al.*, 1998 and Amekura *et al.*, 2006] and Co ions [Tsang *et al.*, 2007 and Guan *et al.*, 2013]. The importance of conducting heat treatment after the implantation process in order to optimize the properties, such as formation of nanoparticles, or to govern the size of the nanoparticles, has been reported in the vast majority of the studies. Formation of Cu and Ag nanoparticles in silica and silicate glass by high-energy Cu and Ag ion implantation and subsequent annealing has also been reported [Pal *et al.*, 2000]. They found a decrease in the radius of Cu NPs during annealing at 600 ^{o}C, while annealing at higher temperatures (between 800 ^{o}C and 1050 ^{o}C) resulted in the formation of larger and more stable Cu particles. Annealing at relatively high temperatures after implantation was found to be essential to precipitate Au nanoparticles in silica and silicate glasses [Battaglin *et al.*, 1996]. Furthermore, ion implantation using Zn ions followed by heat treatment was the main mechanism used by some research groups to form Zn nanoparticles in oxide glasses [Chen *et al.*, 1998 and Amekura *et al.*, 2006]. After ion implantation, Zn nanodots with a diameter of about 5-15 nm were formed beneath the glass surface at a depth of 10-70 nm with no nanoparticles found outside this region. The size of these nanoparticles increased to about 5-40 nm during annealing at 700 ^{o}C and 800 ^{o}C in a vacuum.

2.5.2 Radiation-induced fluidity (RIF)

Ion irradiation-induced flow in glass and amorphous materials has been studied by [Volkert, 1991 and Snoeks *et al.*, 1995]. Trinkaus has shown that an ion deposits its energy in nuclear collisions and electronic excitations during interaction with a solid. This leads to an increase in the local temperature and a decrease in the viscosity [Trinkaus, 1995].

In addition, Mayr *et al.* derived an expression by which the radiation-induced fluidity (RIF) in an amorphous structure can be calculated [Mayr *et al.*, 2003]:

$$H = \frac{1}{\eta\ \emptyset} \text{ ------- } (2\text{-}1)$$

where H, η and ϕ are the radiation-induced fluidity (RIF), viscosity and the irradiation flux, respectively. In brief, they showed that the production of point defects upon the irradiation is a more efficient mechanism in radiation-induced flow [Mayr *et al.*, 2003]. Similarly, Volkert also showed that radiation-enhanced flow will occur in the region where the defect density is high [Volkert, 1991]. In contrast, Snoeks and co-workers reported the absence of any role for the defects created in the flow of silica when irradiated by 1 MeV ions, arguing that, instead, atomic displacements due to nuclear collisions were the main mechanism [Snoeks *et al.*, 1995].

Electron beam irradiation also has an influence on flow in glass and amorphous materials. The fluidity of amorphous materials is higher at higher temperatures as a result of the weakness in the bond lattice due to the broken bonds. Thermal fluctuations and radiation-induced bond breaking are two processes attributed to bond rupture as a result of electron beam irradiation. The rate of generation of broken bonds attributing to flow is directly proportional to both the electron flux density (intensity of irradiation) and the temperature. Electron irradiation-induced fluidity enhancement has been reported and discussed in terms of observing the instability of amorphous materials under e-beam irradiation; in other words, e-beam irradiation-induced morphology changes. While there are only few publications reported this phenomenon at the nanometre scale in glass and amorphous materials, many more studies have been performed to investigate the instability of metal nanoparticles embedded in silica and other amorphous materials under the impact of electron beam irradiation. It is convenient to give a brief discussion of the latter studies prior to the former, since the phenomenon of electron irradiation-induced morphology transformations was first discovered in metal NPs and then a few observations about this phenomenon are reported in glass and amorphous materials.

2.5.2.1 Electron irradiation-induced shape changes in metal nanoparticles

Electron beam irradiation-induced shape changes were first reported in the last century in gold nanoparticles, with instabilities in the structure of Au NPs under the effect of electron irradiation being observed. This happened due to the reduction of the surface energy anisotropy as a result of increasing temperature. Investigating the effect of electron beam irradiation on shape transformation and instabilities within nanoparticles embedded in a silica matrix became a target of many researchers [Ajayan and Marks, 1988 and Be'er *et al.*, 2007]. A vast majority of these studies agreed that the "quasi-melted" state was behind structural and shape changes of the nanoparticles under electron beam irradiation [Marks and Ajayan, 1986]. The activation-energy barriers between various nanoparticle shapes and states are extremely small [Ajayan and Marks, 1988]. This effect makes the nanoparticles to be in the "quasi-molten" state at low temperatures in comparison with their true thermodynamic melting points, i.e. at temperatures well below the melting point. They also reported that "quasi-melting" will happen when the nanoparticle has enough thermal energy to overcome the energy barriers separating the various local minima. Under electron beam irradiation, those nanoparticles which are in poor thermal contact with a support are heated and this results in fluctuation between various structures [Iijima and Ichihashi, 1986 and Wellenberg *et al.*, 1986]). Doraiswamy and Marks, on the other hand excluded the effect of high temperature for the explanation of morphology changes in different nanoparticles under electron beam irradiation [Doraiswamy and Marks, 1996]. Similar to what has been reported in [Ajayan and Marks, 1988], Doraiswamy and Marks argued that for such a phenomenon to happen, at least one energy source is needed to overcome the activation energy barriers between various structures as well as the reasonably low energy barriers between morphologies [Doraiswamy and Marks, 1996]. A recent study has also reported the instability of Au nanoparticles embedded in silica when irradiated by an electron beam, with ellipsoidal to spherical transformations being observed with irradiation. This is reported to be due to a series of effects such as heating, softening of the SiO_2 matrix, radiation enhanced diffusion (RED) of knock-on displaced O and Si atoms, leading to local stress relaxation [Mohapatra *et al.*, 2013].

2.5.2.2 Electron irradiation-induced fluidity and shape changes in glass and amorphous materials

Due to complications in the synthesis and assembly of oxide glasses, they do not have a suitable shape. As a result of this, local change in the size and morphology of these types of glass are possible. It has been shown that a glass can plastically deform via bond breaking and bond-switching processes that mediate the rotation and migration of atomic clusters. Under electron beam irradiation, ionization damage, including Auger processes and bonding changes, are constantly introduced in the material as a result of the interaction between the incident high-energy electrons and the atoms, and this significantly enhances the flow mechanism. This might result in the breakage of a Si-O bond forming a pair of Si and O dangling bonds. In addition, the displacement of a bridging oxygen (BO) atom will form an interstitial O atom leaving a vacancy behind. Hence, the radiation results in the formation of dangling bonds and oxygen vacancies (point defect-like entities in amorphous solids [Mayr *et al.*, 2003]) and even the possibility of releasing some oxygen molecules. The high-energy electrons and the defects they form directly facilitate the atoms to overcome the energy barrier for bond switching and minimising the flow stress. In this regard, ionization-induced diffusion and viscous flow mediated by point defects in amorphous solids has been explained [Mayr *et al.*, 2003].

Fluidisation in glasses occurs as a result of intense electron irradiation due to non-thermal bond rupture and can occur below the glass transition temperature. Modification of glass nanoparticles results from fluidisation of glasses at sufficient high electron flux densities due to surface tension forces.

Ajayan and Iijima have conducted comprehensive studies on electron irradiation-enhanced flow and instability of amorphous structures [Ajayan and Iijima, 1992 and Ajayan and Iijima, 1992]. It has been reported that the radiation-enhanced fluidity is directly proportional to the radiation energy loss (or ion mass) and the radiation-induced viscosity decrease with increasing nuclear energy loss [Snoeks *et al.*, 1995]. The qualitative effect of electron beam radiation on viscous flow in glass, and the quantitative assessment of the radiation-induced fluidity enhancement, have each been well reported by [Möbus *et al.*, 2010]. They derived a useful formula to calculate the radiation-induced fluidity and they also showed the relationship between RIF and the electron energy, and how the intensity of the electron irradiation will affect the fluidity enhancement in the glass. It is important to report that for the radiation-induced fluidity to be observed, the temperature should be sufficiently low. In other words, the electron beam irradiation-induced fluidity increase is more significant at lower temperatures, but it is not quite as obvious at high temperatures due to thermal effects.

Fluidisation of glass at sufficiently high electron flux densities can lead to changes in nanoparticles and holes, such as nano-patterning effects as a result of surface tension forces [Möbus *et al.*, 2008 and Möbus *et al.*, 2010]. The consequences of an increase in electron beam irradiation-induced fluidity can be different and also depend on the sample size. The modification in the glass sample is due to the mechanism of viscous flow, which occurs by the stress generated as a result of surface tension forces. The time required to see the modifications caused by electron beam irradiation-induced fluidisation will be shorter at low viscosity and in nanometre scale samples, while it is longer if the sample size is larger. Shape transformations of glass and amorphous materials under electron beam irradiation can fall into different categories, or can take different forms, such as rounding-off of the glass corners and surfaces, transformations in the overall shape of the amorphous material and, shrinkage in the size of the nanowires and nanopores.

Only a few publications have reported the enhancement of electron irradiation-induced fluidity and shape transformations in oxide glasses. Fluidisation or quasi-melting of micro/nanoparticles under electron beam irradiation has been studied by Möbus *et al*. They showed that this is due to the effect of the bond breaking processes caused by energetic electrons [Möbus *et al.*, 2008 and Möbus *et al.*, 2010]. Under moderate electron beam irradiation with an energy of 200 keV and an e-beam current of about 4 nA, the shape of the glass sample is modified. These modifications include rounding of glass sharp corners, flattening and smoothing of the glass rough surfaces are shown in Fig. 2-10.

The minor rounding observed in the glass corners is the first observation of electron beam irradiation-induced fluidity enhancement. It has been demonstrated that it is impossible for the temperature to be the reason for such a phenomenon, but the role played by the kinetic activation of the fast electrons at a temperature far below the melting point has been confirmed. According to this study, electron beam irradiation significantly reduced the viscosity of borosilicate glass, transforming it to a quasi-melted state. Also in this study, a sudden and unexpected transformation of a glass fragment into a perfect glass bead within less than a second under electron beam irradiation was observed. Möbus *et al*. reported that several criteria such as particle size, shape and the degree of connectivity with the support carbon film could affect this transformation.

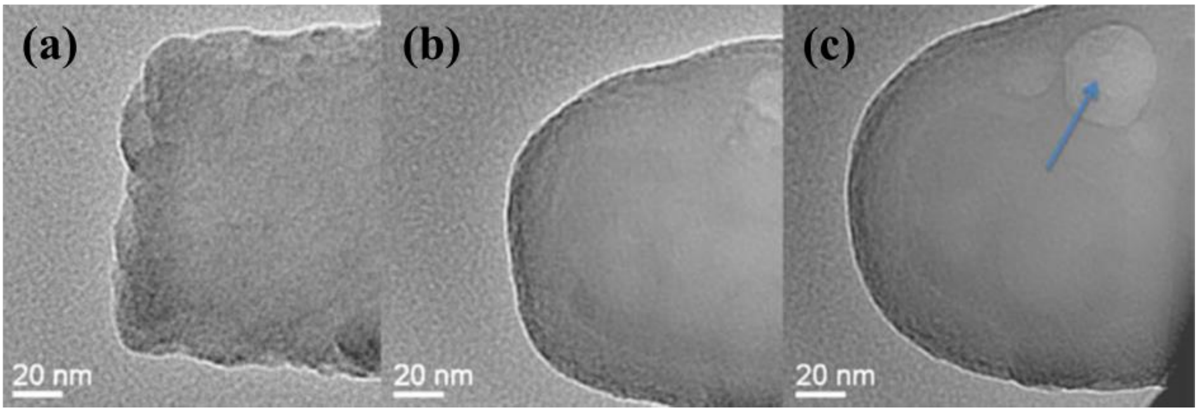

Figure 2-10: (a) glass fragment with rough surfaces prior to electron irradiation, (b) intermediate stage of the irradiation showing flattening of the rough surfaces and (c) glass rounding as a final stage of the irradiation. The blue arrow in (c) indicates a gas bubble [Modified from Möbus *et al.*, 2010].

Transformation in the surface morphology of alkali-silicate glass under fast electron irradiation of various energies has also been reported by Gedeon *et al*. Depending on the electron doses, two distinct phenomena are observed: first, compaction at low doses and second, expansion at higher doses [Gedeon *et al.*, 2007].

Zheng *et al.* studied the effect of a high-energy electron beams on nanoscale amorphous silica [Zheng *et al.*, 2010]. Significant changes in the shape of this material under moderate exposure and low intensity electron beam were reported. Following e-beam irradiation, a spherical shaped amorphous silica nanoparticle was transformed into a pancake-like nanoparticle and became much softer, as shown in Fig. 2-11.

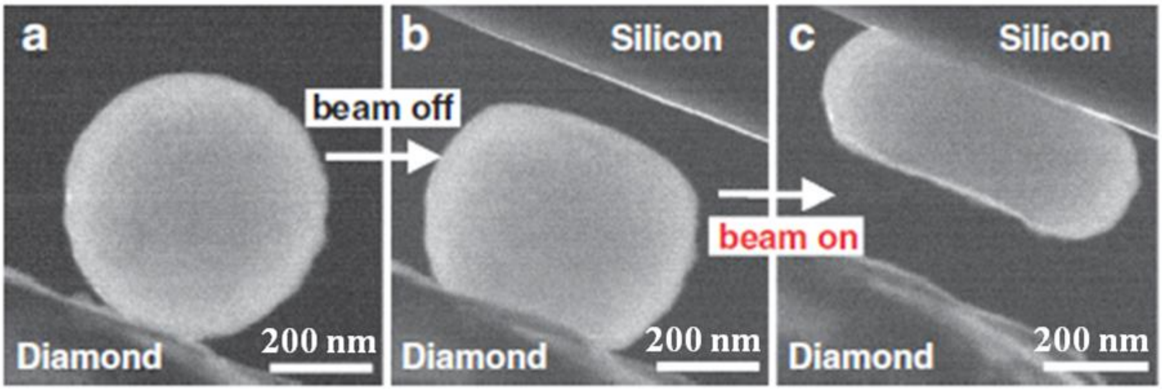

Figure 2-11: TEM images of the nano-compression of amorphous SiO_2 under electron beam irradiation [Modified from Zheng *et al.*, 2010].

Zheng *et al*. exploited the electron beam to penetrate the entire sample in order to promote the defects for flow at room temperature, resulting in super-plasticity in much larger samples. They also discussed in detail the temperature rise in the sample under the e-beam irradiation. They found a minor beam heating of the sample for many reasons: first, the low e-beam current intensity used in the experiment ($\leq 1.8\times10^{-2}$ A/cm^2), which was several orders of magnitude lower than that used in other experiments ($> 1\times10^{8}$ A/cm^2) such as in [Storm *et al.*, 2003 and Storm *et al.*, 2005], second, the good thermal conductivity between the sample and the substrate; and third, a thermal conduction analysis was carried out and demonstrated that the temperature rise was negligible. The glass transition temperature (T_g) for silica is rather high at about 1.373 K and the flow is not predicted to be noticeable at temperatures well below about 0.7 T_g [Zheng *et al.*, 2010]. It was therefore concluded that the brittle nanoparticle amorphous SiO_2 can be easily made ductile under low intensity electron beam irradiation. This is due to the fact that the energetic electron beam will create structural and bonding defects within the entire sample to facilitate the bond-switching mechanism that imparts flexibility to the atomic clusters, allowing their rotation, and their migration to accumulate the flow.

Structural and shape changes of amorphous silica nanowires under *in-situ* electron beam irradiation of 300 keV have been reported recently by Zhu and his co-workers [Zhu *et al.*, 2014]. Under a relatively low current density electron beam irradiation (~ 3.6×10^2 A/cm^2) and a diameter of about 60 nm (indicated by the red circle in Fig. 2-12), a rapid non-homogeneous shrinkage in the diameter of the nanowire (about 45 nm) was observed.

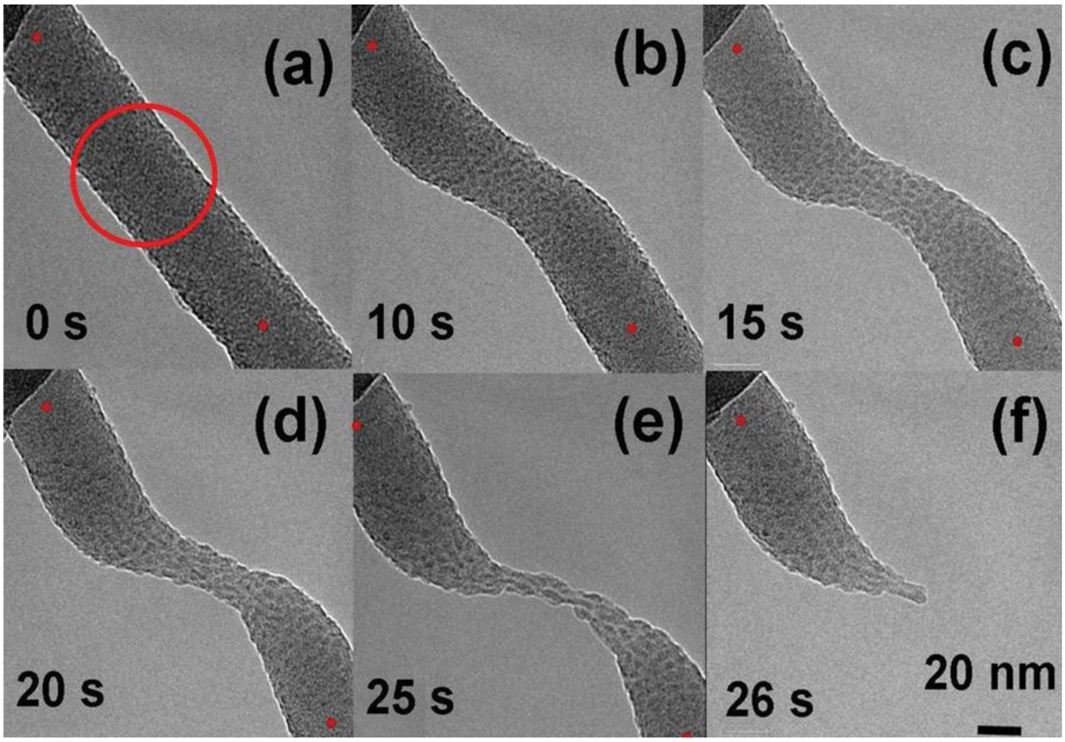

Figure 2-12: Time series TEM micrographs of an amorphous silica nanowire under irradiation by an electron beam with a larger diameter than that of the wire, showing the structural and shape transformations [Zhu *et al.*, 2014].

The higher the intensity, or deposition rate, the faster this shrinkage. The diameter of the nanowire decreased gradually with the irradiation time and eventually resulted in the nanowire breaking after 26 seconds. Such non-homogeneous shrinkage has been referred to as "necking". The occurrence of fast nanowire elongation (between two red spots in Fig. 2-12), within only 25 seconds, and its transformation to an S-shape were also observed under e-beam irradiation. All these three phenomena were reported to be due to irradiation-induced athermal activation, collective migration or plastic flow of massive atoms, with two forces being responsible for this flow: first, the enormously high surface energy of the nanowires as a result of the strong, thermodynamic tendency for the wire to self-contract and, second, the ability of the electron beam irradiation to athermally soften the wire and kinetically activate the contraction and the flow.

When a smaller e-beam diameter of about 25 nm (indicated by the red circle in Fig. 2-13) is used for irradiation, the high beam current density of about 2×10^3 A/cm^2 resulted in a net loss of nanowire volume and an ablation of surface atoms (loss of atoms) as shown in Fig. 2-13.

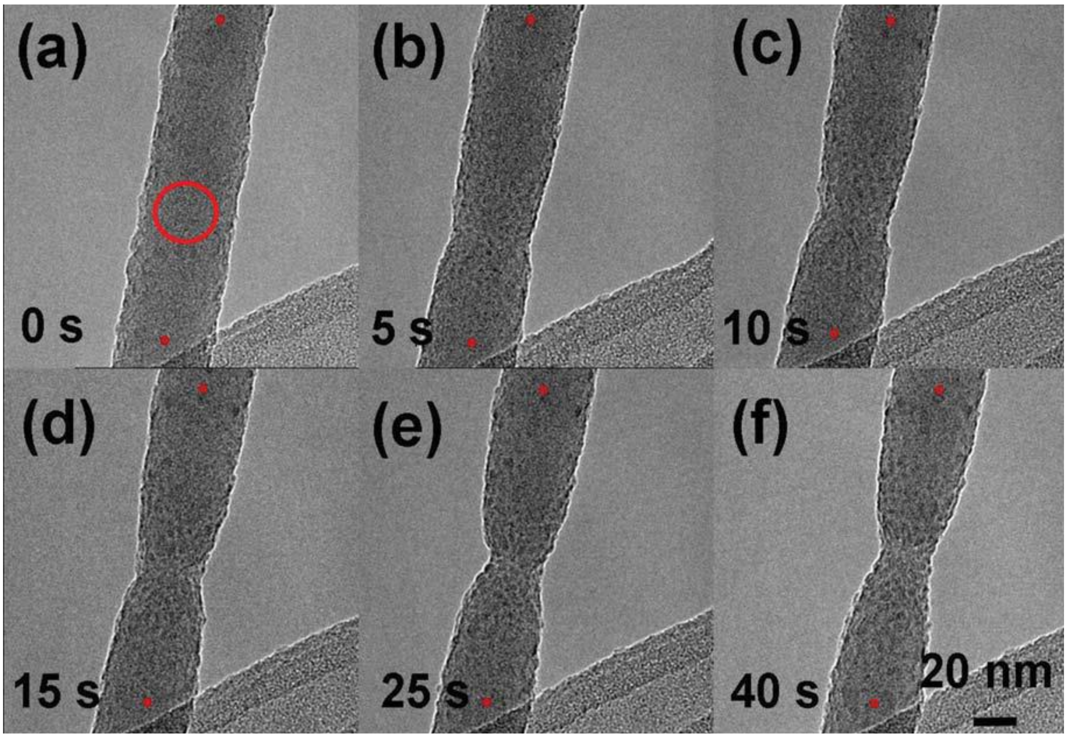

Figure 2-13: Time series TEM micrographs of an amorphous silica nanowire under irradiation by an electron beam with a smaller diameter than that of the wire, showing the structural and shape transformations [Zhu *et al.*, 2014].

Many studies have reported the formation of nano-pores following application of focused electron beam irradiation in an insulating material [Wu *et al.*, 2005]. In addition, the morphological transformation of such nano-pores under the electron irradiation has been reported to be due to minimization of the surface energy and is facilitated by a glass-like behaviour that could occur at low temperature as a result of bond breaking by the electron beam. For instance, the fluidisation phenomenon has been observed by Storm and his co-workers during e-beam-induced formation of nano-pores in amorphous SiO_2 (a SiO_2) nano-membrane [Storm *et al.*, 2003]. Using an electron beam of intensity of about 10^5 to 10^7 A/cm^2, shrinkage in the size of the nano-pores was observed, as shown in Figs. 2-14 and 2-15.

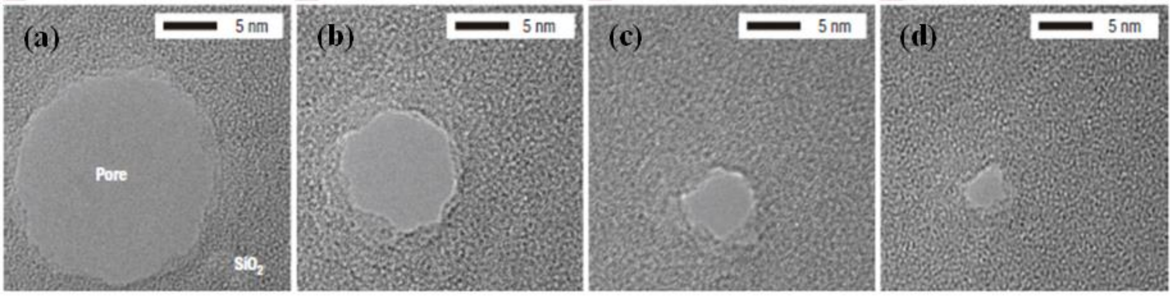

Figure 2-14: TEM images of SiO_2 nano-pore. Electron beam irradiation resulted in a gradual shrinkage in the size of the nano-pore [Modified from Storm *et al.*, 2003].

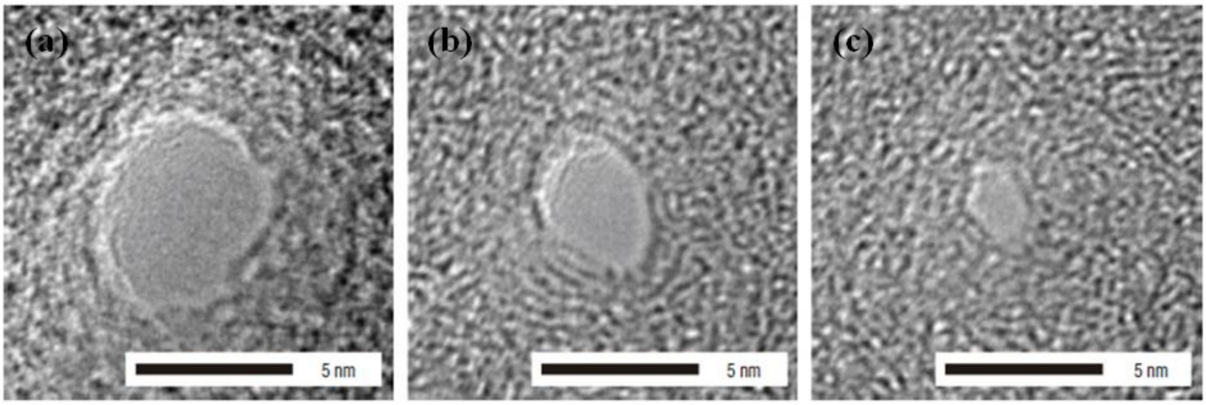

Figure 2-15: TEM images of SiO_2 nano-pore. Electron beam irradiation resulted in shrinkage in the size of the nano-pore from about 6 nm to about 2 nm [Modified from Storm *et al.*, 2003].

Storm *et al*. also observed electron beam irradiation-induced viscous flow in amorphous silica, shape changes and a lack of compositional changes under the electron irradiation. When the suitable morphology is obtained, lowering the intensity of the electron beam will therefore result in SiO_2 being quenched into its initial glassy state.

A similar outcome was observed by Lo and co-workers [Lo *et al.*, 2006], with their research reporting an electron beam irradiation-induced reduction in the size of nano-pores in an amorphous SiN nano-membrane. The difference in their case, however, was the use of a focused ion beam (FIB) to form a nano-pore of about 5 nm in diameter, before irradiating that nano-pore with an 200 kV electron beam in TEM [Lo *et al.*, 2006]. A gradual shrinkage in the size of the nano-pore down to less than 1 nm was achieved, as shown in Fig. 2-16.

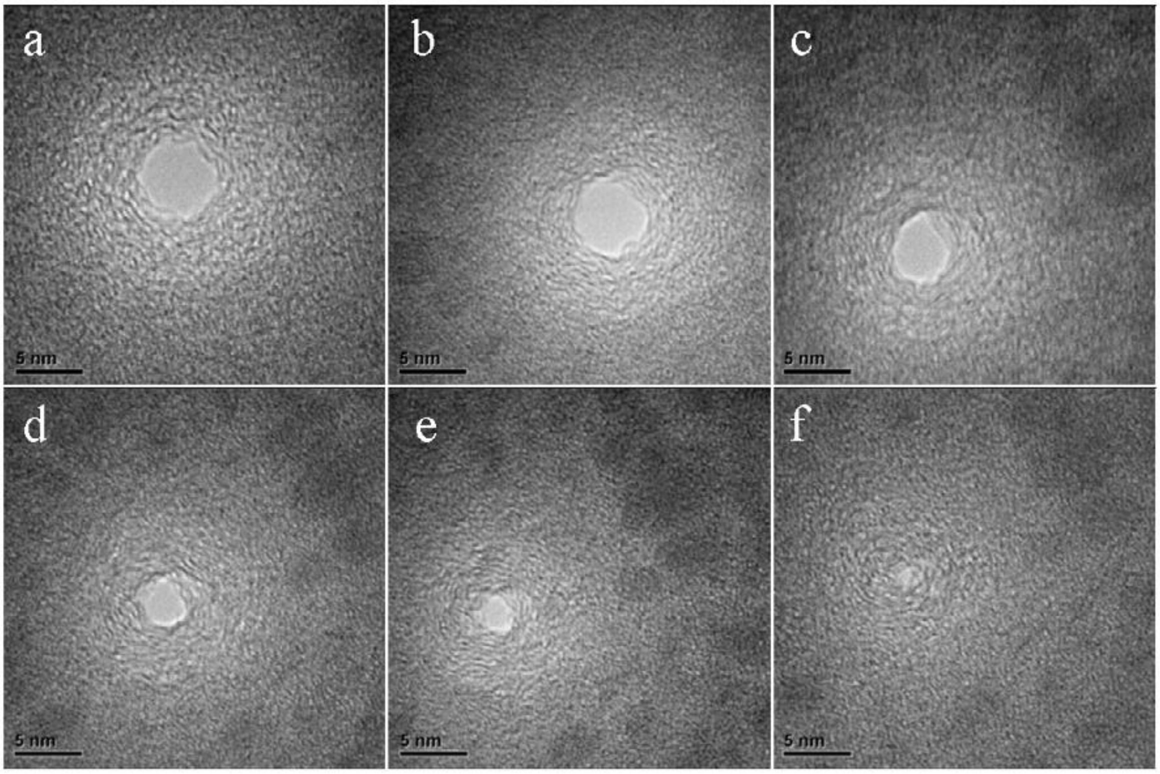

Figure 2-16: TEM images of a nano-pore initially formed by FIB in a SiN nano-membrane. Under the effect of electron beam irradiation, the nano-pore gradually shrunk from about 5 nm to less than 1 nm [Lo *et al.*, 2006].

A possible reason for this observation is that the electron beam irradiation serves to increase the mobility and diffusivity of Si and N atoms, hence resulting in a mass flow directed to the reduction of the surface tension energy. This effective melting of the silicon nitride is the reason behind the decrease in the size of the nano-pore in both FIB and electron beam irradiations.

2.6 Some important applications of the electron beam irradiation in glass research

As can be seen in the earlier sections, the electron beam has the ability to modify the structure, composition and morphology of the glass and amorphous materials. This opens the possibility of creating modified glass for specialist applications.

Ojovan and Lee have demonstrated that it is possible to obtain a desired composition of glass for different applications by adding different species into the glass matrix, owing to its high flexibility [Ojovan and Lee, 2010]. The potential of embedding metal nanoparticles in glass is attracting much attention due to the fact such glass can exhibit unique optical and magnetic properties [Tsang *et al.*, 2007] as well as improved non-linear optical properties [Yamane and Asahara, 2000]. A glass matrix containing metal nanoparticles may find applications, for example, in optoelectronic devices, due to the improvement in the optical susceptibility and picosecond response time [Kim *et al.*, 2007] as well as in nanoplasmonic devices [Lindquist *et al.*, 2012]. Cu nanoparticles embedded in dielectric material, on the other hand can possibly be used in switching devices [Ito *et al.*, 1999].

On the other hand, in optical communication and solar energy device materials, patterning of transparent matrix materials has attracted much interest, and irradiation with electron beam or lasers is one method to add modern functionalities to glass in optical and electronic applications and nanostructures [Qu *et al.*, 2003 and Jiang, 2010]. Furthermore, the high degree of homogeneity of this glass gives the electron beam irradiation the ability to generate extraordinary microstructures or large size dispersion of the generated nanocrystal in the glass matrix. These extraordinary microstructures could be exploited in future generations of optical devices [Singh and Karmakar, 2011].

Irradiation is a versatile, non-contact, wide-field manufacturing technique to change a material's mechanical, optical and chemical properties, such as surface roughness, surface chemical composition, reflectivity and light coupling ability through plasmons. Metal nanoparticles fabricated in glass by electron beam irradiation (metal-glass composite) allows the production of materials with well-defined non-linear properties and can find applications in optical switches, shutters and optical waveguides [Hofmeister *et al.*, 1997 and Jiang *et al.*, 2000]. The electron beam can also produce a heterogeneous glass composition, with modification of the optical properties and hence fabrication of the photonic structure inside glass to nm level accuracy [Jiang *et al.*, 2002].

2.7 References

A.V. Vostokov, A.I. Ignat’ev, N.V. Nikonorov, O.A. Podsvirov, A.I. Sidorov, A.V. Nashchekin, R.V. Sokolov, O.A. Usov and V.A. Tsekhomskii 2009 Effect of electron irradiation on the formation of silver nanoclusters in photothermorefractive glasses *Tech. Phys. Lett.* **35** 812-814.

A.V. Vostokov, A.I. Ignat’ev, N.V. Nikonorov, O.A. Sidorov, A.I Sidorov, A.V. Nashchekin, R.V. Sokolov, O.A. Usov and V.A. Tsekhomskii 2009 Influence of electron beam irradiation on formation of silver nanoclusters in photothermorefractive glasses *Tech. Phys. Lett.* **35** 35-40.

Ajayan P M and Iijima S 1992 Electron irradiation-induced dynamical fluctuations in amorphous structures *J. Non-Cryst. Solids.* **150** 423-428.

Ajayan P M and Iijima S 1992 Electron-beam-enhanced flow and instability in amorphous silica fibers and tips *Philos. Mag. Lett.* **65** 43-48.

Ajayan P M and Marks L D 1988 Quasimelting and phases of small particles *Phys. Rev. Lett.* **60** 585-587.

Almeida J M P, De Boni L, Avansi W, Ribeiro C, Longo E, Hernandes A C and Mendonca C R 2012 Generation of copper nanoparticles induced by fs-laser irradiation in borosilicate glass *Opt. Exp.* **20** 15106-15113.

Amekura H, Umeda N, Sakuma Y, Plaksin O A, Takeda Y, Kishimoto N and Buchal Ch 2006 Zn and ZnO nanoparticles fabricated by ion implantation combined with thermal oxidation, and the defect-free luminescence *Appl. Phys. Lett.* **88** 153119-3.

Antonini M, Manara A, Buckley S N and Manthorpe S A 1985 Microstructural changes induced in borosilicate glasses by 1 MeV electrons *J. Phys. Chem. Sol.* **46** 287-296.

Bando Y, Kurashima K and Nakano S 1996 Modern Applications of a New 300 kV Field Emission Transmission Electron Microscope to the Study of Advanced Materials *J. Euro. Ceram. Soc.* **16** 379-384.

Battaglin G, Arnold G W, Mattei G, Mazzoldi P and Dran J C 1999 Structural modifications in ion-implanted silicate glasses *J. Appl. Phys.* **85** 8040-8049.

Battaglin G, Boscolo-Boscoletto A, Mazzoldi P, Meneghini C and Arnold G W 1996 Gold nanocluster formation in silicate glasses by low fluence ion implantation and annealing *Nucl. Instrum. Methods Phys. Res. B.* **116** 527-530.

Be’er A, Kofman R, Phillipp F and Lereah Y 2007 Spontaneous crystallographic instabilities of Pb nanoparticles in a SiO matrix *Phys. Rev. B.* **76** 075410-5.

Blanford C F and Carter C B 2003 Electron Radiation Damage of MCM-41 and Related Materials *Microsc. Microanal.* **9** 245-263.

Brow R K and Schmitt M I 2009 A survey of energy and environmental applications of glass *J. Eur. Ceram, Soc.* **29** 1193-1201.

Brunov V S, Podsvirov O A, Sidorov A I and Churaev D V 2014 Formation of silver thin films and nanoparticles inside and on the surface of silver-containing glasses by electron irradiation *Tech. Phys.* **59** 1215-1219.

Carrez P, Demyk K, Leroux H, Cordier P, Jones A P and Hendecourt L D 2002 Low-temperature crystallization of $MgSiO_3$ glasses under electron irradiation: Possible implications for silicate dust evolution in circumstellar environments *Meteo. Plane Sci.* **37** 1615-1622.

Cazaux J 1986 Some consideration on the electric-field induced in insulators by electron-bombardment *J. Appl. Phys.* **59** 1418-1430.

Cazaux J 1995 Correlations between ionization radiation damage and charging effects in transmission electron microscopy *Ultramicroscopy.* **60** 411-425.

Cazaux J 1999 Mechanisms of charging in electron microscopy *J. Ele. Spec. Rel. Pheno.* **105** 155-185.

Chen J, Mu R, Ueda A, Wu M H, Tung Y S, Gu Z, Henderson D O, White C W, Budai J D and Zuhr R A 1998 Characterization of zinc implanted silica: Effects of thermal annealing and picosecond laser irradiation *J. Vac. Sci. Technol. A* **16** 1409-1413.

Cohen M H and Grest G S 1979 Liquid-glass transition, a free-volume approach *Phys. Rev. B* **20** 1077-1098.

Cowley J M 2002 Electron nanodiffraction methods for measuring medium-range order *Ultramicroscopy.* **90** 197-206.

De Natale J F and Howitt D G 1982 Radiation damage in a nuclear waste glass *Am. Ceram. Soc. Bull.* **61** 582-584.

De Natale J F and Howitt D G 1984 A Mechanism for Radiation Damage in Silicate Glasses *Nucl. Instrum. Methods Phys. Res. B.* **1** 489-497.

DeNovion C H and Barbu A 1992 Radiation effects in oxide glasses *Sol. State Pheno.* **30-31** 277-296.

Doraiswamy N and Marks L D 1996 Electron beam induced small particle transformations: temperature *Surf. Sci.* **348** L67-L69.

Du X , Takeguchi M, Tanaka M and Furuya K 2003 Formation of crystalline Si nanodots in SiO_2 films by electron irradiation *Appl. Phys. Lett.* **82** 1108-1110.

Du X W, Wang B, Zhao N Q and Furuya K 2005 Structure evolution of silicon nanocrystals under electron irradiation *Scrip. Mater.* **53** 899–903.

Egerton R F 1996 Electron Energy Loss Spectroscopy in the Electron Microscope, 2nd Edition *Plenum, New York.*

Egerton R F, Li P and Malac M 2004 Radiation damage in the TEM and SEM *Micron.* **35** 399-409.

Ehrt D and Vogel W 1992 Radiation effects in glasses *Nucl. Instrum. Methods. Phys. Res. B.* **65** 1-8.

Elmer T H 1991 Porous and reconstructed glasses *ASM International, Engineered Materials Handbook.* **60** 427-432.

Ewing R C, Weber W J and Clinard F W 1995 Radiation effects in nuclear waste forms for high-level radioactive waste *Prog. Nucl. Ene.* **29** 63-127.

Gedeon O, Jurek K and Drbohlav I 2007 Changes in surface morphology of silicate glass induced by fast electron irradiation *J. Non-Cryst. Solids.* **353** 1946–1950.

Gedeon O, Jurek K and Hulinsky V 1999 Fast migration of alkali ions in glass irradiated by electrons *J. Non-Cryst. Solids.* ***246*** *1-8.*

Gnanavel T and Möbus G 2012 In situ synthesis of cobalt nanocrystal hierarchies in a transmission electron microscope *J. Nanopart. Res.* **14** 683-674.

Gonella F 2000 Nanoparticle formation in silicate glasses by ion-beam-based methods *Nucl. Instrum. Methods Phys. Res. B.* **166-167** 831-839.

Goodhew P J and Chescoe D 1980 Microanalysis in the transmission electron microscope *Micron.* **11** 153-181.

Graczyk J F and Moss S C 1969 Scanning Electron Diffraction Attachment with Electron Energy Filtering *Rev. Sci. Instrum.* **40** 424-433.

Greaves G N 1985 EXAFS and the structure of glass *J. Non-Cryst. Solids.* **71** 203-217.

Gryaznov V G, Kaprelov A M and Belov A Y 1991 Real temperature of nanoparticle in electron microscope beams *Philos. Mag. Lett*. **63** 275-279.

Guan W, Ross I M, Bhatta U M, Ghatak J, Peng N, Inksona B J and Möbus G 2013 Nanopatterning by ion implantation through nanoporous alumina masks *Phys.Chem. Chem. Phys.* **15** 4291-4296.

Hobbs L W 1987 Electron-beam sensitivity in inorganic specimens *Ultramicroscopy.* **23** 339-344.

Hofmeister H, Thiel S, Dubiel M and Schurig E 1997 Synthesis of nanosized silver particles in ion-exchanged glass by electron beam irradiation *Appl. Phys. Lett.* **70** 1694-1696.

Howitt D G, Chan H W, DeNatale J F and Heuer J P 1991 Mechanism for the radiolytically induced decomposition of soda-silicate glasses *J. Am. Ceram. Soc.* **74** 1145-1147.

Hua B, Shimotsuma Y, Nishi M, Miura K and Hirao K 2007 Micro-modification of metal-doped glasses by a femtosecond laser *J. Laser Micro/Nanoeng.* 2 36-39.

Humphreys C J 1989 Radiation effects *Ultramicroscopy.* **28** 357-358.

Iijima S and Ichihashi T 1986 Structural instability of ultrafine particles of metals *Phys. Rev. Lett.* **56** 616-619.

Ito Y, Jain H and Williams D B 1999 Electron-beam induced growth of Cu nanoparticles in silica glass matrix *Appl. Phys. Lett.* **75** 3793-3795.

Jencic I, Bench M W, Robertson I M, and Kirk M A 1995 *Electron-beam-induced crystallization of isolated amorphous regions in Si, Ge, GaP, and GaAs J. Appl. Phys.* **78** 974–982.

Jiang N 2005 *In situ* transmission electron energy loss spectroscopy of e-beam modifications in oxide glasses and crystals *Microsc. Microanal.* **11** 736-737.

Jiang N 2010 Electron-beam fabrication of nanostructures in glasses *Microsc. Microanal.* **16** 1660-1661.

Jiang N 2013 Damage mechanisms in electron microscopy of insulating materials *J. Phys. D: Appl. Phys.* **46** 305502-11.

Jiang N and Silcox J 2002 Electron irradiation induced phase decomposition in alkaline earth multi-component oxide glass *J. Appl. Phys.* **92** 2310-2316.

Jiang N, Qiu J and Silcox J 2000 Precipitation of nanometer scale Zn crystalline particles in ZnO-B_2O_3-SiO_2 glass during electron irradiation *Appl. Phys. Lett.* **77** 3956-3958.

Jiang N, Qiu J and Silcox J 2004 Effects of high-energy electron irradiation on heavy-metal fluoride glass *J. Appl. Phys.* **96** 6230-6233.

Jiang N, Qiu J and Spence J C H 2005 Precipitation of Ge nanoparticles from GeO_2 glasses in transmission electron microscope *Appl. Phys. Lett.* **86** 143112-3.

Jiang N, Qiu J, Ellison A and Silcox J 2003 Fundamentals of high-energy electron-irradiation-induced modifications of silicate glasses *Phys. Rev. B.* **68** 064207-11.

Jiang N, Qiu J, Gaeta A L and Silcox J 2002 Nanoscale modification of optical properties in Ge-doped SiO_2 glass by electron-beam irradiation *Appl. Phys. Lett.* **80** 2005-2007.

Jiang N, Su D, Qiu J and Spence J C H 2010 On the formation of Na nanoparticles in femtosecond-laser irradiated glasses *J. Appl. Phys.* **107** 064301-5.

Jiang N, Su D, Spence J C H, Zhou S and Qiu J 2008 Electron energy loss spectroscopy of Na in Na, Na_2O, and silicate glasses. *J. Mater. Res.* **23** 2467-2471.

Johannessen B, Kluth P, Glover C J, Azevedo G de M, Llewellyn D J, Foran G J and Ridgway M C 2005 Structural characterization of Cu nanocrystals formed in SiO_2 by high-energy ion-beam synthesis *J. Appl. Phys.* **98** 024307-9.

Karpukhina N, Hill R G and Law R V 2014 Crystallisation in oxide glasses-a tutorial review *Chem. Soc. Rev.* **43** 2174-2186.

Kim T W, Shin J W, Lee J Y, Jung J H, Lee J W, Choi W K and Jin S 2007 Electron-beam-induced formation of Zn nanocrystal islands in a SiO_2 layer *Appl. Phys. Lett.* **90** 051915-3.

Kleebe H J, Braue W, Schmidt H, Pezzottic G and Ziegler G 1996 Transmission Electron Microscopy of Microstructures in Ceramic Materials *J. Euro. Ceram. Soc.* **16** 339-351.

Kleebe H J, Turquat C and Soraru G D 2001 Phase separation in an SiCO class studied by transmission electron microscopy and electron energy-loss spectroscopy *J. Am. Ceram. Soc.* **84** 1073-1080.

Klimenkov K, Matz W and Borany J V 2000 *In situ* observation of electron-beam-induced ripening of Ge clusters in thin SiO_2 layers *Nucl. Instr. Meth. B.* **168** 367-374.

Klimenkov M, Matz W, Nepijko S A and Lehmann M 2001 Crystallisation of Ge nanoclusters in SiO_2 caused by electron irradiation in TEM *Nucl. Instrum. Methods Phys. Res. B.* **179** 209-214.

Lindquist N C, Nagpal P, McPeak K M, Norris D J and Oh S H 2012 Engineering metallic nanostructures for plasmonics and nanophotonics *Rep. Prog. Phys.* **75** 063501-62.

Lineweaver J L 1963 Oxygen outgassing caused by electron bombardment of glass *J. Appl. Phys.* **34** 1786-1791.

Lo C J, Aref T and Bezryadin A 2006 Fabrication of symmetric sub-5 nm nanopores using focused ion and electron beams *Nanotechnology.* **17** 3264–3267.

Manara A, Antonini M, Camagni P and Gibson P N 1984 Radiation damage in silica-based glasses: point defects, microstructural changes and possible implications on etching and leaching *Nucl. Instrum. Methods Phys. Res. B.* **1** 475-480.

Marks L D and Ajayan P M 1986 Quasi-melting of small particles *Ultramicroscopy.* **20** 77-82.

Mayr S G, Ashkenazy Y, Albe K and Averback R S 2003 Mechanisms of radiation-induced viscous flow: Role of point defects *Phys. Rev. Lett.* **90** 055505-4.

McMillan P 1964 Glass-Ceramics *Academic Press Inc., U.S.*

Mkhoyan K A, Silcox J, Ellison A, Ast D and Dieckmann R 2006 Full Recovery of Electron Damage in Glass at Ambient Temperatures *Phys. Rev. Lett.* **96** 205506-4.

Möbus G, Ojovan M, Cook S, Tsai J and Yang G 2010 Nano-scale quasi-melting of alkali-borosilicate glasses under electron irradiation *J. Nucl. Mater.* **396** 264-271.

Möbus G, Tsai J, Xu X J, Bingham P and Yang G 2008 Nanobead formation and Nanopatterning in Glasses *Microsc Microanal*. **14** 434-435.

Mohapatra S, Mishra Y K , Ghatak J, Avasthi D K 2013 *In-situ* TEM observation of electron irradiation induced shape transition of elongated gold nanoparticles embedded in silica *Adv. Mat. Lett.* **4** 444-448.

Molchanova O S 1957 Region of anomalous glasses in the system Na_2O-SiO_2-B_2O_3 *Glass and Ceramics* **14** 157-159.

Müller S A, Aebi U and Engel A 2008 What transmission electron microscopes can visualize now and in the future *J. Struct. Bio.* **163** 235-245.

N.V. Nikonorov, A.I. Sidorov, V.A. Tsekhomskii, A.V. Nashchekin, O.A. Usov, O.A. Podsvirov and S.V. Poplevkin 2009 Electron-beam modification of the near-surface layers of photosensitive glasses *Tech. Phys. Lett.* **35** 309-311.

N.V. Nikonorov, I.A. Sidorov and A.V. Tsekhomskii 2010 Silver nanoparticles in oxide glasses: technologies and properties *Silver Nanoparticles*, Ed. by D.P. Perez (In-Tech, Vukovar, Croatia), 177-200.

Newbury D E and Williams D B 2000 The electron microscope: The materials characterization tool of the millennium *Acta. Mater.* **48** 323-346.

Ojovan M I and Lee W E 2010 Glassy wasteforms for nuclear waste immobilization *Metall. Mater. Trans. A.* **42** 837-851.

Ojovan M, Yang G and Möbus G 2010 On spinodal decomposition of e-beam irradiated borosilicate glasses *WM Conference, Phoenix, AZ.* 1-8.

Ollier N, Rizza G, Boizot B and Petite G 2006 Effects of temperature and flux on oxygen bubble formation in Li borosilicate glass under electron beam irradiation *J. Appl. Phys.* **99** 073511-6.

Pal U, Hernandez A B, Fernandez L R and Wong J C C 2000 Effect of thermal annealing on the optical properties of high-energy Cu-implanted silica glass *J. Non-Cryst. Solids* **275** 65-71.

Paul A 1982 Chemistry of Glasses *Chapman & Hall, London.*

Pfaender H G 1966 Schott guide to glass, 2nd Edition *Chapman & Hall, New York.*

Pham L Q, Sohn J H, Park J H, Kang H S, Lee B C and Kang Y S 2011 Comparative study on the preparation of conductive copper pastes with copper nanoparticles prepared by electron beam irradiation and chemical reduction *Radia. Phys. Chem.* **80** 638-642.

Pye L D, Stevens H J and LaCourse W C 1972 Introduction to glass science *Plenum Press, New York and London.*

Qin L C and Hobbs L W 1995 Energy-filtered electron diffraction study of vitreous and amorphized silicas *J. Non-Cryst. Solids.* **192/193** 456-462.

Qiu J, Shirai M, Nakaya T, Si J, Jiang X, Zhu C and Hirao K 2002 Space-selective precipitation of metal nanoparticles inside glasses *Appl. Phys. Lett.* **81** 3040-3042.

Qu S, Gao Y, Jiang X, Zeng H, Song Y, Qiu J, Zhu C and Hirao K 2003 Nonlinear absorption and optical limiting in gold-precipitated glasses induced by a femtosecond laser *Opt. Communi.* **224** 321-327.

Rauf I A 2008 Direct observation of the birth of a nanocrystalline nucleus in an amorphous matrix *Appl. Phys. Lett.* **93** 143101-3.

Risbud S H 1982 STEM and EELS analysis of multiphase microstructure in oxide and non-oxide glasses *J. Non-Cryst. Solids.* **49** 241-251.

Sacchi M, Antonini M, Buckley S N and Manara A 1985 Alkali effects on bubble formation in irradiated borosilicate glasses *Mater. Lett.* **4** 10-12.

Shelby J E 2005 Introduction to Glass Science and Technology, 2nd Edition *The Royal Society of Chemistry.*

Sheng J, Chen S, Zhang J, Li J and Yu J 2009 UV-light irradiation induced copper nanoclusters in a silicate glass *Inter. J. Hydro. Energ.* **34** 1119-1122.

Shin J W, Lee J Y, No Y S, Kim T W, Choi W K and Jin S 2008 The formation mechanism of periodic Zn nanocrystal arrays embedded in an amorphous layer by rapid electron irradiation *Nanotechnology* **19** 295303-6.

Silva C, Coelho J M P, Ruivo A and de Matos A P 2010 Infrared nanosecond laser effects on the formation of copper nanoparticles *Mater. Lett.* **64** 705-707.

Singh S P and Karmakar B 2011 In situ electron beam irradiated rapid growth of bismuth nanoparticles in bismuth-based glass dielectrics at room temperature *J. Nanopart. Res.* **13** 3599–3606.

Slayter G 1952 Strength of Glass *Am. Ceram. Soc. Bull.* **31** 276-278.

Snoeks E, Weber T, Cacciato A and Polman A 1995 MeV ion irradiation-induced creation and relaxation of mechanical stress in silica *J. Appl. Phys.* **78** 4723–4732.

Stanworth J E 1950 Physical Properties of Glass *Oxford University Press*, London.

Stenn K and Bahr G F 1970 Specimen damage caused by the beam of the transmission electron microscope, a correlative reconsideration *J. UltraStruct. Res.* **31** 526-550.

Storm A J, Chen J H, Ling X S, Zandbergen H W and Dekker C 2003 Fabrication of solid-state nanopores with single-nanometre precision *Nat. Mater.* **2** 537-540.

Storm A J, Chen J H, Ling X S, Zandbergen H W and Dekker C 2005 Electron-beam-induced deformations of SiO_2 nanostructures *J. Appl. Phys.* **98** 014307-8.

Sun K, Wang L and Ewing R C 2003 EFTEM study of phase separation in borosilicate glasses under electron beam irradiation *Microsc. Microanal.* **9** 128-129.

Sun K, Wang L M and Ewing R C 2003 Analytical electron microscopy study of electron radiation damage in iron phosphate glass waste forms *Mater. Res. Soc. Symp. Proc.* **757** 135-140.

Sun K, Wang L M and Ewing R C 2008 Fabrication of nano-/micro-patterns on iron phosphate glass surfaces by focused energetic beams *Nucl. Instrum. Methods Phys. Res. B.* **266** 3133-3137.

Sun K, Wang L M, Ewing R C and Weber W J 2004 Electron irradiation induced phase separation in a sodium borosilicate glass *Nucl. Instrum. Methods Phys. Res. B.* **218** 368-374.

Sun K, Wang L M, Ewing R C and Weber W J 2005 Effects of electron irradiation in nuclear waste glasses *Philosophical Magazine.* **85** 597-608.

Trinkaus H 1995 Local stress relaxation in thermal spikes as a possible cause for creep and macroscopic stress relaxation of amorphous solids under irradiation *J. Nucl. Mater.* **223** 196-201.

Tsang W M, Stolojan V, Wong S P, Linder J K N, Sealy B J and Silva S R P 2007 The structural and electron field emission properties of ion-beam-synthesised metallic-dielectric nanocomposites *Rev. Adv. Mater. Sci.* **15** 179-184.

Usher D M 1981 Sodium ion migration in glass on electron beam irradiation *J. Phys. C: Solid State Phys.* ***14*** *2039-2048.*

V.S. Brunov, O.A. Podsvirov, A.I. Sidorov and D.V. Churaev 2014 Formation of silver thin films and nanoparticles inside and on the surface of silver-containing glasses by electron irradiation *Tech. Phys.* **59** 1215-1219.

Vedishcheva N M, Shakhmatkin B A and Wright A C 2003 Thermodynamic modelling of the structure of sodium borosilicate glasses *Phys. Chem. Glasses.* **44** 191-196.

Vogel W 1985 Chemistry of Glass *The American Ceramic Society Inc., Columbus, Ohio.*

Volkert C A 1991 Stress and plastic flow in silicon during amorphization by ion bombardment *J. Appl. Phys.* **70** 3521–3527.

Vostokov A V, Ignat’ev A I, Nikonorov N V, Sidorov O A, Sidorov A I, Nashchekin A V, Sokolov R V, Usov O A and Tsekhomskii V A 2009 Influence of electron beam irradiation on formation of silver nanoclusters in photothermorefractive glasses *Tech. Phys. Lett.* **35** 35-40.

Wackerow S and Abdolvand A 2014 Generation of silver nanoparticles with controlled size and spatial distribution by pulsed laser irradiation of silver ion-doped glass *Opt. Exp.* **22** 5076-5085.

Wang Y H, Peng S J, Lu J D, Wang R W, Mao Y L and Cheng Y G 2009 Optical properties of Cu and Ag nanoparticles synthesized in glass by ion implantation *Vacuum* **83** 408-411.

Wang Z L 2003 New Developments in Transmission Electron Microscopy for Nanotechnology *Adv. Mater.* **15** 1497-1514.

Weber W J 1988 Radiation effects in nuclear waste glasses *Nucl. Instrum. Methods Phys. Res. B.* **1** 471-479.

Weber W J 1991 The effect of radiation on nuclear waste forms *J. Minerals, Metals Mater. Soc.* **43** 35-39.

Weber W J, Ewing R C, Angell C A, Arnold G W, Cormack A N, Delaye J M, Griscom D L, Hobbs L W, Navrotsky A, Price D L, Stoneham A M and Weinberg M C 1997 Radiation effects in glasses used for immobilization of high-level waste and plutonium disposition *J. Mater. Res.* **12** 1946-1978.

Wellenberg L R, Bovin J O, Petford-Long A K and Smith D J 1986 Atomic-resolution study of structural rearrangements in small platinum crystals *Ultramicroscopy.* **20** 71-76.

Williams D B and Carter C B 1996 Transmission Electron Microscopy: A Textbook for Materials Science. Plenum Press. New York and London.

Wu M Y, Krapf D, Zandbergen M, Zandbergen H and Batson P E 2005 Formation of nanopores in a SiN/SiO_2 membrane with an electron beam *Appl. Phys. Lett.* **87** 113106-3.

Yamane M and Asahara Y 2000 glasses for photonics *Cambridge University Press, Cambridge.*

Yang G, Möbus G and Hand R J 2006 Cerium and boron in doped borosilicate glasses examined by EELS *Micron.* **37** 433-441.

Yang K J, Wang T S, Zhang G F, Peng H B, Chen L, Zhang L M, Li C X, Tian F and Yuan W 2013 Study of irradiation damage in borosilicate glass induced by He ions and electrons *Nucl. Instrum. Methods Phys. Res. B.* **307** 541-544.

Yen M Y, Chiu C W, Chen F R, Kai J J, Lee C Y and Chiu H T 2004 Convergent electron beam induced growth of copper nanostructures: Evidence of the importance of soft template *Langmuir*. **20** 279-281.

Zallen R 1998 The physics of amorphous solids *Wiley VCH.*

Zeng H, Yang Y, Jiang X, Chen G, Qiu J and Gan F 2005 Preparation and optical properties of silicate glasses containing Pd nanoparticles *J. Cryst. Growth.* **280** 516-520.

Zheng K, Wang C, Cheng Y Q, Yue Y, Han X, Zhang Z, Shan Z, Mao S X, Ye M, Yin Y and Ma E 2010 Electron-beam-assisted superplastic shaping of nanoscale amorphous silica *Nat. Communications.* **24** 1-8.

Zhonghong J 1989 Some aspects of phase separation in glasses *J. Non-Cryst. Sol.* **112** 48-57.

Zhou R, Wu X, Hao X, Zhou F, Li H and Rao W 2008 Influences of surfactants on the preparation of copper nanoparticles by electron beam irradiation *Nucl. Instrum. Methods Phys. Res. Sect. B.* **266** 599-603.

Zhu X, Su J, Wu Y, Wang L and Wang Z 2014 Intriguing surface-extruded plastic flow of SiO_x amorphous nanowire as athermally induced by electron beam irradiation *Nanoscale* **6** 1499-1507.

Chapter Three

Materials and Methods

3.1 Introduction

This chapter describes the starting materials used in this study as well as the wide range of instruments which are used to perform the experiments. Section 3.2 starts with the glass selected for this study and the method used to prepare it. The next section, 3.3, describes the sample preparation for transmission electron microscopy (TEM). Section 3.4 gives a brief description of the X-ray diffraction (XRD) technique, used to examine the annealed glass powder. Transmission electron microscopy (TEM), electron-matter interaction and the electron sources used in this study will be discussed fully in section 3.5. This section also presents the operational principle of the TEMs used in this study. The next section, 3.6, is focused on the irradiation techniques used for the purpose of e-beam-induced precipitation, nanoparticle (NP) formation, patterning and morphology change experiments. The methods used to analyse the precipitated/fabricated NPs are set out in section 3.7. In the last section, 3.8, a brief description of scanning electron microscopy (SEM) will be given.

3.2 Selection of glass

In this study, two sets of borosilicate glass were used for two different purposes. The first group was chosen to study patterning and electron irradiation-induced precipitation. The types of glass used here are Zn-loaded borosilicate glass, Cu-loaded borosilicate glass and Ag and Ce-doped borosilicate glass. The second group consists of types of glass chosen to study electron irradiation-induced shape transformations; mainly alkali-borosilicate (ABS) glass with either high-Si or high-B content. More details about the composition of these types of glass and the motivation behind their use, will be presented in the relevant results chapters (chapter 4 for Zn-borosilicate glass, chapter 5 for Cu-borosilicate glass, chapter 6 for Ag-doped borosilicate glass and chapter 7 for the glasses used in e-beam-induced morphology transformations).

3.2.1 Synthesis of the glass batches

For the purpose of glass batch preparation, raw materials of oxides, carbonates and nitrides were prepared (these raw materials will be set out in each of the results chapter). The raw materials for each component were weighed separately using an accurate scale in order to obtain the desired weight (300 g in total for each batch). The chemicals were then thoroughly mixed together, manually, for about 15 min using a spatula in order to obtain a homogeneous mixture.

3.2.2 Glass melting

The oxide glasses were produced by a conventional melting method. After finishing the glass batch preparation, the batch is then poured into a suitable crucible. Selection of the crucible essentially depends on the melting temperature, as well as on the glass composition. In this study, a platinum (Pt) crucible was usually used, except for the coloured glasses (Cu- and Ag-borosilicate glasses), where a mullite crucible was used. The size limitation of the crucible meant that it was difficult to pour the whole batch into the crucible at one time; hence the melting process was performed in three stages. The electric furnace used in the melting has an internal volume of 147.5 cm^3 with the SiC elements used. The crucible was first filled until it was slightly more than half full and then placed into the furnace at the pre-defined temperature (the melting temperature of all the glass types is given in the respective result chapter). After approximately 5-10 minutes, the crucible was taken out from the furnace using iron nippers and more batches were poured on top of the melt until the crucible was again half, or slightly more than half, full. This technique was used until the entire batch had been added into the crucible. The whole melting process lasted about 5 hours. After 1 hour of glass melting, and in order to obtain a homogeneous melt free from curds and bubbles, a platinum stirrer was put into the crucible at a height of approximately 1 cm from the bottom of the crucible and this was rotated at 60 rpm for about 4 hours (the stirring process was conducted at the same melting temperature).

After completing the melting process and depending on the type of experiments needed, two glass samples were obtained. About 80-90% of the melt was cast into a pre-heated steel mould with a size of about 2×2×10 cm to form a rectangular shaped glass block. Then, the glass block was placed in an annealing furnace for slow cooling to room temperature at 1 ^{o}C/ min. This helped to reduce the stress on the cooling glass. The rest of the melt (about 10-20%) was used to obtain a glass frit. This was done by pouring this amount of the melt rapidly into a cold steel bowl containing water inside a bigger cold steel bowl. The process of glass preparation is summarised in Fig. 3-1.

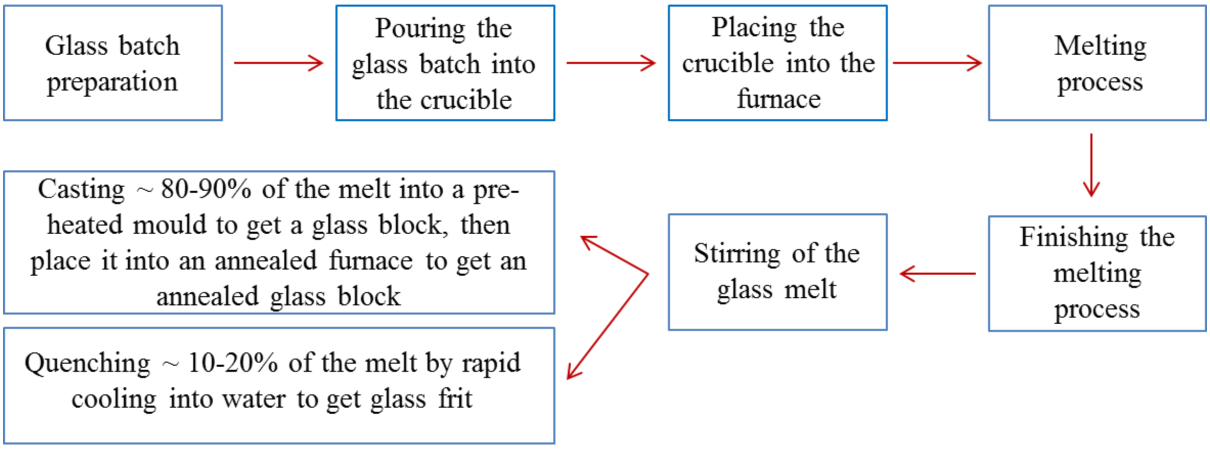

Figure 3-1: Schematic illustration of the stages of glass preparation.

3.3 Sample preparation for TEM studies

The samples for TEM studies needed to be as thin as possible in order to be appropriate for TEM studies. TEM analysis is in principle similar for both quenched and annealed glass, but there are different preparation procedures. In this study, the method used is that of crushing the glass materials to obtain a powder. Since this is a manual method, various shapes, sizes and thicknesses of glass fragments are obtained. More details are provided in the following sections.

3.3.1 TEM specimen of quenched glass

The glass frits were manually ground into a fine powder using a pestle and mortar. The powder was then mixed with a suspension liquid such as acetone. The mixture was then ultrasonicated for about 15 min to minimise the amount of agglomeration. Transmission electron microscope specimens were then prepared by picking up a small amount of the powder suspended in acetone by immersing the grid supported by a holey carbon film into the liquid for few seconds. The TEM grids used in this study were all Cu, except those for the Cu-borosilicate glasses for which Au grids were used so as to avoid any overlapping of Cu energy dispersive X-ray (EDX) signals between the glass and the grid.

3.3.2 TEM specimen of annealed glass

The procedure for preparing a TEM specimen of annealed glass was similar to that used for the glass frit. In the case of the annealed glass, however, the glass block was cut twice in cross-section with a diamond cutting saw into a thin slice of about 2×2 cm cross-section. This slice was then ground with pestle and mortar as described for the frit, making sure that the outer regions of the cross-sectional slice were cut off and excluded before grinding, since these might be less typical due to their faster cooling rate in contact with air or the metal mould. In addition, the annealed glass was also examined by X-ray diffraction (XRD) and, therefore, the powder obtained from the grinding was also used in XRD analysis.

3.4 X-ray diffraction (XRD)

The principle of this technique is based on Bragg's law [Bragg, 1913]:

$$2d\ \sin\theta = n\lambda \text{ -------- (3-1)}$$

where *d* the is distance between the planes and θ is known as the Bragg angle, which is between the planes and the incident radiation, *n* is an integer (n = 1, 2, 3 …) and λ is the wavelength of the x-rays (Fig. 3-2). X-ray diffraction is a common technique used to identify the phases existing in a material. For XRD analysis, the specimen is usually positioned in the path of an X-ray with a known radiation wavelength, such as copper. X-rays will diffract from the crystals at different angles, determined by the d-spacing. If the incident X-rays are between 0 and 90^{o} the diffracted beams are collected and, the XRD pattern can be obtained and the phases readily analysed.

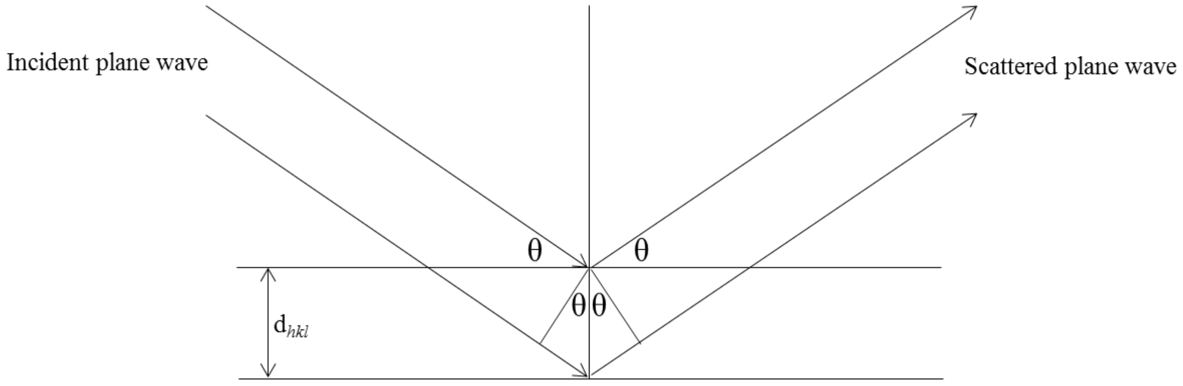

Figure 3-2: The principle of X-ray diffraction (XRD) [Cited in Williams and Carter, 1996 and Massa, 2002].

In our study, the annealed glass was analysed in a STOE STADI P system with an X-ray source of Cu-radiation. For this purpose, a few grams of annealed glass powder were loaded into a disk shaped aluminium sample holder. The powder was sandwiched between two ultra-thin foils in order to ensure that it was homogeneously distribute in the sample holder and was then transferred to the XRD machine for analysis.

3.5 Transmission electron microscopy (TEM)

Transmission electron microscopy (TEM) was invented in Germany (Berlin) by Max Knoll and Ernst Ruska [Knoll and Ruska, 1932]. A few years later, TEMs were developed by different commercial companies such as Metropolitan Vickers, Hitachi, Japanese Electron Optics Laboratory (JEOL) and Philips. At the present time, TEMs are the most efficient and versatile instruments for materials characterisation. Today's enhancements in TEMs have made them suitable for high resolution imaging as well as for chemical analysis, studying the crystallography and electronic structures via different analysis facilities.

A transmission electron microscope comprises three main parts: the illumination system, sample stage and imaging system. The illumination part of the TEM consists of an electron gun, which is the source of the electrons, and two condenser lenses. The sample stage, on the other hand, is used to load the specimen into the TEM. Finally, the imaging system, consists of objective and projector lenses used to obtain magnified images for the specimen. This will be either on a fluorescent screen, a photographic film or on the screen of a charged coupled device (CCD) camera system.

3.5.1 Electron beam-matter interaction

As the electron beam in the TEM has been used in this study for irradiation, patterning as well as for imaging, it is useful to give a brief description of the interaction between the electron beam and the specimen.

When the electron beam hits the specimen, a wide range of signals will be produced. These signals are useful in giving chemical information and many other details about the specimen. Figure 3-3 illustrates the signals produced upon electron-specimen interaction [Williams and Crater, 1996].

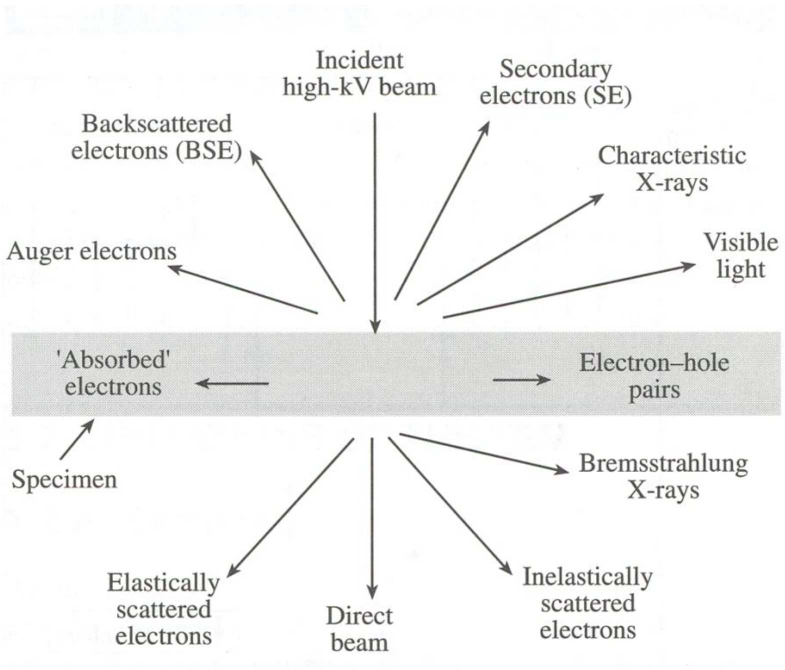

Figure 3-3: The generated signals upon interaction of high-energy electrons with the specimen [Cited in Williams and Crater, 1996].

Characteristic X-rays and inelastic scattered electrons are the two important signals used in our study to obtain chemical information about the precipitated/formed nanoparticles and also information about the glass matrix. Further details about these two signals are in sections 3.7.1 and 3.7.2. Secondary and backscattered electrons are also useful signals for imaging. While the former escape from the specimen with energies lowers than ~ 50 eV, the latter usually carry high energies [Goodhew *et al.*, 2001]. Elastically scattered electrons, on the other hand, maintain an unchanged energy level.

3.5.2 The source of electrons (electron gun)

The two most common types of electron guns are thermionic and field emission (FE), depending on their operating principle. In the thermionic gun, the essential filaments are tungsten (W) or lanthanum hexaboride (LaB_6). The main electron sources in the field emission gun, on the other hand, are Schottky (ZrO/W) or field emission (cold-W).

3.5.2.1 Thermionic gun

In this type of electron source, the electrons will be produced when heated. The principle of the operation is as follows: when the source of electrons is heated to defined temperature (T), the energy given to the electrons will exceed the natural barrier that inhibits the electrons from escaping. This barrier is called the "work function" ($\emptyset$). When the energy given to the electrons is greater than the work function, the electrons will be able to escape from the source and form an electron beam. This phenomenon is termed as thermionic emission.

The physics of thermionic emission is given in Richardson's Law [Egerton, 2007]. In this law, the current density (J) from the electron source and the temperature (T) are both related together as shown below:

$$J = AT^2 \, e - \frac{\emptyset}{kT} \text{ --------- } (3\text{-}2)$$

where k is Boltzmann's constant (8.6×10^{-5} eV/K) and A is Richardson's constant in units A/m^2K^2 and depends on the source material.

A higher total current intensity and high acceleration voltage (300 kV) is available in the thermionic gun TEM used in this study. These are exploited to perform experiments on e-beam-induced precipitation and the formation of nanoparticles and nanocrystals in oxide glasses in addition to electron beam-induced morphology transformation.

3.5.2.2 Field emission gun (FEG)

The electrons in the field emission gun are produced when an intense electric field is applied to it. The principle of operation in this type is completely different than in thermionic gun that an electric field (E) significantly increases at sharp points of the source due to applying a voltage (V) to a spherical point of radius r as shown below:

$$E = \frac{V}{r} \text{ -------- (3-3)}$$

The high voltage applied to the source of electrons will increase the electric field and decrease the work function barrier and hence the electrons will be able to escape from the source and produce an electron beam. Field emission guns can be sub-divided into Schottky and cold field emission guns. The emission current in a Schottky gun is much higher than that of the thermionic gun, while the temperature is lower in a Schottky gun than in a thermionic gun. On the other hand, the cold field emission gun operates at room temperature, which is significantly lower than the high temperature utilised in both the Schottky and thermionic guns.

A very fine probe can be obtained with a field emission gun and hence the possibility to illuminate a smaller region in the specimen. This makes the electron beam more coherent, with a larger current density and brightness than the thermionic gun. This very fine, intense, electron beam has been used in this project for some applications such as line-scan irradiation and patterning experiments, as well as hole drilling tests.

3.5.3 Description of TEMs used

3.5.3.1 JEOL JEM 2010F transmission electron microscope

A field emission gun TEM (Fig. 3-4) at an accelerating voltage of 200 kV was used. In this TEM, a fine electron beam of size less than 1 nm can be achieved. This gives a high intensity e-beam irradiation and an image resolution of about 0.19 nm. An attached Gatan CCD camera was used for imaging. This TEM was equipped with an Oxford instruments ultra-thin window energy dispersive X-ray (EDX) detector and a magnetic prism spectrometer for electron energy loss spectroscopy (EELS). The TEM was used in this study for the purpose of inducing nano-precipitation and, nano-patterning in the glass, as well as for imaging. The chemistry of the formed and precipitated nanoparticles was identified using both EDX and EELS.

Figure 3-4: The University of Sheffield field emission gun (FEG) TEM.

3.5.3.2 JEOL JEM 3010 transmission electron microscope

This is a LaB_6 thermal filament TEM operating at a maximum accelerating voltage of 300 kV. The maximum available beam current could be achieved in this TEM. The image resolution is about 0.17 nm and a TVIPS system was attached for imaging. Electron irradiation-induced precipitation and nanoparticle formation in the glass, glass transformation, line-scan and imaging were the main reasons for using this TEM in this study. In addition, an *in-situ* heating experiment was also performed with this TEM.

3.5.3.3 PHILIPS 420 transmission electron microscope

The tungsten gun transmission electron microscope operating at an accelerating voltage of 120 kV was used at the initial stage of this research work to study the morphological changes in the glass fragments under e-beam irradiation.

Table 3-1 illustrates a comparison in terms of the type of electron gun, accelerating voltage and the corresponding image resolution between the three different TEMs used in this study.

Table 3-1: Comparison of three different transmission electron microscopies

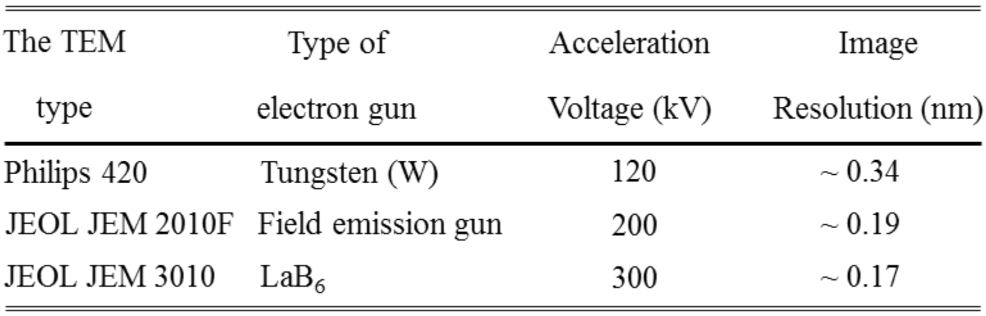

The TEM type	Type of electron gun	Acceleration Voltage (kV)	Image Resolution (nm)
Philips 420	Tungsten (W)	120	~ 0.34
JEOL JEM 2010F	Field emission gun	200	~ 0.19
JEOL JEM 3010	LaB_6	300	~ 0.17

3.6 Irradiation and imaging procedures

In this study, TEM was used for two purposes: firstly to exploit the e-beam in the TEM for irradiating the glass and hence inducing nano-precipitation, nano-crystal formation, nano-patterning and morphological transformation; and second, for imaging. Two different modes were used in the irradiation, including stationary and line-scan irradiation modes. While the first mode was used for e-beam-induced precipitation, pattering and morphological changes, the second mode was used for nano-patterning only. Different electron beams with varying intensities at different modes are used in irradiation. In addition, *in-situ* heating experiments were conducted in JEOL JEM 3010 using a Gatan single-tilt heating holder. If not specified, all irradiation was conducted with the largest condenser aperture (CA) and largest spot size. Evaluation of the images and calculation of the d-spacing in the HRTEM images and in the electron diffraction patterns were conducted using image J and digital micrograph software.

3.6.1 Stationary irradiation mode (SIM)

In this mode of irradiation, an electron beam of diameter larger than 100 nm was usually used to irradiate the glass fragments. This was done by placing the electron beam in a fixed manner over the glass fragment for a certain period of time. In this mode of irradiation, *in-situ* monitoring of the modifications in the glass is possible. Time-series irradiation was also applied via the stationary irradiation mode.

3.6.2 Line-scan irradiation mode (LSIM)

Line-scan irradiation means scanning the electron beam manually across the glass material using the two shift buttons available in the TEM in their fine and coarse modes. The word "line" refers to the product resulting from the e-beam scanning. In other words, scanning the electron beam over the glass fragment results in a line being produced: this line has two sharp edges separating the irradiated and un-irradiated regions. Line-scan irradiation differs from stationary irradiation in two essential aspects: first, line-scan irradiation was conducted using a focused electron beam. In the JEOL 2010F TEM, a sub-10 nm diameter electron beam was used in the line-scan irradiation experiment, while in the JEOL 3010 TEM, an electron beam of diameter < 100 nm would normally be used for such an experiment, second, it is difficult track the changes in the glass fragment under irradiation *in-situ* due to the electron beam being focused to its smallest size. Usually in this irradiation mode, the movement of the electron beam is controlled manually, such as by stopping the electron beam for a certain period of time for each movement, with the step-length being smaller than the beam diameter so as to generate a continuous line, or by conducting the line-scan irradiation without stopping the e-beam.

In both irradiation modes, the probe diameter was set up outside the glass fragment before the beam was moved into the glass material so as to minimize changes prior to the irradiation. Furthermore, spreading the e-beam to >> 100 nm during imaging of the results was necessary to stop further irradiation modifications. Fig. 3-5 and Fig. 3-6 give a simple visualization of how the process of line-scan irradiation is conducted in both FEG TEM and LaB$_6$ TEM, respectively, and the form of the produced line in both TEMs.

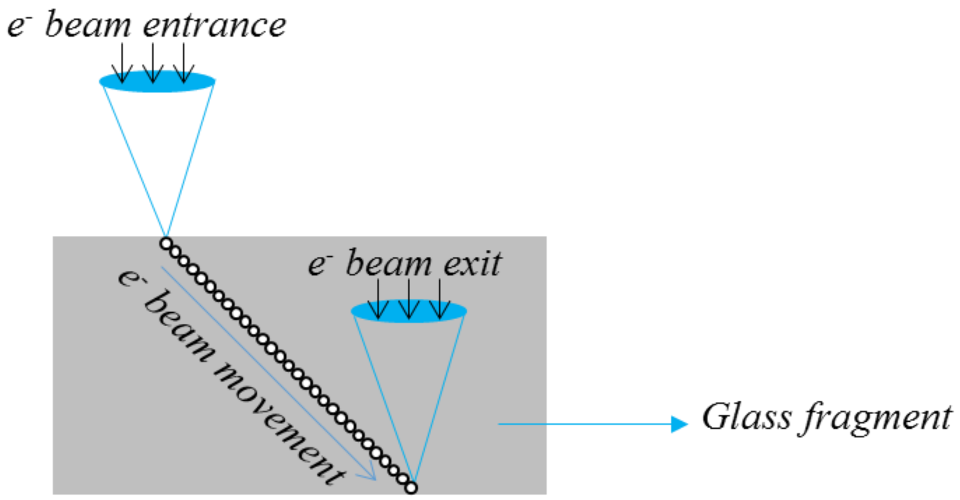

Figure 3-5: A descriptive diagram of the line-scan irradiation mode using electron beam of sub-10 nm diameter in FEG TEM.

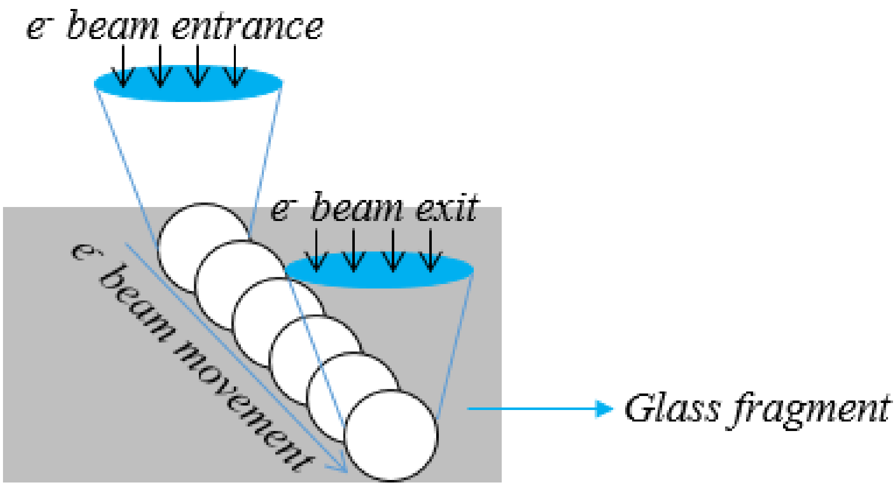

Figure 3-6: A descriptive diagram of the line-scan irradiation mode using electron beam of < 100 nm diameters in LaB_6 TEM.

3.7 Chemical analyses of the precipitated/formed NPs

All chemical analyses were conducted in a JEOL JEM 2010F TEM to identify the chemistry of the nanoparticles and nanocrystals being precipitated and formed in the glass after electron irradiation. These analyses were undertaken using electron energy loss spectroscopy (EELS) and energy dispersive X-ray (EDX) as well as high resolution transmission electron microscopy (HRTEM) imaging. In addition, annular dark field scanning transmission electron microscopy (ADF STEM) was used to confirm the atomic number contrast in high-Zn borosilicate (ZBS-A) glass.

There is a lack of characterisation techniques which may be used for the identification of the NPs in JEOL JEM 3010 TEM. HRTEM imaging was possible, however.

3.7.1 Electron energy loss spectroscopy (EELS)

Important chemical and structural information of the specimen can be obtained via electron energy loss spectroscopy (EELS) [Egerton, 1996]. The principle of EELS is that when the electron energy is sufficiently high and the specimen is thin enough, almost all of the incident electrons are transmitted to the spectrum analyser without any reflection or absorption. This means that the interaction occurs in the specimen and a fraction of the energy from the transmitted electrons will be lost via scattering, with the electrons of the atoms carrying useful information about the internal structure of the specimen. In our study, EELS (Gatan GIF 200) was utilised in a JEOL JEM 2010F FEG TEM to identify the chemistry of the precipitated/formed nanoparticles.

Figure 3-7 shows a typical EELS spectrum. The first dominant peak in the EELS spectrum is the zero-loss peak. This peak consists of electrons which suffer negligible inelastic scattering [Goodhew *et al.*, 2001] and do not lose any energy. Next to the zero-loss peak, there is the low-loss peak, which contains a series of peaks arise from inelastic scattering by outer shell electrons [Egerton, 1996]. This region consists of electrons which have lost up to ~ 50 eV. The most considerable energy feature in this region of an EELS spectrum is the plasmon loss. The low-loss peak is produced as a result of the collective oscillations of the weakly bound electrons. For analytical purposes, the characteristic edges at higher energy losses (core-loss) are necessary. The electrons in this region suffer high energy losses and the peak itself corresponds to the inelastic interaction of the electrons with the inner shell electrons. The energy of any edge in this region is usually between 100 eV and 2000 eV [Goodhew *et al.*, 2001].

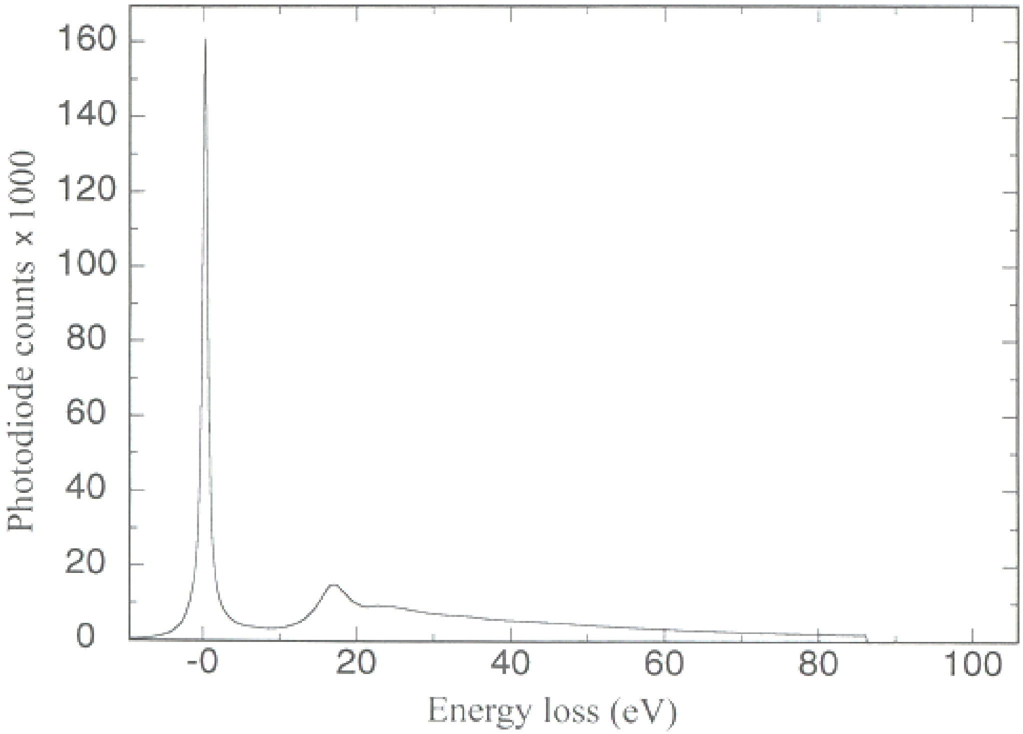

Figure 3-7: A typical EELS spectrum showing zero loss and low loss regions [Goodhew *et al.*, 2001].

3.7.2 Energy dispersive X-ray (EDX)

When an incident electron passes through the specimen, it can remove the tightly bound electron from the inner-shell leaving a vacancy behind. An electron from the outer-shell will then jump to fill this vacancy [Williams and Crater, 1996]. This will result in emission of a characteristic X-ray. These characteristic X-rays carry useful information about the chemistry and the elements existing in the specimen. Figure 3-8 is an illustration showing the emission of a characteristic X-ray. This figure also explains the electron energy loss (EEL).

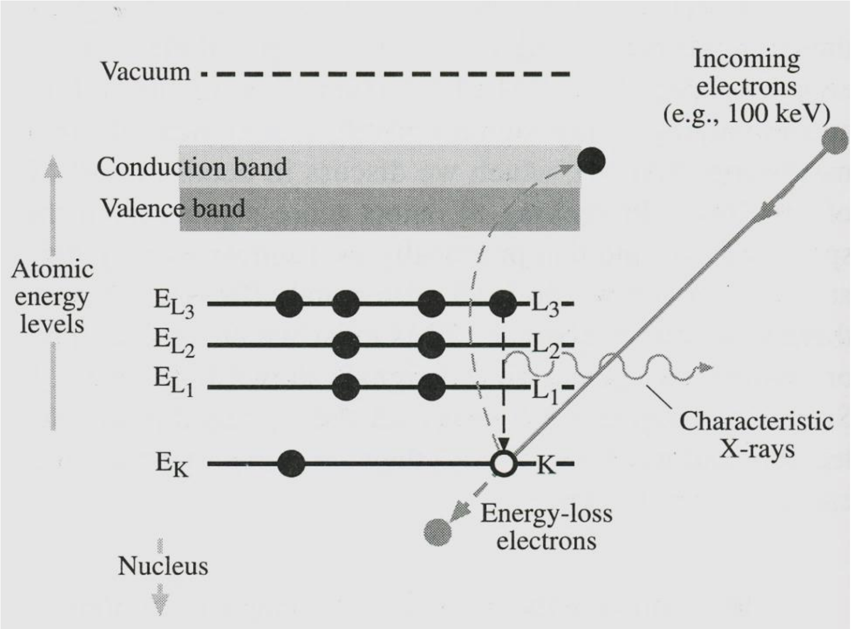

Figure 3-8: The principle of X-ray emission [Williams and Crater, 1996].

In this research, energy dispersive X-ray (EDX) was used to identify the chemistry of the precipitated nanoparticle/nanocrystal as well as of the glass particle. For this purpose, an Oxford Instruments ultra-thin window energy dispersive X-ray detector associated with Oxford ISIS software in a JEOL JEM 2010F FEG TEM was used.

3.7.3 Scanning transmission electron microscope (STEM)

In scanning transmission electron microscopy, a finely focused electron beam of diameter < 1 nm is scanned over the sample and only the transmitted electrons are detected by the detector and used to form images. Two kinds of images can be obtained in STEM mode; bright field (BF) and annular dark field (ADF) images. The latter strongly depends on the atomic number (Z contrast) of the materials. It is useful to analyse samples containing heavy materials (high atomic number) such as in our case, in high-Zn borosilicate (ZBS-A) glass, in which the precipitated particles of metallic Zn appeared bright in the ADF STEM image.

3.8 Scanning electron microscopy (SEM)

Scanning electron microscopy (SEM) is a widely used instrument in materials characterization. The interaction of the electron beam with the specimen will generate various types of signals such as secondary electrons (SEs), backscattered electrons (BSEs), characteristic X-rays and other photons of different energies. These signals can be used to examine different characteristics of the specimen such as surface topography, crystallography and composition. Secondary electrons together with backscattered electrons are of interest in surface tomography [Goldstein *et al.*, 2003].

In our study, a FEI Inspect F scanning electron microscope (SEM) operating at 20 kV and equipped with EDX was used for two purposes: (i) for imaging the dendrite precipitates in the annealed CuNBS-A glass and (ii) for chemical analyses of these dendrites as well as the glass matrix via point EDX.

The sample used in SEM analysis was prepared by cutting the glass block twice from its cross-section using a diamond cutting saw into a thin slice of about 2×2 cm cross-section (as mentioned in section 3.3.2). This slice was then ground using various grit wheels such as 120, 400, 800 and 1200 for about 15 min each and polished with a diamond paste of 6 micron. Finally, in order to prevent charging, and prior to SEM analysis, the sample was carbon coated with a carbon coater unit one (CCU1).

3.9 References

Bragg W L 1913 The diffraction of short electromagnetic waves by a crystal *Proc. Camb. Phil. Soc.* 43-57.

Egerton R F 1996 Electron Energy-Loss Spectroscopy in the Electron Microscope, 2nd Edition. Plenum Press. New York and London.

Egerton R F 2007 Physical Principles of Electron Microscopy: An Introduction to TEM, SEM and AEM. Springer Science and Business Media, LLC.

Goldstein J I, Newbury D E, Joy D C, Lyman C E, Echlin P, Lifshin E, Sawyer L and Michael J R 2003 Scanning Electron Microscopy and X-Ray Microanalysis, 3rd Edition. Springer Science and Business Media, Inc.

Goodhew P J, Humphreys J and Beanland R 2001 Electron Microscopy and Analysis, 3rd Edition. Taylor and Francis. New York and London.

Knoll M and Ruska E 1932 The electron microscope *Z Phys.* **78** 318-335.

Massa W 2002 Crystal Structure Determination, 2nd Edition. Springer-Verlag Berlin Heidelberg New York.

Williams D B and Carter C B 1996 Transmission Electron Microscopy: A Textbook for Materials Science. Plenum Press. New York and London.

Chapter Four

Electron irradiation experiments in zinc-loaded borosilicate glass

4.1 Introduction

In this research, two Zn borosilicate glass of different compositions were selected for the purpose of electron irradiation-induced precipitation and also for spatial patterning. The two glasses were labelled as ZBS-A for the high Zn-loaded glass and ZBS-B for the low Zn-loaded glass, respectively. The glass compositions are listed in table 4-1.

Table 4-1: Compositions of Zn-borosilicate glass (mol.%)

	Compositions (mol.%)			
Glass/Oxide	ZnO	Na_2O	B_2O_3	SiO_2
ZBS-A	60	0	20	20
ZBS-B	30	5	15	50

The raw materials used to prepare the glasses were zinc oxide (ZnO, purity > 99.0%), boric acid (H_3BO_3, purity > 99.5%), sodium carbonate (Na_2CO_3, purity ~ 99.1%) and silica sand (SiO_2, purity ~ 99.5%). The melting temperatures were 1450 ^{o}C for the ZBS-A glass and 1300 ^{o}C for the ZBS-B glass. The ZnO and H_3BO_3 were sourced from Sigma-Aldrich, while Na_2CO_3 and SiO_2 were sourced from Glassworks Services Ltd, Doncaster.

High-Zn borosilicate glass has been known since the last century from the work of Kawazoe *et al.* [Kawazoe *et al.*, 1989]. The optical properties for this glass have been studied after being irradiation with UV light. Zn borosilicate glass with a high amount of Zn has also been investigated by Jiang *et al.* [Jiang *et al.*, 2000 and Jiang *et al.*, 2003] and has been reported to have high irradiation sensitivity. For this reason, it has been chosen as a suitable candidate for both irradiation and patterning. The low Zn-content borosilicate glass, meanwhile, has been synthesized for this study to investigate several anticipated significant advantages. First, a high Zn contrast between particle and matrix is expected to be shown by Zn pattering. In addition, in comparison to the high Zn-content borosilicate glass (ZBS-A), this glass (ZBS-B) is expected to solve the problems of high irradiation sensitivity in pre- and post-pattering imaging. Third, from industrial point of view, ZBS-B provides better compatibility with standard composition ranges of borosilicate glasses broadly used in various fields such as laboratory glasses and nuclear waste glasses. By studying both high-Zn content and low-Zn content borosilicate glasses together, therefore, it will be possible to perform a fundamental study of the compositional impact of the irradiation and patterning.

Our study of Zn nanoclusters and nanocrystal formation derives its importance from the ability to generate nanoplasmonic near-surface arrays in a transparent matrix, e.g., for light-coupling applications.

This research advances the previous methodology of electron beam-induced precipitation of Zn nanoparticles in Zn borosilicate glass by using TEM with a variety of e-beam diameters, and also nanoscale pattern formation by TEM direct-write, assessing the influence of glass composition and tracking particle formation *in-situ*.

As reported earlier in this chapter, the main objective is to investigate irradiation-induced precipitation. When conducting this experiment, however, various other phenomena and effects were observed, and these are worth reporting.

In the following sections, therefore, the results of the electron irradiation-induced precipitation will first be presented, followed by the other electron irradiation-induced phenomena.

4.2 Results

4.2.1 Electron irradiation-induced precipitation of metallic Zn nanoparticles

Experiments in electron irradiation-induced precipitation of Zn nanoparticles in Zn-borosilicate glasses are arranged into stationary electron beam irradiation and line-scan patterning. These will be presented in detail below.

4.2.1.1 Stationary electron beam irradiation

The mechanism of stationary electron beam irradiation consists of preparing an electron beam with a certain diameter (after finishing the alignment processes) and then placing that electron beam into a certain region in the specimen for a certain time, followed by spreading the electron beam and imaging the results. Figure 4-1 shows TEM images of a high Zn-loaded borosilicate (ZBS-A) glass fragment prior to electron beam irradiation (Fig. 4-1(a)) and the same position in the glass after successive steps of irradiation (Fig. 4-1(b-e)). The selected area electron diffraction (SAED) pattern collected from the irradiation region in Fig. 4-1(e) is also shown in Fig. 4-1(f). Prior to the electron irradiation, the glass fragment shown in Fig. 4-1(a) was homogeneous and extremely clean with no nanoparticles evident. Time-series electron beam irradiation was then applied, starting with an irradiation period of 3 min, as shown in Fig. 4-1(b). This resulted in the precipitation and uniform distribution of nanoparticles with a diameter of about 3-10 nm. This precipitation and uniform distribution continued when the glass fragment was irradiated for a further 3 min, with the size of the nanoparticles now increasing to about 5-15 nm, as shown in Fig. 4-1(c). Another 3 min of irradiation resulted in a further increase in the size of the nanoparticles, and various shapes can be seen at this stage such as spherical (diameter ~ 20 nm), hexagonal and square as shown in Fig. 4-1(d). The final 3 min of the irradiation resulted in a significant growth in the size of nanoparticles, with some of these now exhibiting a large spherical morphology with a diameter of about 40 nm as shown in Fig. 4-1(e). In both Figs. 4-1(d) and 4-1(e) the rate of the glass ablation is high and some nanoparticles are found near the edges of the glass fragment.

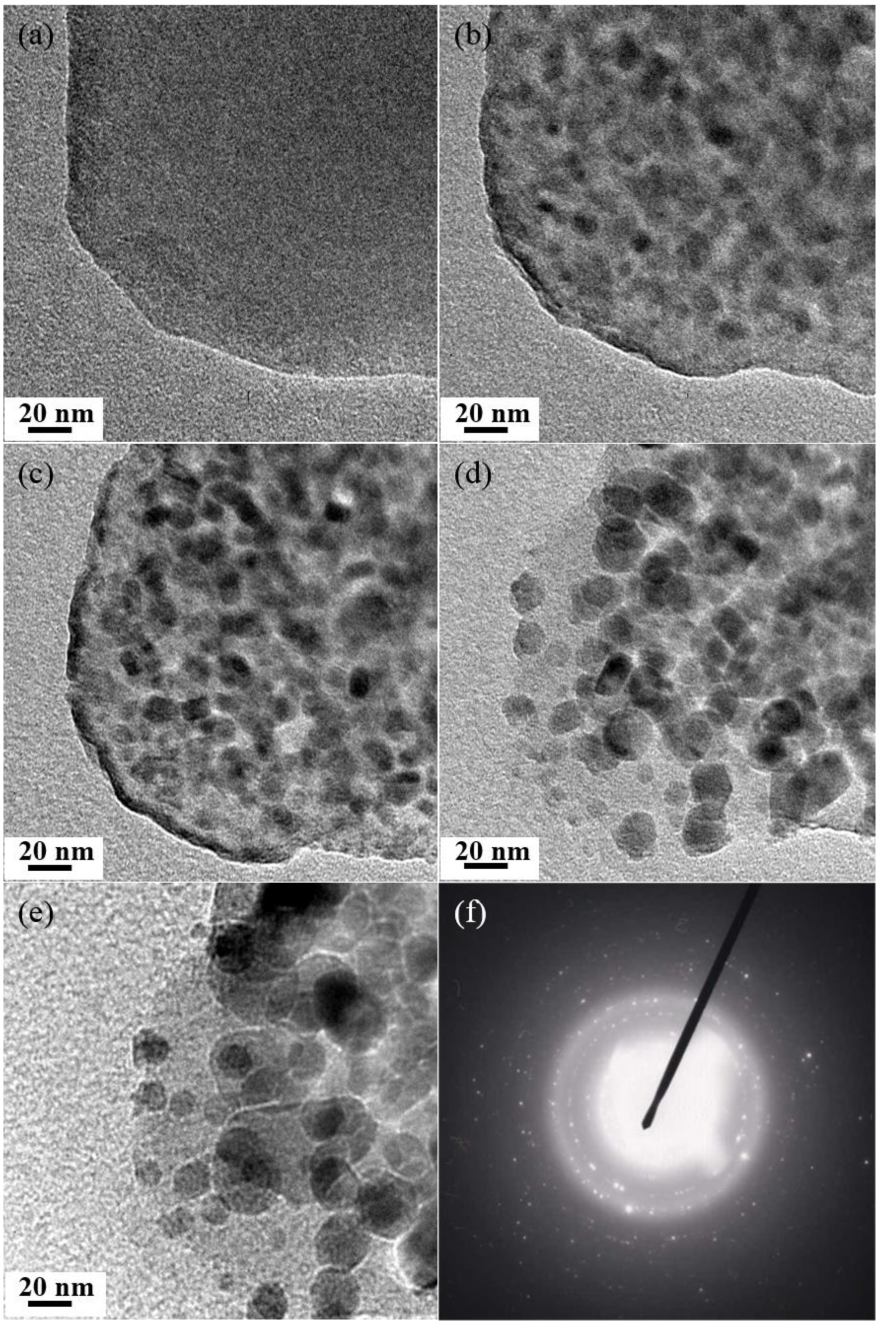

Figure 4-1: Time series TEM images of a ZBS-A glass fragment at (a) 0 min and (b-e) after 3 min, 6 min, 9 min and 12 min electron beam irradiation, respectively. (f) SAED pattern of the irradiated region in (e). JEM TEM 2010F at 200 keV.

The crystalline nature of the precipitated nanoparticles is clearly seen in Fig. 4-1(f). These diffraction patterns were then evaluated in order to calculate the d-spacing and it was found that the vast majority of the precipitated Zn nanoparticles are metallic.

Figure 4-2 presents bright field (BF) and annular dark field (ADF) micrographs of a high Zn-loaded borosilicate (ZBS-A) glass fragment after prolonged electron beam irradiation.

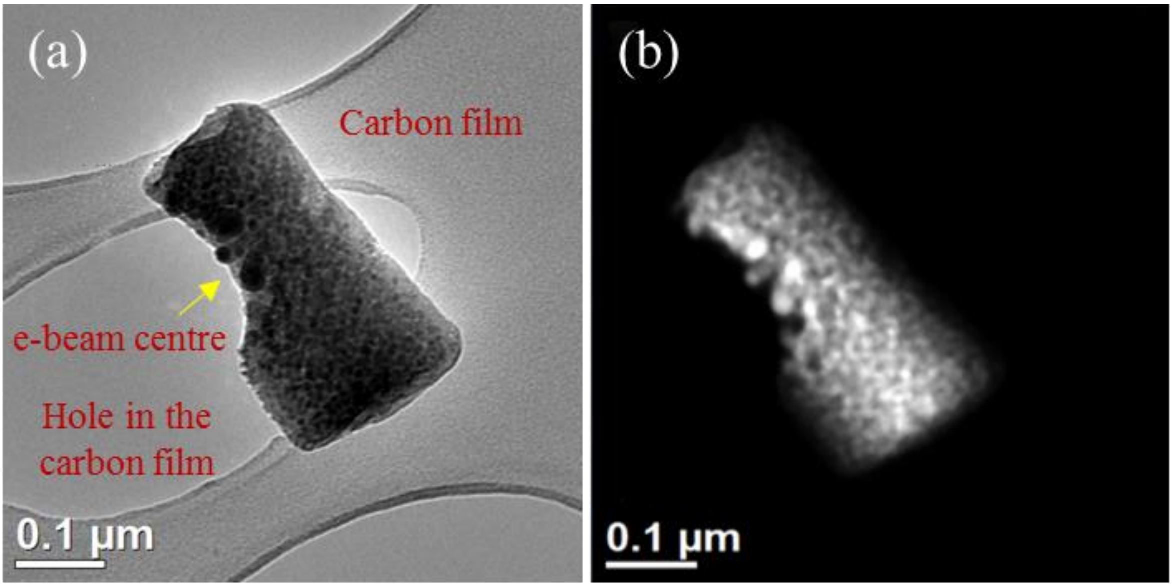

Figure 4-2: (a) Bright field (BF) TEM and (b) annular dark field (ADF) STEM images of a high Zn-loaded borosilicate (ZBS-A) glass fragment after prolonged electron beam irradiation. JEM TEM 2010F at 200 keV.

Initially, the entire fragment was fully irradiated using a low intensity electron beam for a prolonged time (~ 15 min). This resulted in precipitation of small nanoparticles of about 5-7 nm in size throughout the entire glass fragment. A high intensity electron beam was then used to irradiate the lower edge of the glass fragment (the yellow arrow in Fig. 4-2(a)). Electron beam irradiation at this stage resulted in the formation of nanoparticles of between 20-40 nm in size, with most of these having spherical shapes. Here, the competition between partial glass ablation and nanoparticle formation can be seen, as evidenced by the existence of nanoparticles on the outside edge of the glass fragment, giving a kind of surface decoration.

Another confirmation of the formation of metallic Zn nanoparticles was obtained using annular dark field (ADF) images in the STEM mode. Since Zn is the heaviest atom among those (boron, silicon and oxygen) in this glass (its atomic number is 30), these nanoparticles show as a bright atomic number contrast in the ADF image (Fig. 4-2(b)).

In order further to confirm the formation of metallic Zn nanoparticles, an electron energy loss spectroscopy (EELS) spectrum was acquired from the region subjected to electron beam irradiation in Fig. 4-2(a), and this spectrum is shown in Fig. 4-3.

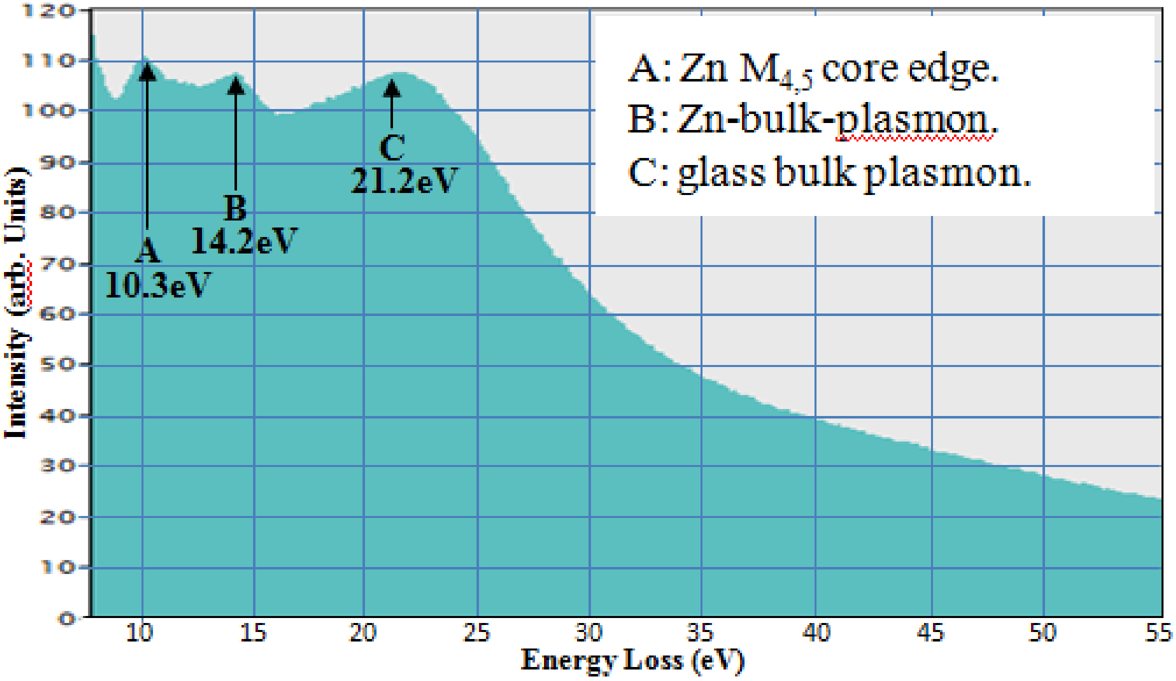

Figure 4-3: Electron energy loss spectroscopy (EELS) spectrum for a high Zn-loaded borosilicate glass (ZBS-A) fragment after prolonged electron beam irradiation.

Three noticeable peaks can be identified from the EELS spectrum in Fig. 4-3. These peaks are around 10.3 eV, 14.2 eV and 21.2 eV, respectively. The first peak at around 10.3 eV (labelled A in Fig. 4-3) has an onset just below 10 eV that matches the core level excitation ($M_{4,5}$ edge) of metallic Zn. The second peak, around 14.2 eV (labelled B in Fig. 4-3), closely matches the bulk plasmon of metallic Zn. Since these two values are in a good agreement with the values of metallic Zn, and since the plasmon peak of ZnO at 18.8 eV [Ahn *et al.*, 1983] was not observed in this study, it can be concluded that the precipitated nanoparticles are metallic Zn. Finally, the third peak, at around 21.2 eV (labelled C in Fig. 4-3), is the bulk plasmon of the borosilicate glass acquired mainly from a hole of the carbon carrier film in Fig. 4-2(a).

Other studies have reported that a peak at about 14.5 eV represents the bulk plasmon (E_p) for metallic Zn, while a peak at about 9.9 eV is as a result of the core level excitations ($M_{4,5}$ edge) from Zn 3d bands to the empty states [Gorobchenko *et al.*, 1985 and Widder *et al.*, 1997]. In the region subjected to electron beam irradiation, the secondary and Auger electron excitations will produce a local repulsive electrostatic interaction resulting in the movement of Zn^{2+} from their original positions. The Zn^{2+} will be neutralized into Zn^0 as a result of the capture of the secondary and/or Auger electrons, with some kinetic energy being transferred from those electrons. The precipitation of the metal particles is also dependent on the presence of non-bridging oxygen (NBO), since the cations binding to NBO are likely to be removed. With larger amounts of NBO, a higher amount of cations might be released and there is therefore a higher possibility of particles forming.

Further evidence for the crystallinity of the precipitated Zn nanoparticles is shown in a high resolution transmission electron microscopy (HRTEM) image. Figure 4-4 shows a corner of the glass after prolonged electron beam irradiation along with a HRTEM image of a typical Zn nanocrystal. The electron beam has been placed at the corner of the glass and irradiated for a long period of time using a stationary electron beam. This resulted in the formation of mostly spherical nanoparticles of various sizes, with the larger nanoparticles avoiding the glass fragment edge while the smallest nanoparticles preferred to be close to the edge, as shown in Fig. 4-4(a).

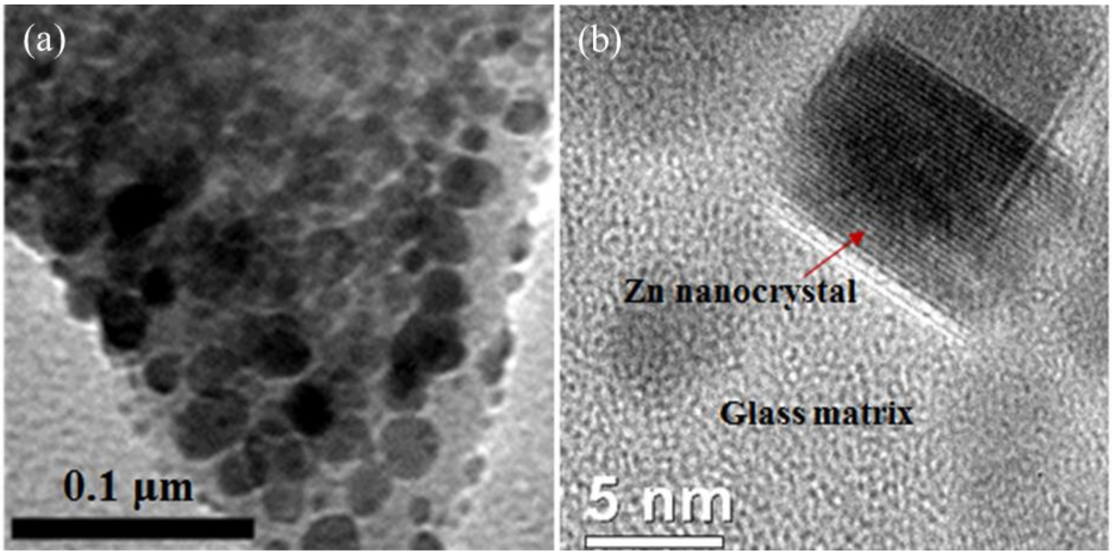

Figure 4-4: (a) A high Zn-loaded borosilicate (ZBS-A) glass fragment after prolonged electron beam irradiation and (b) HRTEM image of a typical Zn nanocrystal. JEM TEM 2010F at 200 keV.

A high resolution image of an ideal Zn nanocrystal is shown in Fig. 4-4(b). As can be seen, this particle has sharp fringes, indicating a crystalline Zn nanoparticle. An evaluation of the lattice fringes and the d-spacing calculations (d = 220 nm) show that the precipitated nanoparticle is metallic Zn of $(01\bar{1}0)$ plane.

Figure 4-5 shows TEM micrographs of a low-Zn-alkali borosilicate (ZBS-B) glass fragment prior to stationary electron beam irradiation and the same region after time series electron irradiation.

From the figure, it is clear that the thin edge of the glass fragment is suspended on a holey carbon film (obvious at the left bottom edge), while most of the field-of-view shows the glass over a carbon film.

From Fig. 4-5(a), it can be seen that at t = 0 min, the glass fragment is relatively homogeneous apart from surface roughness and the speckle characteristic of the amorphous structure.

Once the high intensity electron beam was applied the two parallel effects of partial glass ablation and nanoparticle formation were observed (Fig. 4-5(b)).

Irradiation at rest using a stationary electron beam resulted in the formation of nanoparticles, the vast majority of which had a ring-like morphology. The size range of these nanoparticles was inversely proportional to the distance from the centre of the electron beam, indicating a nucleation and growth process that was most advanced under the peak intensity. At this stage of electron beam irradiation (t = 1 min), three large nanoparticles had been formed at the centre of the electron beam. The spherical nanoparticle indicated by the red ring in Fig. 4-5(b) had a diameter of about 32 ± 1 nm, while that indicated by the white arrow had dimensions of about 43 ± 1 nm by 24 ± 1 nm. Furthermore, the other large nanoparticle had a diameter of around 39 ± 1 nm. Further away from this region, nanoparticles of smaller sizes could be found with still smaller nanoparticles evident even further away from the electron beam centre.

After increasing the irradiation time to 3 min, the spherical nanoparticle indicated by the red ring in Fig. 4-5(b) coalesced and merged with the adjacent nanoparticle indicated by the white arrow in Fig. 4-5(b) to form a larger rectangular nanoparticle with a diameter of 26-66 nm (indicated by the green ring in Fig. 4-5(c)).

This rectangular nanoparticle transformed to a faceted-shaped nanocrystal after the irradiation time had increased to 6 min. The final nanocrystal has a 35-46 nm oval morphology indicated by the yellow circle in Fig. 4-5(d).

At this stage, the nanoparticles close to the centre of the electron beam are further grown to about 12 nm and 22 nm for those indicated by the red arrows in Fig. 4-5(d), respectively.

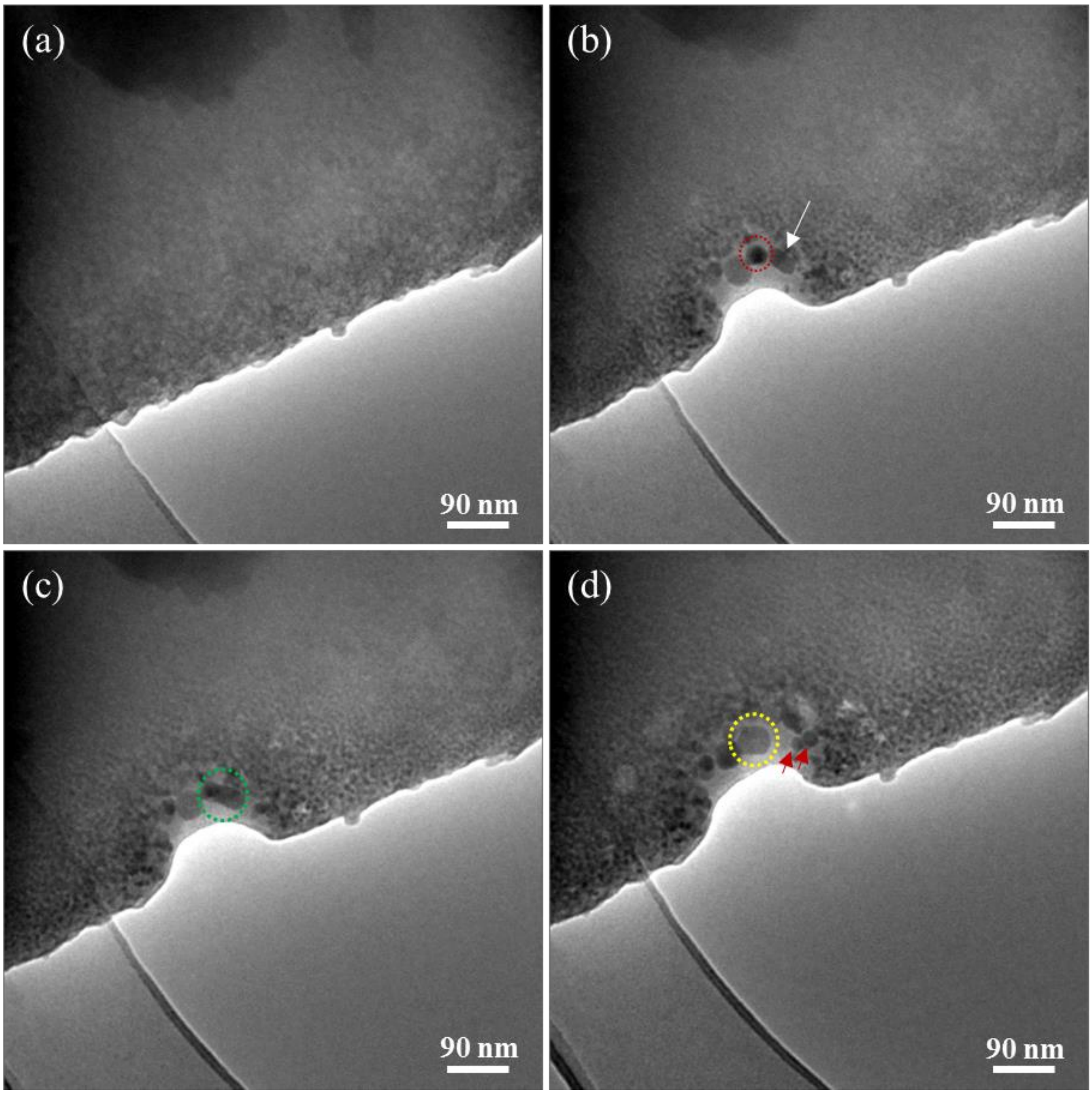

Figure 4-5: A low-Zn-alkali borosilicate (ZBS-B) glass fragment, (a) prior to electron beam irradiation and (b-d) after 1 min, 3 min and 6 min electron beam irradiation, respectively. JEM TEM 3010 at 300 keV.

A broad electron beam was used to irradiate another fragment of a low-Zn-alkali borosilicate (ZBS-B) glass as shown in Fig. 4-6. Prior to the electron beam irradiation, the glass fragment was very clean and with no indication of any precipitates in the fragment, as shown in Fig. 4-6(a). The electron beam was then placed on the region indicated by the red ring in Fig. 4-6(a).

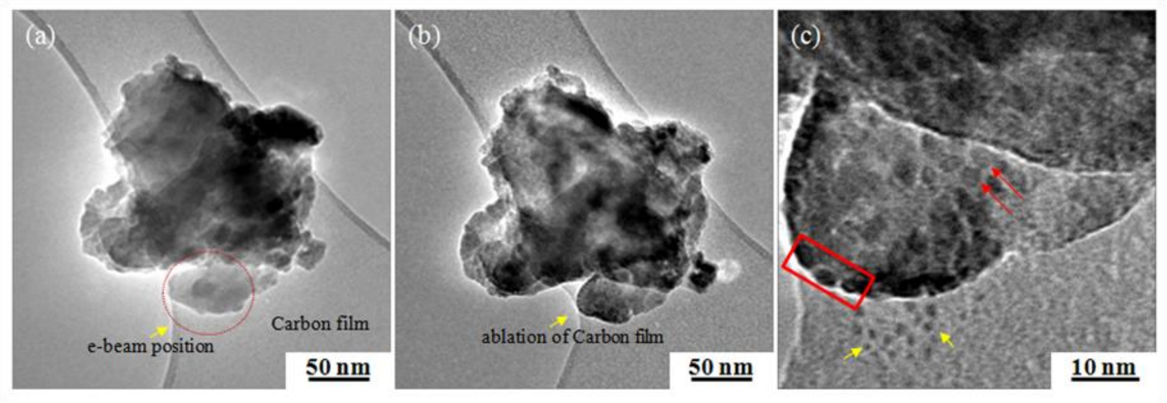

Figure 4-6: A low-Zn-alkali borosilicate (ZBS-B) glass fragment, (a) prior to electron beam irradiation and (b) after ~ 20 min electron beam irradiation of the red ring region in (a). (c) a high magnification image of the irradiated region in (b). JEM TEM 3010 at 300 keV.

This region was also clean and with no indication of any particle-like abnormalities, except for a small piece of glass particle attached to the top of this region. After about 20 min of irradiation, the formation of nanoparticles was observed in the irradiated region. A higher magnification image of the irradiated region (Fig. 4-6(c)) shows the various sizes and morphologies of the formed nanoparticles. Some of these are faceted (red arrows in Fig. 4-6(c)), others are spherical and a few have elliptical shapes. It is essential to report that no glass ablation was observed here and this is due to the medium intensity of the electron beam irradiation. A chain of spherical nanoparticles was observed at the edge of the irradiated glass region, as indicated by the red rectangle in Fig. 4-6(c). Moreover, some ablation of the carbon film due to the prolonged irradiation can be seen in Fig. 4-6(b), which is indicated by yellow arrow. The whole irradiated region has shrunk and there is smoothing and rounding of the rough surfaces of the glass fragment being irradiated (this phenomenon will be explored further in chapter seven). Furthermore, the higher magnification image shows that a few nanoparticles of about 1-2 nm in diameter are found next to the irradiated region, located on the carbon film (yellow arrows in Fig. 4-6(c)). This is due to the enhancement of diffusivity induced by the medium intensity electron-beam, which serves to facilitate growth of pre-nucleated nanoparticles.

Live observation of nanoparticle growth under electron beam irradiation has therefore been verified for a low-Zn-alkali borosilicate (ZBS-B) glass fragment as shown in Fig. 4-7. Prior to the irradiation, the condenser aperture of the TEM was removed, allowing irradiation at a relatively high current to be spread over the entire glass fragment.

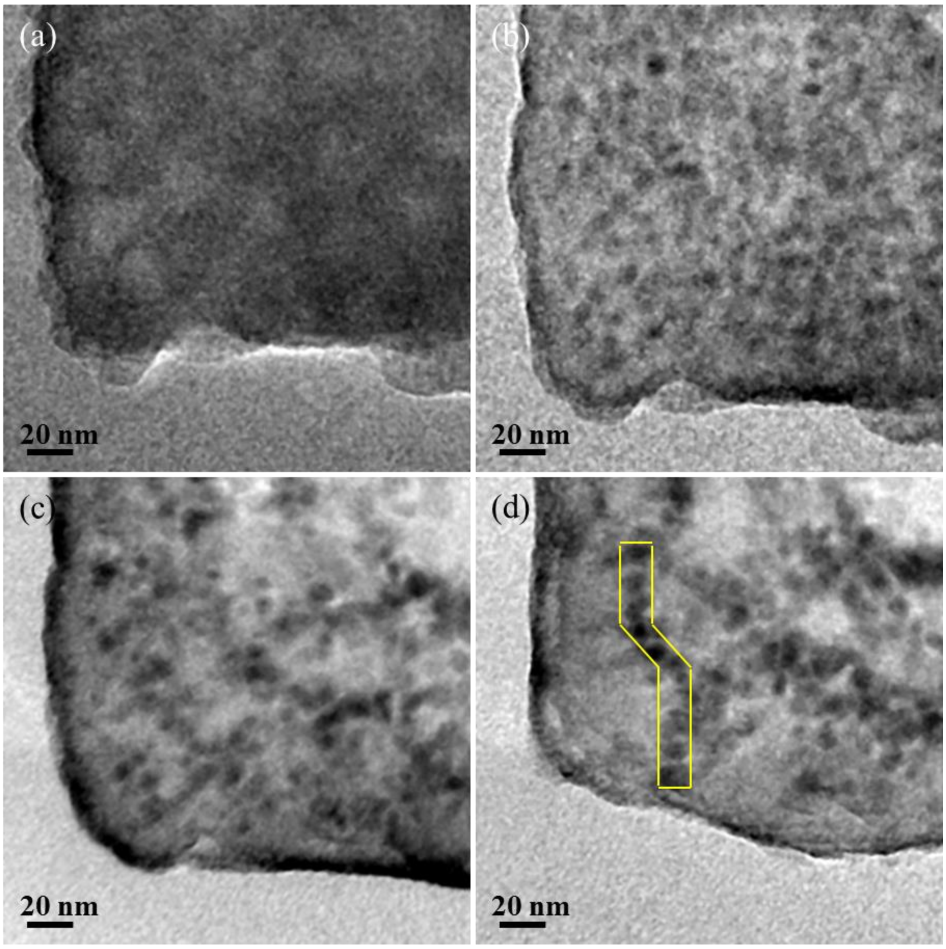

Figure 4-7: Time series TEM images of a low-Zn-alkali borosilicate (ZBS-B) glass fragment at (a) 0 min, (b) 3 min, (c) 6 min and (d) 9 min electron beam irradiation, respectively. The yellow contour in (d) is a chain of nanoparticles. JEM TEM 2010F at 200 keV.

As can be seen in Fig. 4-7(a), the glass fragment was initially (t = 0 min) homogeneous with no indication of nanoparticles, but the surfaces of the fragment were rough. After 3 min of electron beam irradiation, however, nanoparticles with an average diameter of about 5 ± 2 nm were observed to be uniformly distributed via homogeneous nucleation and precipitation processes as shown in Fig. 4-7(b). When the irradiation time was increased to 6 min (Fig. 4-7(c)), the nanoparticle size increased marginally, but now with a degree of heterogeneity being introduced to the distribution of the nanoparticles. This occurs with clusters of dark looking nanoparticles separated by very bright bands of Zn-depleted borosilicate glass. A further 3 min of electron irradiation resulted in the formation of nanoparticle chains, with the longest being ~ 100 nm long and consisting of 11 nanoparticles (NPs), highlighted by the yellow contour in Fig. 4-7(d).

The condenser aperture was then re-inserted and the irradiation was applied using a more focused electron beam. The electron beam was moved across the centre/right region of the field-of-view in Fig. 4-8(a). At this point, a sudden growth in the nanoparticles was observed and various nanoparticle shapes such as hexagonal, square and spherical could be seen. The sizes of the latter nanoparticle, for instance, were about 16 ± 7 nm, and the appearance of even larger patches of nanoparticle-free glass indicates that the growth mechanism is sustained by ripening and not by further precipitation. Here, it is quite possible that the glass was already losing its Zn content during the initial irradiation steps shown in Figs. 4-7(a) and 4-7(b), with all subsequent transformations being driven simply by the rearrangement of metallic Zn. Further irradiation over the entire field-of-view at high intensity resulted in the formation of even larger nanoparticles, up to a maximum size of about 35 nm, as shown in Fig. 4-8(b). Here, different nanoparticle morphologies such as faceted cubic, hexagonal and spherical were found. Figure 4-8(c) is a high magnification image of the yellow ringed region in Fig. 4-8(b). This is a fully spherically shaped Zn nanoparticle, with a diameter of about 8 nm, situated at the edge of the glass fragment. On the other hand, a HRTEM image of a typical Zn nanocrystal is shown in Fig. 4-8(d). This was obtained from the irradiated region in Fig. 4-8(b). Evaluating these lattice fringes in order to calculate the d-spacing (d = 0.210 nm) confirmed that the precipitated Zn nanoparticle was metallic of ($\bar{1}101$) plane.

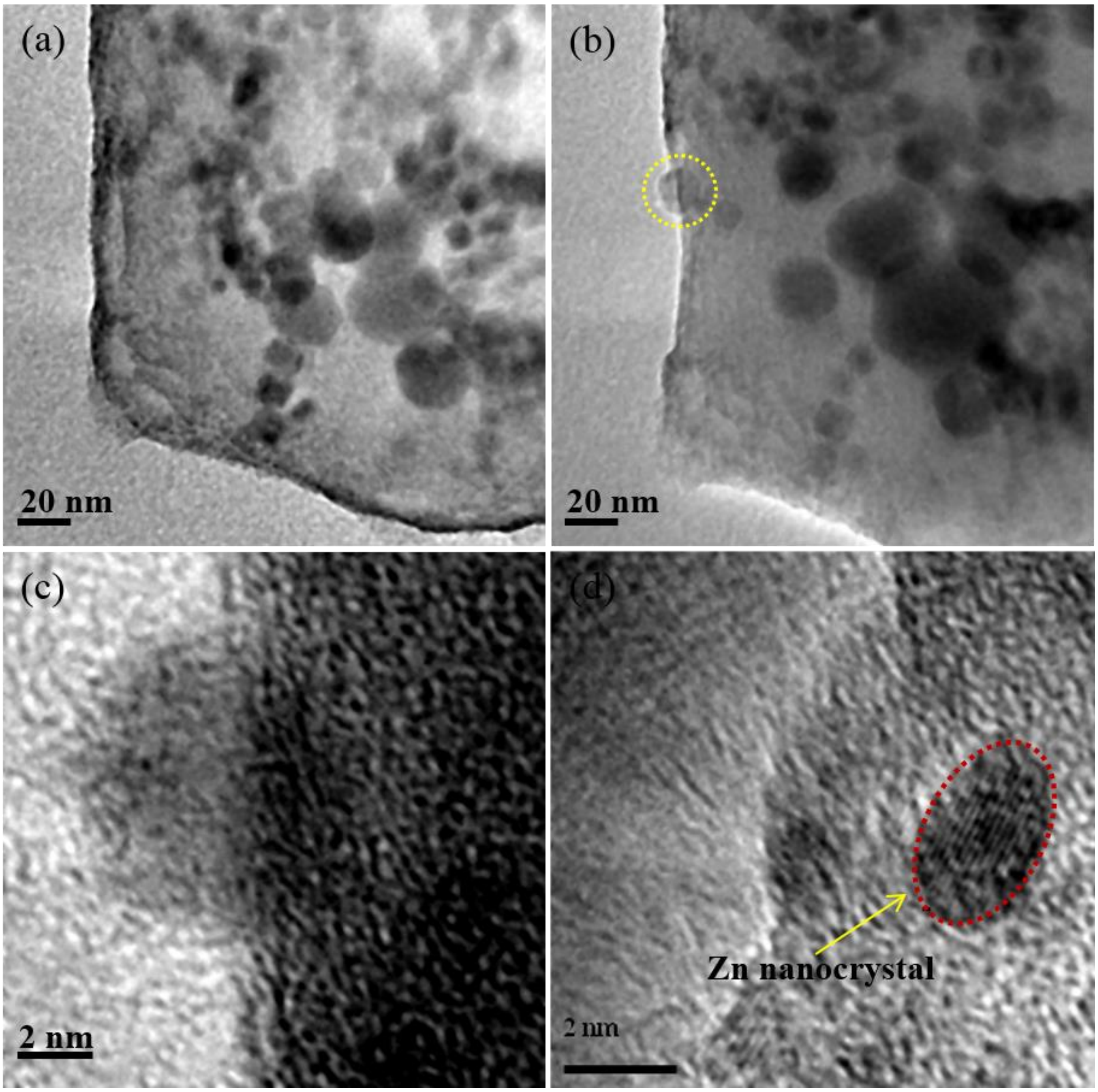

Figure 4-8: (a, b) TEM images of a low-Zn-alkali borosilicate (ZBS-B) glass fragment following a more focused electron beam irradiation initiating growth of nanoparticles > 10 nm in diameter. (c) a higher magnification image of the yellow-circled area in (b) and (d) is a HRTEM image showing a typical Zn nanocrystal. JEM TEM 2010F at 200 keV.

4.2.1.2 Line-scan electron beam irradiation and patterning

Line-scan irradiation and patterning was conducted by manual scanning of the electron beam across the glass material. Probes of different diameters using different guns were applied. Since the field emission gun (FEG) and LaB_6 thermal gun TEMs have different electron sources, different findings were achieved.

Throughout this experiment, the electron beam was usually set up at a far enough distance from the glass fragment prior to moving it into the glass-material. This served to reduce the changes in the glass fragment before the irradiation.

Figure 4-9 shows a glass fragment of a high-Zn-loaded borosilicate (ZBS-A) glass before and after the line-scan electron beam irradiation using a thermal gun TEM.

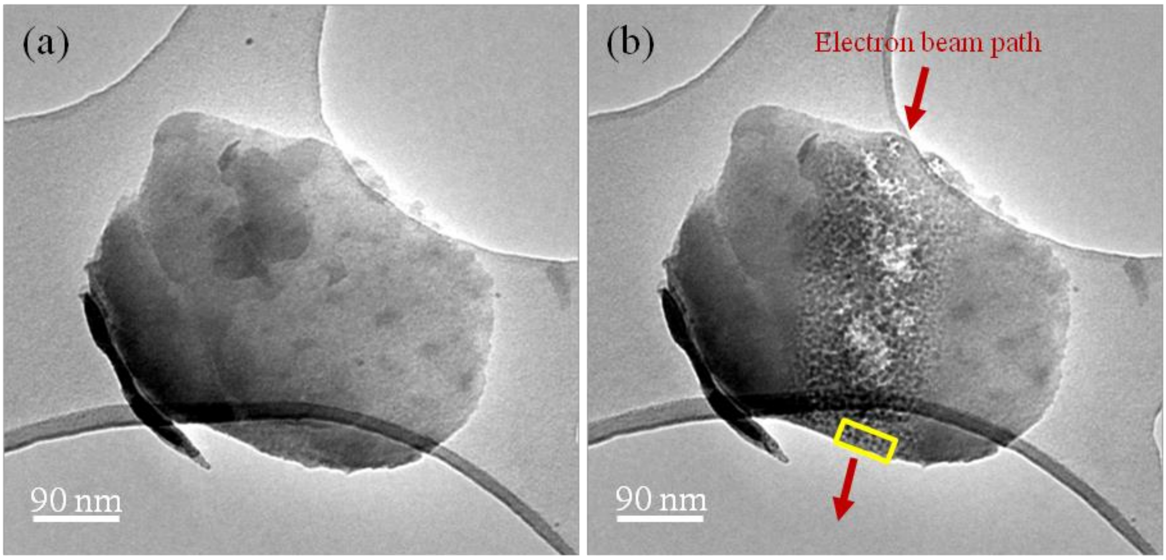

Figure 4-9: TEM images of a high-Zn-loaded borosilicate (ZBS-A) glass fragment, (a) before and (b) after line-scan irradiation. JEM TEM 3010 at 300 keV.

A roundish-shaped glass fragment about 400 nm in diameter was initially homogeneous with no indication of any nanoparticle-like aberrations evident, except for some small attached glass fragments in various regions shown in Fig. 4-9(a). This fragment was then traversed vertically by an electron beam of a diameter of sub-100 nm. After scanning the electron beam in 10 steps of 1-2 sec exposure along a line indicated by the red arrows in Fig. 4-9(b), a graded pattern of spherical nanoparticles was formed with the nanoparticle size reducing the further the lateral distance from the electron beam path.

As can be seen in Fig. 4-9(b), the outside border line where the finest nano-precipitates close to un-disturbed glass matrix is rather sharp. This gives an indication that the beam intensity drop-off, rather than the temperature distribution was the key effect, while also showing that there is no evidence that the nanoparticles were generated without irradiation. It is also believed that the size distribution follows the Gaussian shape of the beam. Possible glass ablation can also be seen at the centre of the line, indicated by bright batches, although no ablation is observed at the edges of the glass fragment. Nanoparticle chain with a periodic order of arrangement of neighbouring nanoparticles can be seen at the bottom edge of the glass fragment, where the glass matrix is thinnest, indicated by the enclosed yellow rectangle in Fig. 4-9(b) (more details are in section *4.2.2.1*). In contrast, this ordering is invisible in the thicker regions due to random 3D projection effects.

A finer electron beam can be obtained more easily when a FEG TEM is used than with a LaB_6 gun TEM. In this case, a sub-10 nm diameter focused electron beam was used to conduct line-scan patterning in a high-Zn-loaded borosilicate glass (ZBS-A) fragment, as shown in Fig. 4-10. The electron beam, with a diameter of ~ < 10 nm, was manually scanned over the glass fragment with the step-length being smaller than the electron beam diameter in order to produce a continuous line. Each irradiation point in the scan was held for about 10 sec. This was sufficient for partial glass ablation in the centre of the line. It is clear from Fig. 4-10(b) that, for most of the scan, the nano-precipitates were found at either side of the centre, thereby generating two dark lines of small nanoparticles. In addition, a few larger nanoparticles with sizes of about 14 nm were found at the centre of the line-scan region close to the electron beam exit edge; these are indicated by yellow-dashed rings in Fig. 4-10(b).

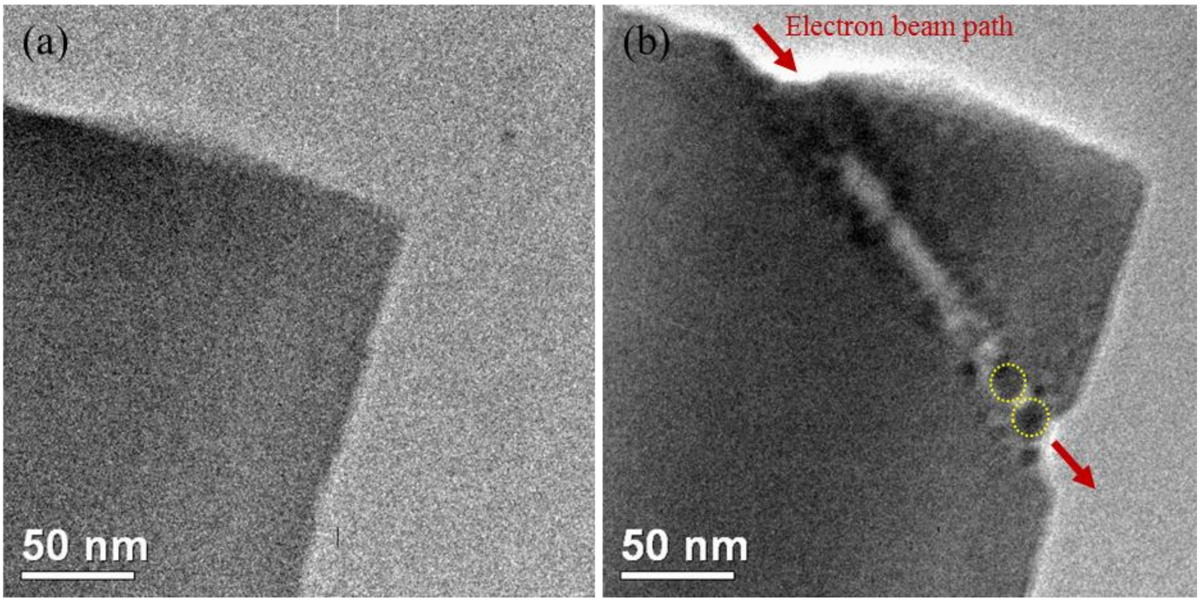

Figure 4-10: TEM images of a high-Zn-loaded borosilicate (ZBS-A) glass fragment, (a) before and (b) after line-scan irradiation using a sub-10 nm e-beam. JEM TEM 2010F at 200 keV.

Another line-scan irradiation using a sub-10 nm diameter focused electron beam was conducted in a rod of high-Zn-loaded borosilicate (ZBS-A) glass. This rod was subjected to the electron beam for the purpose of patterning. A pattern of three parallel lines was achieved, as shown in Fig. 4-11. The produced pattern is indicated by the line numbers 1, 2 and 3, with a distance of about 127.5 nm from line number 1 to line number 2 and of about 202 nm from line number 2 to line number 3, with the lines themselves having a width of about 10 nm.

The glass rod used here for patterning is rather thick and the electron beam itself was scanned in a rather quick state without any stop. This resulted in the formation of two black lines of metal Zn on either side of the main formed line.

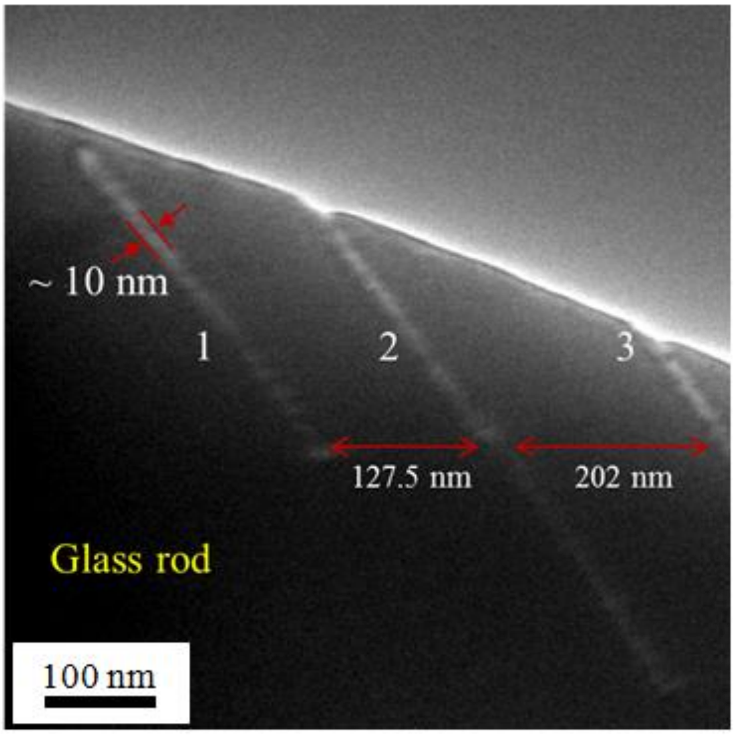

Figure 4-11: Pattern formation in a high-Zn-loaded borosilicate (ZBS-A) glass fragment by focused electron beam. Three parallel lines of width of about 10 nm were made. JEM TEM 2010F at 200 keV.

4.2.2 Secondary electron irradiation effects

As reported at the beginning of this chapter, the fundamental objective of this research is to examine e-beam-induced precipitation and patterning in glass. These experiments also revealed some details worth reporting in the field of general irradiation physics of oxide glasses. In the following sections, various electron irradiation-induced effects will be presented.

4.2.2.1 Particle ordering

One feature of the experiments in this study is the occurrence of chains of nanoparticles, or sequences of nano-precipitates with ordered spacing. Although it has not previously been reported to have occurred with electron beam irradiation, inducing order into a precipitation process in glass has been achieved in the past with external patterning techniques such as via laser gratings. For example, Nishiyama *et al.*, reported the periodic precipitation of Ge nanoparticles of about 20-40 nm diameter in Ge-B-SiO_2 glass by a laser irradiation and successive annealing process at 600 ^oC [Nishiyama *et al.*, 2004], whereas Guan *et al.* achieved the same effect with ion implantation masks [Guan *et al.*, 2013]. On the other hand, Shin *et al.* reported the fabrication of periodic Zn nanocrystals in amorphous materials by rapid electron beam irradiation [Shin *et al.*, 2008]. In the study presented here, 50 sec of irradiation was sufficient to form Zn nanoparticles of about 7 nm in diameter in a periodic state and to control their size and spacing (interspacing distance of 23 nm).

In contrast to these studies, in which nanoparticle formation in a periodic mode was the main purpose, it has been showed that silver nanoparticles have a tendency to self-order in a periodic mode in silicate glass via thermally assisted hydrogen permeation [Mohr *et al.*, 2001]. They explained this effect based on the Ostwald theory, assuming that hydrogen and silver ions are mobile species.

The novelty in our findings of nanoparticle ordering in a high-Zn-loaded borosilicate (ZBS-A) glass are that Zn NPs have a tendency to accumulate spontaneously and align in an ordered manner near the edge of the glass fragment after being irradiated.

It is well-known that following a nucleation event during phase separation (PS) and precipitation processes, the glass matrix will be locally altered (depleted in the separated element(s)). As a result of that, the statistically most probable random next nucleation event will occur at minimum distance from the first one, related to the diffusion length. At a thin glass fragment edge, where no overlap in imaging direction occurs, the occurrence of nanoparticles with a mean periodic distance from each other and a characteristic gap between each other can therefore be obtained. It seems that this situation is relevant for Fig. 4-9(b) and the details of such observation are shown in Fig. 4-12.

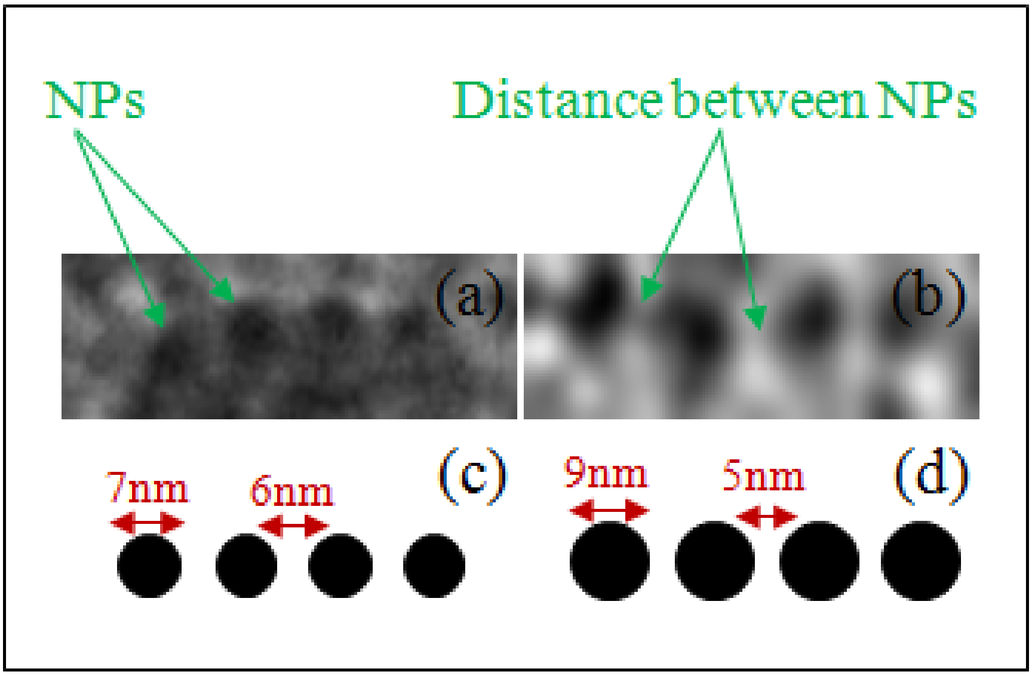

Figure 4-12: (a, b) Nanoparticles (NPs) ordering and (c, d) schematic of (a, b) showing the nanoparticle size and the distance between the nanoparticles.

In contrast, the nanoparticle chain in Fig. 4-7(d) does not agree with this theory of formation. First, the nanoparticles only coagulate after prolonged electron beam irradiation, while they pre-exist without chain-order for shorter irradiation times. Second, the one dimension (1D) chain in Fig. 4-7(d) is not due to edge-geometry but adopted during coagulation. This observation could point to a liquid-like intermediate stage of the Zn nanoparticles, with no necking or merging occurring, which would support this idea; rather some small gaps separating the nanoparticles persist and prevent an atomic-level attachment-chain.

4.2.2.2 Carbon film decoration

Under electron beam irradiation, nanoparticles were found on the carbon film next to the irradiated region, a phenomenon which has been observed in this study and termed "carbon film decoration" and which not been reported before in oxide glasses, although it has been observed in other materials [Möbus and Tsai, 2008, Gnanavel *et al.*, 2011 and Ghatak *et al.*, 2012]. This is due to knock-on collisions, along with electron beam heating as a result of energy transferred from the electron beam.

An example of this phenomenon is shown in Fig. 4-6(c). This is believed to be due to the migration of ablated atoms into a circular zone around the irradiated material on the carbon film. In this region, after enough cooling outside the electron beam, the nuclei stop and ripen into nanoparticles. Since Zn nanoparticles are shown to be aligned on the glass fragment edge under electron beam irradiation, however, it is reasonable to suppose that the migrated Zn stems from pre-precipitated nanoparticles. Alternatively, electron beam-induced electric fields inside the irradiated insulating glass [Cazaux, 1986] might be followed by ejection or charged clusters or by a combination of charged atomic ablation followed by surface diffusion.

4.2.2.3 Cation migration

A thin and long glass rod fragment was found on the carbon film. These occurred by chance due to the grinding process in addition to more common rough particles. The experiments conducted on this rod are summarised in Fig. 4-13. Prior to the irradiation, this rod was homogeneous with a width of about 59 nm (Fig. 4-13(a)). After focusing the electron beam to a diameter exactly matching the rod diameter for about 3 min, the diameter of the rod was observed to widen to about 62 nm (Fig. 4-13(b). This has previously occurred in some rod-irradiation experiments under this kind of moderately focused electron beam, pointing to possible "un-densification", porosity or flattening of the cylindrical rod as an intermediate stage. When the electron beam was once again focused to a diameter matching the diameter of the rod for ~ 13 min, a further widening in the glass up to about 65 nm was observed, as shown in Fig. 4-13(c). This process, however, takes place in competition with ongoing glass ablation.

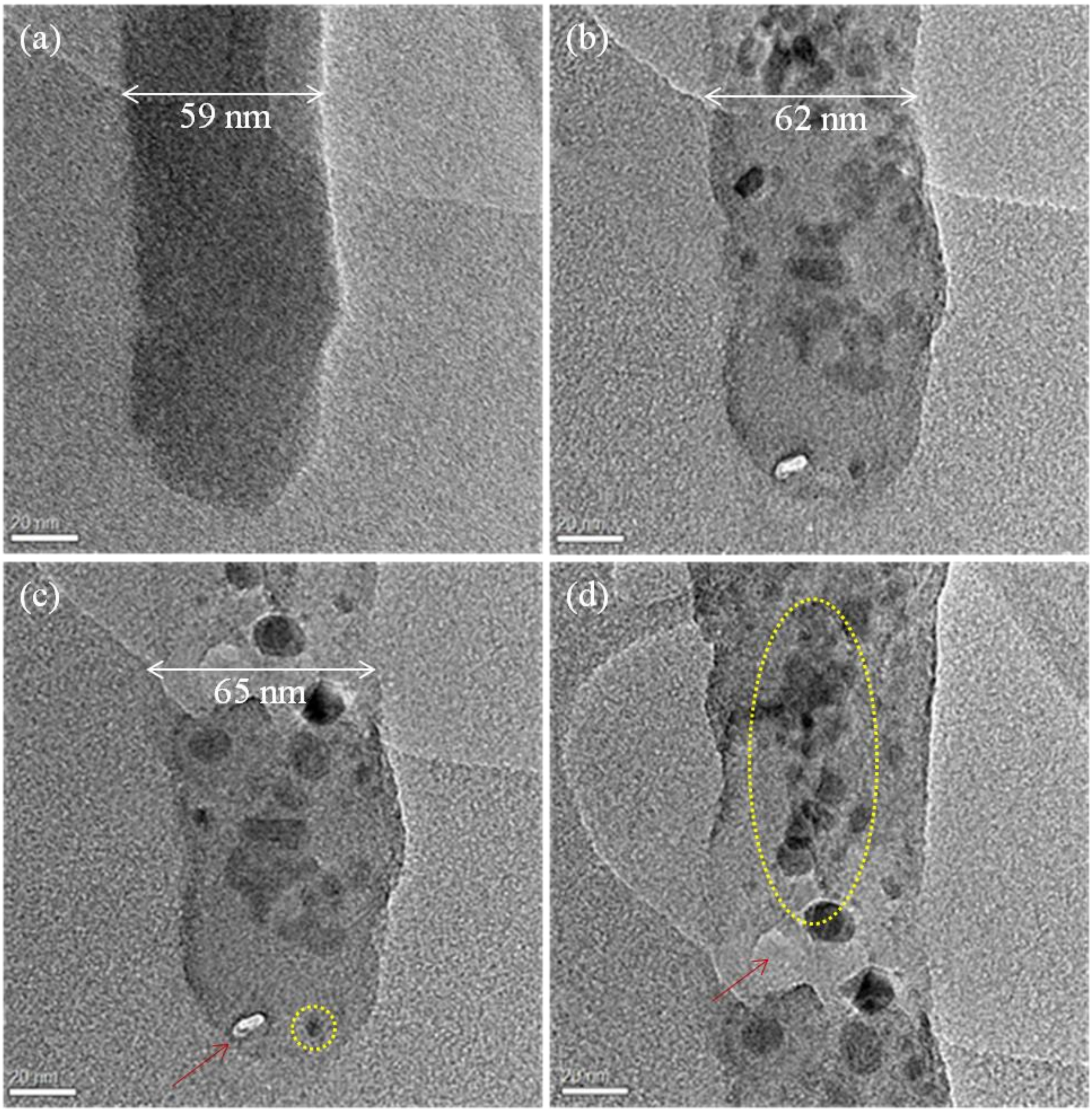

Figure 4-13: TEM micrographs of a high-Zn-loaded borosilicate (ZBS-A) glass rod at 0 min in (a) and at 3 min and 13 min after irradiation in (b) and (c), respectively. (d) an extended vertical region of the glass rod in (c). JEM TEM 2010F at 200 keV.

In this experiment, the current density focused on the glass rod was ~ 1.3 pA/nm^2. It was also observed that focusing the electron beam to a diameter identical to the rod diameter resulted in the precipitation of Zn nanoparticles and that these were aligned right in the centre of the rod, avoiding the regions close to the surface, as shown by the yellow encircled area in Fig. 4-13(d) along with a local glass ablation indicated by the red arrow in Fig. 4-13(d). Focusing the electron beam to diameters smaller than the rod diameter, however, resulted in accelerating brightening (loss of Zn mass thickness contrast) as a result of migration of Zn, expelled from the tip-region at the bottom of the glass rod as shown in Fig. 4-13(c), except for one particle indicated by the yellow circle area in Fig. 4-13(c). The electron beam was then focused to a diameter of about 2 nm (this gives a current density of ~ 1000 pA/nm^2 focused on the glass rod) and this resulted in a complete glass ablation (i.e. hole drilling), as indicated by the red arrow in Fig. 4-13(c).

Figure 4-14 shows another fragment of a high-Zn-loaded borosilicate (ZBS-A) glass, which was relatively thick prior to the electron beam irradiation. This fragment was irradiated for 2 min in the first irradiation stage and then for further 2 min in the second irradiation stage.

The TEM image at t = 0 min clearly reveals the homogeneity of the glass fragment with no precipitates obviously present at this stage (Fig. 4-14(a)). When this fragment was subjected to the electron beam irradiation for 2 min, however, precipitation of nanoparticles within the entire glass fragment can be clearly seen (Fig. 4-14(b)). These nanoparticles had sizes between 5-10 nm and accumulated in the middle regions of the glass fragment, avoiding the glass surface or edge regions. Some white batches are also seen due to e-beam-induced glass ablation.

Comparable bigger particles (with sizes between 10-40 nm) can be seen after a further 2 min irradiation (Fig. 4-14(c)). It is believed that the bigger particles were formed due to the merging of the smaller particles initially formed at t = 2 min irradiation, while the smaller particles are believed to be newly formed at this stage of irradiation. Among these particles, there are circular and also faceted particles.

These nanoparticles are of dark contrast thus indicating Zn nanoparticles, as shown in the inverted image in Fig. 4-14(d). In addition, the glass fragment became much more transparency at this stage of the irradiation.

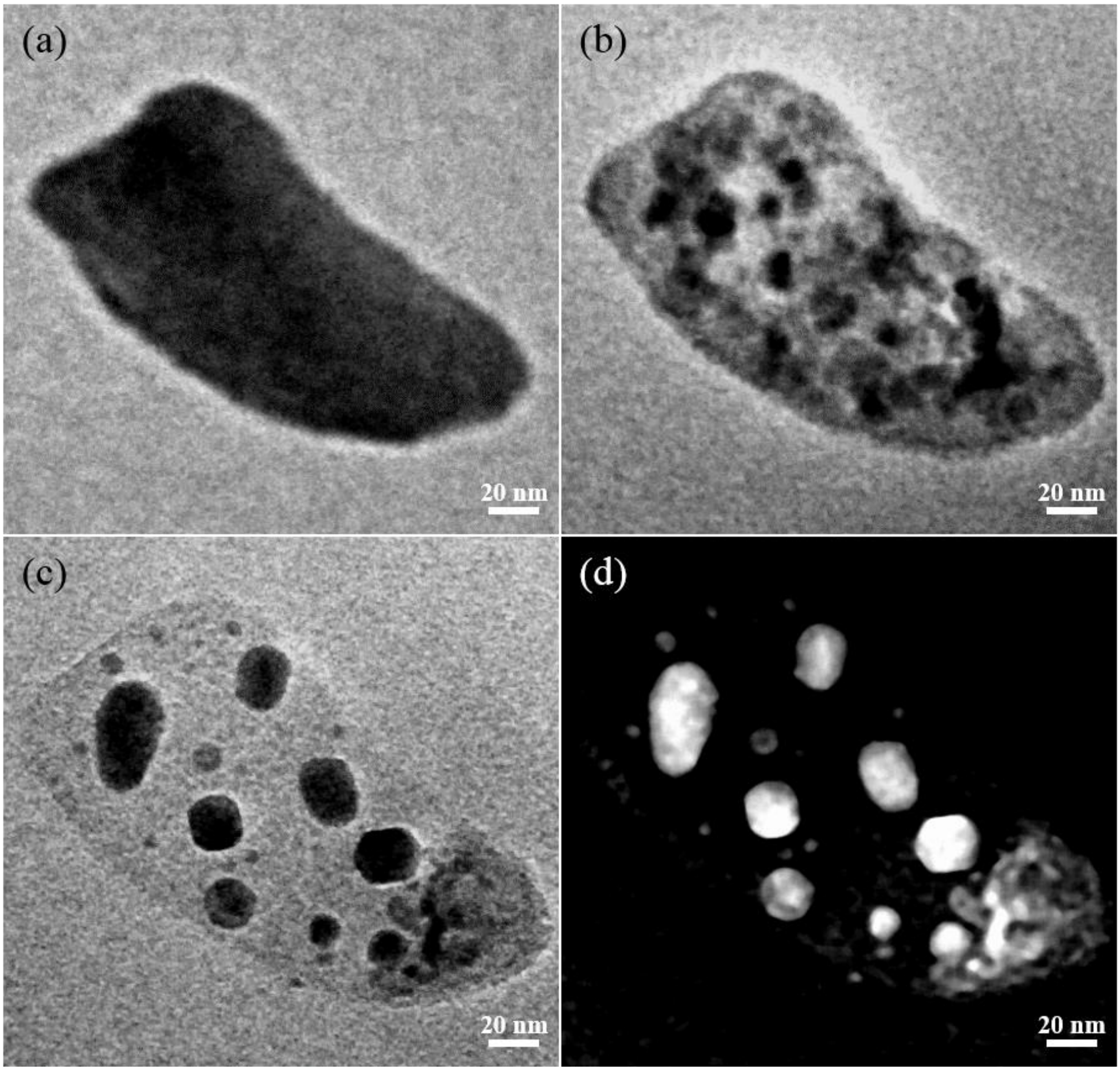

Figure 4-14: TEM micrographs of a high-Zn-loaded borosilicate (ZBS-A) glass fragment, (a) before, and (b,c) after 2 min and a further 2 min of electron irradiation, respectively. (d) the inverted image for (c). JEM TEM 3010 at 300 keV.

4.2.3 In-situ heating experiment

An *in-situ* heating experiment was conducted in a high-Zn-loaded borosilicate (ZBS-A) glass using a Gatan single-tilt heating holder. The experiment commenced by performing a normal irradiation. For this purpose, a glass fragment, shown in Fig. 4-15(a), was subjected to e-beam irradiation for about 2 min. This resulted in the formation of mostly circular nanoparticles of approximately 2-3 nm size and an overall shrinkage of the glass fragment, as shown in Fig. 4-15(b). The electron beam diameter used for irradiation can also be seen clearly. A further 5 min irradiation resulted in the formation of even larger particles with sizes between ~ 10-50 nm, as shown in Fig. 4-15(c). Spherical, faceted and irregular shaped nanoparticles could now be observed.

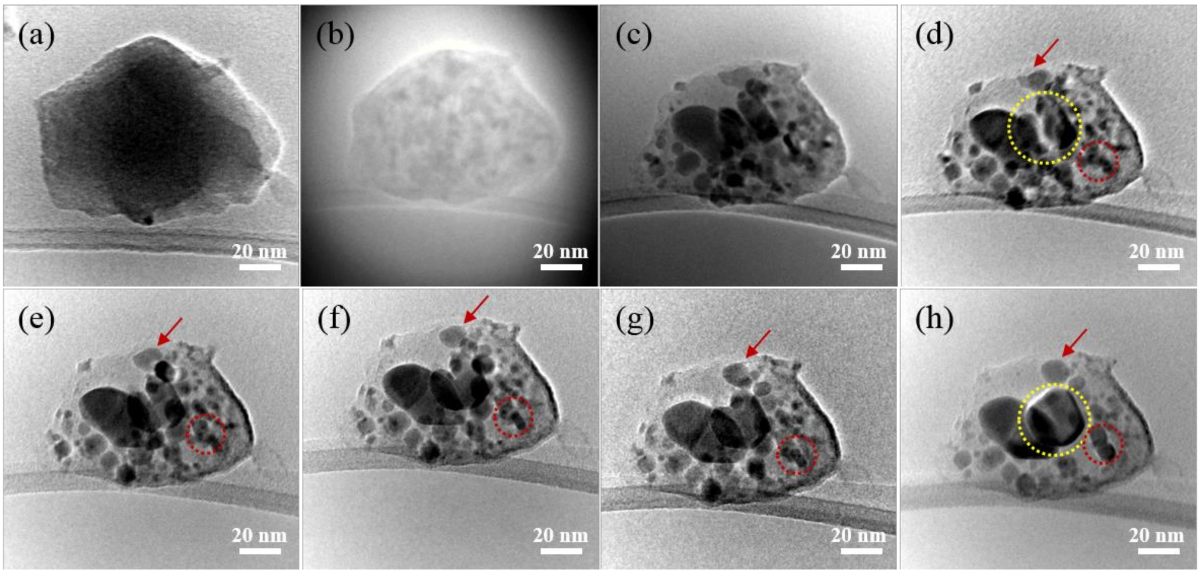

Figure 4-15: A high-Zn-loaded borosilicate (ZBS-A) glass fragment, (a) before, and (b, c) after 2 min and 5 min electron irradiation, respectively. (d-h) *in-situ* heating of the glass fragment between 100-300 ^{o}C, respectively, with increments of 50 ^{o}C between each figure. JEM TEM 3010 at 300 keV.

The next step of the experiment was to perform the *in-situ* heating for this fragment. The heating temperatures were 100 ^{o}C, 150 ^{o}C, 200 ^{o}C, 250 ^{o}C and 300 ^{o}C. During this experiment, the more significant changes observed due to temperature increases were as follow. First, the small particle indicated by the red arrows in Fig. 4-15(d-h) changed its shape gradually as the temperature increased, eventually reaching a ball-shaped particle with a diameter of about 10 nm at 300 ^{o}C, as shown in Fig. 4-15(h). Second, the large particle situated at the centre of the glass fragment, and indicated by the dashed yellow circle in Fig. 4-15(h), was formed at 300 ^{o}C after a gradual merging of the two particles, indicated by the yellow dashed circle in Fig. 4-15(d). Third, a few small nanoparticles (indicated by the dashed red circle in Fig. 4-15(d)) developed as the temperature increased (in the same region from Fig. 4-15(e) to Fig. 4-15(g)). At 300 ^{o}C, these formed two large faceted nanoparticles (red circle in Fig. 4-15(h)), which are attached to one surface.

Next, another glass fragment was selected to perform *in-situ* heating only, with no electron beam irradiation involved. This fragment was next to the glass fragment previously reported and discussed in Fig. 4-15. The purpose of this experiment was to see the effect of heating alone when no irradiation was involved. This fragment (indicated by the blue arrows in Fig. 4-16) was *in-situ* heated at 100 ^{o}C, 200 ^{o}C, 250 ^{o}C and 300 ^{o}C, as shown in Fig. 4-16. This fragment has selected to be close to the irradiated glass fragment in order to ease the comparison between them. The two black dots visible in this glass fragment were possibly due to the fact that this glass fragment has experienced some irradiation from the electron beam, due to its proximity to the other irradiated fragment.

A gradual increase in temperature from 100 ^{o}C to 200 ^{o}C and then to 250 ^{o}C, and finally to 300 ^{o}C, did not lead to any changes in the glass fragment in terms of precipitation and particle formation, as is clear in Fig. 4-16. The electron beam irradiation can therefore be seen to be the key influence in terms of precipitating and forming nanoparticles compared to the *in-situ* heating alone. On the other hand, it is believed that the importance of heating might appear after irradiation process since it could affect particle growth or particle melting. *In-situ* heating-induced formation of nanoparticles (at these temperatures) and changes to the overall glass fragment without irradiation were not observed.

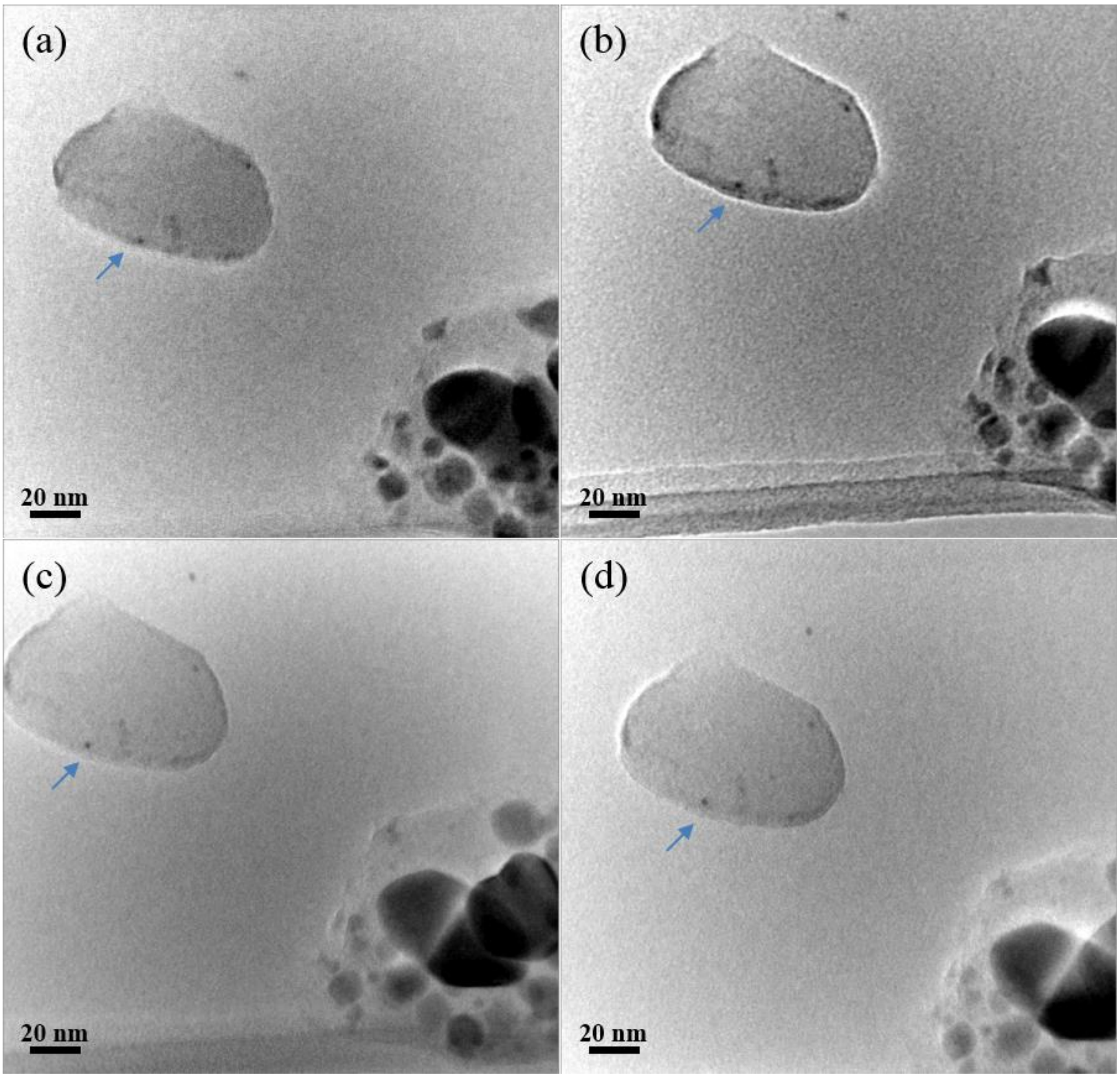

Figure 4-16: *In-situ* heating of a glass fragment indicated by the blue arrow at (a) 100 ^{o}C, (b) 200 ^{o}C, (c) 250 ^{o}C and (d) 300 ^{o}C. JEM TEM 3010 at 300 keV.

4.3 Summary

Metallic Zn nanoparticles were generated in two compositional ranges of borosilicate glass upon 200 and 300 keV electron beam irradiation in a transmission electron microscope. Irradiation effects were studied via both a stationary electron beam as a time series and spatially varying beams for line-scan patterning. The size of the Zn nanoparticles formed was found to be inversely related to the distance from the centre of the electron beam and the nanoparticles were observed to grow from 5 to 50 nm over time via ripening. Line-scan patterning by means of both thermal gun and field emission gun electron irradiation was successfully achieved. These findings also show the occurrence of self-organized particle ordering such as the formation of chains. Metal nanoparticles had a tendency to migrate toward the centre of the glass fragment, unless high intensity radiation ablates the glass matrix, in which case Zn particles remained decorating the surface. Electron energy loss spectroscopy, high-resolution transmission electron microscopy imaging and scanning transmission electron microscopy were used to confirm particle identity. In addition, *in-situ* heating experiments were conducted in a JEOL JEM 3010 using a Gatan single-tilt heating holder.

4.4 References

Ahn C C, Krivanek O L, Burgner R P, Disko M M and Swann P R 1983 Electron energy loss spectroscopy Atlas (ASU HREM Facility and Gatan, Inc.,).

Cazaux J 1986 Some consideration on the electric-field induced in insulators by electron-bombardment *J. Appl. Phys.* **59**, 1418-1430.

Ghatak J, Guan W and Möbus G 2012 *In situ* TEM observation of lithium nanoparticle growth and morphological cycling *Nanoscale* **4**, 1754-1759.

Gnanavel T, Kumar S and Möbus G 2011 In-situ fabrication of 3D nickel nanobeads by electron beam induced transformation *J. Nanoscience and Nanotechnology* **11** 1019-1024.

Gorobchenko V D, Zharnikov M V, Maksimov E G and Rashkeev S N 1985 Experimental and theoretical investigations of plasma oscillations of electrons in zinc and cadmium *Sov. Phys. JETP* **61** 398-406.

Guan W, Ross I M, Bhatta U M, Ghatak J, Peng N, Inkson B J and Möbus G 2013 Nanopatterning by ion implantation through nanoporous alumina masks *Phys. Chem. Chem. Phys.* **15** 4291-4296.

Jiang N, Qiu J and Silcox J 2000 Precipitation of nanometer scale Zn crystalline particles in $ZnO-B_2O_3-SiO_2$ glass during electron irradiation *Appl. Phys. Lett.* **77** 3956-3958.

Jiang N, Qiu J, Ellison A and Silcox J 2003 Fundamentals of high-energy electron-irradiation-induced modifications of silicate glasses *Phys. Rev. B* **68** 064207-11.

Kawazoe H, Suzuki R, Inoue S and Yamane M 1989 Mechanism of photochromism in oxide glasses containing a large amount of CdO and ZnO *J. Non-Cryst. Solids.* **111** 16-28.

Möbus G and Tsai J 2008 Nanopatterning and Grain Growth in Fluorides *Microsc. Microanal.* **14 (Suppl 2)** 248–249.

Mohr C, Dubiel M and Hofmeister H 2001 Formation of silver particles and periodic precipitate layers in silicate glass induced by thermally assisted hydrogen permeation *J. Phys. Cond. Mat.* **13** 525-536.

Nishiyama H, Miyamoto I, Matsumoto S-I, Saito M, Fukumi K, Kintaka K and Nishii J 2004 Periodic precipitation of crystalline Ge nanoparticles in $Ge-B-SiO_2$ thin glass films *Appl. Phys. Lett.* **85** 3734-3736.

Shin J W, Lee J Y, No Y S, Kim T W, Choi W K and Jin S 2008 The formation mechanism of periodic Zn nanocrystal arrays embedded in an amorphous layer by rapid electron beam irradiation *Nanotechnology* **19**, 295303-6.

Widder K, Knupfer M, Knauff O and Fink J 1997 Plasmon behavior of Zn from electron-energy-loss spectroscopy *Phys. Rev. B.* **56**, 10154-10160.

Chapter Five

Electron irradiation-induced formation of copper nanocrystals in copper-loaded borosilicate glasses

5.1 Introduction

Cu-loaded borosilicate glasses have been widely studied and the formation of Cu nanoparticles in these glasses has become a topic of great interest. Cu nanoparticles are the most studied metallic nanoparticles as a result of being low-cost and highly abundant while showing high conductivity. Despite a few studies on the formation of Cu nanoparticles of different diameters in various materials by electron beam irradiation, to the best of our knowledge there is no research to date on electron irradiation-induced precipitation of Cu nanoparticles in glass, although there is one study on pre-existing Cu nanoparticles in glass [Ito *et al.*, 1999].

In this research, a study has been made to fill this gap in the literature by attempting *in-situ* precipitation and formation of Cu nanoparticles in glass via electron beam irradiation.

Two Cu-borosilicate glasses, one with high and the other with low Cu-loading, were chosen for the purpose of investigating the electron irradiation-induced precipitation and nanoparticle formation. Those two glasses are here given the acronyms of CuNBS-A for the high Cu-loaded glass and CuNBS-B for the low Cu-loaded glass, respectively, and the compositions are listed in table 5-1. The raw materials used to prepare these glasses consist of copper oxide (CuO, purity > 99%), boric acid (H_3BO_3, purity > 99.5%), sodium carbonate (Na_2CO_3, purity ~ 99.1%) and silica sand (SiO_2, purity ~ 99.5%), giving a melting temperature of 1400 ^oC.

The CuO and H_3BO_3 were sourced from Sigma-Aldrich, while the Na_2CO_3 and SiO_2 were sourced from Glassworks Services Ltd, Doncaster.

Table 5-1: Compositions of Cu-borosilicate glass (mol.%)

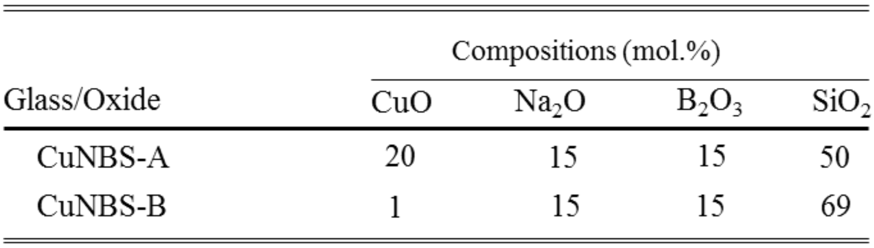

	Compositions (mol.%)			
Glass/Oxide	CuO	Na_2O	B_2O_3	SiO_2
CuNBS-A	20	15	15	50
CuNBS-B	1	15	15	69

The motivation for the selection of these compositions was to explore the concentration range of Cu from multiple perspectives: high concentration so as to provide compatibility with the earlier work on borosilicate glasses loaded with Zn (discussed in chapter-4), or low concentration to compare both with the high concentration Cu glass in terms of the response to the electron irradiation and also to compare with the laser patterning of various Cu-silicate glass [Teng *et al.*, 2010 and Almeida *et al.*, 2012]. In both types of glass, however, the Cu concentrations were sufficiently low to fall inside the glass forming region of the underlying ternary N-B-S phase diagram.

5.2 Results

The findings of this study differ in several respects from all other reported Cu glass studies. First, precipitation of Cu nanoparticles in glass was achieved via electron beam irradiation in TEM. Second, the formation of Cu nanocrystals was observed at the surface of the glass, or deposited far away from the original glass fragment, when high level electron irradiation was used. Third, the formation of nano-rings of metallic Cu NPs was observed in the glass a when focused electron beam was used for irradiation. Fourth, patterning was achieved in the Cu-glass using the line-scan irradiation mode.

All these experiments are novel, since electron beam irradiation has never previously been used either to precipitate Cu nanoparticles, or to do patterning in Cu glass.

5.2.1 CuNBS-A glass

5.2.1.1 TEM irradiation of quenched CuNBS-A glass

5.2.1.1.1 Stationary irradiation mode

5.2.1.1.1.1 Electron irradiation-induced Cu nanoparticle precipitation

Figure 5-1 shows a glass rod before and after electron irradiation using a stationary electron beam with a diameter exactly matching that of the glass rod.

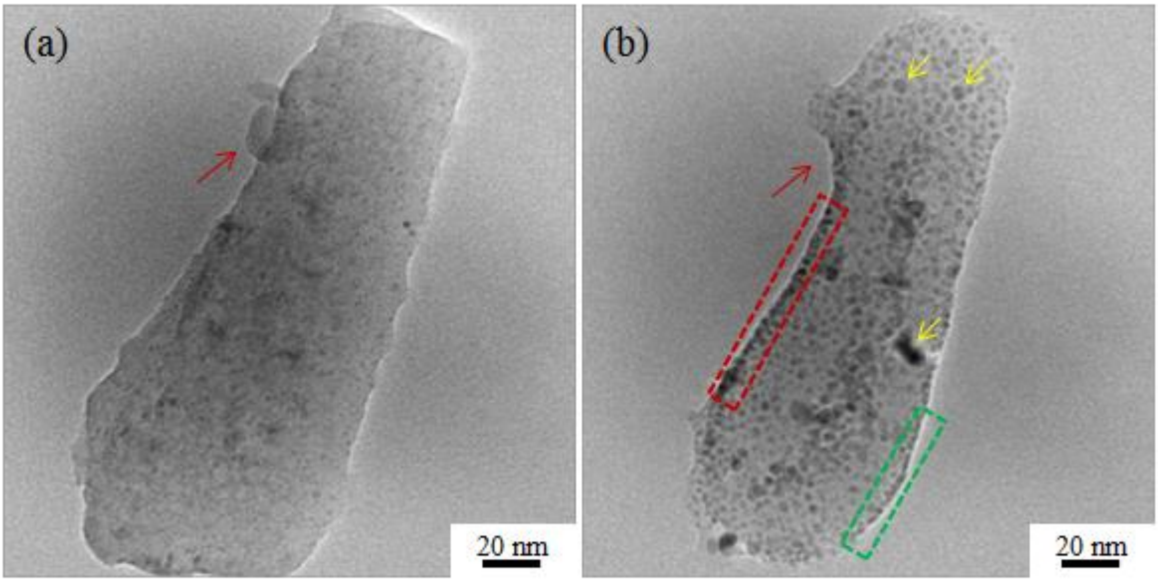

Figure 5-1: TEM micrographs of the CuNBS-A glass fragment, (a) before and (b) after about 3 min of electron beam irradiation. The red and green dashed areas in (b) are chains of nanoparticles. JEM TEM 3010 at 300 keV.

It can be seen from Fig. 5-1(a) that the initial glass rod with a size approximately 60 nm × 250 nm is rather homogeneous, except for a few speckles. It is believed that these very tiny particles might have formed during the early stages of focusing and preparing the electron beam for irradiation. The entire glass rod was then irradiated by converging the electron beam to a diameter slightly larger than 200 nm for ~ 3 min. Under the influence of electron beam irradiation, three significant phenomena were observed: (i) Firstly, circular-shaped nanoparticles were precipitated throughout the entire glass rod. These nanoparticles were rather homogeneously distributed with diameters ranging from about 1 nm to about 5 nm, except for a few which have diameters between 6-12 nm (indicated by yellow arrows in Fig. 5-1(b)). Secondly, smoothing of the rough surfaces of the glass rod and rounding of the glass corners was observed. This also includes a merging between the main glass and an originally separate attached glass particle, as indicated by the red arrow in Fig. 5-1(a,b). This glass material flow accompanied an overall shrinkage in the volume of the glass fragment, which indicates that some ablation of the glass occurs in addition to Cu being expelled. Thirdly, formation of particle chains in the glass rod under electron beam irradiation was observed. The first chain was about 90 nm long and consists of about 23 nanoparticles (indicated by the red dashed area in Fig. 5-1(b)), while the opposite second chain (green dashed area in Fig. 5-1(b)) is shorter (about 50 nm). Both these particle chains are just inside the edge of the glass fragment along its long aspect. Another glass fragment with a sharp edge was selected for irradiation using the largest condenser aperture and spot size 1, and this is shown in Fig. 5-2.

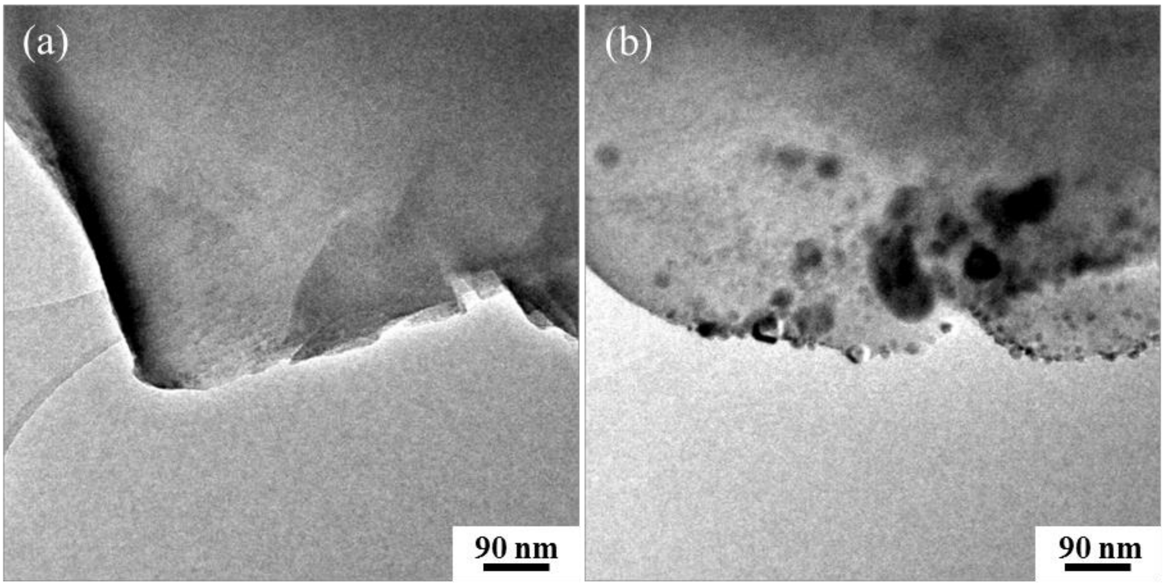

Figure 5-2: TEM images of CuNBS-A glass, (a) before and (b) after 2 min electron irradiation. JEM TEM 3010 at 300 keV.

The initial glass fragment was clean and homogeneous and no trace of particle precipitation prior to the irradiation could be seen (Fig. 5-2(a)). A wide electron beam illumination was then used to irradiate the sharp edge and all the area on its right. After about 2 min irradiation, modifications in the region under irradiation had occurred, such as nanoparticle precipitation (Fig. 5-2(b)). These nanoparticles were of different sizes and had mostly circular shapes. It can be seen that the larger nanoparticles were formed inside the glass fragment, while smaller nanoparticles of a few nanometres were located at the surface of the fragment giving it a kind of surface decoration. A massive glass surface rounding could also be seen after irradiation.

While the above sub-10 nm particles prove stable under further wide-beam "imaging" irradiation, it is interesting to explore the end-state of precipitation if exceptionally high irradiation currents are applied. Figure 5-3 shows another glass rod irradiated after removing the condenser aperture.

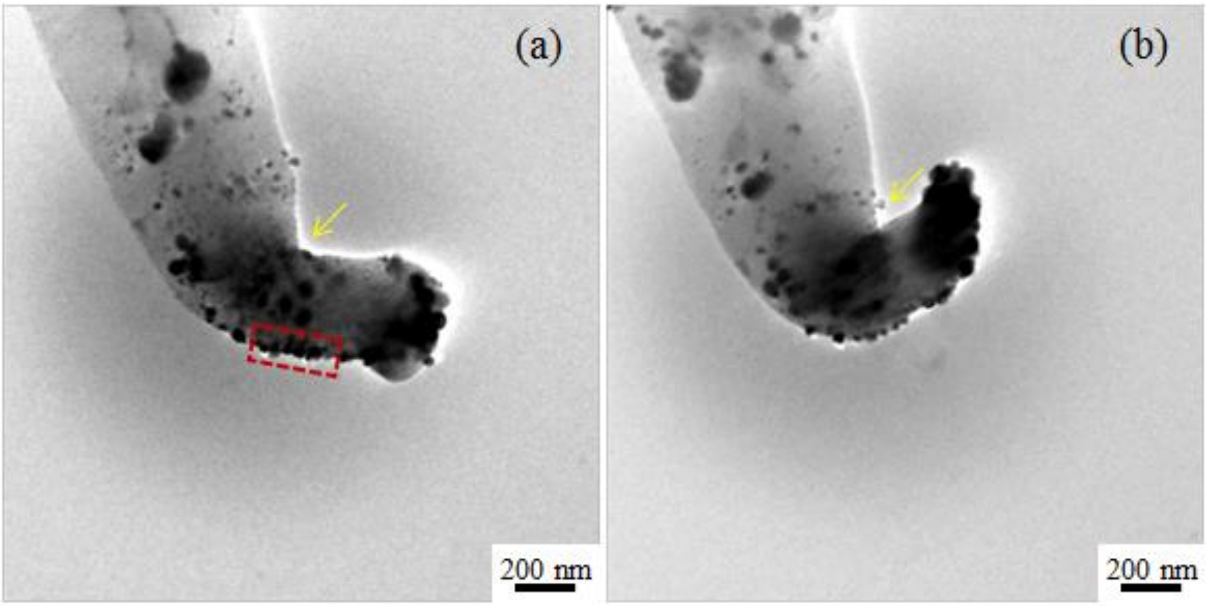

Figure 5-3: Irradiation of a rod of CuNBS-A glass at a very high beam current for about 2 min in (a) and for further 2 min in (b). JEM TEM 3010 at 300 keV.

After electron beam irradiation for about 2 min, relatively large nanoparticles with mostly circular morphologies were formed but were non homogeneously distributed through the glass rod, leaving several areas of glass matrix, larger than 200 nm, Cu-particle-free; the light contrast visible in the glass rod also indicated that no Cu was left in the glass at all. Several small nanoparticles are also stacked outside the glass rod touching its edges and some others of diameter of about 50 nm were found in an ordered state outside the glass rod, close to the edge; indicated by the red dashed area in Fig. 5-3(a). The diameter of these nanoparticles (~ 50 nm) was larger than the distance between them (~ 10 nm). Another distinct feature was that the originally straight rod, bent under the impact of electron irradiation centred at the right of the centre of the rod, as shown by the yellow arrow in Fig. 5-3(a). Also the rod became rounded due to radiation-induced fluidity (RIF). A further 2 min irradiation did not result in much change in terms of precipitation or the size of nanoparticles except for more pronounced glass rod bending (yellow arrow in Fig. 5-3(b)) and more rounding in the lower region of the glass rod.

Figure 5-4 shows exposure-time series irradiation at a constant current. The formation of clusters and small round particles over multiple applications of 3 min additional irradiation was revealed. This series started with pre-irradiation levels already triggering cluster formation in Fig. 5-4(a), but as the experiment switching to a higher current, shown in Fig. 5-4(b), the small particles in Fig. 5-4(a) were not seen to grow, but were rather replaced by mostly new and larger particles. This coincides with the morphing of the glass into a more roundish shape. In Fig. 5-4(c) and Fig. 5-4(d), however, it can be seen that the precipitation saturates quickly and that no ripening occurs, indicating a lack of long-range diffusion.

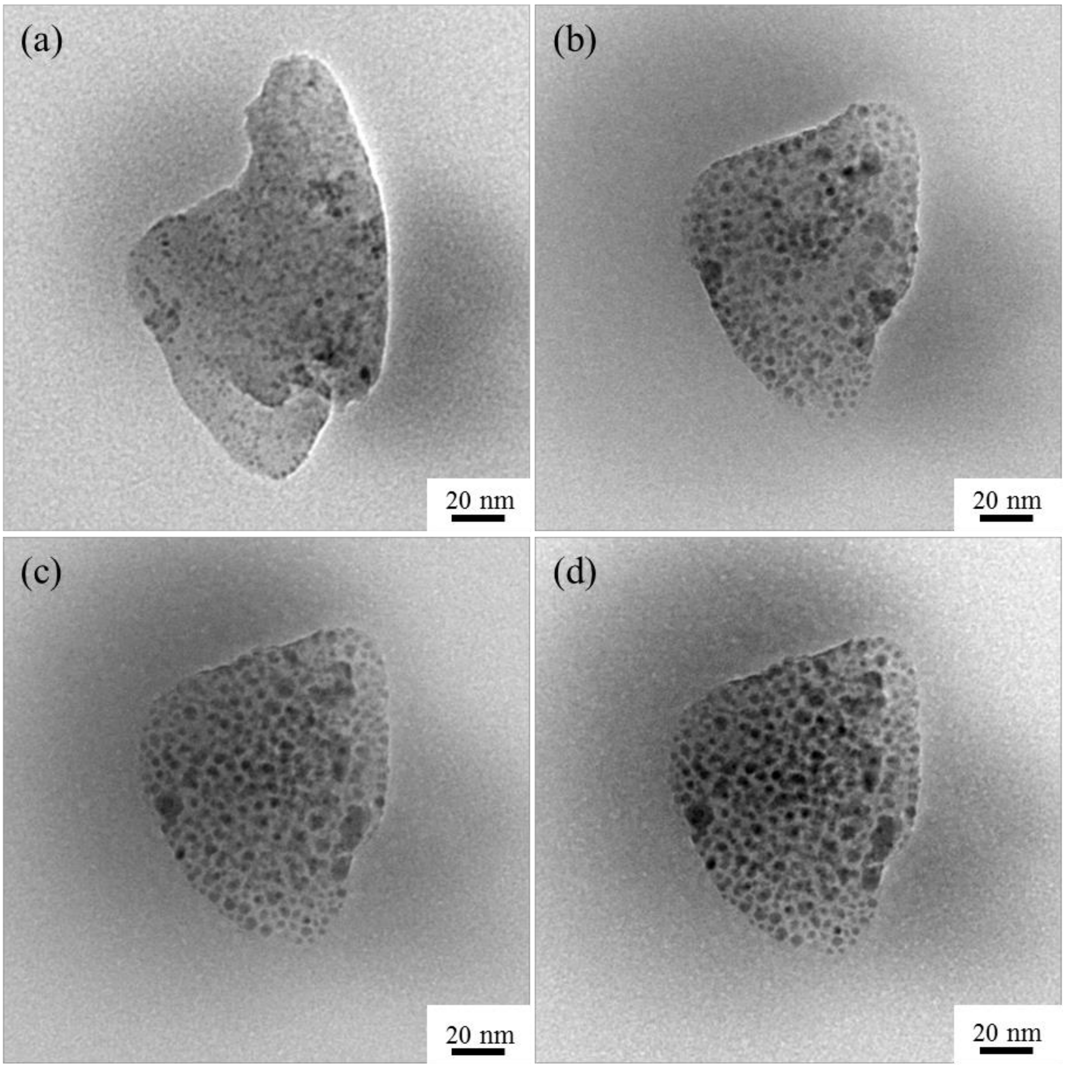

Figure 5-4: Time series irradiation at constant intensity, including intervals of 3 minutes additional irradiation between each image. JEM TEM 3010 at 300 keV.

5.2.1.1.1.2 Focused electron beam-induced ring formation of Cu nanoparticles

No research has been identified to date about electron beam irradiation-induced ring formation in any Cu-loaded glass. In this research, however, a nanoring of metallic Cu NPs was successfully formed using a focused electron beam in FEG TEM. Figure 5-5 shows the ability to form a nano-ring structure of nanoparticles in the CuNBS-A glass using electron beam irradiation in a FEG-TEM, as well as subsequent chemical analysis using EELS and HRTEM imaging. The medium intensity electron beam with a diameter of about 140 nm was focused on the glass fragment for approximately 5 min (Fig. 5-5(a)). The irradiation generated nanoparticles with sizes between 8-15 nm along the ring, and smaller sub-10 nm nanoparticles inside the ring. In order to identify the precipitated nanoparticles, EELS spectrum was acquired from the region of irradiation in Fig. 5-5(a) and this is shown in Fig. 5-5(b).

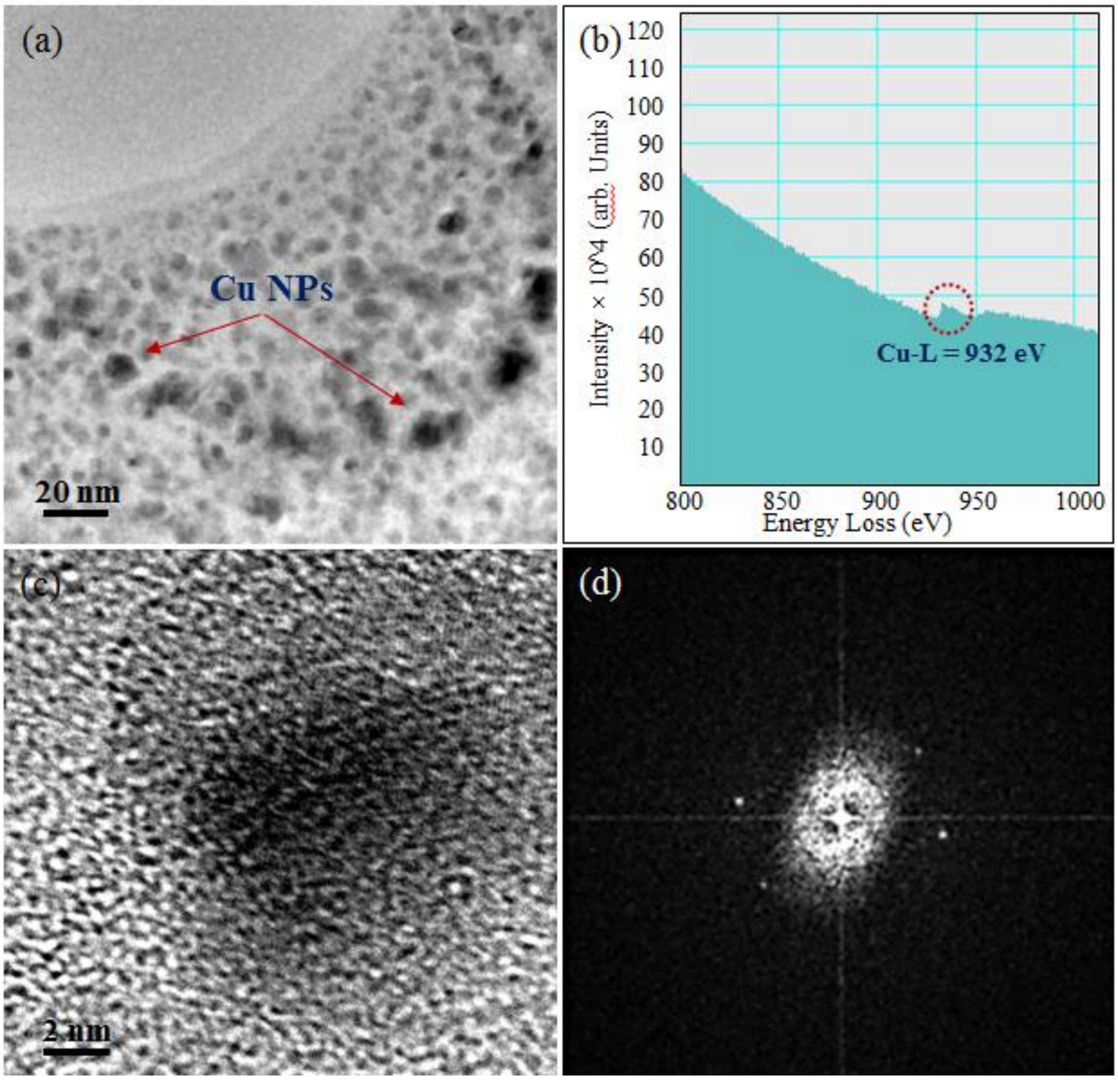

Figure 5-5: (a) Nano-ring formation in CuNBS-A glass under focused electron beam irradiation. (b) EELS spectrum from the region of irradiation in (a) showing the L-edge for metallic Cu. (c, d) HRTEM image for a typical Cu nanoparticle and corresponding FFT respectively. JEM TEM 2010F at 200 keV.

A distinct peak at around 932 eV with an onset around 929 eV appeared in the EELS spectrum after about 5 min of electron irradiation corresponding to the Cu-L edge. Comparing data in the literature for fine structures between Cu, CuO and Cu_2O [Long, 1986, Ito *et al.*, 1999 and Yang *et al.*, 2014], the shape of the L-edge shown in Fig. 5-5(b) clearly matches metallic Cu, as oxides would show two high-contrast "white lines", which were not observed in this study.

For further confirmation that the precipitated Cu nanoparticles were metallic, high resolution transmission electron microscopy (HRTEM) image of a typical precipitate nanoparticle was obtained from the irradiated region in Fig. 5-5(a) with corresponding fast Fourier transformation (FFT) and these are shown in Figs. 5-5(c) and 5-5(d), respectively. The d-space calculations for the lattice fringes and the corresponding FFT can be extracted and are compatible with metallic Cu. The outcome of irradiation with a more focused electron beam in a thicker glass fragment area is shown in Fig. 5-6, demonstrating the generation of a dark ring with one central dark particle separated by significantly lighter areas due to Cu-depletion and/or glass matrix ablation.

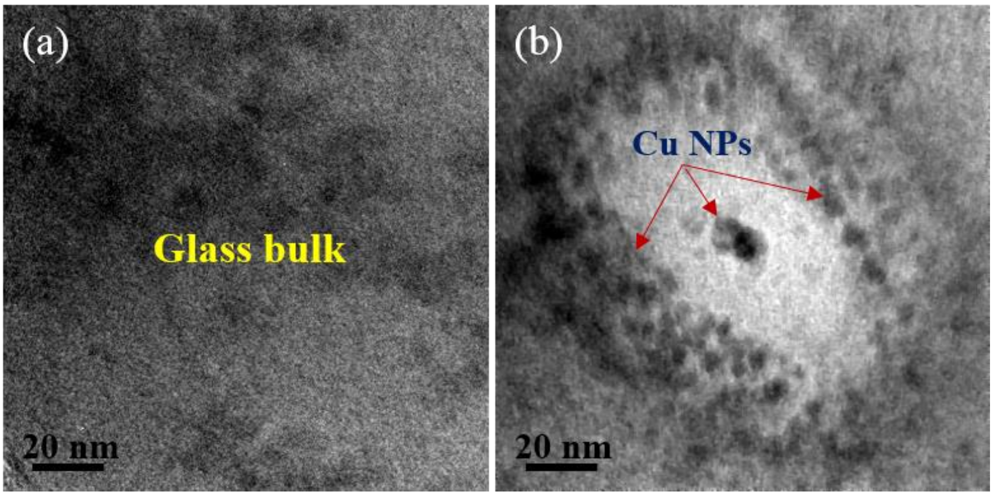

Figure 5-6: TEM micrographs of the CuNBS-A glass fragment, (a) before, and (b) after nano-ring formation under focused electron beam irradiation. JEM TEM 2010F at 200 keV.

The bright and dark patches can be interpreted via mass-thickness scattering contrast (atomic number sensitive) with metallic Cu (atomic number = 29) appearing far darker than the Na-B-Si-O matrix.

5.2.1.1.1.3 Electron irradiation-induced deposition of Cu nanocrystals on the glass surface and on the C-film

It is worth expanding these experiments to cases where expelled Cu not only precipitates inside the glass but is also deposited on the fragment surface, or even in its vicinity on the support film, as shown in Fig. 5-7. Prior to the electron beam irradiation, the glass fragment was rather homogeneous with few particles visible, as can be seen in Fig. 5-7(a). The condenser aperture was removed and the glass fragment was irradiated for ~ 2 min. This resulted in the formation of surface-deposited nanoparticles that can be, distinguished by their well-faceted morphology and shapes, typical of single crystals of metallic Cu, and clearly shown in Fig. 5-7(b). Nanoparticles of roundish-shape, on the other hand, were formed inside the original glass with a diameter of about 5-35 nm, except for two large NPs of about 77 nm indicated by yellow arrows in Fig. 5-7(b). Amongst the faceted surface-decorating crystals, a rectangular morphology of about 60 nm × 34 nm, indicated by the red arrow in Fig. 5-7(b), was found. Another nearby glass fragment was also irradiated after removing the condenser aperture. In this case, well-faceted nanocrystals were formed, the largest of these, indicated by the red arrow in Fig. 5-7(c), has dimensions of about 260 nm × 64 nm. These nanocrystals were found in a region slightly more than 1 μm away from the original glass fragment which itself became transformed into a perfect ball with a diameter of about 1 μm, as can be seen in Fig. 5-7(c).

It is believed that the sequence of these phenomena is as follows: (i) Firstly, electron irradiation-induced precipitation of metallic Cu, (ii) followed by electron beam ablation of both Cu and glass matrix with re-deposition of metallic Cu onto the C-film away from the original glass fragment, and (iii) finally, transformation of the residual, but not yet ablated, glass fragment into a perfect ball due to surface tension.

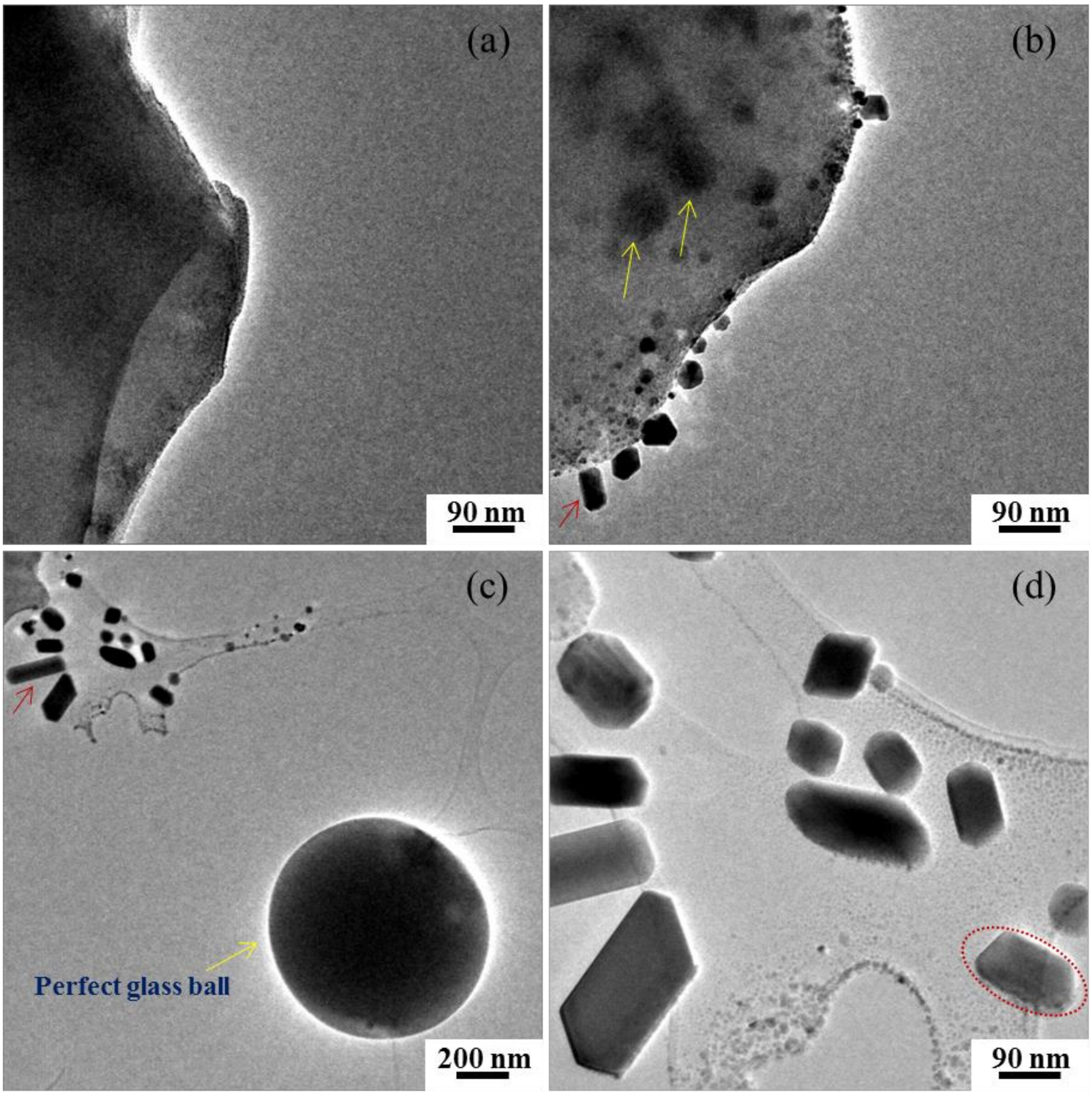

Figure 5-7: TEM images of a CuNBS-A glass fragment, (a) before, and (b) after about 2 min of electron irradiation. (c) de-localised formation of Cu nanocrystals on C-film and sudden transformation of the glass fragment into a perfect glass ball under a very high level of irradiation. (d) high magnification image for the deposited Cu nanocrystals on the C-film away from the original glass fragment. JEM TEM 3010 at 300 keV.

For further confirmation of the nature of the Cu nanocrystals, one of the well-faceted nanocrystals, indicated by the red circle in Fig. 5-7(d), was analysed in FEG TEM making use of the significant chemical analysis facilities available in this TEM. EELS analysis was performed for this nanocrystal and the spectrum is shown in Fig. 5-8.

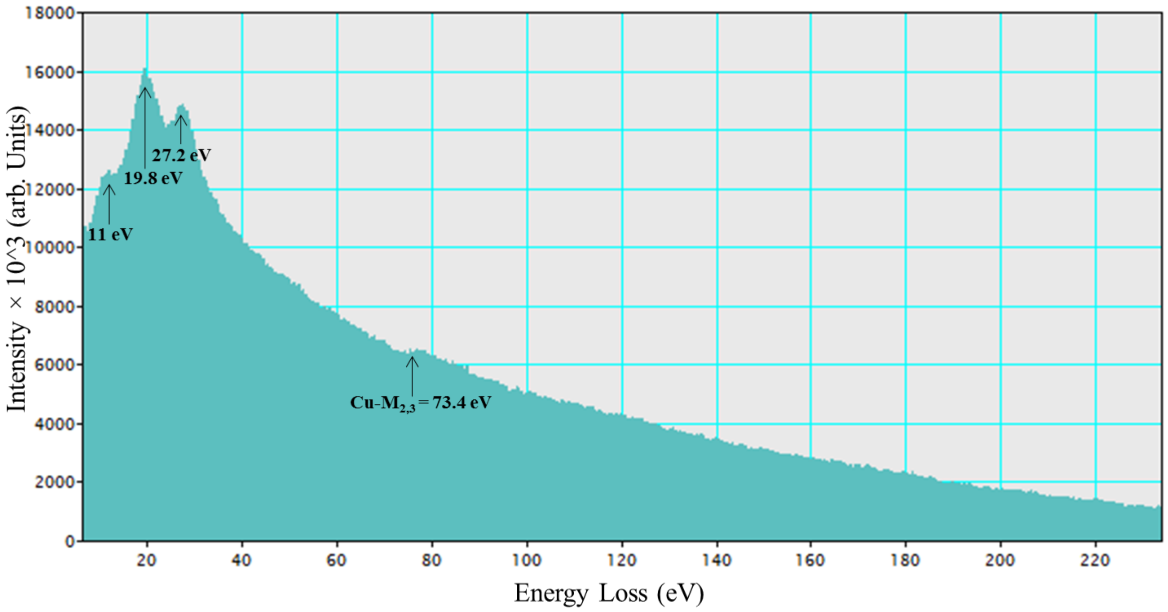

Figure 5-8: Low loss EELS spectrum showing plasmon-range peaks and the $M_{2,3}$ edge for metallic Cu.

From Fig. 5-8, the peak with onset around 73.4 eV matches the $M_{2,3}$ edge, although it is not able to distinguish between metal and oxides [Ahn *et al.*, 1983]. Two distinguishing peaks at around 19.8 and 27.2 eV, respectively however, match metallic Cu well [Ahn *et al.*, 1983], as the oxide would show a single broad peak around 22 eV. Together with the small peak at around 11 eV all of these three peaks match with metallic Cu, while the origin of these "plasmon-range" peaks has been attributed to d-band interband transitions in [Hébert *et al.*, 2011]. In addition, EDX analysis was conducted and the obtained data is shown in Fig. 5-9.

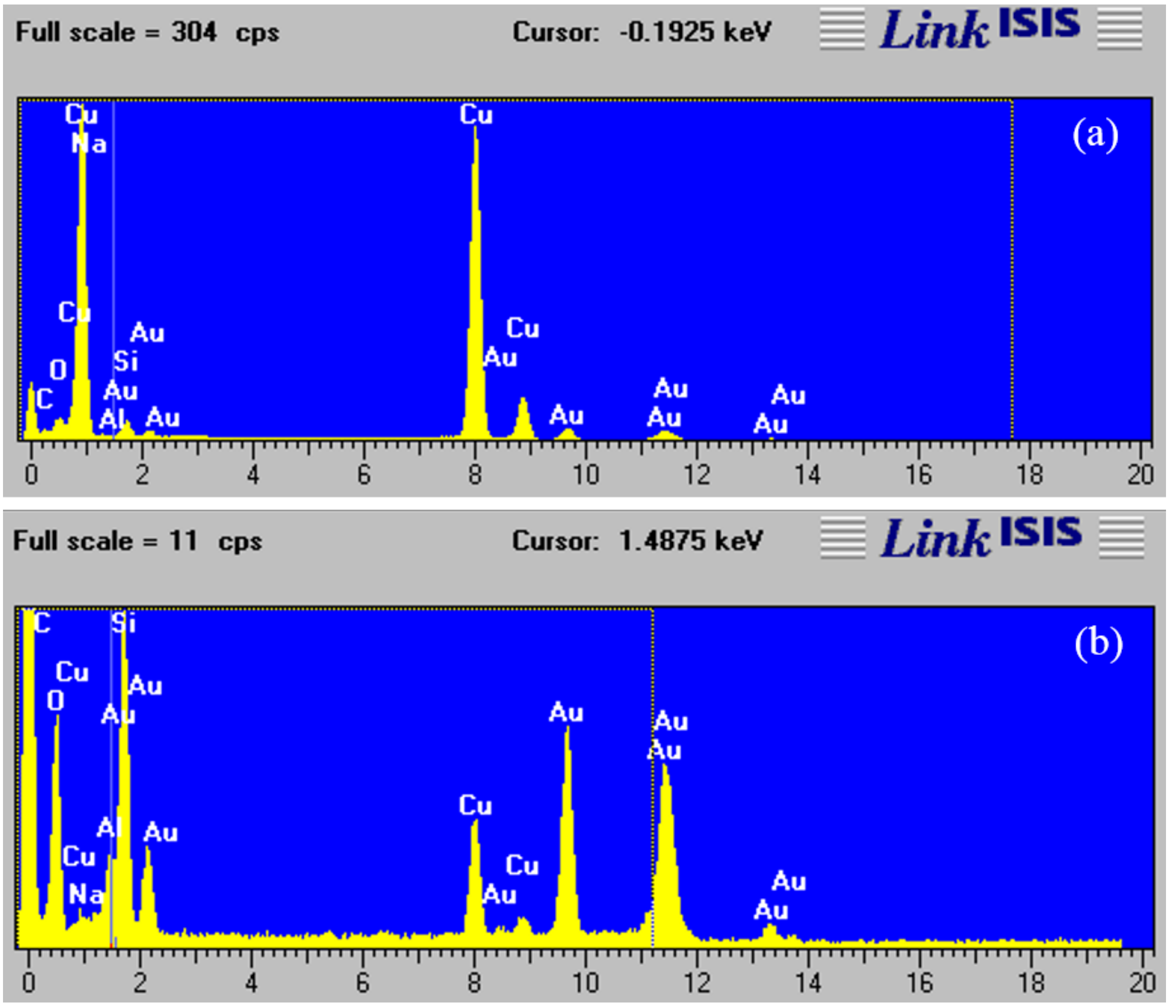

Figure 5-9: EDX spectrum for (a) Cu nanocrystal indicated by the red-circled area in Fig. 5-7(d) and for (b) the perfect glass ball particle in Fig. 5-7(c).

From Fig. 5-9(a), it is clear that the deposited Cu nanocrystal is surely metallic, since two major Cu peaks are dominant with the absence of both silica and oxygen signals. A very weak Al signal is believed to be a residue from the crucible used in glass melting and the Au signals are due to the gold grid used in the TEM sample preparation. Fig. 5-9(b) on the other hand, indicates that the perfect ball microparticle is glass.

The same phenomenon was also observed on another occasion, when Cu nanocrystals were precipitated under the impact of electron irradiation, and then deposited between 500 nm and 1 µm away from the original glass particle, with the latter transforming into a perfect glass bead of about 2 µm diameter, as shown in Fig. 5-10.

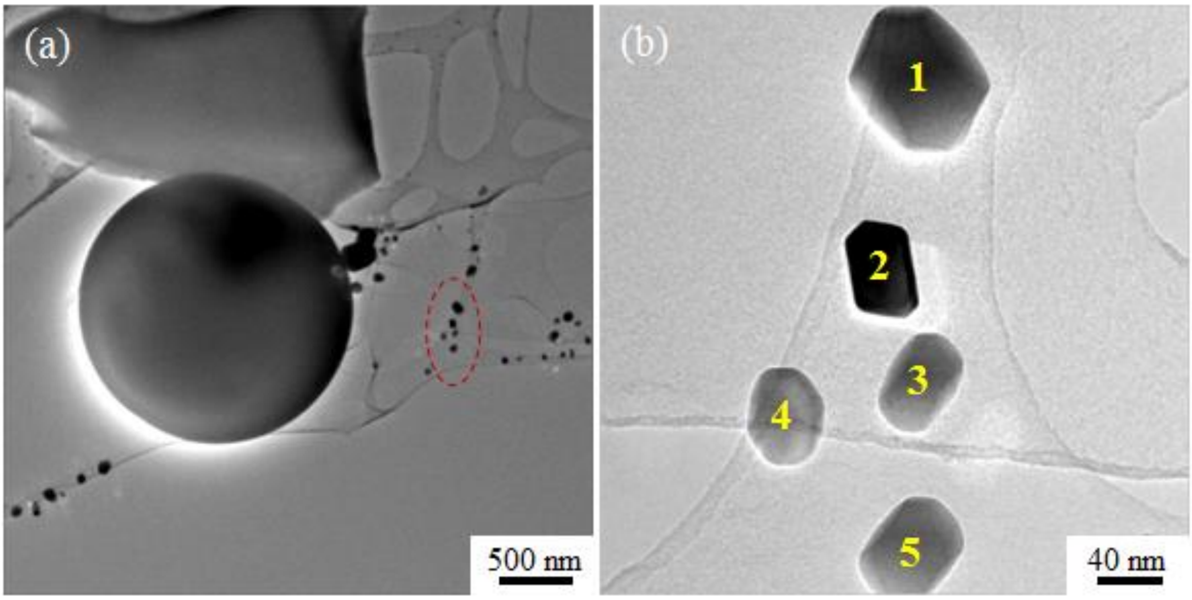

Figure 5-10: (a) Electron irradiation-induced deposition of Cu nanocrystals in the carbon film away from the original glass particle. (b) high magnification TEM image of the red-dashed area in (a). JEM TEM 3010 at 300 keV.

The dimensions of the five nanoparticles shown in Fig. 5-10(b), numbered 1-5, have been calculated and are listed in table 5-2.

Table 5-2: Dimensions of Cu NPs shown in Fig. 5-10(b)

No. of NPs	Dimensions (nm^2)
1	93×93
2	42×61
3	45×67
4	52×65
5	53×75

Another example of the precipitation of Cu nanoparticles on the fragment surface is shown in Fig. 5-11. Prior to the irradiation, the condenser aperture was removed and a maximum current density obtained. The initial fragment looked clean, since there is no trace of any precipitates before irradiation (Fig. 5-11(a)).

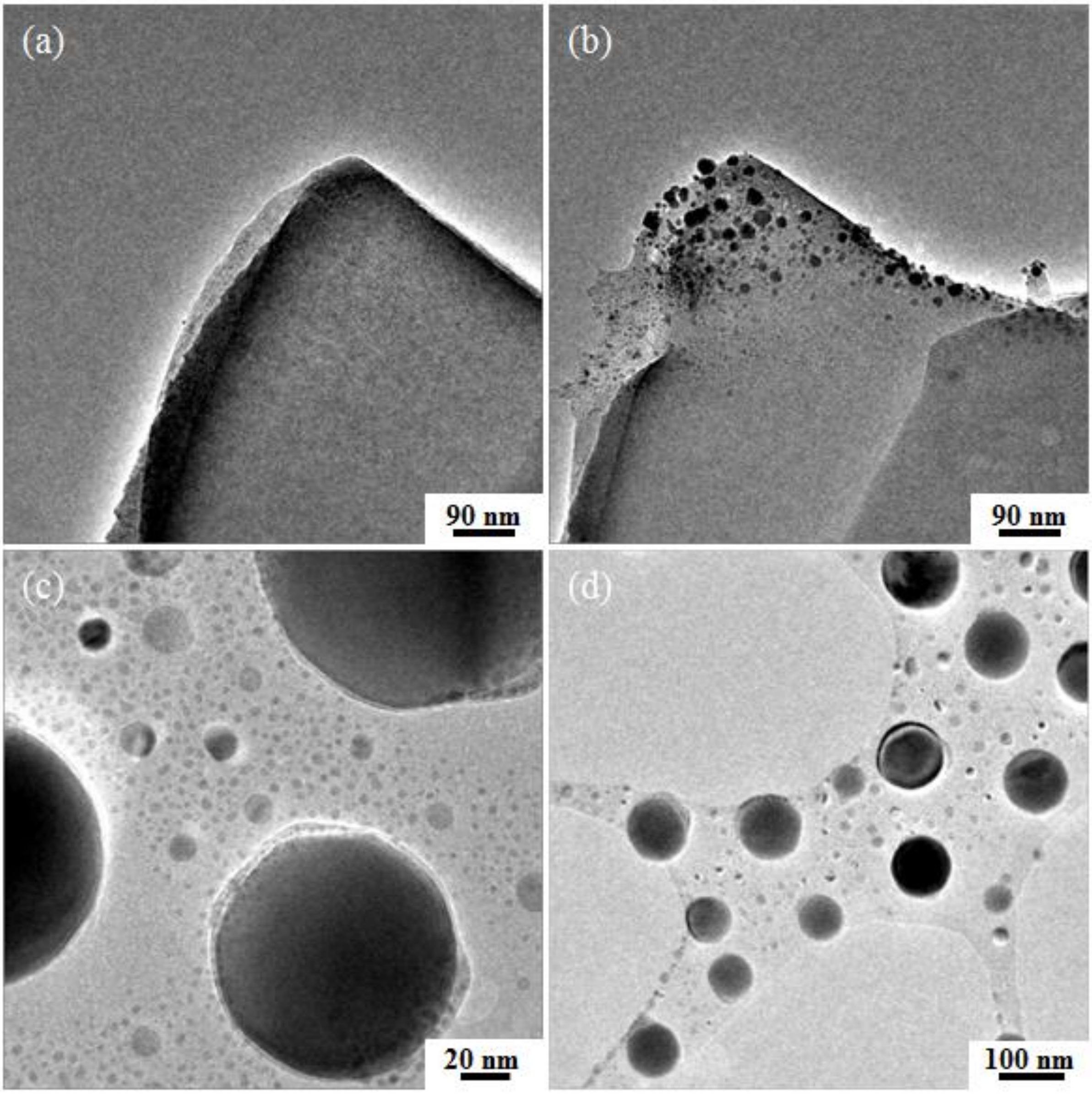

Figure 5-11: TEM images of CuNBS-A glass, (a) before, and (b) after 2 min irradiation. (c, d) are TEM images at different magnifications showing the formation of spherical particles. JEM TEM 3010 at 300 keV.

After about 2 min irradiation, nanoparticle precipitation within the illuminated region inside and at the glass surface can be seen (Fig. 5-11(b)). The glass fragment in Fig. 5-11(b) is slightly shifted to the left during imaging in order to show the entire irradiated area in the field of view. Interestingly, after focusing the electron beam into the same region (the irradiated region in Fig. 5-11(b)) for second time, the original glass fragment has been transformed into nanoparticles with different sized spherical morphologies (Figs. 5-11(c, d)). These are located on the carbon support film. Nanoparticles of three different diameters can be seen. The large nanoparticles of about 100 nm in diameter are surrounded by two other smaller nanometre-sized particles with diameters of about 5 nm and 20 nm. The depleted regions between the large and the small nanoparticles are also obvious.

5.2.1.1.2 Line scan irradiation mode

The line-scan irradiation was carried out using a fixed electron beam diameter but variable exposure times (constant intensity and different doses). In order to perform the line-scan irradiation, a relatively thin rod of CuNBS-A glass was selected. This rod had a sharp edge (Fig. 5-12(a)) and the intention was to produce patterns by scanning the electron beam across the glass material starting from the rod edge, as shown in Fig. 5-12.

The first pattern (line) was drawn by scanning the electron-beam through the glass rod and then stopping it for about 3 sec for each step or click. The step length is much smaller than the beam diameter and hence it was possible to achieve a continuous line (Fig. 5-12(b)). Small nanoparticles of ~ 2-3 nm were formed inside the e-beam. Another pattern was produced via line-scan irradiation, as shown in Fig. 5-12(c). Here, the electron beam was left focused on the glass rod for about 10 sec for each motion, and electron beam-induced formation of nanoparticles inside the e-beam path can be clearly seen. These nanoparticles are larger in size compared to those formed inside the previous pattern. The next pattern, shown in Fig. 5-12(d), was achieved by scanning the electron-beam across the glass rod and then leaving it for about 15 sec for each step. Larger nanoparticles were formed than in the previous two patterns. It is interesting to report that there are three similar effects observed in these three patterns: (i) nanoparticle formation and glass ablation are in competition, but the ablation is higher at higher exposures, (ii) a dark contrast is seen at the e-beam edge, which corresponds to metallic Cu and (iii) the large nanoparticles are located at the centre of the e-beam, while the smaller ones are located slightly away from the e-beam centre. Lower exposure times were also used to generate a pattern in this glass rod. In this case, the electron beam was scanned across the rod and left for about 1 sec for each 2 clicks (Fig. 5-12(e)). This resulted in a line being generated in which the ablation rate exceeded the rate of particle formation. Tiny particles can be seen at the start point of the line-scan irradiation near the rod edge, which is due to possible pre-irradiation effects.

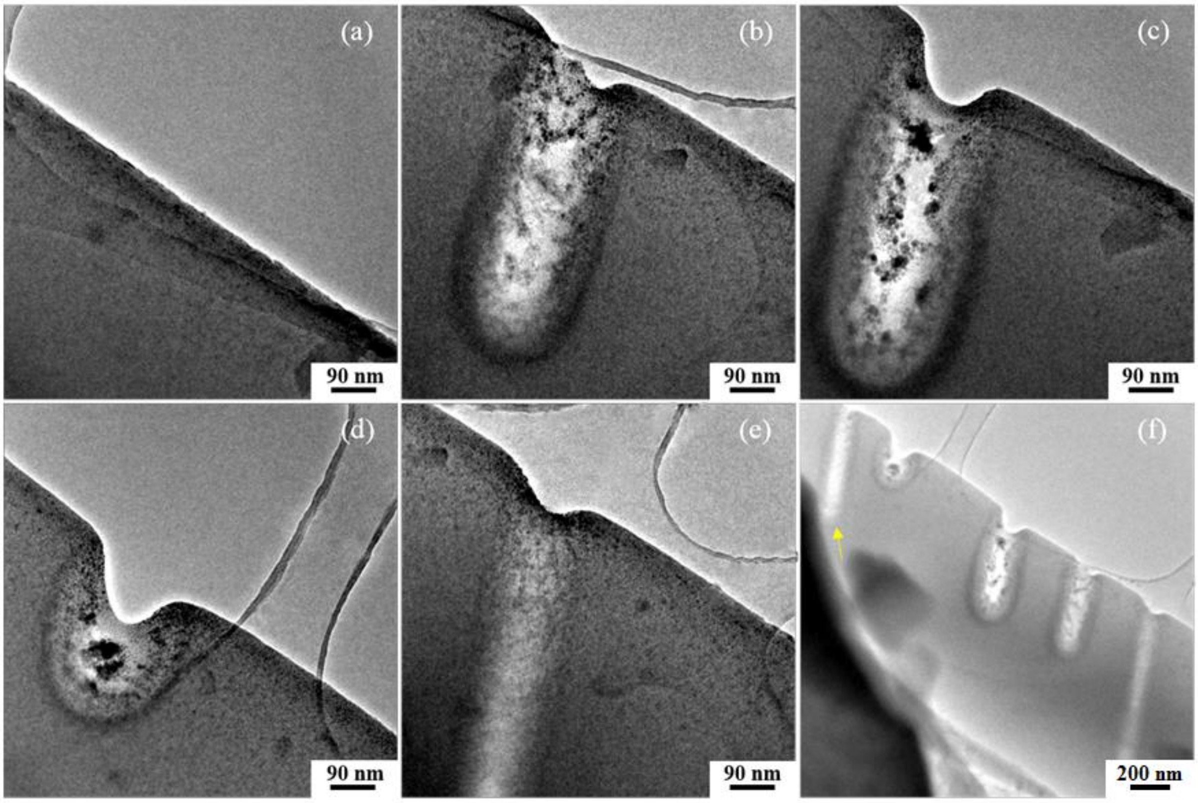

Figure 5-12: Pattern formation via line-scan irradiation mode at various exposure times in a rod of CuNBS-A glass. JEM TEM 3010 at 300 keV.

All four of the aforementioned patterns were produced using slow e-beam scanning. Fast e-beam scanning was also applied to generate a pattern in this glass rod (indicated by the yellow arrow in Fig. 5-12(f)). The same effect was evident here as was seen in the pattern shown in Fig. 5-12(e). Irradiation at such low exposures (the last two patterns) did not form any metal lines at the e-beam edges in comparison with those at higher exposures (the first three patterns).

5.2.1.2 Analysis of the annealed CuNBS-A glass

5.2.1.2.1 TEM and SEM imaging of the annealed CuNBS-A glass

The annealed version of CuNBS-A glass was investigated. TEM images of this glass are shown in Fig. 5-13. The precipitated nano/micro-particles found exhibited dendrite-like shapes which are sorted by the degree of completeness of dendrite development from Figs. 5-13(a) towards 5-13(d); the perfect dendrite particle is shown later in Fig. 5-14. The presence of various shapes, starting from spherical particles up to well-developed dendrite branching systems, is due to different thermal histories and temperature gradients. It is believed that the spherical nanoparticles were initially formed during the cooling and annealing schedule via a nucleation process, followed by gradual growth into dendrite-like structures. These dendrites have a central backbone and multi-branch structures, as shown in Fig. 5-13(b) and 5-13(c). The fact that in Fig. 5-13(c) and 5-13(d) the dendrite was preserved in the centre of the fragment with its backbone oriented parallel to the fracture surface during grinding indicates mechanical toughening of the glass composite material by the Cu-dendrites. While the inclusion of near-surface material was avoided by cutting it off, the remaining inner glass would still have experienced a cooling speed gradient as a radial function from the centre distance.

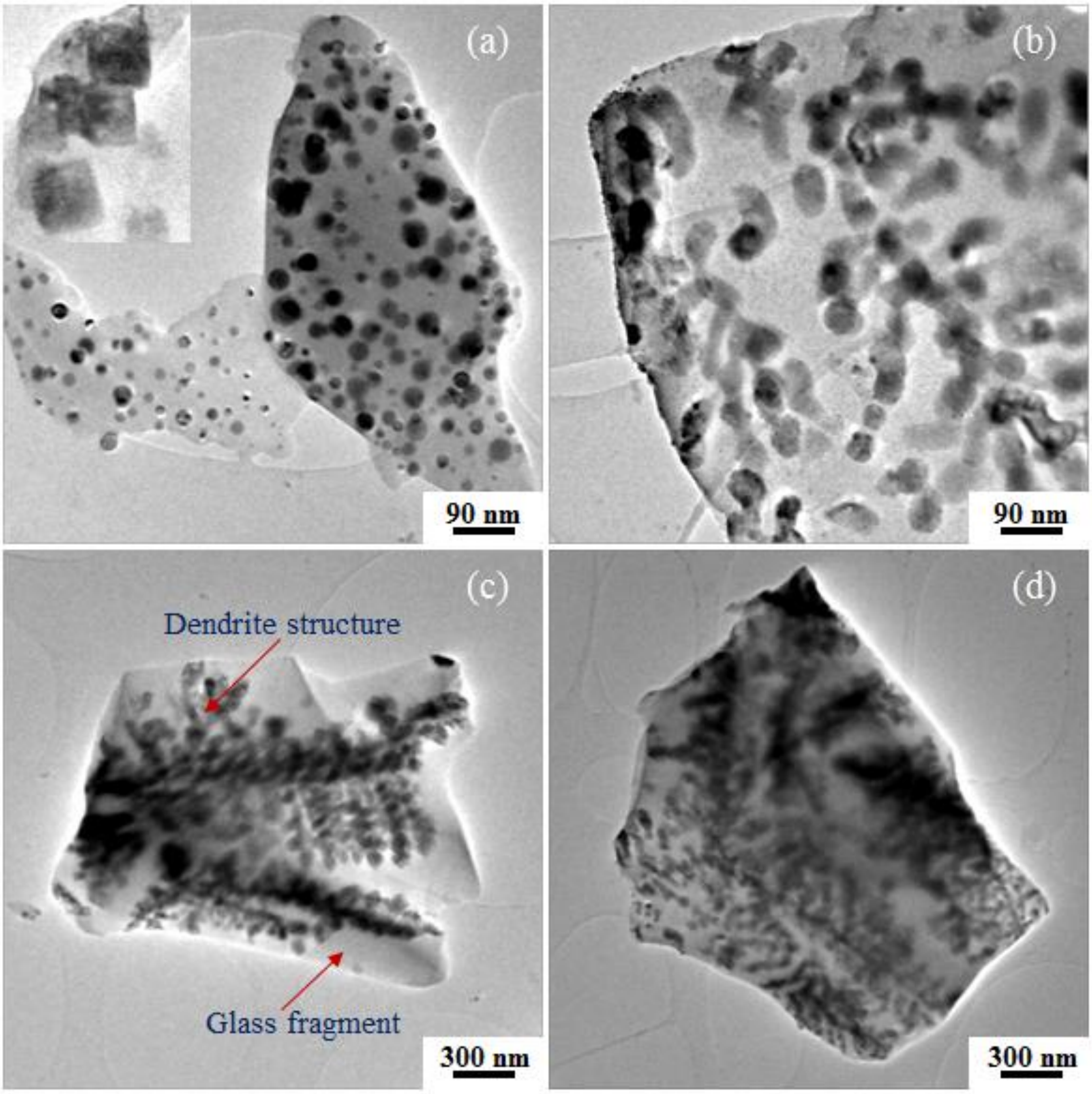

Figure 5-13: TEM images of annealed CuNBS-A glass showing spherical (a), square (the inset in (a)) and dendritic (b-d) shapes of Cu_2O precipitates. JEM TEM 3010 at 300 keV.

The overall length of the dendrites were between 20-50 µm with sub-branches a few µm long, as confirmed by SEM imaging and shown in Figs. 5-14(a) and 5-14(b). EDX spectra were acquired from both a small branch of the dendrite and the glass matrix. The EDX spectrum obtained from the dendrite is shown in Fig. 5-14 (c). The two strong peaks of Cu and O reveal that the dendrite crystal formed during the annealing process is Cu_2O. The reason that the Si and Na peaks are present in the spectrum, however, is because of the use of a slightly wide electron beam for the analysis, since this covers the dendrite as well as the neighbouring glass matrix (the yellow circle in Fig. 5-14(a)). For the glass matrix (the red square in Fig. 5-14(b)), the acquired EDX is shown in Fig 5-14(d). All the expected elements appeared in the spectrum (Cu, Na, O and Si). In addition, the C peak visible in Fig. 5-14(c) is due to the coating of the glass with carbon to prevent charging during SEM analysis, while a small Al peak is believed to be a residue from the crucible used in glass melting.

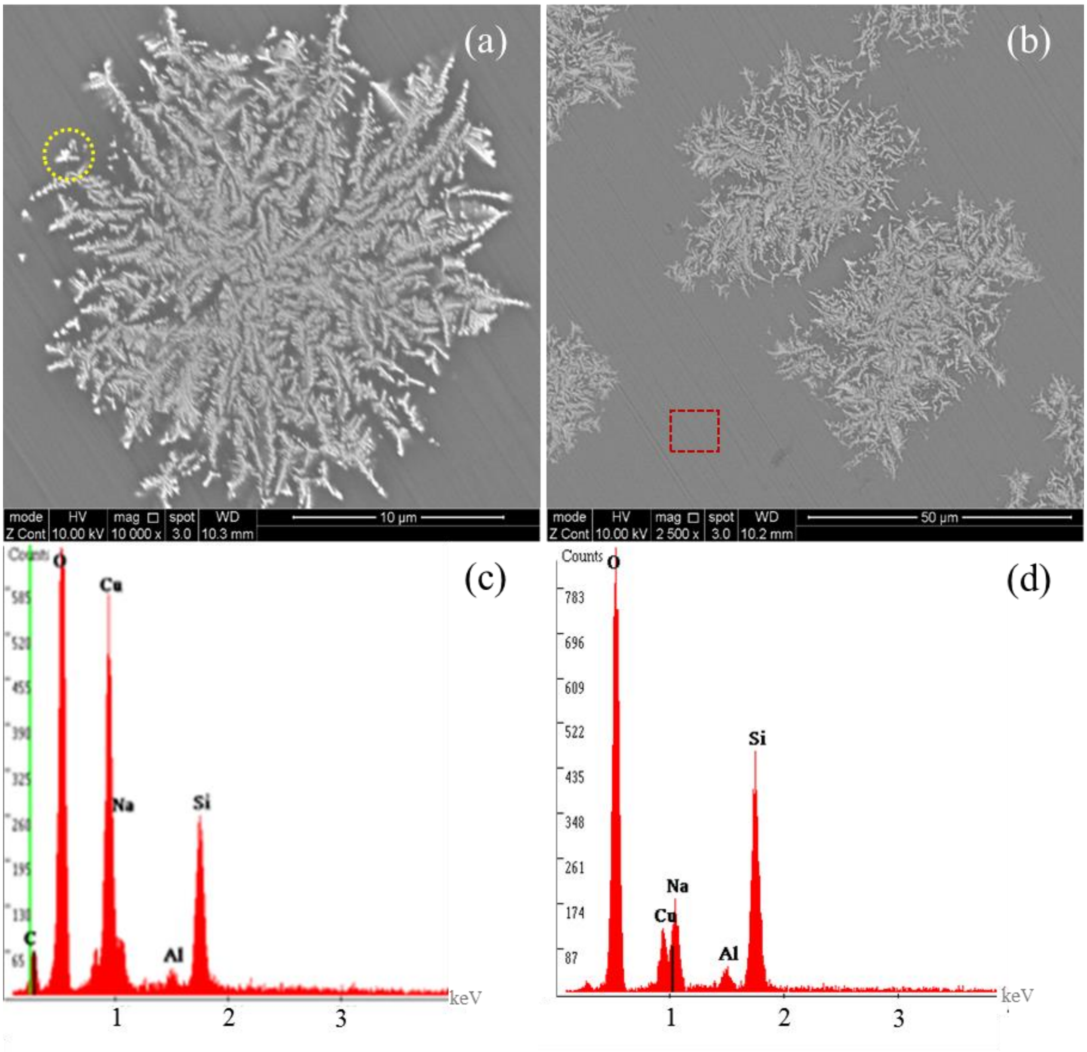

Figure 5-14: (a, b) SEM images of typical dendrite copper oxide particles at different magnifications. (c, d) point EDX spectrum of the sub-branch of dendrite particle (yellow circle in (a)) and glass matrix (red dashed area in (b)), respectively. FEI SEM Inspect F at 20 kV.

5.2.1.2.2 Powder XRD pattern of the annealed CuNBS-A glass

Figure 5-15 shows an XRD pattern of the annealed CuNBS-A glass. It can be seen that dominant peaks at 2θ = 36.4° (d=2.466 Å), 2θ = 42.3° (d=2.135 Å), 2θ = 61.34° (d=1.510 Å) and 2θ = 73.5° (d=1.287 Å) correspond to the planes of (111), (200), (220) and (311) of the cubic Cu_2O phase, respectively, along with a relatively weak peak at 2θ = 77.3° (d=1.233 Å) corresponding to (222).

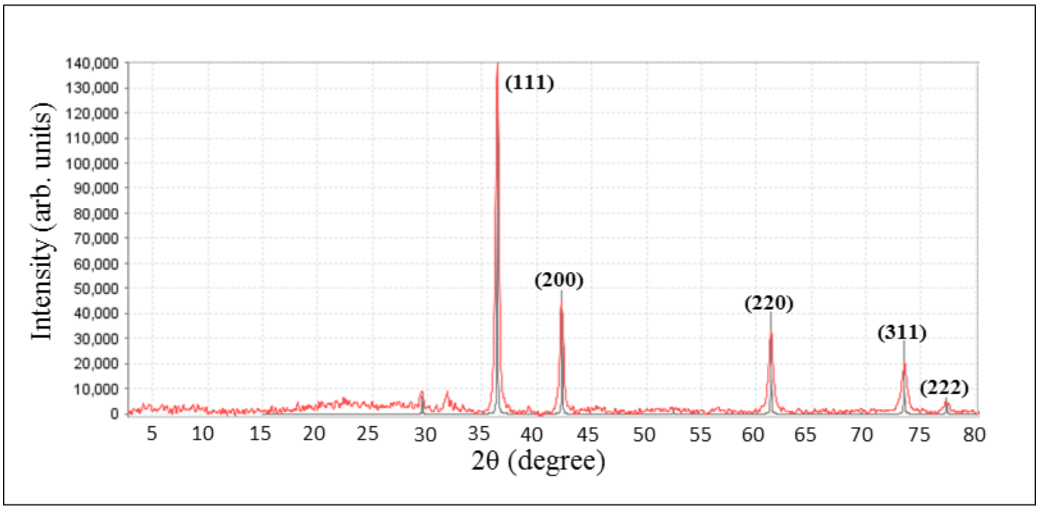

Figure 5-15: Powder XRD pattern of the annealed CuNBS-A glass showing planes corresponding well to the cubic Cu_2O phase.

A comparative study of quenched and annealed glass fragments was presented in order to explain the necessity for suppression of thermal precipitation, confirming that a cooling-rate at least as fast as in this study's frit-quenching is required. On the other hand, the reason that Cu_2O is produced via thermal annealing while the electron beam produces metallic Cu is because of the air-furnace heating used for annealing, while the TEM is a low-oxygen environment with the electron beam acting as the reducing agent.

5.2.1.2.3 Electron irradiation of the annealed CuNBS-A glass in TEM

A glass rod with an embedded dendrite structure was subjected to time-series electron beam irradiation, as shown in Fig. 5-16.

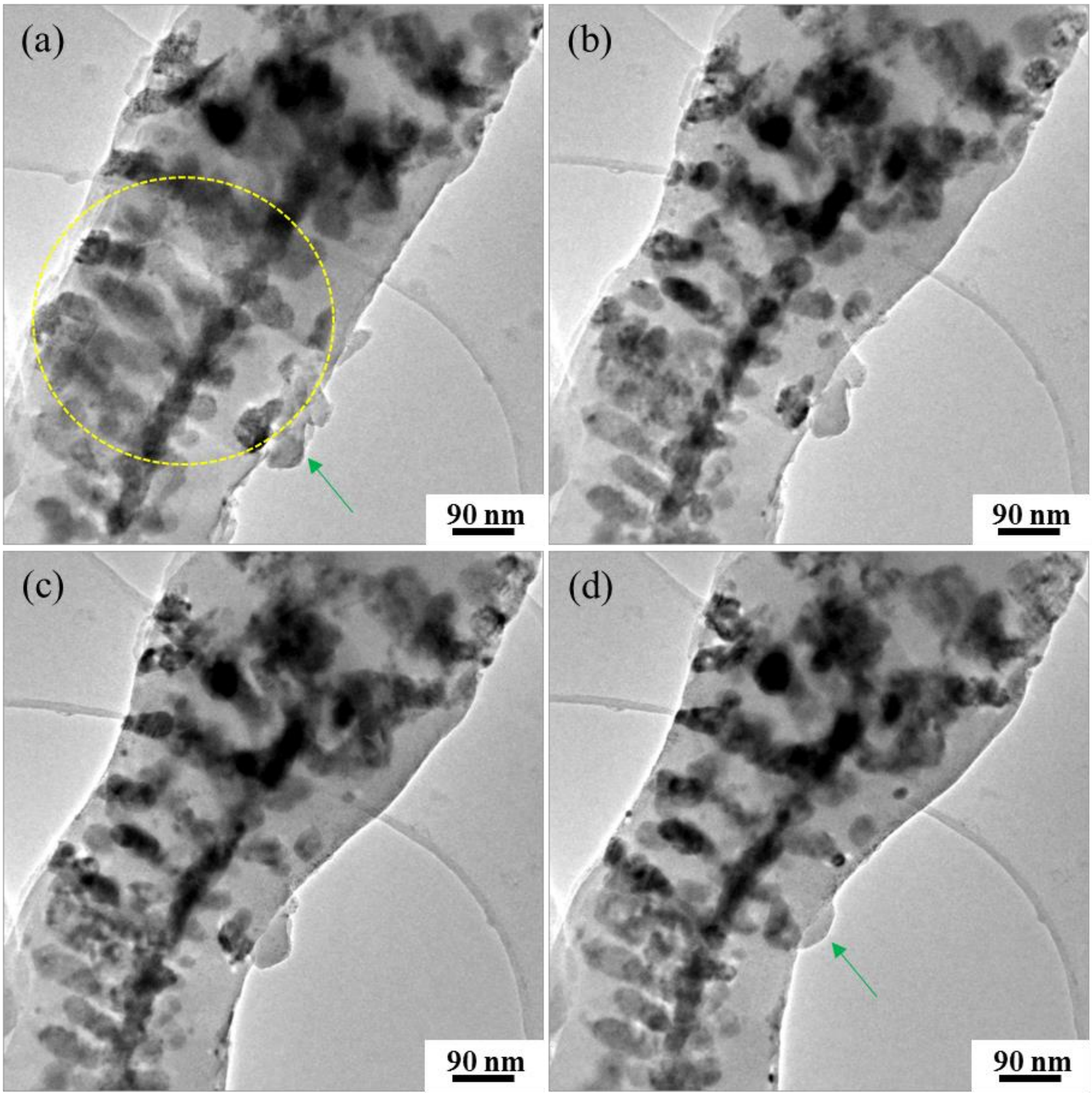

Figure 5-16: Time-series TEM images of the annealed CuNBS-A glass, (a) before, and (b-d) after 2 min, 4 min and 6 min electron irradiation. JEM TEM 3010 at 300 keV.

From the above figure, it is clear that increasing the irradiation time on the glass rod from 2 min to 4 min and then to 6 min did not cause significant changes to the embedded dendrite.

This gives proves the robustness of such structures under e-beam irradiation. Only two obvious effects of the irradiation can be seen: first, glass ablation at both edges of the rod being irradiated (yellow circle area in Fig. 5-16(a)), increases with increasing irradiation time. Second, a merging of the small pieces of glass fragments existing at the edge of the main glass rod as the irradiation time was increased (green arrows in Fig. 5-16(a) and 5-16(d)).

5.2.2 CuNBS-B glass

Low-Cu-doped sodium borosilicate (CuNBS-B) glass was also subjected to electron beam irradiation at 300 keV (TEM LaB_6) in order to give a comparison with the high-Cu-loaded sodium borosilicate glass (CuNBS-A). The irradiation process was performed via time-series irradiation.

A relatively thin glass fragment was selected for electron irradiation, as shown in Fig. 5-17(a). This fragment initially had no particles within it at all, and it was very clean. The electron beam was placed in the region indicated by the green spot in Fig. 5-17(a). The initial 2 min irradiation did not form any visible particles at the irradiated region (Fig. 5-17(b)). The next 2 min irradiation also did not form particles (Fig. 5-17(c)), and neither did the final 2 min irradiation, shown in Fig. 5-17(d)). The only significant effect of the electron beam irradiation was glass ablation at the irradiated regions (red arrows in Figs. 5-17(b-d)). In addition, a small piece attached to the glass fragment surface, indicated by the yellow arrow in Fig. 5-17(a), had gradually shrunk as the irradiation time increased until it had totally disappeared by the end of the irradiation (yellow arrows in Figs. 5-17(b-d)) due to merging with the original glass fragment.

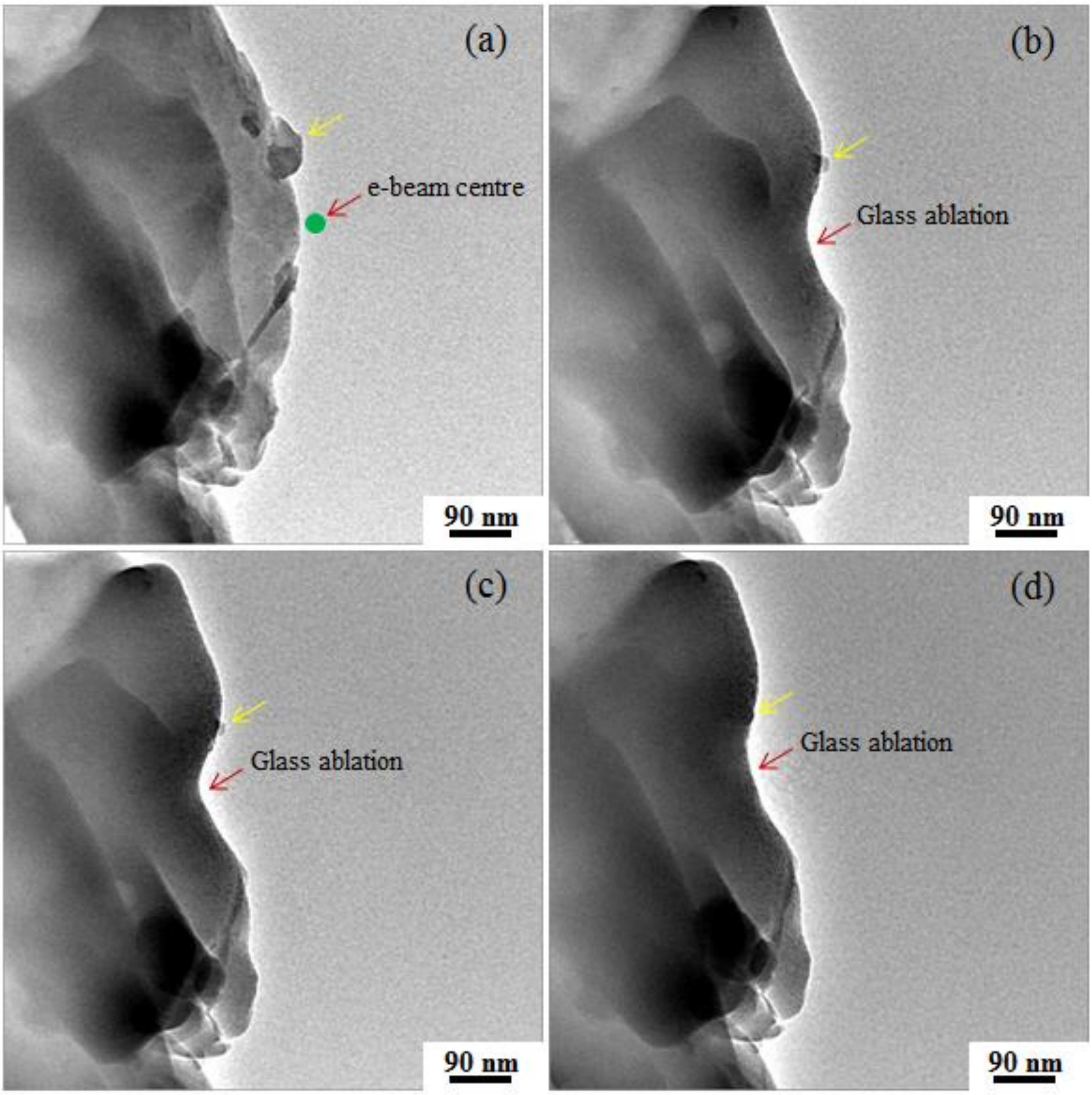

Figure 5-17: Time-series TEM images of a fragment of a CuNBS-B glass, (a) before, and (b-d) after 2 min, 4 min and 6 min of electron beam irradiation. JEM TEM 3010 at 300 keV.

A rod of this glass was also subjected to electron beam irradiation for an even longer time-series than the previous glass fragment shown in Fig. 5-17. This rod was thick and had a sharp edge, as shown in Fig. 5-18(a). The electron beam was directed at this sharp edge for 3 min, 6 min and 9 min. Even with such prolonged irradiation, no visible Cu particles were formed here either, although a glass ablation was a significant effect of e-beam irradiation

(Fig. 5-18(b-d)) and also a carbon film ablation that occurred at 9 min irradiation (the red arrow in Fig. 5-18(d)).

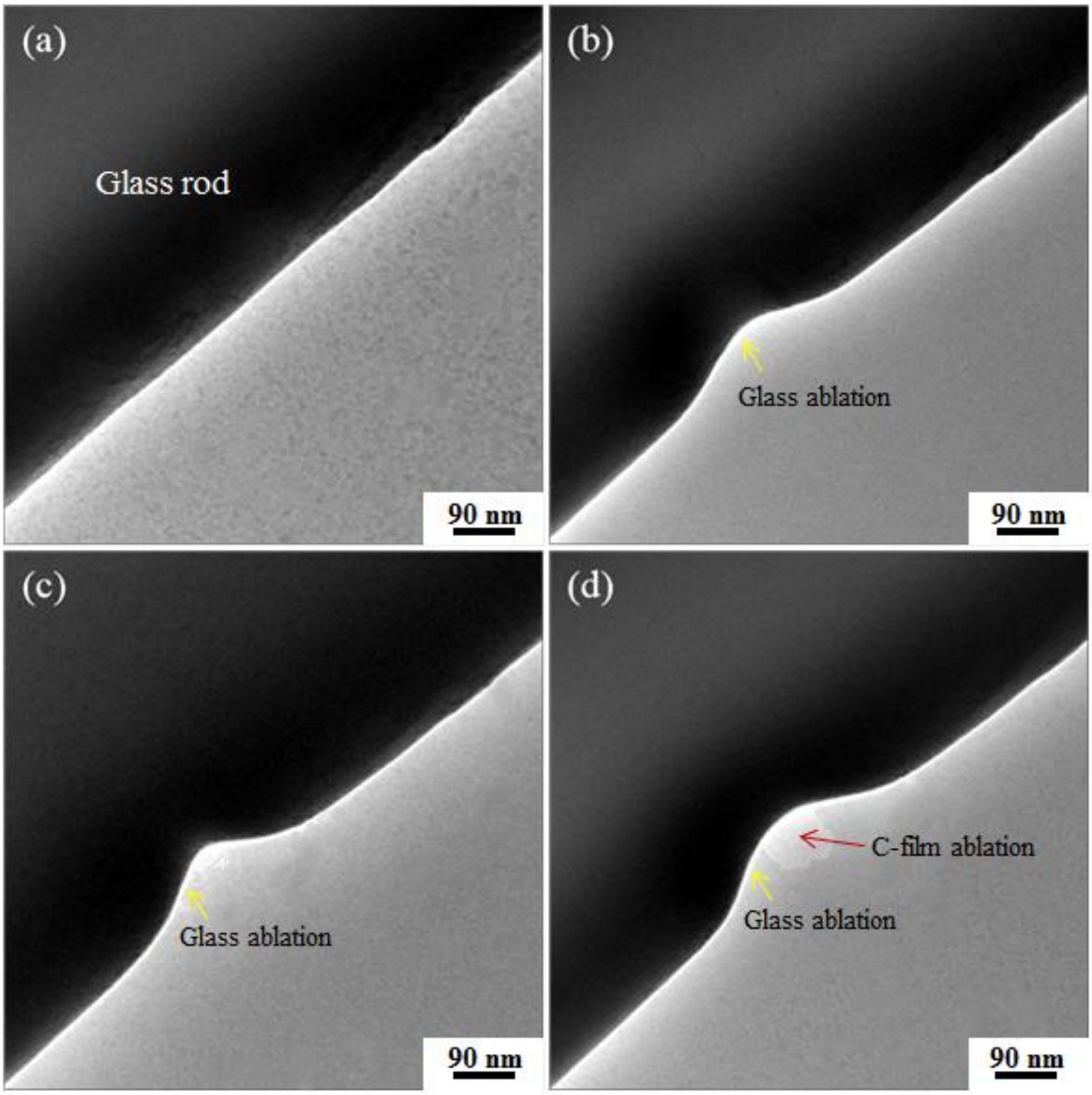

Figure 5-18: Time-series TEM images of a rod of CuNBS-B glass, (a) before, and (b-d) after 3 min, 6 min and 9 min electron beam irradiation. JEM TEM 3010 at 300 keV.

5.3 Summary

The formation of Cu nanoparticles in glass was induced using electron irradiation through transmission electron microscopy at energies of 200-300 keV. Two types of Cu borosilicate glass, one with high and another with low Cu loading were tested. The formation of Cu nanoparticles in a variety of shapes and sizes using different irradiation conditions was achieved. Electron energy loss spectroscopy analysis combined with high-resolution transmission electron microscopy imaging confirmed the irradiation-induced precipitated nanoparticles as metallic, while furnace annealing of the glass triggered dendrite-shaped particles of copper oxide (Cu_2O) as confirmed via X-ray diffraction (XRD). Various patterns of nanoparticle rings and chains under focused electron beam irradiation were also created and line-scan irradiation was successfully achieved. Conclusively, electron beam patterning of Cu-loaded glass is a promising route to precipitate nm-sized Cu particles in glass.

5.4 References

Ahn C C, Krivanek O L, Burgner R P, Disko M M and Swann P R 1983 Electron energy loss spectroscopy Atlas (ASU HREM Facility and Gatan, Inc.,).

Almeida J M P, De Boni L, Avansi W, Ribeiro C, Longo E, Hernandes A C and Mendonca C R 2012 Generation of copper nanoparticles induced by fs-laser irradiation in borosilicate glass *Opt. Exp.* **20**, 15106-15113.

Hébert C, Alkauskas A, Löffler S, Jouffrey B and Schattschneider P 2011 Capturing EELS in the reciprocal space *Eur. Phys. J. Appl. Phys.* **54**, 33510-7.

Ito Y, Jain H and Williams D B 1999 Electron-beam induced growth of Cu nanoparticles in silica glass matrix *Appl. Phys. Lett.* **75**, 3793-3795.

Jiang N, Hembree G G, Spence J C H, Qiu J, Garcia de Abajo F J and Silcox J 2003 Nanoring formation by direct-write inorganic electron-beam lithography *Appl. Phys. Lett.* **83**, 551-553.

Long N J and Petford-Long A K 1986 In-situ electron-beam-induced reduction of CuO: A study of phase transformations in cupric oxide *Ultramicroscopy* **20**, 151-159.

Teng Y, Qian B, Jiang N, Liu Y, Luo F, Ye S, Zhou J, Zhu B, Zeng H and Qiu J 2010 Light and heat driven precipitation of copper nanoparticles inside Cu^{2+}-doped borate glasses *Chem. Phys. Lett.* **485**, 91-94.

Yang G, Cheng S, Li C, Zhong J, Ma C, Wang Z and Xiang W 2014 Investigation of the oxidation states of Cu additive in colored borosilicate glasses by electron energy loss spectroscopy *J. Appl. Phys.* **116**, 223707-6.

Chapter Six

Electron irradiation of silver-doped borosilicate glass

6.1 Introduction

Despite the fact that a variety of methods such as standard annealing processes, sol-gel preparation, ion-exchange by diffusion, ion implantation and irradiation with lasers have been used to prepare Ag nanoparticles in various types of oxide glass, electron beam irradiation has only rarely been reported for this glass-metal system.

In this research, electron beam irradiation was exploited to irradiate two Ag-doped glasses as listed in table 6-1 and given acronyms of NBS-AC and KBS-ACFN.

Table 6-1: Compositions of Ag-doped borosilicate glass (mol.%)

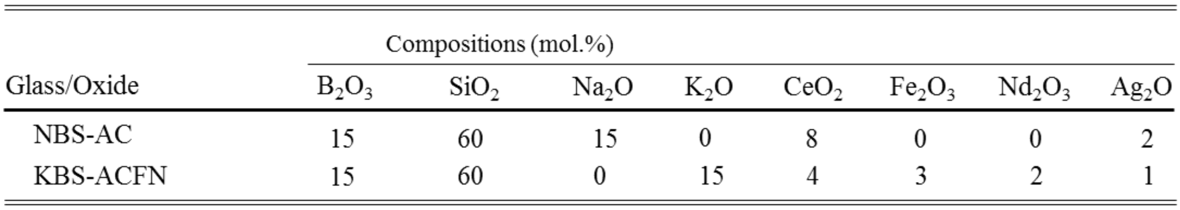

	Compositions (mol.%)							
Glass/Oxide	B_2O_3	SiO_2	Na_2O	K_2O	CeO_2	Fe_2O_3	Nd_2O_3	Ag_2O
NBS-AC	15	60	15	0	8	0	0	2
KBS-ACFN	15	60	0	15	4	3	2	1

Initially, KBS-ACFN glass was available from the previous study of [Yang *et al.*, 2010], where it was used for the purpose of vitrification of radionuclides. In this research work, however, this glass was subjected to e-beam irradiation in order to study precipitation and also to perform nanoscale patterning via line-scan irradiation. In addition, a new similar glass was produced with a few modifications such as (i) eliminating the un-justified elements (Fe and Nd) which existed in the KBS-ACFN glass, (ii) doubling the percentage of the target elements of Ag and Ce and (iii) exchanging K with Na in order to be consistent with the other types of glass produced in this research work.

The NBS-AC glass, meanwhile, was prepared by using the raw materials of boric acid (H_3BO_3, purity > 99.5%), silica sand (SiO_2, purity ~ 99.5%), sodium carbonate (Na_2CO_3, purity ~ 99.1%), cerium oxide (CeO_2, purity 99.9%) and silver nitrate ($AgNO_3$, purity 99.8%). The initial melting temperature (T_m) of 1400 ºC was reduced to 1350 ºC after 5 h due to the fluidity. The CeO_2 and H_3BO_3 were sourced from Acros Organics and Sigma-Aldrich, respectively, $AgNO_3$ was sourced from Fisher Scientific, while Na_2CO_3 and SiO_2 were sourced from Glassworks Services Ltd, Doncaster.

Two kinds of TEMs were used in this research: (i) a JEOL JEM 2010F field emission gun (FEG) at 200 keV and (ii) a JEOL JEM 3010 LaB_6 thermal filament at 300 keV. The experiments conducted here used the stationary irradiation mode with electron beam diameters >> 100 nm, as well as the line-scan irradiation mode to demonstrate patterning. The HRTEM images obtained in the JEOL JEM 3010 were useful to identify the nature of the precipitated Ag nanoparticles.

6.2 Stationary electron beam irradiation mode

A non-moving electron beam was used to perform irradiation via a stationary electron beam. In this mode of irradiation, a wide e-beam at the largest condenser aperture and spot size resulted in the occurrence of both phase separation and particle formation at the same time.

6.2.1 The NBS-AC glass

The experiment was started by selecting a fragment of this glass to conduct the stationary irradiation via time-series. Two irradiation conditions were used. The first was to irradiate the fragment at the default irradiation conditions (largest condenser aperture and spot size 1) for about 4 min, 8 min and 12 min, as shown in Fig. 6-1.

The initial state of this fragment was homogeneous (Fig. 6-1(a)) like all the other types of glass prepared in this research work by the quenching method. What can be seen from the field-of-view in this figure is that the fragment had a sharp peak and also two sharp edges giving the fragment a mount-like shape. In order to perform the irradiation process, the electron beam was positioned in such a way that it covered this region. The first 4 min of electron irradiation at rest resulted in modifications in the glass at the region of irradiation, as can be seen in Fig. 6-1(b).

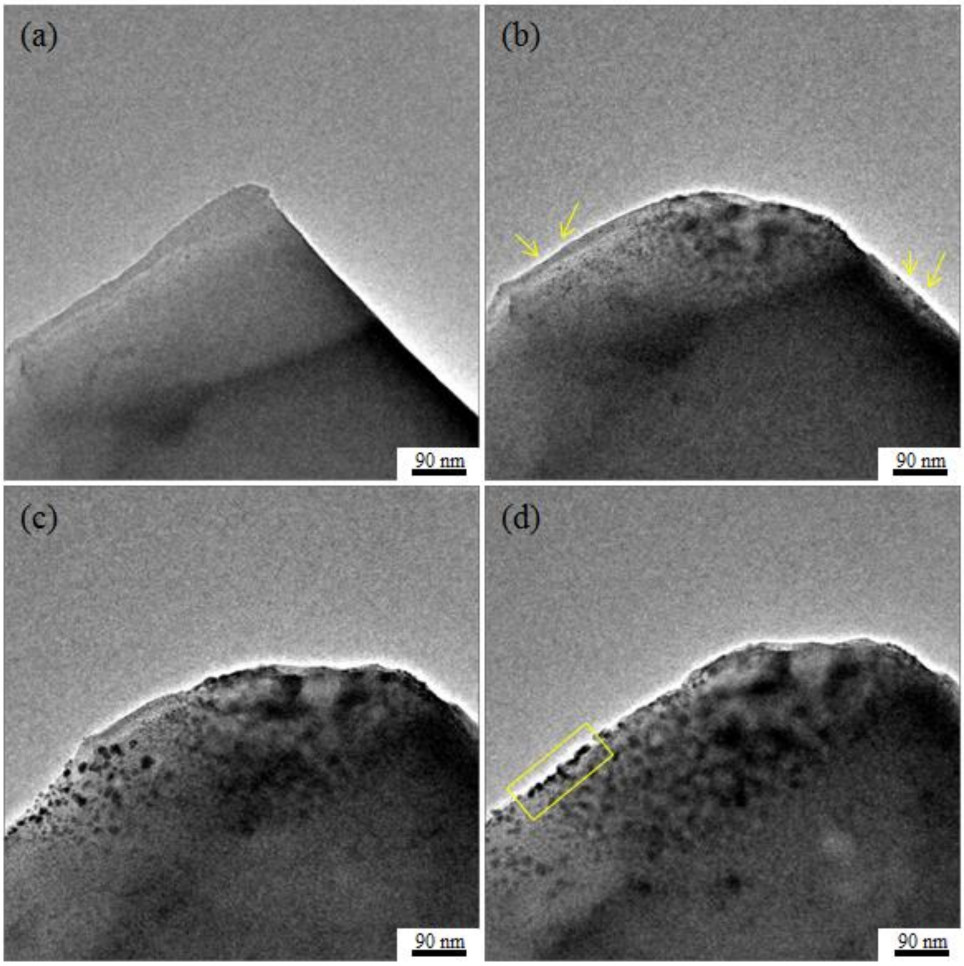

Figure 6-1: Time series TEM images of a NBS-AC glass fragment, (a) before and (b-d) after 4 min, 8 min and 12 min of electron irradiation, respectively. The occurrence of both amorphous phase separation and nanoparticle formation is obvious. JEM TEM 3010 at 300 keV.

Under the impact of the e-beam irradiation, amorphous phase separation into black and white regions occurred in the e-beam centre in addition to the formation of tiny particles at both sides of this region, as indicated by yellow arrows in Fig. 6-1(b); these nanoparticles were relatively small (~ 1-3 nm). The next 4 min of irradiation resulted in more modifications in the phase separated region and an increase in the size of the nanoparticles up to about 10 nm (Fig. 6-1(c)). The final 4 min of irradiation did not result in a significant increase in the size of the nanoparticles, but showed more modification in the phase separated region. At this stage, some of the nanoparticles moved to the glass edge and were arranged in an ordered manner (indicated by yellow rectangle in Fig. 6-1(d)). As a side effect of the electron beam irradiation, the transformation of the sharp glass corner into a rounded shape is very obvious (Fig. 6-1(b-d)).

The second irradiation was performed at a maximum current density with the condenser aperture removed (Fig. 6-2). The same region of irradiation that was shown in Fig. 6-1(d) was irradiated for about 2 min in this experiment. The influence of the high level irradiation is very obvious. At the region of irradiation, amorphous droplets of various sizes were formed, indicated by the red-dashed circles in Figs. 6-2(a-c). In addition, the small particles initially formed at the first irradiation condition, and shown in Figs. 6-1(b-d), were now distributed in-homogeneously at both the glass edge and also on the carbon film due to nucleation and growth, indicated by the green rectangle in Fig. 6-2(a) and the yellow arrows in Fig. 6-2(b) and Fig. 6-2(c). These nanoparticles were of different sizes, with some of them exhibiting faceted sharp surfaces. The HRTEM image of a few particles is shown in Fig. 6-2(d), proving the crystallinity of these nanoparticles (indicated by numbers 1 to 4).

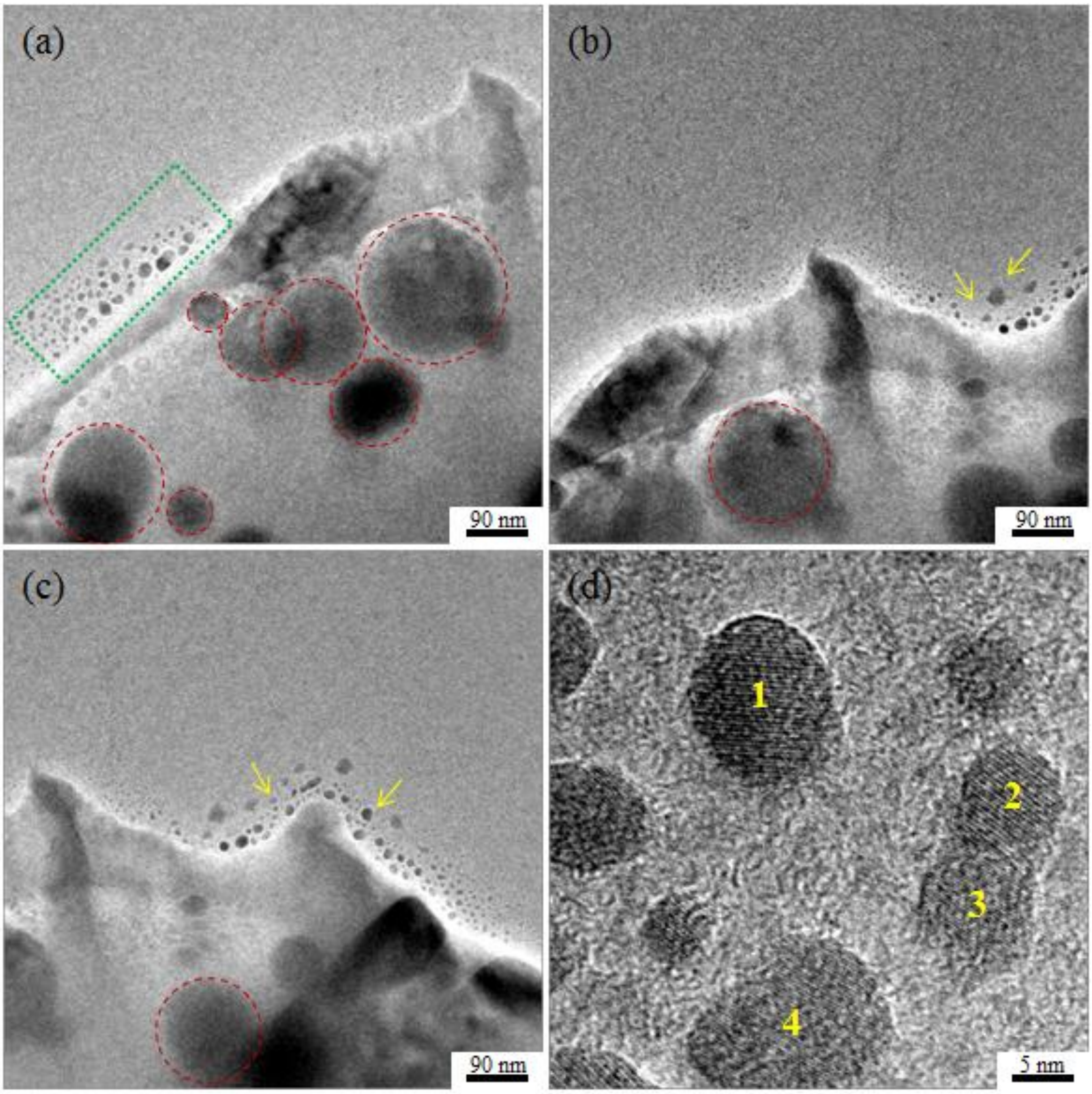

Figure 6-2: High level irradiation resulted in the formation of large amorphous droplets inside the glass fragment and small nanoparticles in the carbon film close to the glass edge (a-c). (d) HRTEM image showing a few nanoparticles on the carbon film of well-seen lattice fringes. JEM TEM 3010 at 300 keV.

Another fragment of this glass with an aspect ratio equal to ~ 710 nm: 535 nm was irradiated after removing the condenser aperture to obtain maximum current density. A wide electron beam with a diameter identical to that of the fragment was used in the irradiation. Figure 6-3 shows a fragment of this glass prior to the irradiation in Fig. 6-3(a), and after time-series electron irradiation (Fig. 6-3(b-d)).

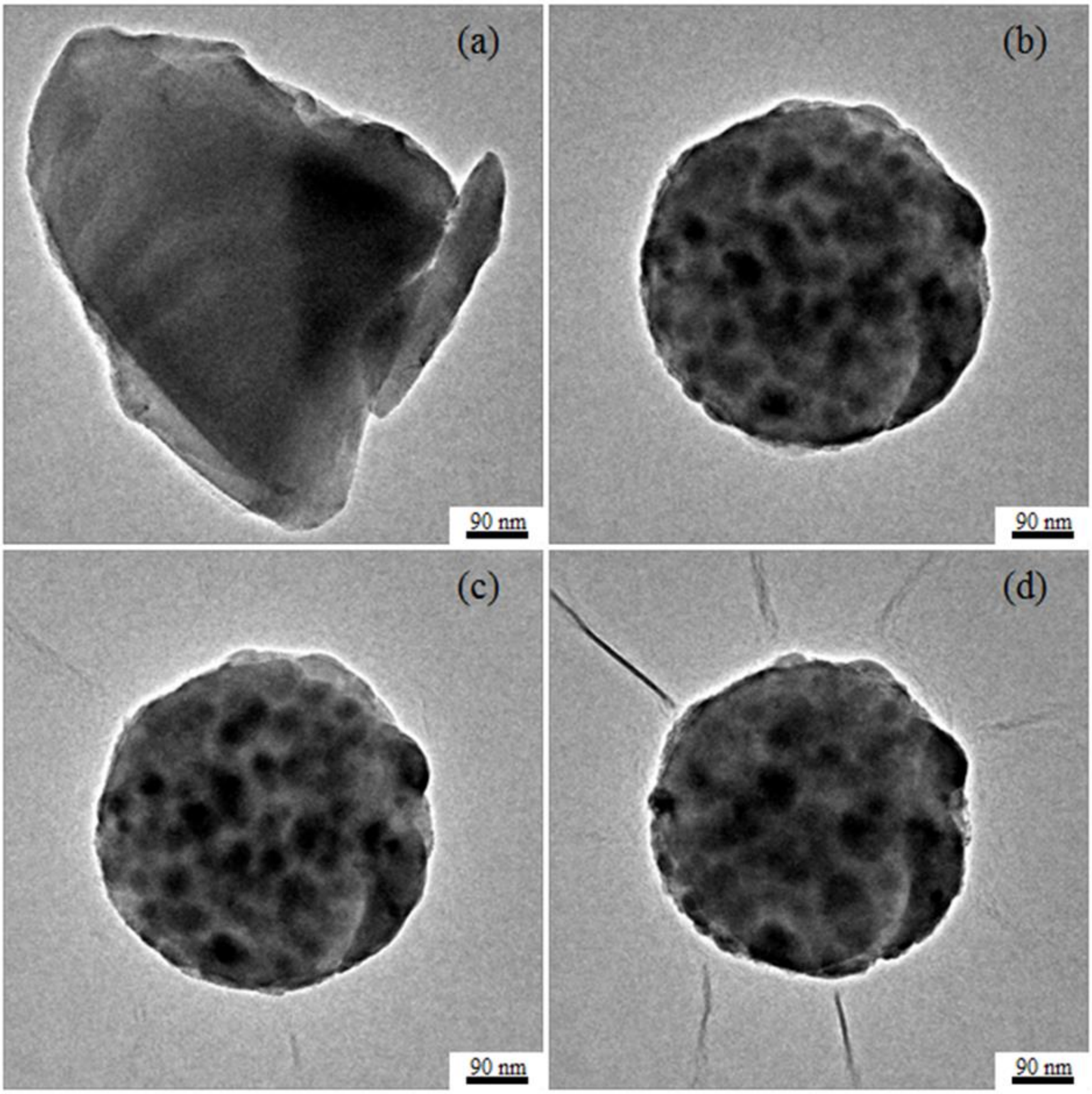

Figure 6-3: TEM images of a NBS-AC glass fragment, (a) before and (b-d) after 2 min, 4 min and 6 min electron irradiation, respectively. JEM TEM 3010 at 300 keV.

The NBS-AC glass fragment was homogeneous and clean before starting the electron irradiation process as shown in Fig. 6-3(a). Changes occurred in the fragment, however, after the glass was exposed to electron irradiation for about 2 min. The initially homogeneous glass was separated into black and white regions, as shown in Fig. 6-3(b). Transformation of the original glass fragment into a ball-shaped particle of diameter of ~ 508 nm was also observed. After a further 2 min of irradiation, the black and white regions were relatively stable under e-beam irradiation, although the sizes of the white regions increased slightly, as shown in Fig. 6-3(c). A slight shrinkage in the diameter of the ball-shaped particle to ~ 495 nm was also observed. An increase in the sizes of the white regions and a decrease in the sizes of the black regions occurred after the final 2 min irradiation, as shown in Fig. 6-3(d), along with further shrinkage in the diameter of the ball-shaped particle to ~ 471 nm. According to the Z-contrast, the black regions may have high average Z composition with the white regions have low average Z composition. As can be seen in Fig. 6-3(c) and Fig. 6-3(d), the presence of a few constriction lines in the carbon film give an indication of the carbon film damage.

Figure 6-4 shows a rod of this glass irradiated after removing the condenser aperture. The initial glass rod had a relatively sharp and thick edge, as shown in Fig. 6-4(a). An electron beam of diameter of ~ 500 nm was used for irradiation and the imprint is shown in Fig. 6-4(b). Another effect is observed here. Irradiation for about 2 min resulted in the formation of circular nanoparticles with a diameter of about 1-10 nm. These nanoparticles were surrounded by a region of amorphous phase separation (Fig. 6-4(b)). A further 2 min irradiation for the same region did not lead to any further changes in the nanoparticles, but obvious modifications in the phase separated region can be seen, as shown in Fig. 6-4(c). The red lines shown in Fig. 6-4(b) and Fig. 6-4(c) are drawn for the purpose of showing the effect of irradiation-induced glass ablation. These lines represent the original edge of the glass rod before electron irradiation. The distance between these lines and the glass material increases as the irradiation time increases, indicating that more glass ablation has occurred with longer exposure to the electron beam.

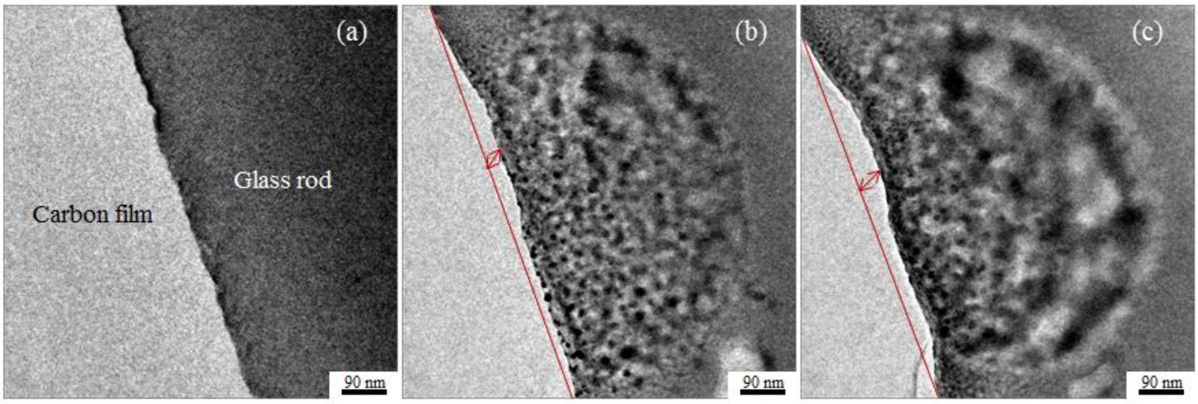

Figure 6-4: TEM images of a rod of a NBS-AC glass, (a) before irradiation and (b, c) after 2 min and a further 2 min irradiation, respectively. The red lines in (b) and (c) represent the original edge of the glass rod. The formed nanoparticles are surrounded by a region where phase separation has occurred. JEM TEM 3010 at 300 keV.

In order to analyse the irradiated region chemically, energy dispersive X-ray (EDX) spectra were acquired and are shown in Fig. 6-5. Part (a) of this figure shows the EDX spectrum from the white phase of the irradiated region. Two major peaks of Si and O can be seen in addition to the peaks of both Ag and Ce. Due to the high mobility of Na under electron irradiation, there is a very weak signal for this element. Part (b) of this figure, however, shows the EDX spectrum from the dark phase of the irradiated region. What can be noticed from this spectrum is the enhancement of the signals of both Ag and Ce in comparison to that seen in Fig. 6-5(a). This gives an indication of the enrichment of this phase with both Ag and Ce.

Furthermore, the reason that there is no signal for B in the spectra is because of its low atomic number and therefore it cannot be detected by the EDX detector. Also, the Al signal is from the mullite crucible used during the glass melting process.

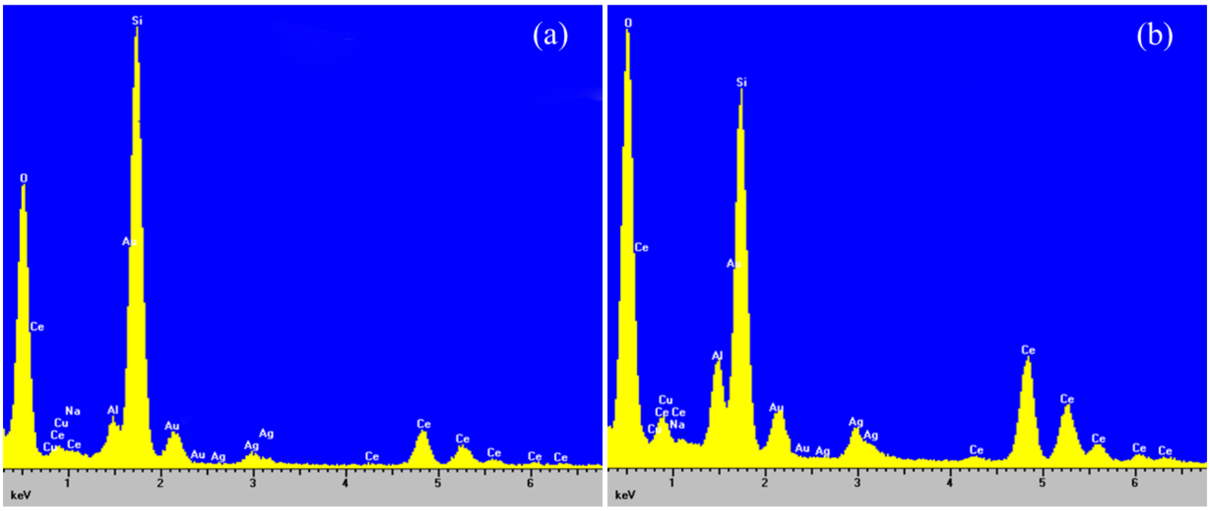

Figure 6-5: Energy dispersive X-ray (EDX) spectra of, (a) the white phase and (b) the dark phase of the irradiated region.

6.2.2 The KBS-ACFN glass

A rod of the KBS-ACFN glass has been selected for a relatively prolonged irradiation using the stationary mode as shown in Fig. 6-6. The electron beam was placed in the region of the glass rod indicated by the yellow-dashed circle in Fig. 6-6(a). After ~ 15 min of electron beam irradiation, modifications had occurred in the region of the glass rod which was under irradiation. Dark and bright regions were formed indicating the occurrence of amorphous phase separation. These were surrounded by nanoparticles of few nanometres diameter, which was the opposite of what was observed in Fig. 6-4. Damage in the carbon support film was observed after irradiation as shown by the lower black arrow in Fig. 6-6(b).

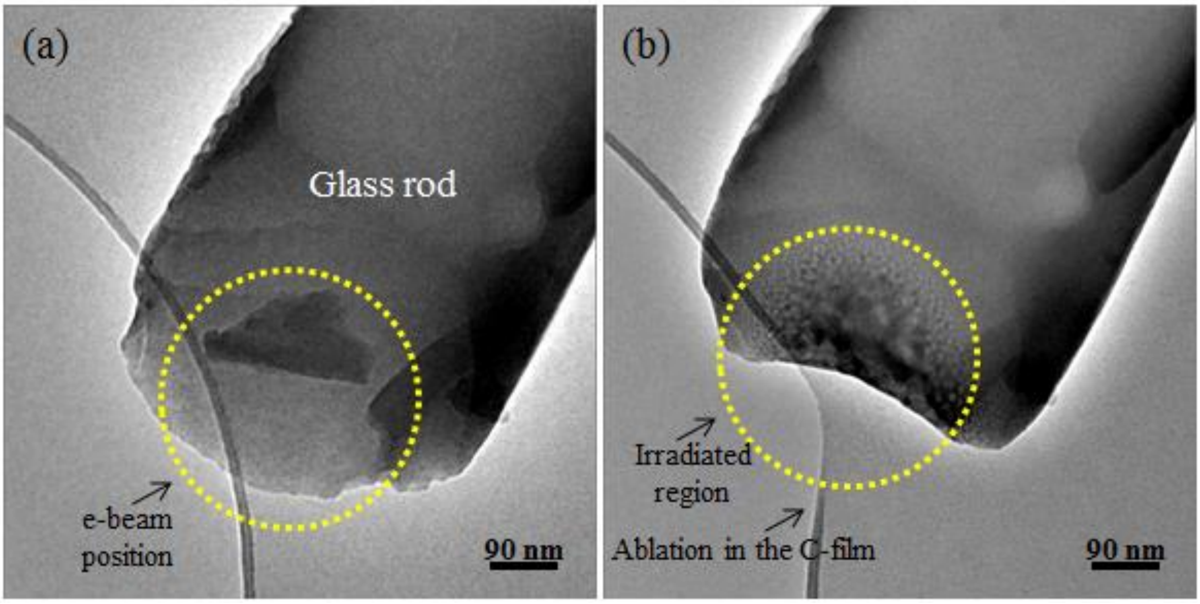

Figure 6-6: TEM images of a KBS-ACFN glass rod, (a) before and (b) after ~ 15 min of electron irradiation. The phase separation region is surrounded by nanoparticles of few nanometres diameter. JEM TEM 3010 at 300 keV.

A fragment of this glass with a mount-like shape was also analysed in the FEG TEM at 200 keV, as shown in Fig. 6-7(a). There were a few black dots visible in the initial glass fragment, which might have been formed at the early stage of imaging. In order to start the irradiation, the electron beam was directed for about 4 min at the top region of this fragment, as indicated by the black circle in Fig. 6-7(a). This resulted in a partial glass ablation along with the formation of a ring structure. Circular nanoparticles of about 7 nm in diameter were found inside the ring, as shown in Fig. 6-7(b). The distance between these NPs (indicated by yellow arrows in Fig. 6-7(b)) was found to be about 9 nm. The dark contrast at the edge of the ring indicates possible alkali migration. Further irradiation, however, did not reveal the formation of any new particles, but instead black and bright regions occurred, indicating an amorphous phase separation, as shown in Fig. 6-7(c). The last stage of the irradiation shown in Fig. 6-7(d) resulted in an increase in the size of the phase separation.

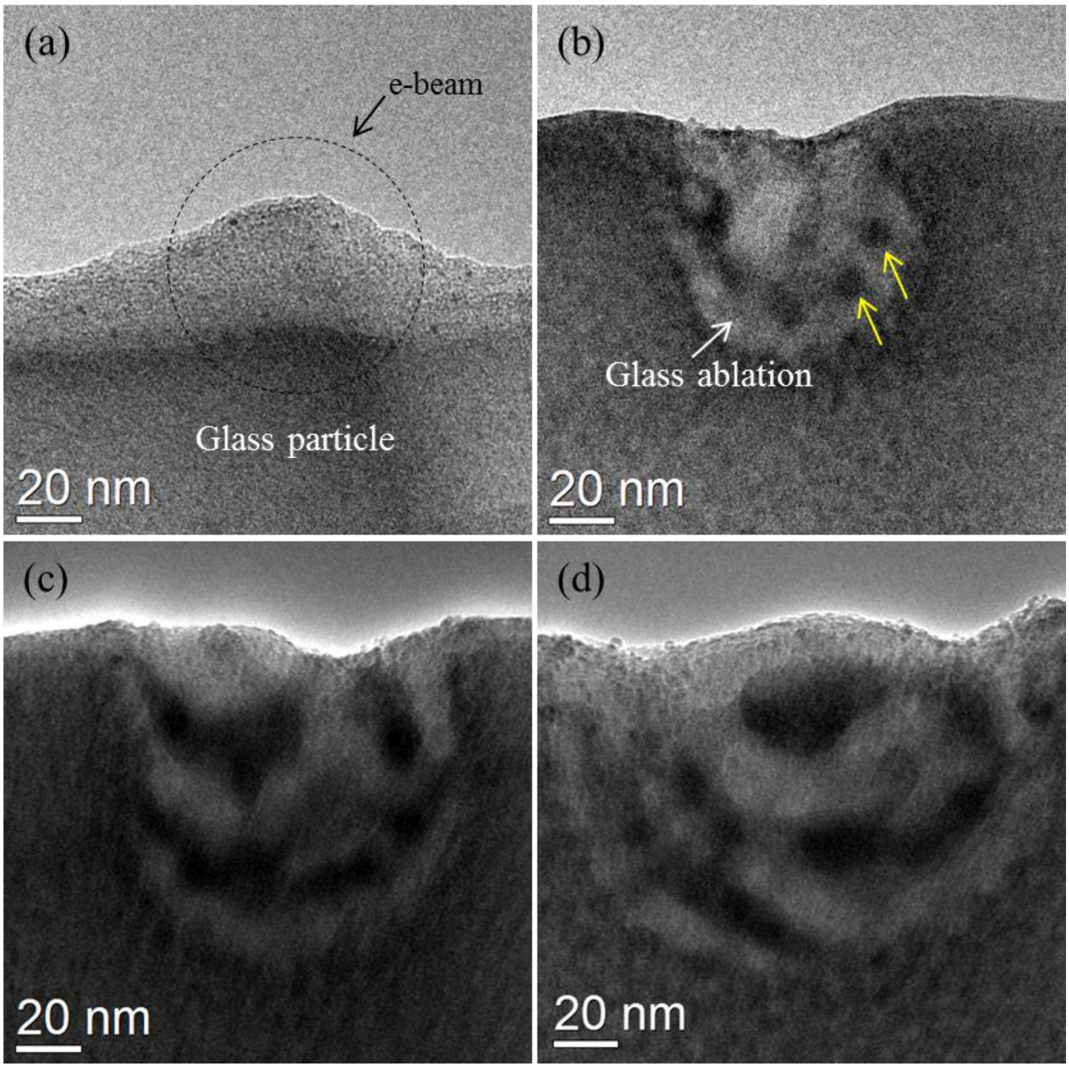

Figure 6-7: TEM images showing electron beam irradiation-induced nanoparticle formation and amorphous phase separation in a fragment of the KBS-ACFN glass. JEM TEM 2010F at 200 keV.

6.3 Line-scan electron beam irradiation mode

Irradiation in line-scan mode was conducted, as previously reported, by scanning the electron beam manually across the glass material and achieving pattern structures. In order to perform this experiment, typical rods out of hundreds of particles distributed on the carbon support film in a TEM specimen were found to be suitable for line-scan irradiation, in particular those of small width in order to see both the start and finish points of the scanned line.

6.3.1 The NBS-AC glass

The first series of line-scan irradiation was conducted on a rod of the NBS-AC glass. The line-scan irradiation is summarised in Fig. 6-8. The electron beam traversed horizontally across the glass rod (Fig. 6-8(a)) from its middle region, as indicated by the red arrows shown in Fig. 6-8(b). During this process, the electron beam was stopped at each scan movement for about 10 sec. A ~ 400 nm long and ~ 90 nm wide line was therefore drawn. In addition, and as was commonly observed during electron beam irradiation in the rod experiments, when the electron beam was positioned at the edge of the rod, partial glass ablation occurred at the first 10 sec stopping point of the electron beam, i.e. at the point at which it entered the rod. The detail of the line is as follows: two lines of circular nanoparticles of diameters of about 7 nm were formed at both sides of the electron beam centre, along with glass matrix ablation at the centre of the electron beam. Smaller sized nanoparticles were found further away from the centre of the beam.

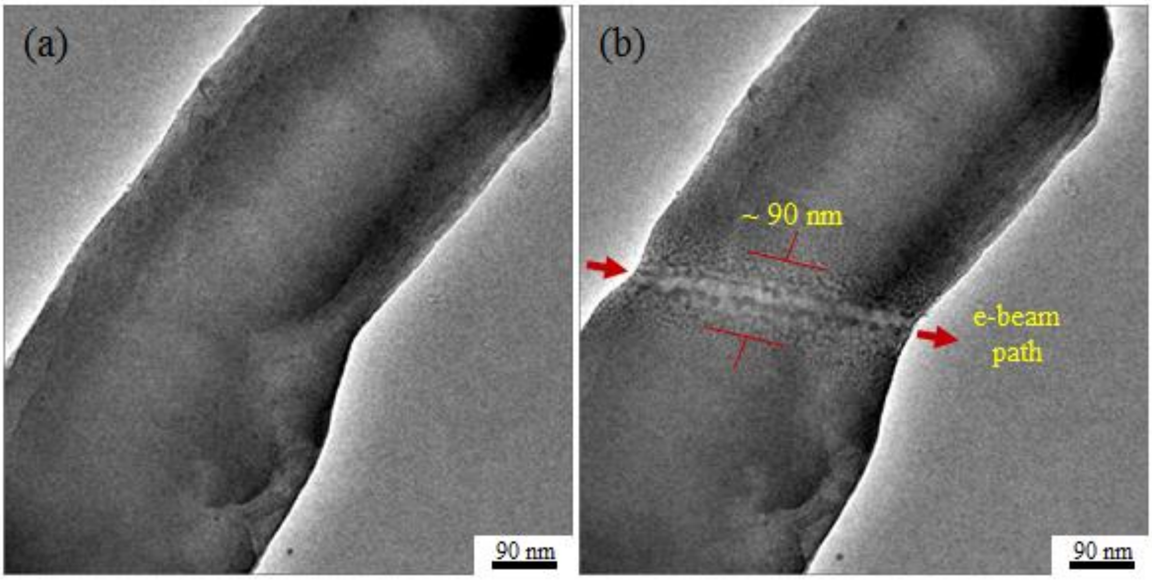

Figure 6-8: TEM images showing a rod of a NBS-AC glass, (a) before and (b) after line-scan irradiation when scanning the electron beam horizontally through the rod. JEM TEM 3010 at 300 keV.

6.3.2 The KBS-ACFN glass

A relatively thin and tall rod of KBS-ACFN glass was selected to perform the line-scan irradiation (Fig. 6-9(a)). The width of this rod was about 230 nm. Initially, the rod had been irradiated from its lower region by scanning the electron beam click-by-click horizontally through it without any stopping points within the rod (shown by the yellow arrows in Fig. 6-9(b)).

The produced pattern had a width of ~ 130 nm. Furthermore, the initial width of the glass rod of ~ 230 nm, which now represented the pattern length, had been reduced to ~ 180 nm due to electron beam induced glass ablation, which was visible at both the entrance and the exit positions of the electron beam. It is possible that electron beam irradiation induced amorphous phase separation within its path, as can be seen in Fig. 6-9(b).

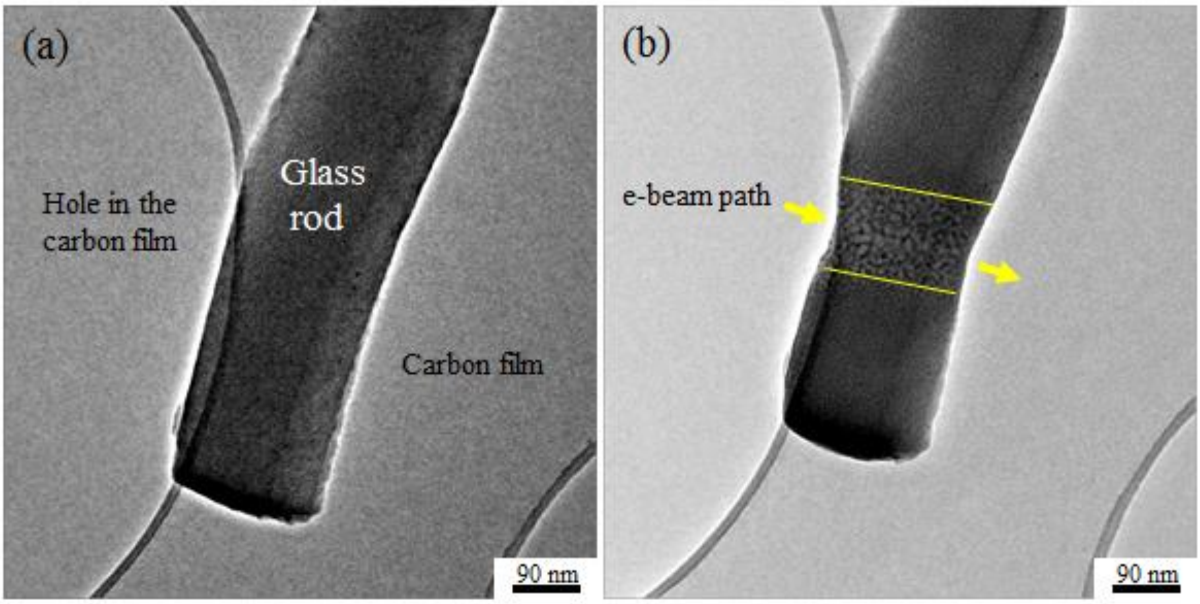

Figure 6-9: TEM images showing a rod of KBS-ACFN glass, (a) before and (b) after line-scan irradiation without stopping the electron beam on the glass rod. JEM TEM 3010 at 300 keV.

The same rod was irradiated from its middle region by scanning the electron beam horizontally across this region. Here, at each scan step, the electron beam was stopped for about 15 sec. The drawn line was ~ 180 nm long and ~ 190 nm wide. The line-scan irradiation is detailed in Fig. 6-10 and Fig. 6-10(b) shows the synchronous occurrence of precipitation and phase separation in the line-scan region. Smaller nanoparticles of 1-2 nm in size were also found at either side of the electron beam edges. Furthermore, possible glass ablation can also be seen in the irradiated region.

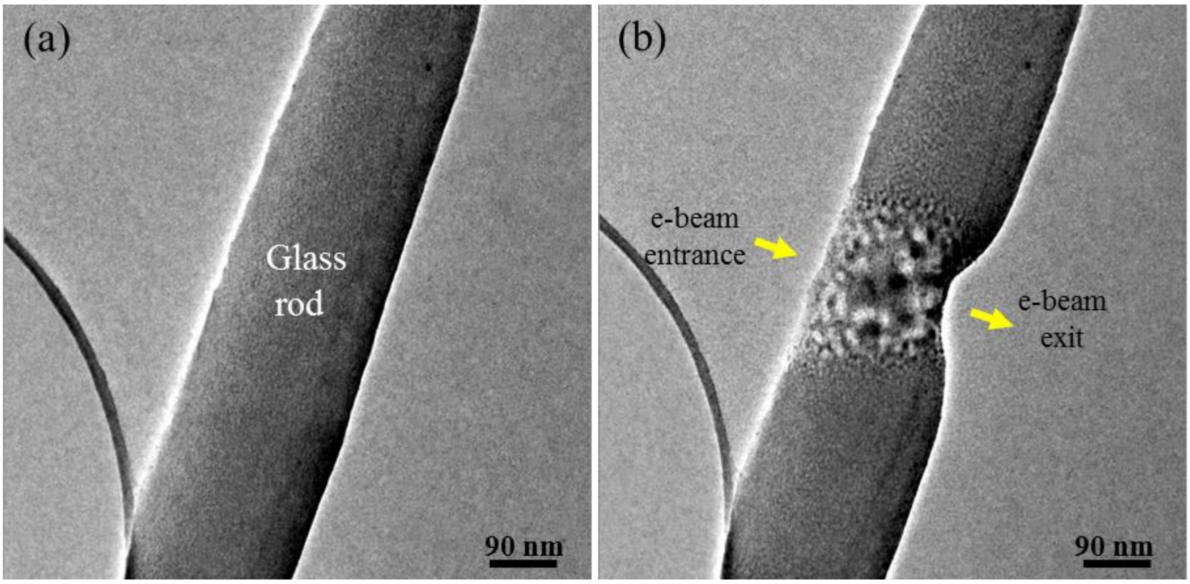

Figure 6-10: TEM images showing a rod of a KBS-ACFN glass, (a) before and (b) after line-scan irradiation. The electron beam was stopped for about 15 sec on the glass rod for each scan step. JEM TEM 3010 at 300 keV.

The region of irradiation in Fig. 6-10(b) was photographed at higher magnifications and these are reproduced in Fig. 6-11. The images shown in Figs. 6-11(a-c) reveal the formation of small nanoparticles of ~ 1-2 nm in diameter on the carbon support film (indicated by red arrows in Fig. 6-11(a)) near the exit region of the electron beam, due to the mechanism of nucleation and growth. Furthermore, Fig. 6-11(d) shows a HRTEM image of a typical Ag nanoparticle from the region of irradiation inside the glass rod (due to inhomogeneous surface precipitation). This nanoparticle had sharp lattice fringes, and in order to identify the nature of the precipitated Ag particle, the d-spacing value was calculated to be 0.202 nm for the (200) plane, confirming that the precipitated Ag nanoparticle is metallic.

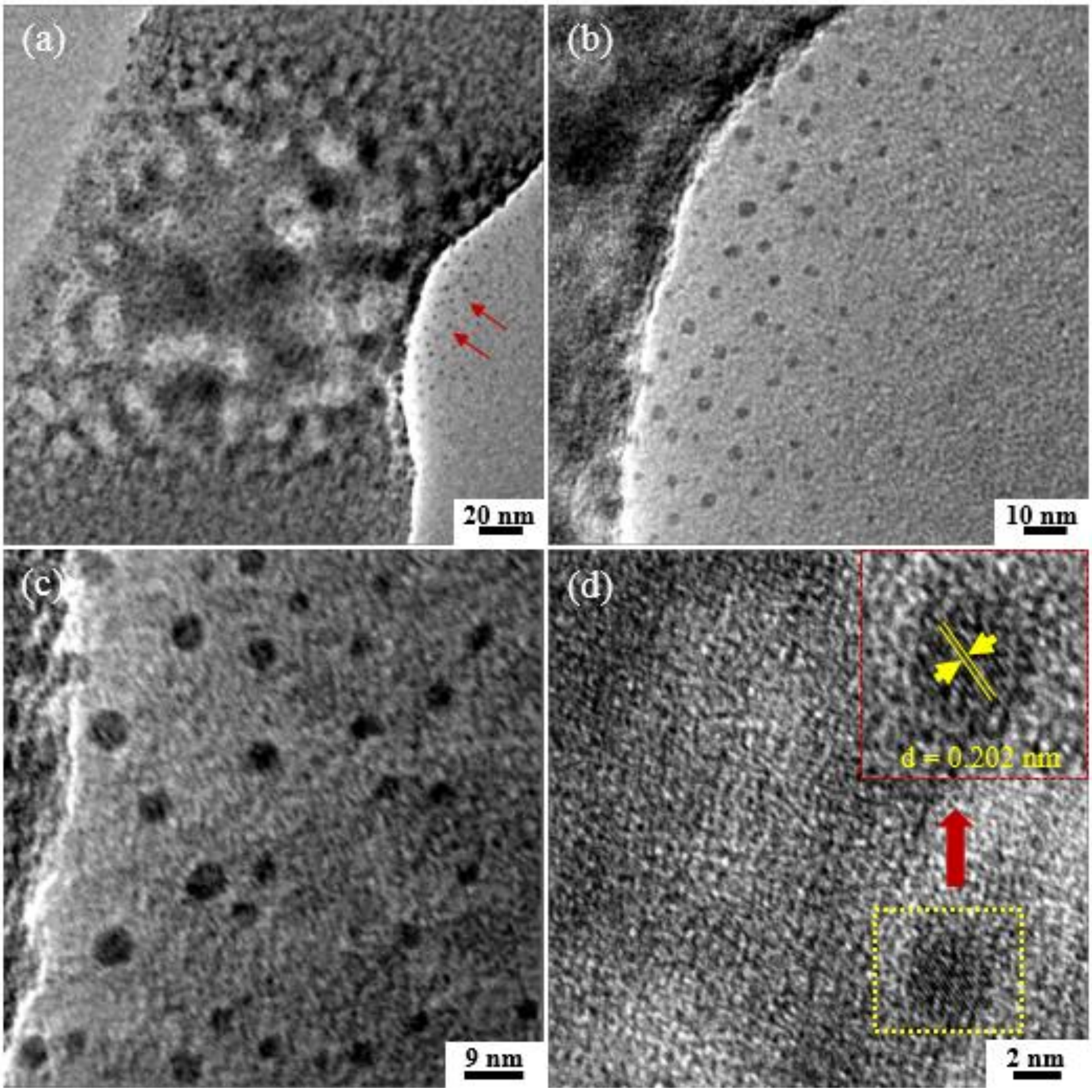

Figure 6-11: (a-c) high magnification TEM images of the irradiated region in Fig. 6-10(b) and (d) a HRTEM image showing a typical Ag NP. JEM TEM 3010 at 300 keV.

The phase separation attributed to the electron beam irradiation was also observed in the NLBS-CCZ glass shown in Fig. A5 and Fig. A6 in appendix I.

6.4 Summary

Two types of Ag-doped borosilicate glass were subjected to electron beam irradiation in transmission electron microscopy at energies of 200-300 keV. The effects of electron irradiation were studied via stationary irradiation and line-scan patterning. The concurrent occurrence of precipitation and phase separation was observed in these glasses upon irradiation. The precipitated Ag nanoparticles were confirmed as metallic via high-resolution transmission electron microscopy imaging. The transformation of sharp glass corners into rounded shapes was also observed. Pattern formation via line-scan irradiation was also conducted successfully.

6.5 References

Yang G, Cook S, Hand R J and Möbus G 2010 CeO_2 nano-precipitation in borosilicate glasses: A redox study using EELS *J. Euro. Ceram. Soc.* 30 831-838.

Chapter Seven

Electron irradiation-induced morphological transformations in various borosilicate glasses

7.1 Introduction

Live observations of changes in oxide glass under electron beam irradiation give an opportunity to discover novel kinds of nanoscale material transformations. This chapter displays the novel phenomena of electron irradiation-induced morphological transformations in different borosilicate glasses. These transformations include morphological changes of glass fragments either into perfect glass beads or glass rounding under e-beam irradiation. The former phenomenon was observed during the earlier electron irradiation-induced precipitation experiments in a high-Zn-loaded borosilicate (ZBS-A) and in a high-Cu alkali-borosilicate (CuNBS-A) glasses, discussed previously in chapters 4 and 5 of the thesis, respectively. The latter phenomenon was also observed in the earlier study of Ag-doped borosilicate (NBS-AC) glass, which was discussed in detail in chapter-6 in addition to the two other glass types selected for the deliberate electron irradiation-induced shape changes, as listed in table 7-1.

Table 7-1: Compositions of glass (mol.%)

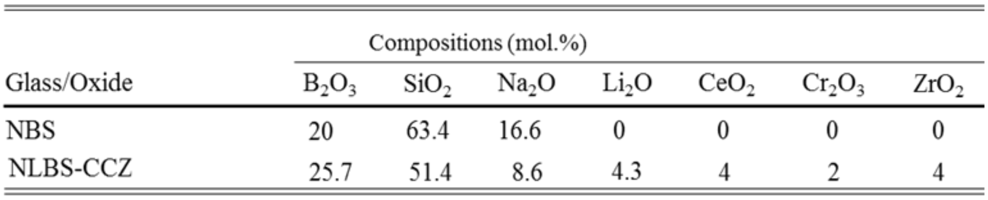

	Compositions (mol.%)						
Glass/Oxide	B_2O_3	SiO_2	Na_2O	Li_2O	CeO_2	Cr_2O_3	ZrO_2
NBS	20	63.4	16.6	0	0	0	0
NLBS-CCZ	25.7	51.4	8.6	4.3	4	2	4

The first glass investigated was a sodium borosilicate (NBS) glass, while the second glass was a sodium lithium borosilicate glass doped with extra dopant elements (CeO_2, Cr_2O_3 and ZrO_2) and given an acronym of NLBS-CCZ. This had already been prepared for the previous project and was used for that specific purpose. These glasses were re-used in this study for the completely new and different purposes mentioned above. The TEMs used to perform these experiments were: (i) JEOL JEM 3010 TEM at 300 keV (LaB_6 electron source), (ii) JEOL JEM 2010F TEM at 200 keV (FEG electron source) and (iii) PHILIPS 420 TEM at 120 keV (Tungsten electron source).

7.2 Electron irradiation-induced glass bead formation

One of the novelties of the current study is the sudden (rapid) transformation of a glass fragment into a particle of bead shape (spherical shape). This phenomenon has previously been reported just once before in a borosilicate glass [Möbus *et al.*, 2010] when a glass particle was spontaneously transformed into a bead (sphere) shape, but in this case no image was available of the glass fragment prior to this transformation. Here, a fragment of a high-Cu alkali-borosilicate (CuNBS-A) glass was photographed prior to the electron irradiation (Fig. 7-1). The electron beam was then converged to a diameter of less than 1 μ to cover the entire glass fragment. In just a few seconds (~ 2-3 sec), the glass fragment was entirely transformed into a spherically shaped particle as shown in Fig. 7-1(b).

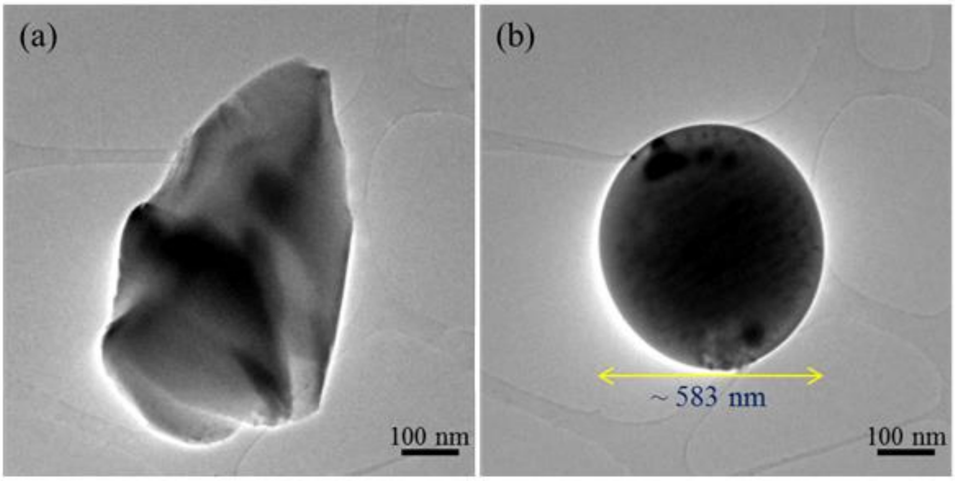

Figure 7-1: Transformation of a high-Cu alkali-borosilicate (CuNBS-A) glass fragment into a sphere shape within a few seconds of irradiation. JEM TEM 3010 at 300 keV.

Figure 7-2 shows another example of this phenomenon in the same glass. The diameters of the two glass balls shown in Fig. 7-2(a) and Fig. 7-2(b) are about 1 μ and 2 μ, respectively. The other obvious effects shown in the figure were previously discussed and detailed in chapter-5.

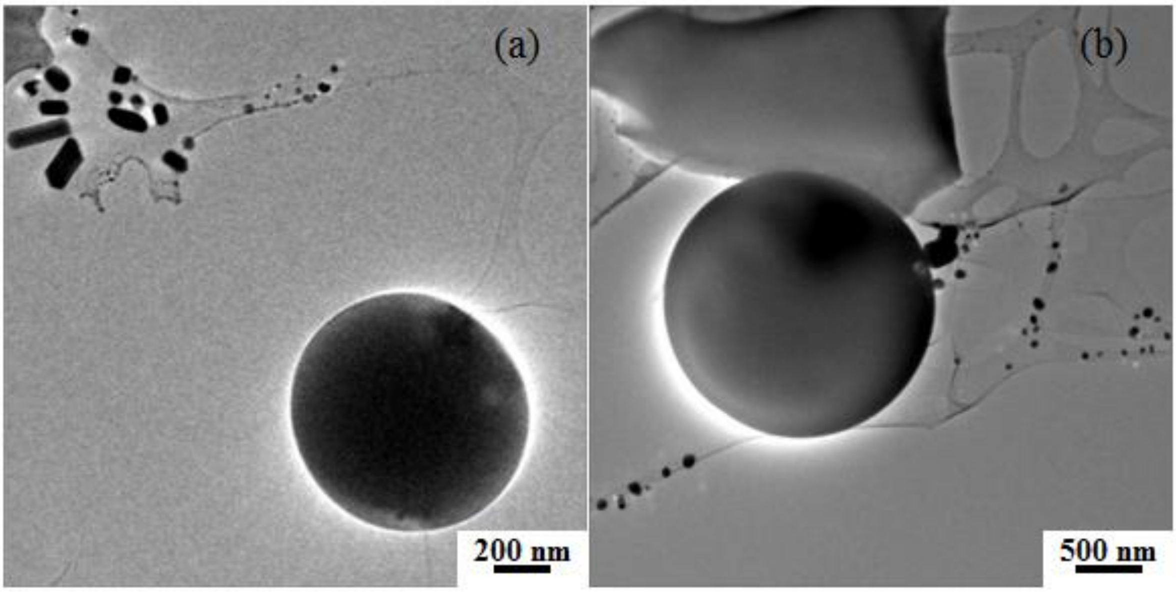

Figure 7-2: Formation of glass beads in a high-Cu alkali-borosilicate (CuNBS-A) glass under electron beam irradiation. JEM TEM 3010 at 300 keV.

A spontaneous transformation of a glass fragment into a full spherical shape was also observed in a high-Zn borosilicate (ZBS-A) glass, as shown in Fig. 7-3. This was observed by chance on the carbon film near an irradiated glass particle. Combination experiments using both electron beam irradiation and *in-situ* heating were being conducted on this glass when this observation was happened and, therefore, the reason for this transformation could either be the electron irradiation or the effects of increased temperature due to the heating experiment. It is possible to exclude the latter effect in the explanation of this transformation (as detailed in chapter-4 and later in chapter-8).

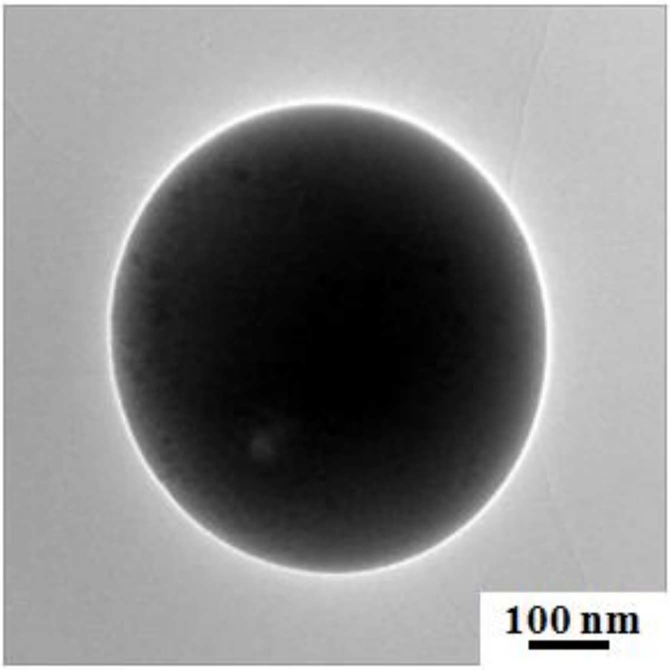

Figure 7-3: A spontaneous transformation of a fragment of a high-Zn borosilicate (ZBS-A) glass into a fully spherically shaped particle. JEM TEM 3010 at 300 keV.

The glass particle has a tendency to occupy a smaller size state, as the surface area to volume ratio would increase.

7.3 Electron irradiation-induced rounding of glass fragment

The shape and surface details of the glass fragment were significantly altered under e-beam irradiation. These alterations included rounding of the glass fragment and also smoothing of its rough surfaces. While the glass bead formation was a fast transformation process, occurring within just a few seconds, the phenomenon of glass rounding was a slower process, controllable and, indeed stoppable at any desired morphology and dimension by lowering the electron beam intensity.

A fragment of sodium borosilicate (NBS) glass was irradiated for about 5 minutes. This fragment initially had some roundish corners as well as some sharp edges. Live observations during the irradiation process revealed that after about 1 min of irradiation, the glass fragment started to change its shape and the rough surfaces of the fragment became smoother. The roundness of the corners also increased and the sharp edges became more curved. After the full 5 min of irradiation the fragment had turned into an overall rounded-shape and was halfway to forming a perfect bead, which is believed would be achieved with further irradiation. The details are shown in Fig. 7-4.

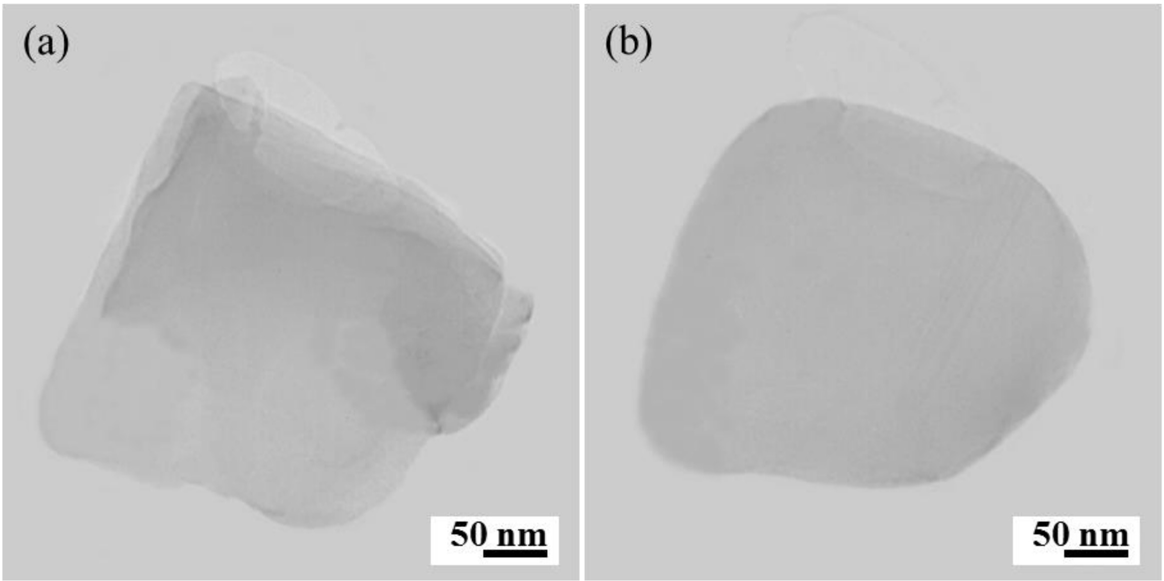

Figure 7-4: TEM images of a fragment of sodium borosilicate (NBS) glass, (a) before, and (b) after 5 min of electron irradiation. PHILIPS TEM 420 at 120 keV.

In order to see the extent of changes happening to the glass fragment after irradiation, the particle achieved after 5 min irradiation was superimposed onto the original glass particle as shown in Fig. 7-5. The transformed glass particle went beyond the original particle as a result of e-beam-induced material flow.

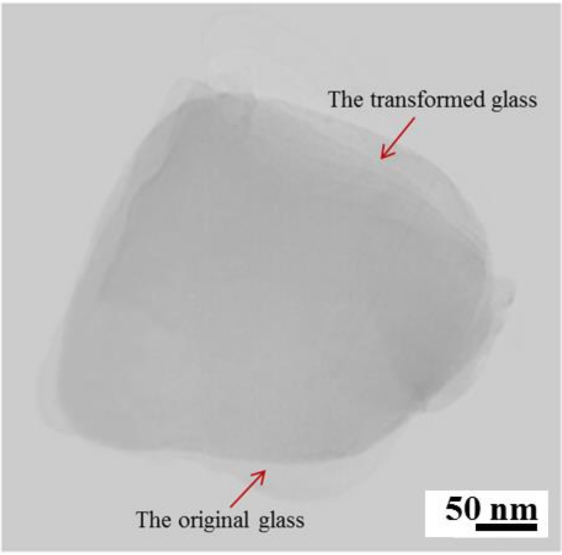

Figure 7-5: Overlaying the transformed sodium borosilicate (NBS) glass particle with the un-irradiated glass particle in order to the see the extent of changes under electron beam irradiation.

Another fragment of this glass was examined in a FEG TEM in order to perform e-beam-induced shape changes. Figure 7-6 shows a fragment of this glass before and after electron beam irradiation. After subjecting the fragment in Fig. 7-6(a) to the electron beam for about 1 min, it underwent a significant transformation such as massive rounding of the entire fragment, as clearly seen in Fig. 7-6(b).

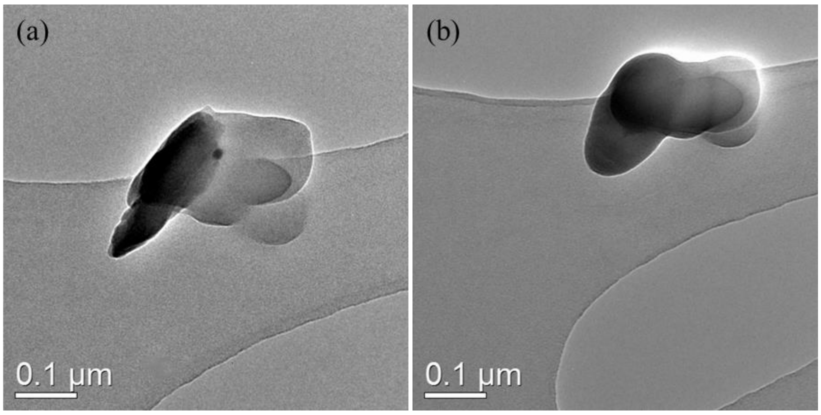

Figure 7-6: Shape transformation of a sodium borosilicate (NBS) glass fragment under the impact of electron beam irradiation. JEM TEM 2010F at 200 keV.

Time-series irradiation and intermediate images rather than just one image before and one image after are very important and necessary to track the step-by-step changes in the glass fragment under the effect of electron irradiation. Figure 7-7 shows significant modifications of a fragment of NLBS-CCZ glass under electron beam irradiation.

The electron beam was directed to irradiate the fragment shown in Fig. 7-7(a). Figs. 7-7(b-f) are bright field images photographed after a sequence irradiation of the fragment at 1 min, 2 min, 3 min, 4 min and 5 min, respectively. From these images, it is clear that the changes in the morphology of the glass fragment increased as irradiation time increased, and a significant rounding of the entire glass fragment is very obvious. A decrease in the long diameter of the glass fragment against an increase in the short diameter can be seen. The reduction in the overall glass volume with the increase in irradiation time is also obvious.

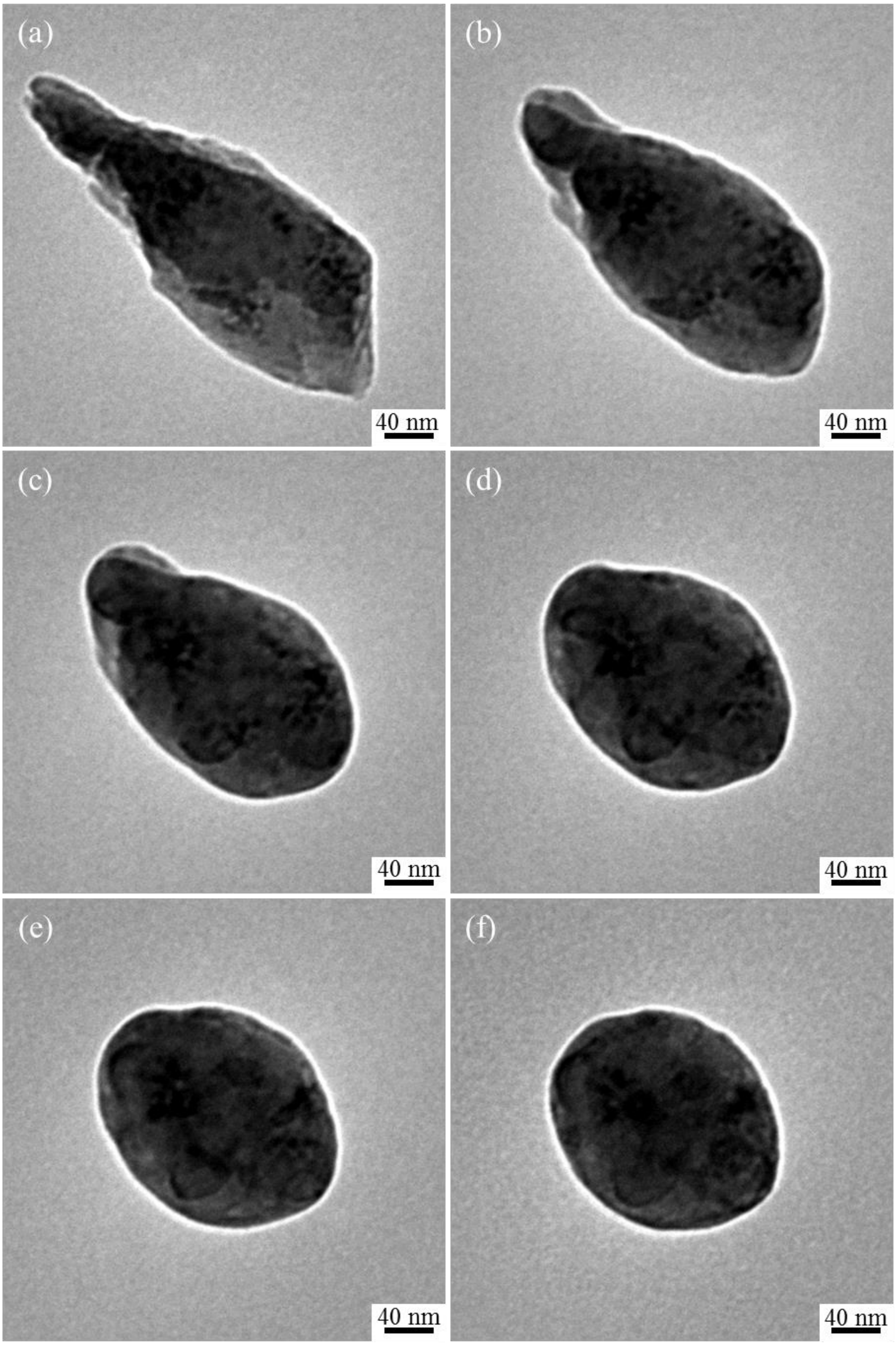

Figure 7-7: TEM images of a NLBS-CCZ glass, (a) before, and (b-f) after 1 min, 2 min, 3 min, 4 min and 5 min electron irradiation, respectively. JEM TEM 3010 at 300 keV.

Similar to Fig. 7-5, the transformed glass fragment at 5 min irradiation (shown in Fig. 7-7(f)) was overlaid onto the original fragment (shown in Fig. 7-7(a)) as shown in Fig. 7-8.

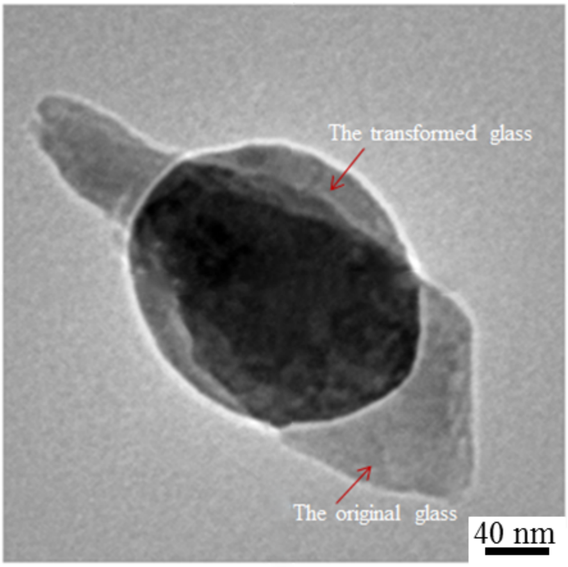

Figure 7-8: The transformed glass particle on top of the un-irradiated glass particle showing the massive change in the morphology due to electron beam irradiation.

In order to track the changes in the glass fragment due to the effect of electron irradiation, the aspect ratio was calculated from t = 0 min to t = 5 min by dividing the fragment length (the tall diameter) by the fragment width (the short diameter) to obtain the graph shown in Fig. 7-9. The uncertainty in both the length and the width is ± 2.

The initial aspect ratio value of about 2.6 prior to the irradiation (at t = 0 min) reduced as the irradiation time increased, until it reached about 1.2 by the end of the irradiation (at t = 5 min). The latter value of the aspect ratio is very close to that of a sphere, which is equal to 1.

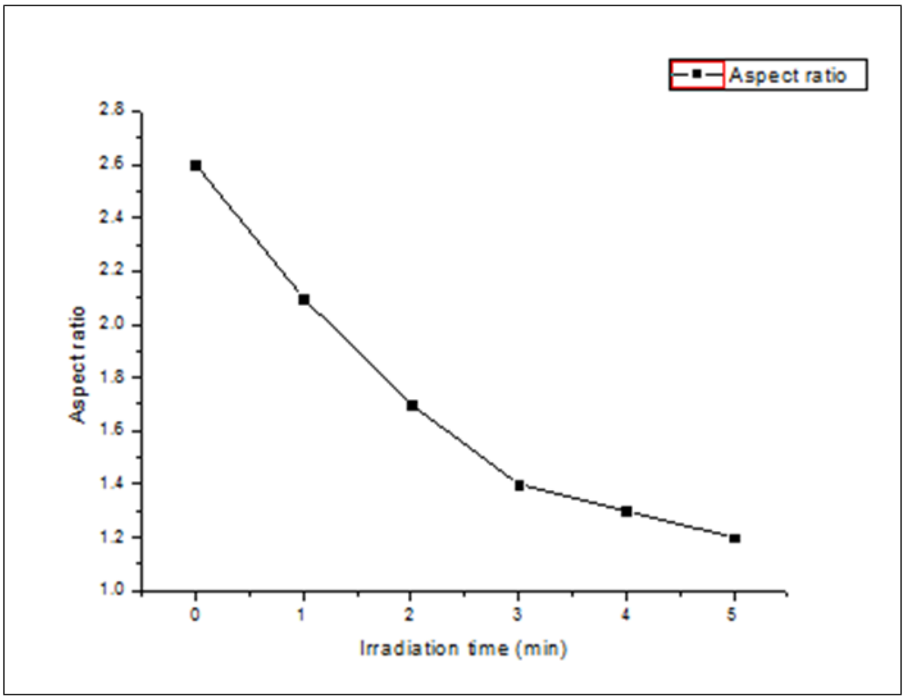

Figure 7-9: Aspect ratio (AR) values of the glass fragments shown in Fig. 7-7(a-f).

Another time-series irradiation was applied to a further fragment of this glass. The initial fragment had a few sharp corners and rough surfaces, as shown in Fig. 7-10(a). After 1 min irradiation, no obvious changes had occurred, i.e. both the sharp corners and the rough surfaces were still there (Fig. 7-10(b)). After 2 min irradiation, however, the sharp corners and the rough surfaces had begun to become rounded and smoothed, respectively, as shown in Fig. 7-10(c). Further irradiation resulted in more rounding and smoothing (Figs. 7-10(d,e)). For example, the two sharp corners located at the right side of the fragment started to lose their sharpness gradually with increasing irradiation time. At the final stage of the irradiation (Fig. 7-10(f)), no sharp corners and rough surfaces can be seen at all.

In addition, shrinkage of the overall glass fragment under e-beam irradiation is another obvious effect. As a side-effect, and at the same time as glass rounding under e-beam irradiation, phase separation into two phases within the entire glass fragment occurred.

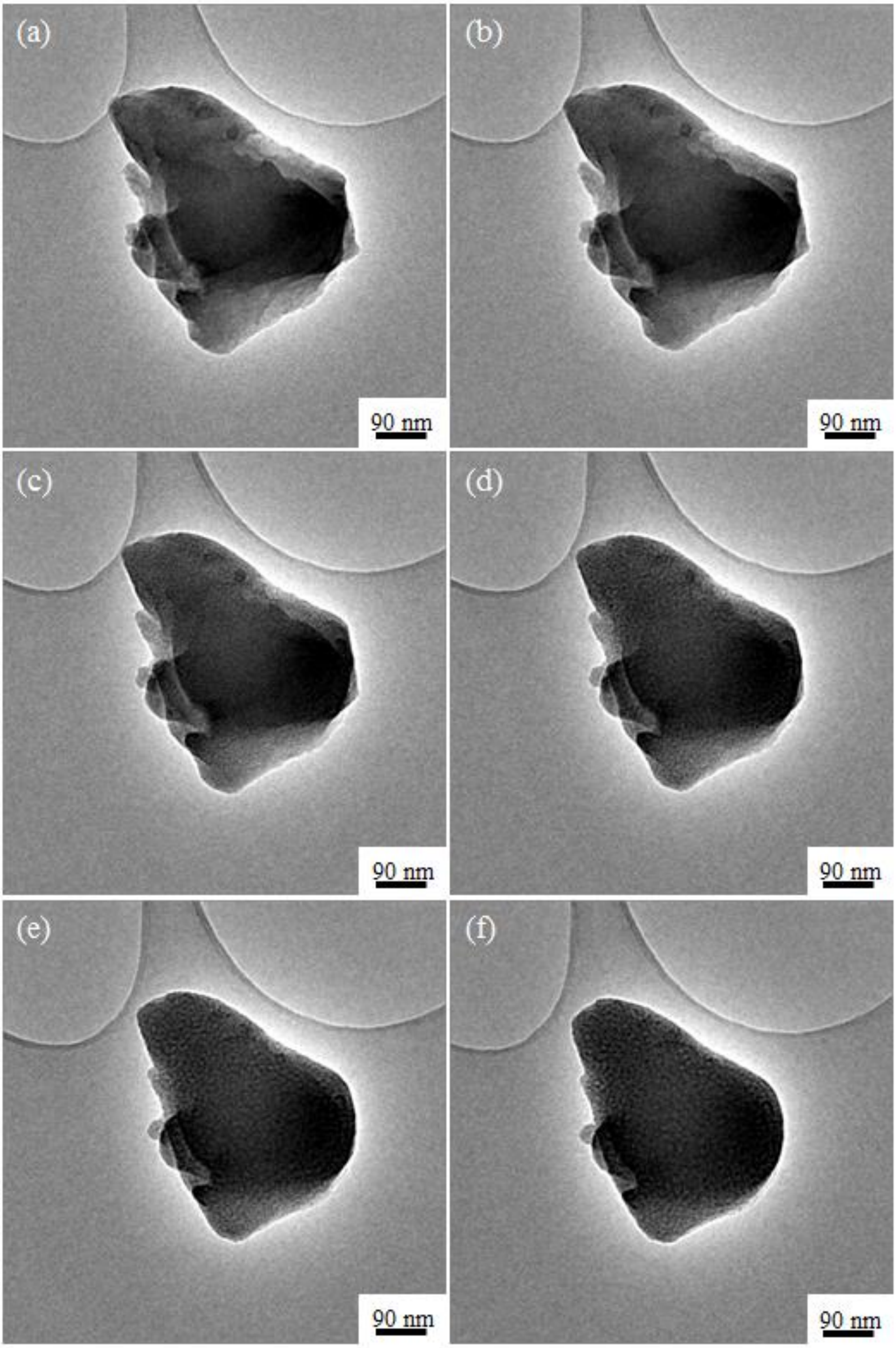

Figure 7-10: Time-series TEM images of a NLBS-CCZ glass, (a) prior to the irradiation and (b-f) after e-beam irradiation between 1-5 min, respectively. JEM TEM 3010 at 300 keV.

One approach to estimate the decrease in the glass particle size is to determine the diameter of the particle. Figure 7-11 shows a graph of the diameters of the glass fragment with the irradiation time. It shows that the particle diameter decreases as the irradiation time increases.

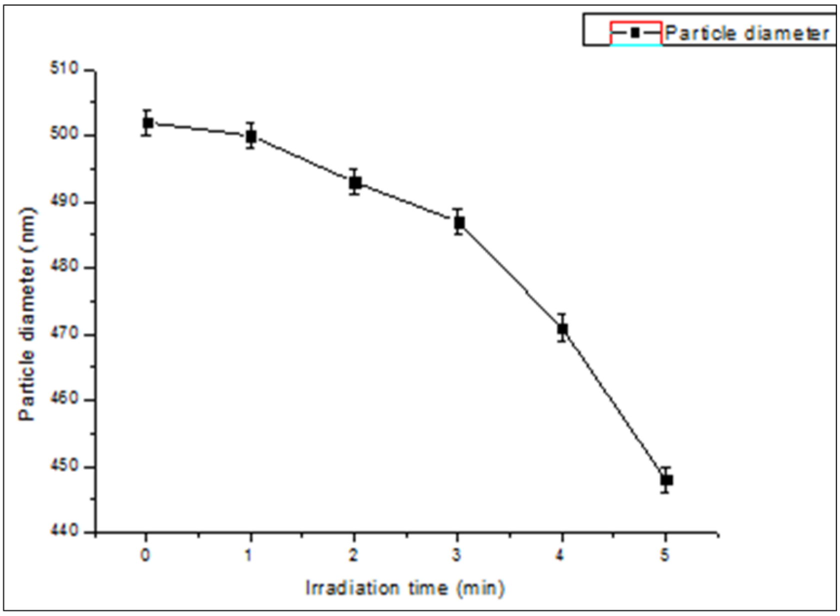

Figure 7-11: A graph showing the reduction in the glass particle diameter with the increase in irradiation time.

Another transformation in the overall glass fragment was observed in a silver-doped borosilicate (NBS-AC) glass as shown in Fig. 7-12. This transformation was rather slow and occurred under a high level of electron beam irradiation, which was achieved after removing the condenser aperture of the TEM. After irradiating the glass fragment for about 2 min, a significant rounding occurred to the fragment in Fig. 7-12(a) transforming it completely into a ball-shaped particle (Fig. 7-12(b)).

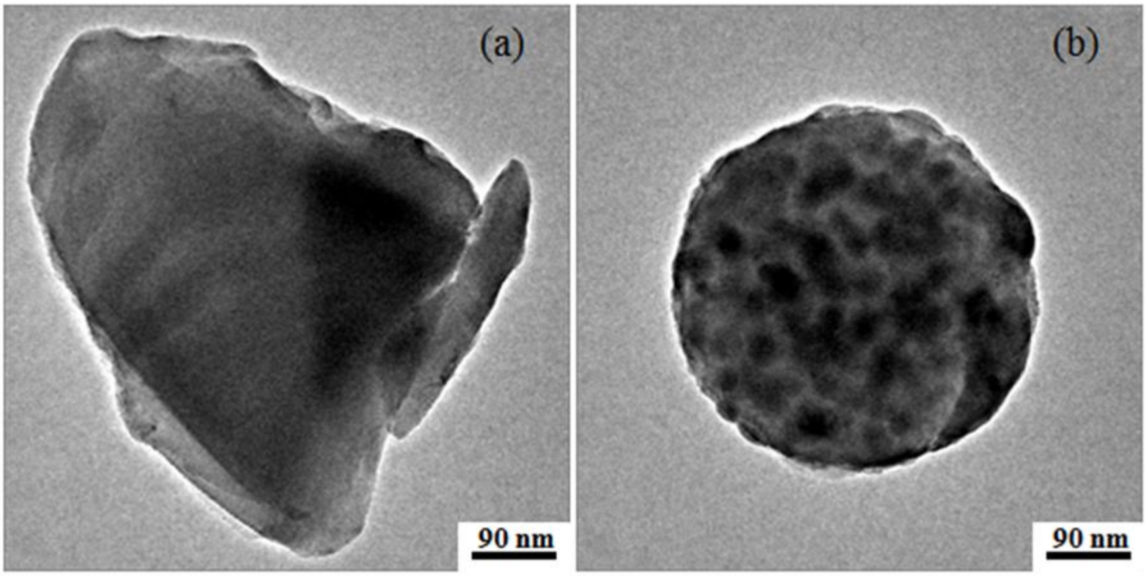

Figure 7-12: Transformation of a fragment of a silver-doped cerium sodium-borosilicate (NBS-AC) glass into a ball shaped particle after ~ 2 min of electron beam irradiation. JEM TEM 3010 at 300 keV.

7.4 Summary

The morphological transformations of glass particles under electron irradiation in 120, 200 and 300 keV transmission electron microscopy were observed. Local changes in the shape of the glass particle under electron irradiation can be achieved, including glass rounding and glass surface smoothing. The phenomenon of glass rounding was found to be a slow and controllable process. In contrast, the transformation of a glass particle into a perfect bead under electron irradiation was found to be a fast transformation process, occurring within a few seconds of irradiation.

7.5 References

Möbus G, Ojovan M, Cook S, Tsai J and Yang G 2010 Nano-scale quasi-melting of alkali-borosilicate glasses under electron irradiation *J. Nucl. Mater.* **396** 264-271.

Chapter Eight

Discussion

8.1 Electron irradiation-induced nanoprecipitation

The precipitation of nanoparticles in a variety of cation-loaded borosilicate glasses is discussed here in the light of the results set out in chapters 4-6. Stationary electron irradiation and line-scan electron irradiation modes resulted in precipitation of various patters, which were also shown to be dependent on the level of the electron irradiation. Moderate electron irradiation with a slightly focused beam (~ 120 pA/cm^2 in the LaB$_6$ TEM) resulted in precipitation of Zn nanoparticles as well as partial glass ablation in such a way that these two mechanisms are in competition, meaning that Zn nanoparticles are located slightly away from the glass fragment edge (e.g. Fig. 4-5). When a stationary focused electron beam in FEG TEM was used for irradiation, however, the rate of glass ablation was higher than the rate of Zn nanoparticle precipitation. In this case, Zn nanoparticles were decorated at the glass fragment surface and the glass suffered no ablation (e.g. Figs. 4-1(d, e) and 4-2).

In Cu glass, on the other hand, the same moderate irradiation level was actually the level of saturation so that no further growth in Cu nanoparticles occurred with further irradiation (e.g. Figs. 5-1 and 5-4). On the other hand, extreme irradiation at great densities was obtained when the condenser aperture was removed (which we also referred to as "open aperture" irradiation). Irradiation at such a level resulted in several observations. First, non-localized Cu particles were formed, and were distributed very in-homogeneously through the glass rod (Fig. 5-3). This gives an indication of electron beam-induced heating, which results in long-range Cu diffusion. Based on these experiments, it could be concluded that inserted-aperture irradiation involved negligible heating effects, and the electron beam functioned to perform both nucleation and growth but that once the condenser aperture was removed, heating had a significant effect. Second, Cu nanocrystals were found away from the original glass fragment near the hole on the C-film and appeared to give the carbon support film a kind of decoration (Fig. 5-7(c, d)). It was proposed that these nanocrystals favoured a kind of "thermal evaporation" deposition or were created as a result of a limited sputtering effect, as has been proposed for Ag [Li and Zhang, 2010]. Earlier studies have suggested that Cu nanostructures are deposited under the influence of electron beam irradiation on the carbon support film where the areas are at a relatively low temperature [Liu and Bando, 2003]. These earlier works showed that C-film is a suitable substrate for Cu deposition and re-nucleation, especially at the edges of the holes in the C-film, where the surface is relatively rough.

The sub-100 nm beam diameter used in line-scan experiments in the LaB_6 TEM resulted in the formation of mainly spherical nanoparticles inside the drawn line. The time required to form Zn nanoparticles in ZBS-A glass in this irradiation mode was found to be lower than that used to form Cu nanoparticles in CuNBS-A glass. In the FEG TEM, the sub-10 nm e-beam generated nano-lines in which the region of the glass at the centre of the e-beam was ablated, while the nanoparticles had the tendency to accumulate at both sides of the e-beam, generating two metal lines (Figs. 4-10(b) and 4-11). In these experiments, it was impossible to track the precipitation of nanoparticles *in-situ* with the irradiation time, due to the electron beam being focused to its smallest possible diameter. Also, it was not practical to disturb the pattern by spreading the e-beam for imaging and then attempting to revert to the point where the e-beam was spread, since this would destroy the patterning process.

Focusing the electron beam inside the glass fragment resulted in nano-ring formation. The formation of nano-rings in CuNBS-A glass under focused electron beam irradiation in FEG TEM (Fig. 5-6) provides novel findings in comparison with the earlier study of Jiang *et al.* in 2003 [Jiang *et al.*, 2003], which reported the fabrication of nano-rings of amorphous Ge and

Nb_2O_5 in silicate glasses using a 100 keV scanning transmission electron microscope (STEM). Our fabricated nano-ring was different from that, since it was made of metal Cu nanoparticles. Generally, non-bridging oxygen (NBO) is generated due to the addition of metal ions to silicate. Upon electron beam irradiation, an Auger cascade will be produced, and this converts the negatively charged non-bridging oxygen into a positively charged ion. After that, the ionic bond between the non-bridging oxygen and the metal ion will break, releasing the metal ion from the glass network. This results in migration of the metal ions to the adjacent region in the repulsive electrostatic field that is induced by the Auger cascade and the excitation of the secondary electrons in the region of irradiation, thereby forming nano-ring. In addition, we found that there is a region of stationary Cu nanoparticles at the centre of the nano-ring structure, with a few Cu NPs remaining at this region and not migrating to the e-beam edge. This could be due to the fact that there was no force to move them to the e-beam edge. This mechanism is also applicable for the line-scan patterning experiments. In addition, it is believed that non-bridging oxygen has a critical role in the precipitation of nanoparticles in glass under electron beam irradiation [Jiang *et al.*, 2003].

When a high electron beam interacts with a specimen, there are three possible events: heating, knock-on and radiolysis [Hobbs, 1987]. In this work, heating effects were negligible at moderate irradiation when the condenser aperture was inserted, but they became significant when the condenser aperture was removed. Estimating the temperature rise in glass when irradiated in TEM is a matter of debate and earlier studies have reported a range of temperature values from a few degrees to a few hundreds of degrees [Gryaznov *et al.*, 1991, Klimenkov *et al.*, 2000, Blandford and Crater, 2003, Du *et al.*, 2003 and Du *et al.*, 2005]. The knock-on mechanism, on the other hand, causes displacement of the atom from its original site and therefore needs to be taken into consideration when irradiating materials that contain light elements, such as glass, since these are vulnerable at high energy irradiation [Egerton and Malac, 2004]. These borosilicate glasses are also loaded with heavy metal cations (Zn, Cu, and Ag). In general, the atom is displaced from its original site when the maximum energy transferred (E_{max}) from the electron beam to the atom is larger than the displacement energy (E_d) of the atom, i.e., $E_{max} > E_d$ [Hobbs, 1987]. In this case, the atom will be displaced from its position to an interstitial or vacancy, and produce a Frenkel pair in the bulk [Jiang and Spence, 2012]. If the maximum energy transferred (E_{max}) is larger than the surface displacement energy (E_s), the atom will be sputtered far from the surface into a vacuum. The maximum energy transferred from the electron beam to an atom is given by:

$$Emax = \frac{2Up\ (Up+2mc^2)}{Mc^2} \text{ ---------- (8-1)}$$

where (E_{max}) is the maximum energy transferred from an electron beam of accelerating voltage (U_p) and a rest mass (m) to an atom of a nucleus of mass (M). The velocity of light is indicated by (c) in the above relationship. The value of mc^2 is 511 keV (rest mass of the electron (9.11×10^{-31} kg) × the square of the velocity of light (9×10^{16} $m^2.s^2$)). By putting the value of M_{Zn}, M_{Cu} and M_{Ag} as $65.38 \times 1.66 \times 10^{-27}$ kg, $63.55 \times 1.66 \times 10^{-27}$ kg and $107.87 \times 1.66 \times 10^{-27}$ kg, respectively, the maximum transferred energy (E_{max}) from an electron beam of 200 and 300 keV to the Zn, Cu and Ag atoms during irradiation is listed in table 8-1, along with a list of the values of the displacement energy (E_d) [Bradley and Zaluzec, 1989] of the bulk atom, and the surface displacement energy (E_s) [Bradley and Zaluzec, 1989].

Table 8-1: Values of E_{max}, E_d and E_s

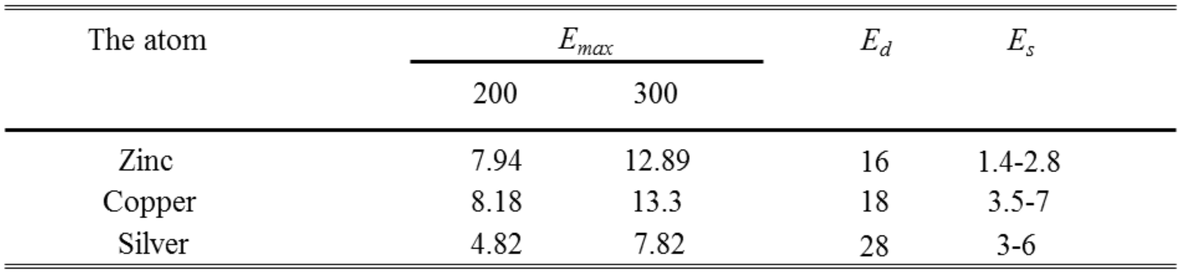

The atom	E_{max}		E_d	E_s
	200	300		
Zinc	7.94	12.89	16	1.4-2.8
Copper	8.18	13.3	18	3.5-7
Silver	4.82	7.82	28	3-6

The table clearly shows that the values for maximum transferred energy (E_{max}) are smaller than the values for displacement energy (E_d) at 200 and 300 keV, and hence the maximum transferred energy is not enough to displace Zn, Cu and Ag atoms from their position inside the bulk. The maximum transferred energy (E_{max}), however, is larger than the surface displacement energy (E_s) of Zn, Cu and Ag atoms and hence surface displacement is possible. Knock-on is proposed as the main mechanism in the formation of crystalline Si nanoparticles in SiO_2 under a 200 keV e-beam irradiation [Du *et al.*, 2003], in which the maximum transferred energy to remove Si from the glass is larger than the displacement energy (E_{max} = 19.57 eV and E_d = 14 eV).

Partial glass ablation, on the other hand, also occurred due to the fact that the maximum energy transferred to the glass matrix's elements (B, O, Si, Na and K) other than the loaded and dopant elements at 200 and 300 keV is larger than the displacement energy of these atoms. The values of E_{max} transferred to these elements are listed in table 8-2.

Table 8-2: Values of maximum transferred energy (in eV) to the glass matrix

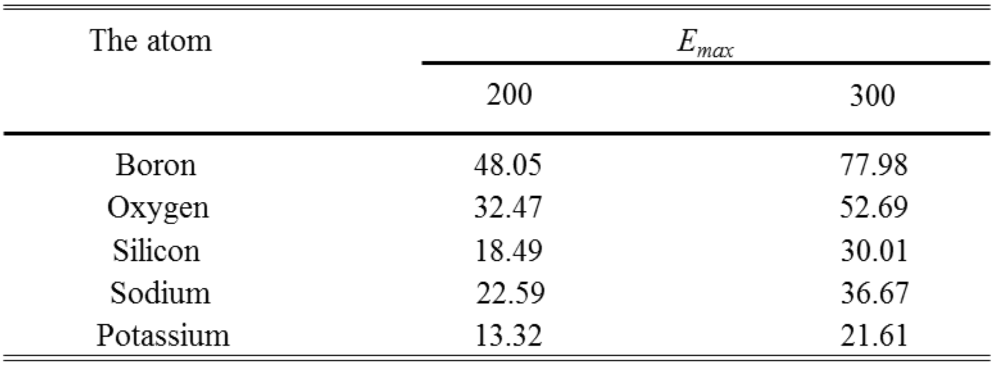

The atom	E_{max}	
	200	300
Boron	48.05	77.98
Oxygen	32.47	52.69
Silicon	18.49	30.01
Sodium	22.59	36.67
Potassium	13.32	21.61

The *in-situ* heating test which was conducted on the high-Zn-loaded borosilicate (ZBS-A) glass showed no evidence of nanoparticle formation, except for the observation of some morphological changes in the nanoparticles already formed by the earlier electron beam irradiation. In addition, the experimental observations revealed the stability of the overall glass fragment when subjected to *in-situ* heating at the temperatures used (100-300 ^{o}C).

These temperatures were also not high enough to melt Zn nanoparticles, since the melting temperature of bulk Zn is about 419 °C, which is higher than the melting temperature of Zn nanoparticles (417.5 °C) [Gunawan and Johari, 2008]. When a fragment of this glass is heated independently at various temperatures, without any e-beam irradiation, no particles formed at all, as is clearly shown in Fig. 4-16. Based on these observations, heating at these temperature ranges cannot precipitate and form nanoparticles.

Ag glasses differ from Zn and Cu glasses in that they contain not only Ag as a dopant, but also a few other dopants that may assist in reducing Ag atoms, especially Ce. Although the effect of Ce on the precipitation of metallic Ag nanoparticles in silicate glasses is unknown in respect to electron beam irradiation, it has been investigated with other types of radiation, such as femtosecond laser irradiation [Dai and Jiang-Rong, 2009] and they have demonstrated the necessity of Ce ions to reduce Ag ions into Ag atoms. The scenario is that when the Ag/Ce-doped silicate glass is irradiated by the femtosecond laser, part of the energy of the laser might be absorbed by the Ce^{3+} ions through multi-photon absorption; this releases free electrons and reduces the concentration of hole-trapped colour centres. Ag ions then capture these free electrons and generate metal Ag atoms (Ag^0). The following annealing process results in aggregation of Ag atoms to generate Ag nanoparticles due to atom diffusion. At further annealing, the formed metal Ag may reduce Ce^{4+} ions to Ce^{3+} ions and this prevents the growth of the Ag nanoparticles. The whole process can be summarised in the following expressions [Dai *et al.*, 2006]:

$Ce^{3+} \xrightarrow{nhv} Ce^{4+} + e (n \geq 3),$ --------------------- (8-2)

$glass \xrightarrow{nhv} h^{+} + e (n \geq 5),$ --------------------- (8-3)

$Ag^{+} + e \xrightarrow{annealing} Ag^{0},$ --------------------- (8-4)

$mAg^0 \xrightarrow{annealing} Ag_m$, --------------------- (8-5)

$Ce^{4+} + Ag^0 \longrightarrow Ce^{3+} + Ag^+$, ------- (8-6)

where n is the number of the photons participating in the multi-photon process and m is the number of Ag atoms aggregating into Ag nanoparticles. Another source of free electrons comes from the excited electrons from the valence band to the conduction band of the glass matrix owing to the femtosecond laser irradiation.

Different results were, therefore, obtained from Ag glasses compared to either Zn or Cu glasses. Irradiation of Ag glasses is mainly attributed to phase separation and, sometimes, the occurrence of synchronous amorphous phase separation and precipitation. Furthermore, the nanoparticle precipitation region was surrounded by a phase separation region (e.g. Fig. 6-4). This consisted of dark and bright regions in which the dark region may correspond to heavy elements (Ag, Ce) and the bright region may correspond to light elements of the glass matrix. The region of phase separation was characterised by the diffuse interface formed by electron irradiation [Ojovan *et al.*, 2010].

This research work was not focused on studying the influence of Ce on the precipitation of Ag, but a few experimental observations did show that the nanoparticles formed on the C-film (e.g. Fig. 6-2) and that the precipitated nanoparticles at the glass surface (e.g. Fig. 6-11(d)) were metallic Ag. An earlier study has showed that Fe_2O_3 and Nd_2O_3 were dissolved in KBS-ACFN glass [Yang *et al.*, 2010]. What remains to precipitate are Ag or Ce, both of which of high atomic number (Z_{Ag} = 47 and Z_{Ce} = 58). The maximum transferred energy (E_{max}) to the Ce atoms by 200 and 300 keV are 3.7 and 6 eV, respectively (using Eq. 8-1). According to the literature [Yasunaga *et al.*, 2006], there is no reported value of the displacement energy (E_d) for Ce and therefore the value of E_d of 40 eV for U will be considered. This value is much higher than the value of E_{max} at both 200 and 300 keV and therefore the Ce atoms cannot displace from their sites through knock-on. A few considerations give an indication that the precipitated nanoparticles under electron beam irradiation are metallic Ag. First, in comparison to all multi-valent redox couples presence in the KBS-AFCN glass, Ag is the easiest element to reduce (redox couples for silver = 1, 0 [Schreiber, 1986]) and therefore formation of metal Ag nanoparticles is to be expected. Second, the earlier study of the KBS-ACFN glass confirmed that no Ce nanoparticles were found to be precipitated in this glass under e-beam irradiation, which gives an indication that CeO_2 was fully dissolved in the glass matrix [Yang *et al.*, 2010]. This also should be the case in the NBS-AC glass. Third, based on our experimental results, there are a few particles which show crystallinity from their lattice fringes in the HRTEM images (at the glass surface and also on the carbon film). The precipitated particle in the glass surface has been proven to be metallic Ag (Fig. 6-11(d)). Nevertheless, the amount of black contrasts in the irradiated region could have different sources and might not come only from the 1% or 2% Ag in the glass.

8.2 Electron irradiation-induced morphological transformation

Morphological transformation of glass particles, usually under moderate electron irradiation, is an obvious phenomenon observed frequently throughout this research work. Some of these transformations were slow and enhanced with irradiation time, while other transformations occurred spontaneously (usually sudden ball formation). The energy delivered by the high electron beam to the glass fragment is able to transform this fragment into a new form, partially or completely different from the original fragment.

The glass fragment shown in Fig. 7-1(a) transformed into a spherical shape particle (Fig. 7-1(b)) under the effect of electron beam irradiation in just few seconds. Therefore, the two particles are both of the same glass. Transformation of metal particles into a spherical shape has been reported in an earlier study [Xu and Tanaka, 1998]. These metal particles have a tendency to react with the C-film to form graphitic shells which encapsulate the particles during TEM analysis. Carbon contamination is another possible reason why a carbon ball was formed, but no such shells were found in our case (shown in Fig. 7-1) and hence the reported carbon encapsulation is omitted. This is also applicable to other spherical shapes of glass particles formed under e-beam irradiation, as shown in Figs. 7-2 and 7-3.

Fluidisation, or quasi-melting, of glass under the impact of electron beam irradiation is due to the e-beam breaking bonds and this will result in a reduction in the viscosity (increase in the fluidity) of the glass being irradiated. Electron beam-induced fluidisation has also been reported in the pores experiments in amorphous materials where it has been reported to be as a result of surface tension [Storm *et al.*, 2003].

Based on our experimental observations, the first sign of e-beam-induced fluidity was the rounding of the sharp and rough corners of the glass fragments (e.g. Fig. 7-4, Fig. 7-6 and 7-12). Then, the process of fluidity enhancement was observed to increase with the irradiation time (e.g. Figs. 7-7 and 7-10).

The importance of e-beam-induced fluidisation is that it occurs only in the irradiated regions, and the surrounding regions outside the e-beam remain unchanged due to negligible thermal effects. The glass transforms into liquid (i.e., fluidises) not because of thermal melting but because of e-beam irradiation [Möbus *et al.*, 2010]. This effect can be exploited in order to perform precise nano-transformation. The sudden transformations of glass particles into spherical shape particles (e.g. in Figs. 7-2 and 7-3) occurred when no condenser aperture was inserted, and the irradiation was at an extremely high level. Also, there is no intermediate stage between the original glass particle and the ball-shaped particle suddenly formed. This is different from the slow transformation observation when the condenser aperture was inserted and the irradiation level was moderate in which the temperature rise effects are not significant.

In addition, there is no a certain value for the temperature rise in glass particles being irradiated in a TEM (as explained in section 8.1). This is due to a range of criteria such as glass particle size, glass particle thickness, irradiation conditions and the connectivity of the glass particle with the substrate. These transformations occurred at temperatures far below the melting temperatures of the glasses. As the melting temperatures of our glasses were 1400 ^{o}C for CuNBS-A glass, 1450 ^{o}C for ZBS-A glass, 1350 ^{o}C for NBS-AC glass and 1400 ^{o}C for both NBS and NLBS-CCZ glasses, it is hard for the e-beam irradiation to reach these temperatures. Also, based on our experimental findings, the speed of these transformations is not voltage dependent. Although these transformations were observed at the three different voltages of 120, 200 and 300 keV, the sudden ball formation only happened in LaB_6 TEM at 300 keV. As the glass particles used in this study were prepared via manual grinding method using pestle and mortar, these particles have different thicknesses, sizes and shapes. Nonetheless, it was found that the glass particle size is important. Our experiments showed that the smaller the particle size, the faster the morphological transformation was.

The observed spherical particles shown in Figs. 7-1, 7-2 and 7-3 are the cases that were induced due to surface tension forces that minimised the surface area per unit volume. Moreover, under electron beam irradiation, the rounding in the glass fragment goes beyond the original fragment due to material flow by the e-beam irradiation (e.g. Figs. 7-5 and 7-8).

8.3 References

Blanford C F and Carter C B 2003 Electron Radiation Damage of MCM-41 and Related Materials *Microsc. Microanal.* **9** 245-263.

Bradley C R and Zaluzec N J 1989 Atomic sputtering in the analytical electron microscope *Ultramicroscopy* **28** 335-338.

Dai Y and Jiang-Rong Q 2009 The photosensitive effect of Ce on the precipitation of Ag nanoparticles induced by femtosecond laser in silicate glass *Chin. Phys. Soc.* **18** 2858-2863.

Dai Y, Qiu J, Hu X, Yang L, Jiang X, Zhu C and Yu B 2006 Effect of cerium oxide on the precipitation of silver nanoparticles in femtosecond laser irradiated silicate glass *Appl. Phys. B* **84** 501-505.

Du X , Takeguchi M, Tanaka M and Furuya K 2003 Formation of crystalline Si nanodots in SiO_2 films by electron irradiation *Appl. Phys. Lett.* **82** 1108-1110.

Du X W, Wang B, Zhao N Q and Furuya K 2005 Structure evolution of silicon nanocrystals under electron irradiation *Scrip. Mater.* **53** 899–903.

Egerton R F, Li P and Malac M 2004 Radiation damage in the TEM and SEM *Micron* **35** 399-409.

Gryaznov V G, Kaprelov A M and Belov A Y 1991 Real temperature of nanoparticle in electron microscope beams *Philos. Mag. Lett*. **63** 275-279.

Gunawan L and Johari G P 2008 Specific Heat, Melting, Crystallization and Oxidation of Zinc Nanoparticles and Their Transmission Electron Microscopy Studies *J. Phys. Chem. C.* **112** 20159-20166.

Hobbs L W 1987 Electron-beam sensitivity in inorganic specimens *Ultramicroscopy* **23** 339-344.

Jiang N and Spence J C H 2012 On the dose-rate threshold of beam damage in TEM *Ultramicroscopy* **113** 77-82.

Jiang N, Hembree G G, Spence J C H, Qiu J, Garcia de Abajo F J and Silcox J 2003 Nanoring formation by direct-write inorganic electron-beam lithography *Appl. Phys. Lett.* **83** 551-553.

Jiang N, Qiu J, Ellison A and Silcox J 2003 Fundamentals of high-energy electron-irradiation-induced modifications of silicate glasses *Phys. Rev. B.* **68** 064207-11.

Klimenkov K, Matz W and Borany J V 2000 *In situ* observation of electron-beam-induced ripening of Ge clusters in thin SiO_2 layers *Nucl. Instr. Meth. B.* **168** 367-374.

Li K and Zhang F S 2010 A novel approach for preparing silver nanoparticles under electron irradiation *J. Nanopart. Res.* **12** 1423-1428.

Liu Z and Bando Y S 2003 A Novel Method for Preparing Copper Nanorods and Nanowires *Adv.Mater.* **15** 303-305.

Möbus G, Ojovan M, Cook S, Tsai J and Yang G 2010 Nano-scale quasi-melting of alkali-borosilicate glasses under electron irradiation *J. Nucl. Mater.* **396** 264-271.

Ojovan M, Yang G and Möbus G 2010 On spinodal decomposition of e-beam irradiated borosilicate glasses *WM Conference, Phoenix, AZ.* 1-8.

Schreiber H D 1986 Redox processes in glass-forming melts *J. Non-Cryst. Solids* **84** 129-141.

Storm A J, Chen J H, Ling X S, Zandbergen H W and Dekker C 2003 Fabrication of solid-state nanopores with single-nanometre precision *Nat. Mater.* **2** 537-540.

Xu B S and Tanaka S I 1998 Formation of giant onion-like fullerenes under Al nanoparticles by electron irradiation *Acta Mater.* **46** 5249-5257.

Yang G, Cook S, Hand R J and Möbus G 2010 CeO_2 nano-precipitation in borosilicate glasses: A redox study using EELS *J. Euro. Ceram. Soc.* **30** 831-838.

Yasunaga K, Yasuda K, Matsumura S and Sonoda T 2006 Nucleation and growth of defect clusters in CeO_2 irradiated with electrons *Nucl. Instrum. Meth. Phys. Res. B* **250** 114-118.

Chapter Nine

Conclusion

Electron beam irradiation has been shown to be an efficient technique to induce modifications in different types of glass. It has been successfully used to precipitate various nanoparticles locally in various oxide glasses via both stationary and line-scan irradiation modes. Although an earlier study of high-Zn-borosilicate glass showed the formation of 7 nm diameter spherical Zn nanoparticles using STEM mode, our fabricated Zn nanoparticles were between 5-50 nm in size and had various morphologies such as square and hexagonal, in addition to spherical. Further, our novel method of line-scan patterning was promising in generating Zn nanoparticles within the drawn line and also in generating two lines of metal Zn on both sides of the e-beam in the FEG TEM. Comparison of the two glass compositions was undertaken to indicate the influence of the very different nature of the glass network (especially Si content) and the presence of an extra alkali-modifier (Na) in the ZBS-B glass. It was found that the speed and amount of Zn precipitation goes with the high-Zn content (ZBS-A) glass and, therefore, the ZBS-A glass decomposed faster than the ZBS-B glass. This, in turn, gave an advantage to the low-Zn content (ZBS-B) glass in terms of avoiding unwanted pre-precipitation during the e-beam focusing before deliberate irradiation started. It was also confirmed that *in-situ* heating was not able to precipitate Zn particles or change the overall glass morphology at temperature ranges between 100-300 ^{o}C, while it was able to change the morphology of Zn particles already precipitated during the earlier electron irradiation.

Furthermore, our method of electron irradiation was shown to be a promising route in the precipitation and formation of Cu nanoparticles for the first time in Cu-loaded borosilicate glass, since the earlier Cu precipitation was via laser irradiation, with only one study of electron irradiation of pre-existing Cu particles in glass. Depending on the irradiation time, the line-scan irradiation method resulted in the formation of Cu nanoparticles inside the formed patterns as well as at the e-beam edges. In comparison with Cu-loaded glass (CuNBS-A), the Cu-doped glass (CuNBS-B) glass did not form any visible Cu particles when subjected to the electron beam irradiation for a period long enough to ablate the entire glass matrix. On the other hand, the comparative study of the annealed glass fragments was to elucidate the necessity for suppression of thermal precipitation. This study confirmed that a cooling rate at least as fast as in our frit-quenched glass is mandatory. In addition, the reason why thermal annealing formed Cu_2O while electron irradiation in the TEM formed metallic Cu is due to using air-furnace heating for annealing, whereas the TEM exposure is a reducing medium.

The techniques used for chemical analysis of the precipitated Zn and Cu particles such as EELS, HRTEM and EDX were very useful. All these techniques confirmed that these particles are metallic. For the EELS analysis, the Plasmon peaks at the low-loss region in the EELS spectrum were very useful to confirm the metallic nature of the precipitated nanoparticles.

The irradiation of Ag-doped glasses was mainly attributed to phase separation in addition to the occurrence of precipitation at the same time as a synchronous and this e-beam-induced phase separation was characterised by diffuse interfaces. Nevertheless, the metallic nature of the precipitated Ag nanoparticle confirmed from the HRTEM imaging and the evaluation of the d-spacing of a single Ag nanoparticle. Line-scan irradiation was also successfully achieved in the Ag-doped glasses. Overall, it can be concluded from the above experiments that these two different types of Ag glass behaved similarly under electron beam irradiation.

The calculated values of E_{max} were lower than the values of E_d in the bulk materials and therefore this gives a confirmation that neither 200 nor 300 keV was unable to displace Zn, Cu and Ag from their original sites, while surface sputtering was possible, since the values of E_{max} in this case were higher than the values of E_s.

It has therefore been proposed that the key process is the breaking of ionic bonds between the cations and the non-bridging oxygen. This is followed by the migration of the released cations driven by electrostatic fields from local charging as a result of losing secondary and Auger electrons.

The sharp boundary between the irradiated region and the un-irradiated region confirmed the lack of any heating effects, unless removing the condenser aperture resulted in a non-local formation of Cu and Ag particles due to long-range diffusion.

Electron beam irradiation is a one-step method to form nanoparticles in glass, in comparison with other techniques, such as laser irradiation and ion implantation, which are multi-step processes requiring post treatment.

On the other hand, morphological transformation of the glass fragments under electron beam irradiation was believed to be due to radiation-induced fluidity (RIF) which causes sharp corners to become rounded and transformation of glass fragments into perfect beads due to surface tension.

Appendix I

Electron irradiation studies of other materials

This appendix outlines results supplementary to those presented in the main results chapters (4-7) that were obtained from e-beam irradiation studies in some other materials. These materials include some other glass types, free standing cerium oxide (ceria-CeO_2) nanoparticles and a cerium carbonate ($CeCO_3$) precursor.

1. Electron irradiation of other glasses

1.1 Alkali-free glass

This glass has a composition of $8Al_2O_3$-27CaO-$8B_2O_3$-$57SiO_2$ in (mol. %) and is given an acronym of AlCBS. This glass was selected in order to explore e-beam irradiation-induced shape transformation. Figure A1 shows a fragment of this glass prior to the irradiation and after 5 min of electron beam irradiation at 120 keV TEM.

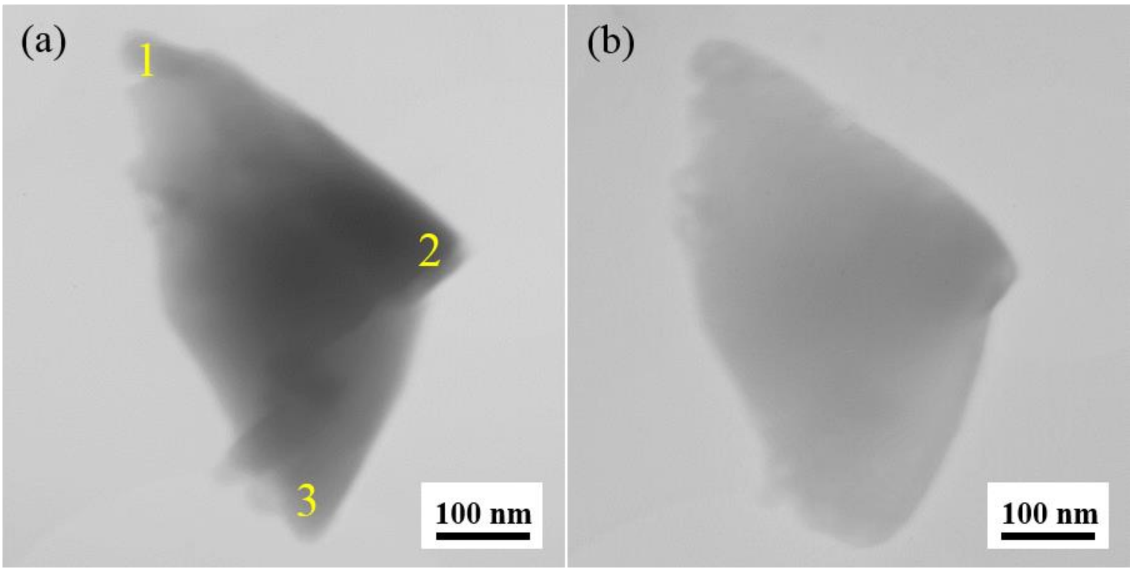

Figure A1: TEM images of a fragment of AlCBS glass, (a) before and (b) after 5 min irradiation. PHILIPS TEM 420 at 120 keV.

This fragment has three relatively round corners, indicated by the numbers 1, 2 and 3 in Fig. A1(a). After irradiation for about 5 min, further rounding was evident at these corners. In order to identify the changes in these corners before and after electron irradiation, the radius of curvature of these corners was calculated and the values are listed in table A1.

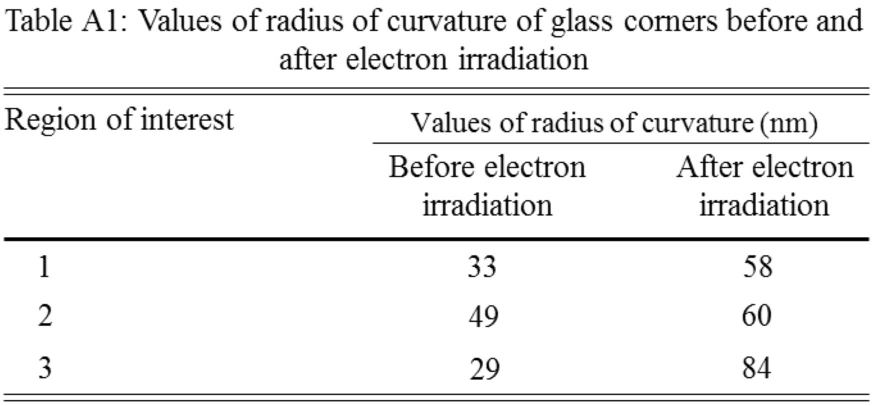

Table A1: Values of radius of curvature of glass corners before and after electron irradiation

Region of interest	Values of radius of curvature (nm)	
	Before electron irradiation	After electron irradiation
1	33	58
2	49	60
3	29	84

Time-series irradiation using a 300 keV TEM was also applied to a rod of this glass with rough surfaces (shown in Fig. A2). The electron beam was placed on the right edge of the rod and electron irradiation-induced transformations were observed, with these increasing as the irradiation time increased. The initial 1 min of irradiation did not cause any significant changes (Fig. A2(b)), but from 2 min of irradiation transformation started to occur involving the smoothing of the rough surfaces and rounding of the corners of the glass rod (Figs. A2(c-f)). This glass edge rounding increased as the irradiation time increased until a perfectly round glass ball with a radius of curvature of about 415 nm was produced (Fig. A2(g)).

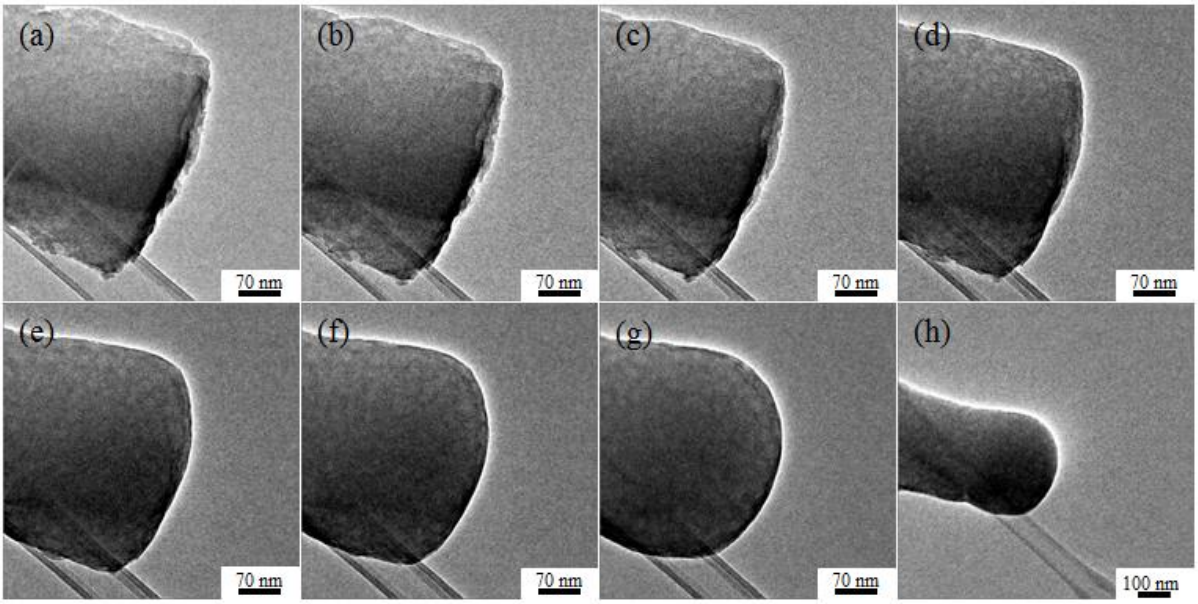

Figure A2: Time-series TEM images of an AlCBS glass rod at (a) 0 min, (b) 1 min, (c) 2 min, (d) 3 min, (e) 4 min, (f) 5 min and (g) 10 min electron irradiation, respectively. (h) TEM image at low magnification of the region of irradiation. JEM TEM 3010 at 300 keV.

1.2 Alkali borosilicate glass

This glass had a composition of 16.6Na_2O-62.55B_2O_3-20.85SiO_2 in mol. % and was given an acronym of NBS-HB. Fig. A3 represents a fragment of the NBS-HB glass irradiated by a 120 keV electron beam for about 5 min. Upon irradiation, the rough surfaces of the fragment (shown in Fig. A3(a)) started to become smooth until no rough surfaces were left and the entire surface was smooth along with increased rounding of the fragment corners, as shown in Fig. A3(b).

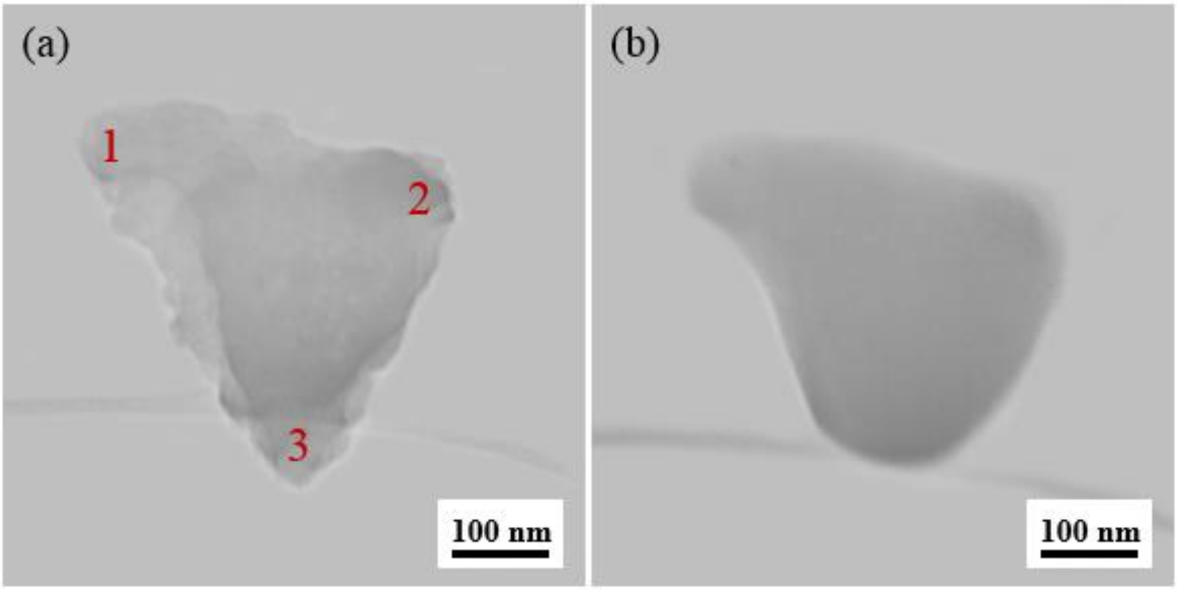

Figure A3: TEM images of a fragment of the NBS-HB glass, (a) before, and (b) after 5 min electron beam irradiation. PHILIPS TEM 420 at 120 keV.

It is worth evaluating the changes in the glass fragment due to electron irradiation by doing some calculations such as measuring the values of the radius of curvature of the corners indicated by numbers 1, 2 and 3 before (Fig. A3(a)) and after irradiation (Fig. A3(b)). These values are listed in table A2.

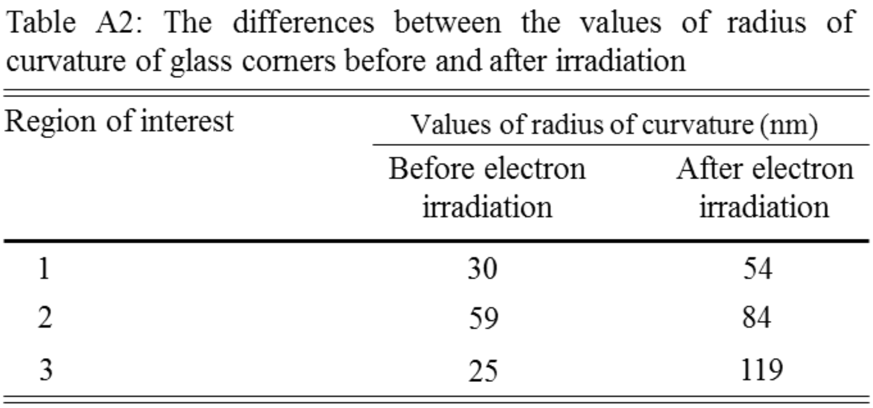

Table A2: The differences between the values of radius of curvature of glass corners before and after irradiation

Region of interest	Values of radius of curvature (nm)	
	Before electron irradiation	After electron irradiation
1	30	54
2	59	84
3	25	119

1.3 Annealed NLBS-CCZ glass

In order to examine the effect of the electron irradiation on the precipitates in the annealed glass, a tree-like dendrite precipitate shown in Fig. A4(a) was irradiated for about 3 min using an electron beam of the diameter visible in Fig. 4(b). No obvious changes occurred to the dendrite at all, confirming the toughness of such structures under electron irradiation. A slight rounding of the bottom corner of the main glass fragment after the irradiation can be seen, however (white dashed area in Fig. 4(a): radius of curvature = 13 nm vs other white dashed area in Fig. 4(c): radius of curvature = 30 nm).

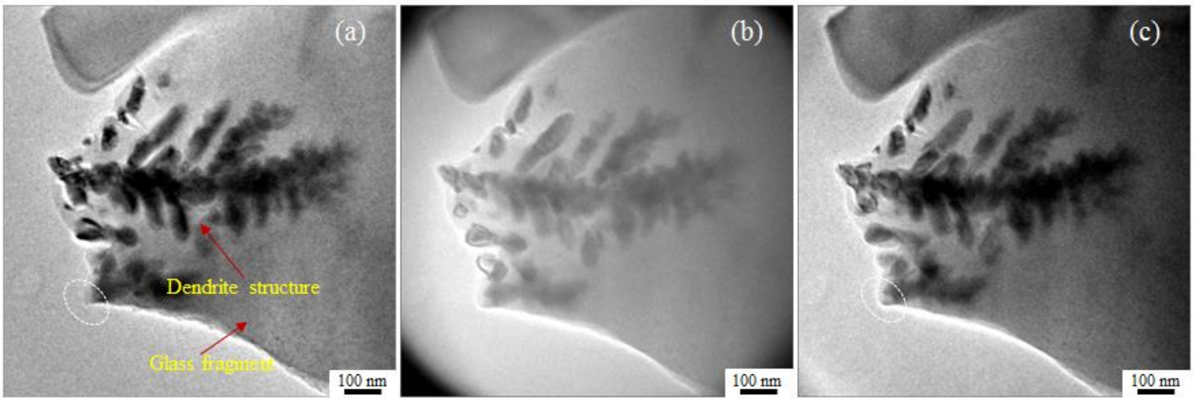

Figure A4: TEM images of a dendrite structure in the annealed NLBS-CCZ glass, (a) before electron irradiation, (b) after 3 min irradiation (e-beam is visible) and (c) the same as in (b) after spreading the electron beam. JEM TEM 3010 at 300 keV.

Outside the series of glass samples used for the purpose of inducing nanoprecipitation, line-scan irradiation was performed once in a fragment of the NLBS-CCZ glass by scanning an electron beam with a diameter of about 90 nm diagonally through the glass fragment, as shown in Fig. A5. A pattern of about 90 nm in width and about 475 nm in length was generated. The line-scan irradiation process was rather quick and done click-by-click without stopping the electron beam in the glass material. As such, the exposure time was low. A localized phase separation occurred within the line region and the region outside of the line was not affected. This effect, together with the sharp boundaries between the irradiated and non-irradiated regions indicates the performance of electron irradiation rather than the heating effects. Fig. A5 shows the details of the line-scan irradiation.

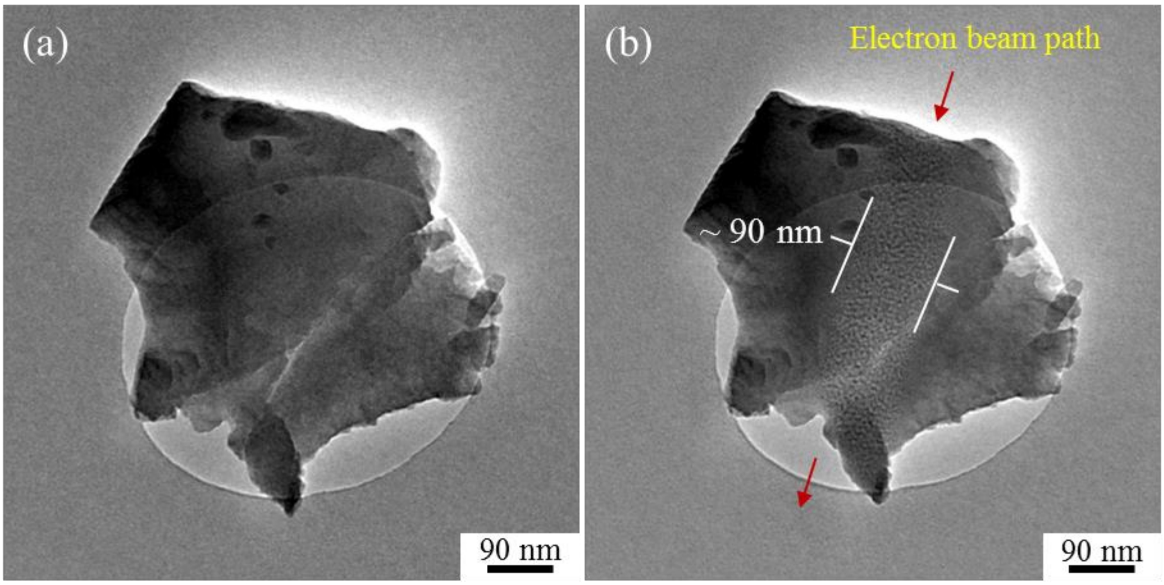

Figure A5: TEM images showing a fragment of the NLBS-CCZ glass, (a) before line-scan irradiation and (b) after performing the line-scan irradiation. JEM TEM 3010 at 300 keV.

The phenomenon of e-beam-induced phase separation was also observed in this glass via stationary electron beam irradiation. A fragment of NLBS-CCZ glass was initially irradiated for about 5 min with the largest condenser aperture and a spot size 1 using a wide diameter electron beam (Fig. A6(a)). Irradiation at such conditions resulted in microstructure modifications in the glass fragment. Possible phase separation can be induced as a result of e-beam irradiation as can be seen in Figs. A6(b, c). Then, the condenser aperture was removed and the fragment in Fig. A6(b) was irradiated for about 3 min under a high level of irradiation (maximum current density). This resulted in significant changes in the glass such as possible coarsening of the phase separated region, morphological changes and shrinkage of the overall glass fragment, as shown in Fig. A6(d).

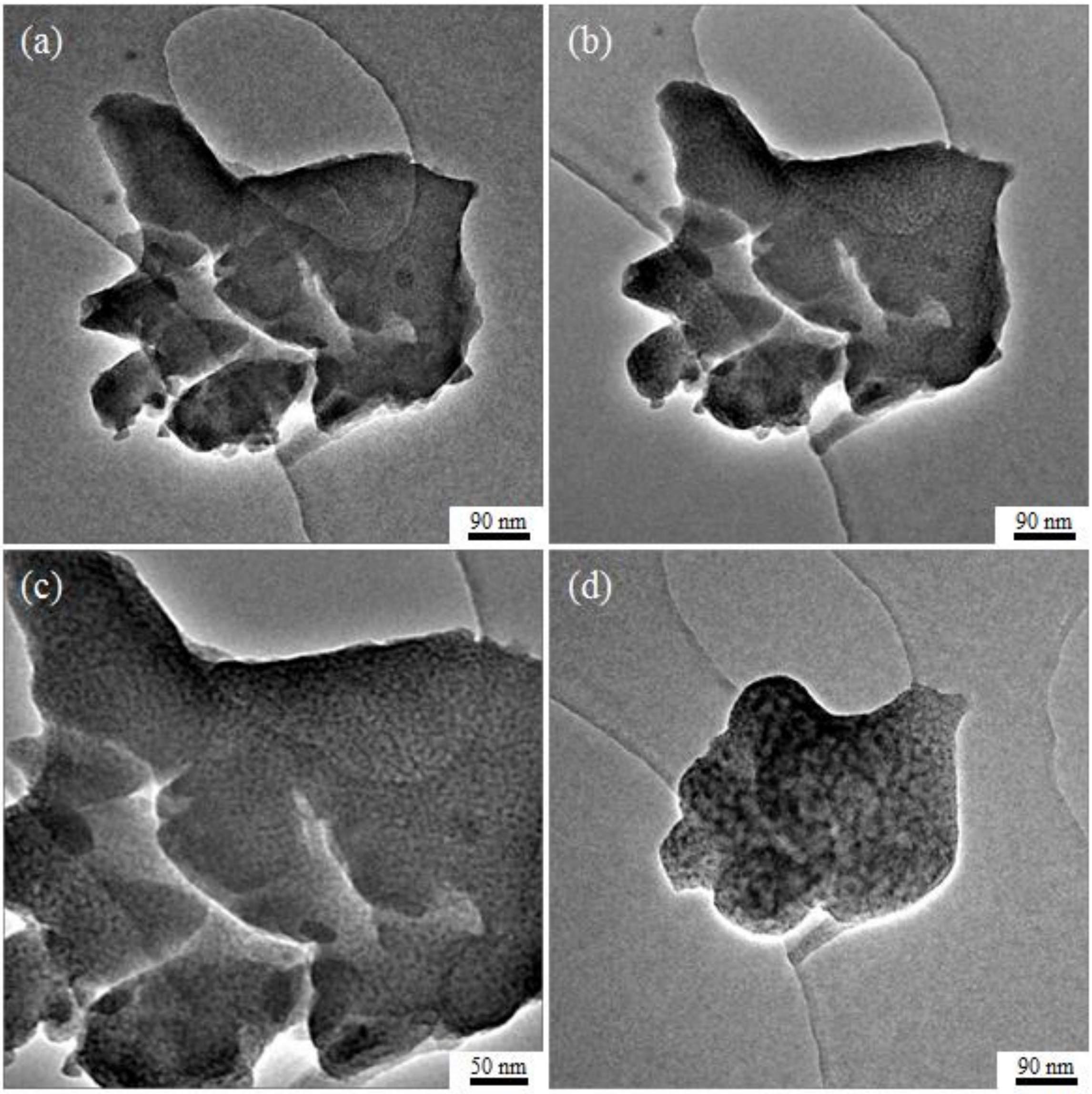

Figure 6: TEM images of a fragment of the NLBS-CCZ glass at (a) 0 min, (b) 5 min after electron irradiation, (c) high magnification image of the fragment in (b) and (d) 3 min after irradiation with no condenser aperture inserted. JEM TEM 3010 at 300 keV.

2. Electron irradiation of free standing cerium oxide (CeO_2) nanoparticle

Under electron beam irradiation, it was noticed that a free-standing ceria nanoparticle that was dispersed on the carbon film had a tendency to change its shape. A small faceted ceria NP of a size of about 30 nm (green dashed circle in Fig. A7(a)) was selected for irradiation. A focused electron beam was directed to this region for about 5 min (Fig. A7(b) was imaged during this irradiation process). Tracking the changes in the nanoparticle under e-beam irradiation was not possible here since the electron beam was focused down to its smallest diameter. Once the electron bean was spread after the irradiation was completed, the original ceria NP could be seen to have changed significantly. The shape had become irregular with a reduction in size to about 10 nm (Fig. A7(c)).

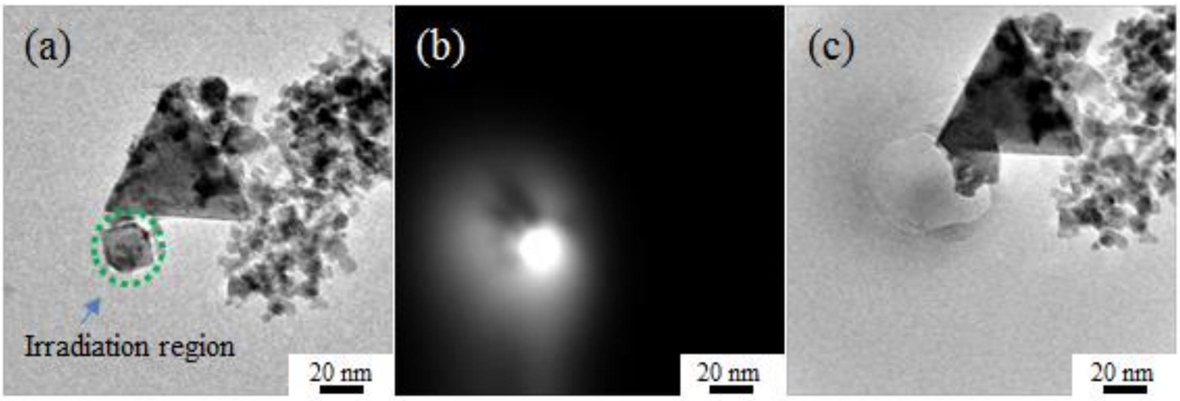

Figure A7: Ceria nanoparticle, (a) before irradiation, (b) during irradiation and (c) after 5 min irradiation. JEM TEM 3010 at 300 keV.

In addition, two significant observations can be seen as a result of irradiation: (i) the original ceria NP moved upwards and merged with a large triangle-shaped NP, which was unaffected by the irradiation as it was outside the electron beam, and (ii) the focused electron beam used in the irradiation resulted in the creation of a hole-like deformation in the carbon support film (visible in Fig. A7(c)).

Another ceria particle was imaged and irradiated at a higher magnification, as shown in Fig. A8. Here, a hexagonal-like shaped ceria particle (Fig. A8(a)) was irradiated for about 5 min. *In-situ* irradiation revealed that the shape of this particle was completely changed under the electron beam irradiation, as shown in Fig. A8(b). No sharp corners and edges were left after irradiation. Once the irradiation process was finished, the electron beam was spread and the final product was imaged, as shown in Fig. A8(c). The nanoparticle was now transformed into a halfway sphere-like shape with a reduction in the overall size. A small nanoparticle with a size of about 15 nm was attached on top of the main ceria nanoparticle, as indicated by yellow circle in Fig. A8(a). This nanoparticle also underwent transformation in its shape under electron beam irradiation, possibly melting and merging with the main ceria NP.

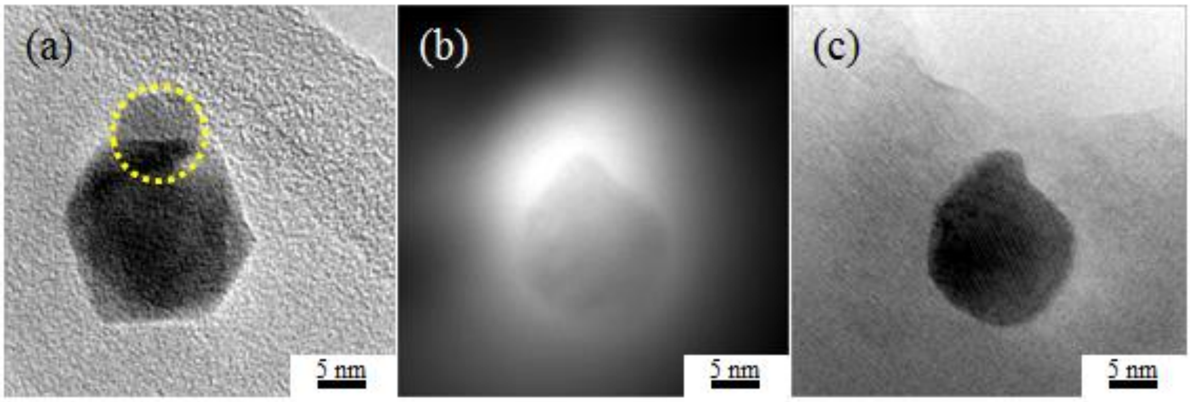

Figure A8: Ceria nanoparticle at a high magnification, (a) before irradiation, (b) during irradiation and (c) after 5 min irradiation; and the lattice fringes are visible. JEM TEM 3010 at 300 keV.

3. Electron irradiation of cerium carbonates ($CeCO_3$) particles

Different studies have been conducted into the e-beam irradiation of precursor materials and these have been reported as materials which are quite sensitive to electron beam irradiation. A commercial sample was used in the experiments conducted on these materials in this study.

A particle of this material was subjected to electron beam irradiation at 300 keV. Figure A9 shows a quite large particle being irradiated at its left edge. The sensitivity of this particle was confirmed, with tiny 1 nm pores being formed even at the very initial stages when the e-beam was being prepared for irradiation (Fig. A9(a)). After about 1 min irradiation, significant modifications in the region of irradiation occurred, as shown in Fig. A9(b)), such as the formation of several nano-pores of various sizes.

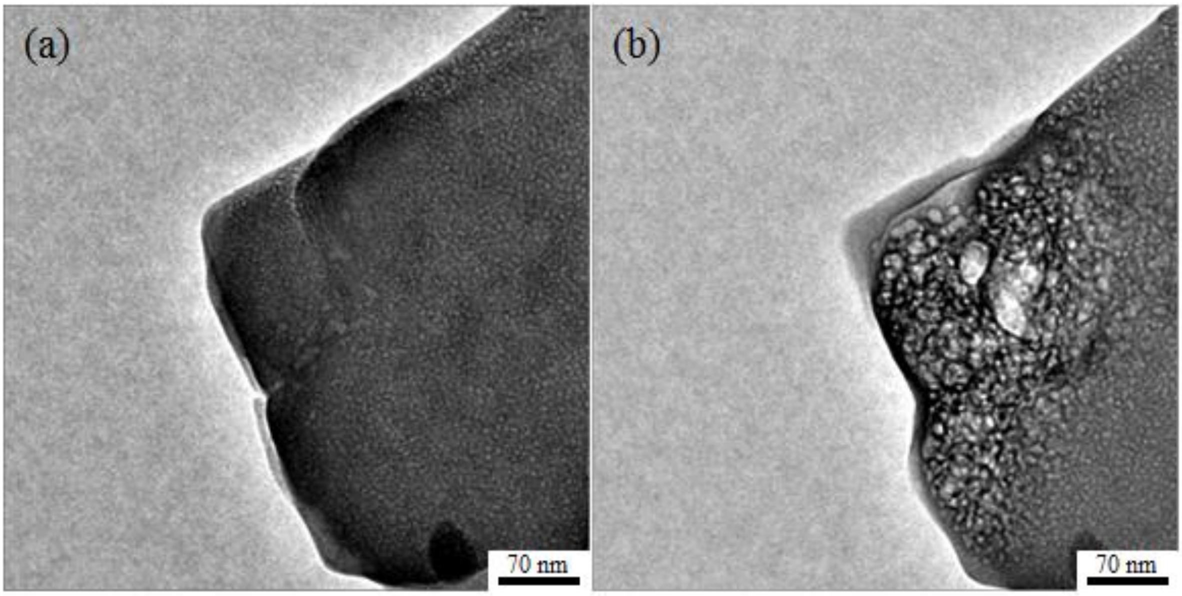

Figure 9: TEM images of a $CeCO_3$ particle at (a) 0 min and (b) ~ 1 min of electron beam irradiation. JEM TEM 3010 at 300 keV.

Another cerium carbonate particle was irradiated for about 2 min and this is shown in Fig. A10. The effect of the e-beam irradiation resulted in the formation of small nanoparticles of between 1-5 nm in size. Several HRTEM images were recorded and lattice fringes can be seen (Fig. A10(d-h). Evaluation of these lattice fringes to calculate the d-spacing showed that the values of the d-spacing all confirm the formation of cerium oxide (111) planes.

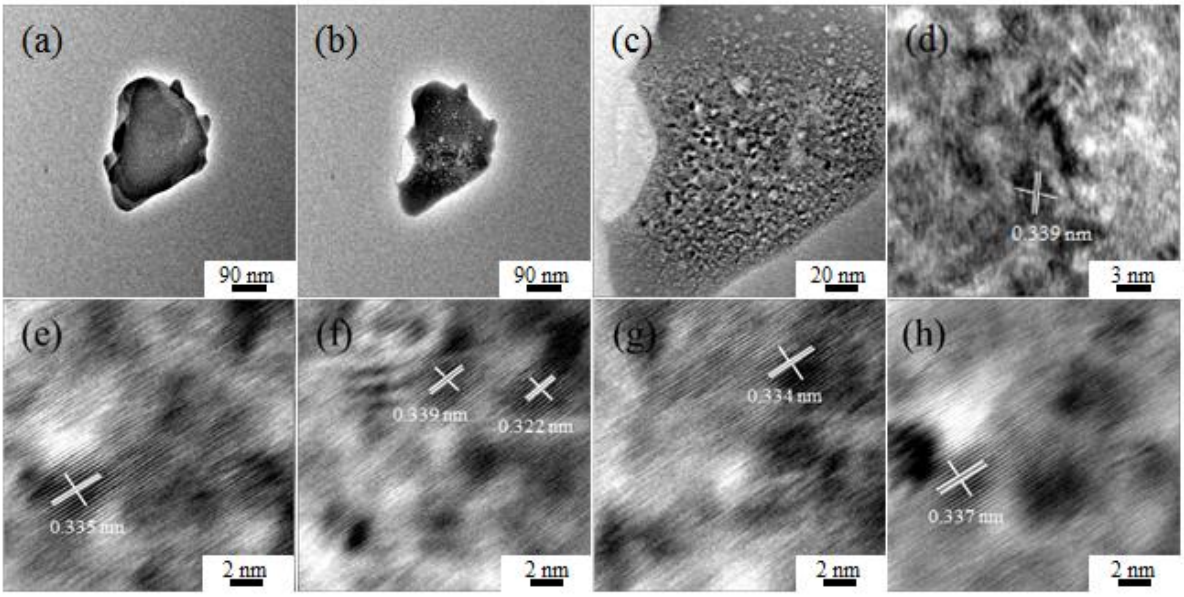

Figure 10: TEM images of a $CeCO_3$ particle at (a) 0 min and (b) ~ 2 min of electron beam irradiation. (c-h) higher magnification images of the irradiated region in (b). JEM TEM 3010 at 300 keV.

Appendix II

Workshops and seminars attended during my PhD study

- Tools for Literature Styles (LIB113) (Monday 29/10/2012).

- Introduction to Referencing Style (LIB112) (Wednesday 07/11/2012).

- Advanced Internet Searching for High Quality Research Information (LIB114) (Tuesday 27/11/2012).

- Introduction to EndNote (LIB116) (Wednesday 28/11/2012).

- Freely Available Academic Research Sources on the Open Web (LIB115) (Tuesday 18/12/2012).

- Getting the Most from Supervision (RIS-004) (Tuesday 21/05/2013).

- Managing and Maintaining your Motivation (RIS-005) (Friday 28/06/2013).

- Collaboration and Impact workshop (Wednesday 03/07/2013).

- Invitation to Research Networking (Monday 08/07/2013).

- DDP Review (Tuesday 23/07/2013).

- Assertiveness Skills-develop your confidence (GRO-015) (Thursday 25/07/2013).

- University of Sheffield Enterprise-PGR Summer Event (USE-001) (Monday 29/07/2013 to Wednesday 31/07/2013).

- STA-Assessment and Feedback (GSC624) (Friday 04/10/2013).

- STA-Small Group Teaching: Laboratory Demonstration (GSC623) (Monday 07/10/2013).

- STA-Research Supervision (GSC625) (Tuesday 08/10/2013).

- STA-Large Group Teaching-Lecturing (GSC622) (Wednesday 09/10/2013).

- Managing Yourself (RIS-006) (Certificate is attached) (Thursday 06/11/2013).

- 10 min presentation filming (Wednesday 15/01/2014).

- Effective Presentation and Seminar Participation (Thursday 23/01/2014).

- Presentation Skills: A master class (Monday 27/01/2014).

- STA-Small Group Teaching: Seminar Facilitation (GSC621) (Wednesday 29/01/2014).

- Effective Presentation and Seminar Participation (Tuesday 04/02/2014).

- Negotiation: Taking control of working relationship (Wednesday 05/02/2014).

- Introduction to Communications and Presentation Skills (RIS-003) (Monday 17/02/2014).

- Introduction to Scientific Thinking (Tuesday 04/03/2014).

- Viva survivor course (Friday 14/03/2014).

- Presenting Yourself and Data at Conferences (Tuesday 06/05/2014).

- Sheffield University GRAD School (Monday 12/05/2014 to Wednesday 14/05/2014).

- Research Data Management (RDM) and effective research practice. Looking after your research data at all stages of your research project and beyond (LIB119) (Thursday 15/05/2014).

- Where to publish and Why (Friday 16/05/2014).

- The MSE Laboratory Induction for Demonstrators (Thursday 18/09/2014).

- IEEE Xplore Workshop. Meet the expert event (Friday 21/11/2014).

- Thesis Writing Seminar (Wednesday 26/11/2014).

- Introduction to MatLab (Monday 01/12/2014).

- Creativity for Researchers (Friday 05/12/2014).

- Thesis Writing Seminar / Faculty of Engineering only (Monday 08/12/2014).

- Large Group Teaching: Problem-Solving (Wednesday 21/01/2015).

- Managing Inappropriate Behaviour by Students (Monday 26/01/2015).

- Half-day Academic Writing Retreat (Friday 29/05/2015).

- Your PhD….What Next? (CAR-010) (Tuesday 09/06/2015).

- The Challenge of Supervising Others (Wednesday 10/06/2015).

- Invitation to attend Focus Group for STA Workshops Review (Monday 29/06/2015).

- Steps Towards Research Independence Symposium (Wednesday 15/07/2015).

Doing both the Sheffield Teaching Assistant (STA) courses and the laboratory induction for demonstrators gave me an opportunity to be a facilitator in a compulsory ethics module for postgraduate research (PGR) students and also to do lab demonstration.